

Express analysis of actual bluntness of AFM probe tips



Thesis submitted in fulfilment of the requirement for the degree of
Doctor of Philosophy

By

Zaynab Naif Rasheed Alraziqi

Institute of Mechanics and Advanced Material Engineering

Cardiff School of Engineering

Cardiff University

United Kingdom

2017

Publications:

- Z. N. Alraziqi, N.F. Mukhtar, and E. B. Brousseau, “Comparison of two AFM probe inspection techniques for three-dimensional tip characterisation.,” Proceedings of the 16th International Conference of the European Society for Precision Engineering and Nanotechnology, pp. 59–60, Nottingham, UK, May 2016.
- Z. N. Alraziqi, E. B. Brousseau, F. M. Borodich, “Studies of actual shapes of probes used for AFM tip-based nanomachining,” in 9th Nano congress for next generation, vol. 7, no. 4, pp. 42, Manchester, UK, Aug.2016. (as presenter)
- Z. N. Alraziqi, E. B. Brousseau, F. M. Borodich, “A new metric to assess the tip condition of AFM probes based on three-dimensional data”, The International Conference for Students on Applied Engineering, Newcastle, UK, October 2016.
- Z. N. Alraziqi, E. B. Brousseau, “Radius evaluation of AFM probe tip using Two Different characterisation device”, Nanoscience: A celebration Conference, Cardiff, UK, May 2017.(as presenter)

DECLARATION

This work has not been submitted in substance for any other degree or award at this or any other university or place of learning, nor is being submitted concurrently in candidature for any degree or other award.

Signed (Zaynab Alraziqi) Date

STATEMENT 1

This thesis is being submitted in partial fulfilment of the requirements for the degree of PhD

Signed (Zaynab Alraziqi) Date

STATEMENT 2

This thesis is the result of my own independent work/investigation, except where otherwise, and the thesis has not been edited by third party beyond what is permitted by Cardiff University's policy on the Use of Third Party Editors by Research Degree Students. Other sources are acknowledged by explicit references. The views expressed are my own.

Signed (Zaynab Alraziqi) Date

STATEMENT 3

I hereby give consent for my thesis, if accepted, to be available for photocopying and for inter-library loan, and for the title and summary to be made available to outside organisations.

Signed (Zaynab Alraziqi) Date

ABSTRACT

The Atomic Force Microscope (AFM) is an invention that has enabled a significant number of studies and discoveries in the field of nanotechnology. It is well-known that the resolution of AFM-based applications is critically dependent on the tip bluntness of the probe utilised. Numerous researchers have proposed different approaches to assess the condition of AFM probe tips. In spite of these efforts, further advances are still needed for the express analysis of the bluntness of such tips. In this context, the overall aim of the research work presented in this Thesis was to investigate a novel in-situ technique for assessing the apex condition of AFM tips. In particular, this technique relies on the analysis of depth-sensing data obtained from the nanoindentation of the probe tip into a soft elastic sample. Nanoindentation is a process that is readily implemented on AFM devices. For this reason, the proposed technique could be a fast and efficient approach for deciding when AFM probes should be replaced. The theoretical argument on which the technique is based is that the current shape of the tip apex in its working position within an AFM device can be approximated as a power-law function and that the exponent of this function can be used as a quantitative measure of the tip bluntness. Based on this approximation and the use of the self-similar (scaling) approach to depth-sensing indentation, it is possible to extract this bluntness parameter, herein also referred to as the degree of tip bluntness, from AFM nanoindentation data.

The practical implementation of this technique was realised using a commercial AFM device and commercial probes. The actual geometry of the apex of these probe was also studied in details using additional experimental methods via the use of Scanning Electron Microscopy and also via the so-called “reverse imaging” method to obtain two- and three-dimensional data about the tip apex of these probes. Among the different

contributions made from the work carried out in this research, the most important conclusion is that a good agreement was found between values of the bluntness parameter evaluated by the proposed technique and the effective bluntness obtained from analysing the actual three dimensional geometry of the AFM tips. Thus, it can be argued that the technique put forward in this work for the express analysis of the bluntness of AFM probe tips using depth-sensing nanoindentation can be considered as a valid method when assessing the condition of AFM probes

ACKNOWLEDGEMENTS

First, I would like to give thanks to Allah the almighty, the all great without whom I could not have completed this educational endeavour.

I am deeply indebted to the Iraqi army and People's Mobilization (*Al-Hashd Al-Sha'abi*) for defencing the homeland against the savage militants (ISIS). Without them, this work would not be possible. That is why, I dedicate this thesis to them with all my love and gratitude.

The dissertation would not have been possible without the many people who took part in my life as a graduate student. They made this time special and memorable for me.

I would like to express sincere gratitude to Dr. Emmanuel Brousseau and Prof. Feodor M Borodich my immediate supervisors, for introducing me into this fantastic research area. They are generous and patient, guiding me in the research from the beginning to the end. Words cannot express my heartfelt gratitude for their efforts towards my development as a good researcher and a future academic. I consider myself ever so lucky to have been mentored by them. Their strong understanding and passion for academic quality resonates with me in every single way and has shaped my future goals as a researcher. They offered unquestionable support through the inevitable ups and downs of this research and kept me focused, giving me sound advice in all aspects of my studentship.

Finally, this research would not have been possible without the never-ending support of my family. My husband Engineer Mukhalad Y.Alkhafaji I hope to make you proud and thanks for your patience, encouragement and support over the past difficult years. Also, My Parents who has been a welcome distraction and ray of sunshine throughout. Many thanks for my brothers for their continues support and for being truly brothers when needed. Thanks as well to Allah for his gift; my beloved Yassin and Zayd.

During my time in Cardiff University, I had the privilege of knowing and working with many great people. Extra special thanks goes to my colleagues, Ali AL-Khafaji, Raheem Al-

Musawi For their continued scientific support. Also, my deep gratitude to Adnan AL-Amili, Ali Al-Zughaibi, Zinah Ahmed and Nur Farah Hafizah. for their consistent encouragement, invaluable guidance and strong support during the course of this study.

I wish to express my sincere thanks to Cardiff University, especially the Manufacturing Engineering Centre (MEC) for the use of the facilities to pursue this research.

I will also take this opportunity to thank my sponsors at Baghdad the high committee for education development in Iraq (HCED) and Ministry of higher education and scientific research, University of technology in Baghdad, Iraq and Iraqi Cultural Attaché in London for their financial support but also for allowing me to gain an industrial perspective for my work

List of Acronym

AFM	Atomic force Microscope
2D	Two-Dimension
3D	Three-Dimension
PSPD	Position Sensitive Photodiode
FFM	Friction Force Microscopy
SEM	Scanning Electron Microscopy
MOCVD	Metal Organic Chemical Vapour Deposition
TEM	Transmission Electron Microscopy
HRTEM	High-Resolution Transmission Electron Microscopy
SWCNTs	Single-Wall Carbon Nanotubes
BTR	Blind Tip Reconstruction
R _a	Roughness
STEM	Scanning Transition Electron Microscope
UNCD	Ultra-Nanocrystalline Diamond
PC	Polycarbonate
PC	Perfect Sphere
PSC	Perfect Spherical Cap

Nomenclature

α_{feature} :	acute apex angle of the scan feature
α_{tip} :	acute apex angle of the tip apex.
P :	Load (nN)
A :	Contact area (mm ²)
a :	Radius of the contact region(nm)
E^* :	Reduced elastic contact modulus (Gpa)
ν_i :	Poisson ratio
B_d :	Function of the indenter heights
D :	Degree of bluntness
α :	Inclined angle of the AFM probe tip 12°
φ :	Total inclined angle of the cantilever after reach the maximum applied load
C_0 :	Tip apex centre at the vertical cross-section
C :	Tip apex centre at working position before indentation
C' :	Tip apex centre at the maximum depth
X	The shifting distance X between C and C'
h_t	Tip height (μm)
k	work hardening exponent of the constitutive stress-strain relationship

P_{\max} :	Maximum load (nN)
h_{\max} :	Maximum respective depth (nm)
h_f :	Residual depth (nm)
$(F-h)$:	Force-displacement
δ :	Deflection of the cantilever (nm)
h :	Nanoindentation depth (nm)
z :	Nanoindentation displacement (nm)
F :	Recorded applied force (nN)
K_n :	Cantilever normal spring constant (N/m)
K_{eff} :	Effective cantilever spring constant (N/m)
h_{max} :	Maximum penetration depth(nm)
h_f :	Residual depth (nm)
z_{max} :	Maximum displacement (nm)
F_{max} :	Maximum applied force (nN)
L :	Cantilever length (nm)
w :	Cantilever width (nm)
S_n :	Normal sensitivity of the PSPD (m/V)
V_{A-B} :	Voltage output of the PSPD corresponding to vertical deflection of the cantilever (V)
Q :	Quality factor of the cantilever

f_0 :	Unloading resonance frequency (KHz)
φ :	The total inclination angle of the cantilever ($^\circ$)
$\Delta\varphi, \gamma$:	The result angle from the cantilever deflection ($^\circ$)
α :	The mounting angle of the cantilever in the AFM ($^\circ$)
E :	The Young's modulus of the cantilever material (Gpa)
I :	The moment of inertia of the cantilever cross section (nm^4)
$h_{tip}(r)$:	a power law function of the tip profile
R :	Radius of curvature of tip profile (nm)
$f(x)$:	Polynomial function fitted to the profile data
$f'(x)$:	The first derivative of $f(x)$
$f''(x)$:	The second derivative of $f(x)$
R_{cu} :	The radius of curvature (nm)
R_{ci} :	The radius of the circle (nm)
a and b :	The coordinates of the centre of the circle on the x and the y axes
y_{ci} :	The y -coordinate of the new points on the fitted circle
n :	The number of profile point on the x axis
y_{tip} :	The real y coordinate on the tip apex profile for a given point on the x axis
V_{tip} :	Tip apex volume (nm^3)

V_{cyl} :	Imaginary cylinder volume (nm ³)
V_{under_tip} :	Volume under the tip (nm ³)
R_* :	Equivalent radius for both the cylinder and the tip (nm)
z_k :	The height of the tip for the k^{th}
n :	The total number of relevant points selected
Δx :	The distance between two pixels along the x axis
Δy :	The distance between two pixels along the y axis
$R_{(0^\circ-180^\circ)}$:	Half of the length of the 0°-180° profile cross section along the horizontal axis
$R_{(90^\circ-270^\circ)}$:	half of the length of the 90°-270° profile cross section along the horizontal axis
V_{ratio} :	Volume ratio
h_1 :	The height of the cap apex region (nm)
r_2 :	The radius of the cap apex region (nm)
h_2 :	Total height (nm)
r_2 :	Total radius (nm)
V_1 :	Volume of a spherical cap region (nm ³)
V_2 :	Volume of an inner cylinder region (nm ³)
V_3 :	Volume of half of a hollow cylinder region (nm ³)

Table of Contents

Chapter one	1
1.1 Background and motivation	2
1.2 Research goals and objectives.....	3
1.3 Structure of the Thesis	4
Chapter Two.....	6
2.1 Aim and Objectives.....	7
2.2 AFM: basic principles	7
2.3 AFM tip characterisation techniques	10
2.3.1 In-situ techniques	11
2.3.1.1 Scan of a tip characteriser made of sharp asperities	12
2.3.1.2 Scan of other specific features	17
2.3.1.3 Blind tip reconstruction method.....	28
2.3.1.4 Scan of the tip apex with an ultra-sharp tip.....	30
2.3.1.5 Estimation of a wear metric	32
2.3.2 Ex-situ techniques	36
2.4 Summary and identified knowledge gaps	39
Chapter Three	44
3.1 Aim and objective	45
3.2 Depth-sensing nanoindentation.....	46
3.2.1 The BASH (Bulychev-Alekhin-Shorshorov) formula.....	48
3.3 Shape of the nanoindenter probe tip.....	49
3.3.1. Hertz approximation and General description of the indenter shapes	50
3.3.2. Quantitative measure of the tip bluntness	52
3.3.3 Shapes of indenters used in Materials Science	55

3.4 The shape of an AFM probe tip in its working position	57
3.5 Contact problems and nanoindentation	60
3.5.1 Theoretical analysis of contact problems related to depth-sensing nanoindentation	60
3.5.2 Scaling transformations and self-similarity of Hertz type contact problems	63
3.6 Methodology for the express analysis of actual bluntness of the AFM probe tip.....	69
3.7 Conclusion	70
Chapter Four	72
4.1 Aim and objectives.....	73
4.2 Introduction	73
4.3AFM nanoindentation	74
4.3.1 Force –displacement curve analysis.....	74
4.4 Experimental set-up and procedure.....	79
4.4.1Microscopy equipment.....	79
4.4.2AFM probes and sample material	83
4.4.3Normal force calibration, F	84
4.4.4Nanoindentation process	92
4.4.5SEM data processing.....	96
4.5Results and discussion	99
4.5.1Nanoindentation	99
4.5.2SEM micrographs	110
4.6Summary	117
Chapter Five	119
5.1 Aim and objectives.....	120
5.2 Introduction	120

5.3 Experimental setup and methodology	122
5.4. Extraction of three-dimensional tip geometry.....	123
5.4.1 Methodology	123
5.4.2: Results and analysis	128
5.5 Tip apex radius measurements	134
5.5.1 Radius measurements applied on 2D SEM data	134
5.5.1.1 Methodology	135
5.5.1.2 Results and analysis	137
5.5.2 Radius measurements applied on 3D AFM data.....	140
5.5.2.1 Methodology	140
5.5.2.2. Results and analysis	140
5.5.3 Comparison the radius measurements between the 2D and the 3D data	145
5.6 Assessment of the degree of tip bluntness from power law fitting on 3D data	146
5.7 Comparison and validation of different tip shape assessment approaches	148
5.7.1 Nanoindentation and power law approaches using 2D and 3D data.....	148
5.7.2 Assessment of the tip shape when approximated as a spherical cap.....	150
5.8Summary	157
Chapter Six	160
6.1 Aim and objectives:.....	161
6.2 Introduction	161
6.3 Mathematical approach	162
6.4 Volumetric data.....	165
6.4.1 Tip volume measurement.....	165
6.4.2 Imaginary cylinder volume measurement	168
6.4.3 Numerical analysis for tip geometry assessment	169
6.5 Results and discussion	171

6.5.1 A new tip shape assessment metric: the volumetric ratio	171
6.5.1.1. Influence of tip linear portions on the <i>Vratio</i> metric	173
6.5.1.2. Method validation	176
6.5.2 Numerical determination of the degree of tip bluntness	178
6.5.3 Comparison of the degree of tip bluntness obtained with different methods	180
6.6 Summary	182
Chapter Seven	185
7.1 Contributions.....	186
7.2 Conclusions.....	187
7.3 Future work and recommendations.....	189

Chapter One

Introduction

1.1 Background and motivation

The Atomic Force Microscope (AFM) was invented by Binnig *et al.* (1982) for the primary purpose of measuring the topography of surfaces with nano-scale resolution. Since its inception, the AFM has also proven to be a powerful tool for other applications in the field of nanotechnology, such as nano-tribology investigations and nano-manufacturing (Tseng and Notargiacomo 2005). The resolution of such AFM-based applications is critically dependent on the tip geometry of the probe utilised. At the same time, the quality of the tip is strongly affected by the degradation of its apex through wear. Therefore, it is very important to implement fast, reliable and repeatable methods for the quantitative and qualitative characterisation of the tip apex.

To date, a relatively large number of research studies, which will be reviewed in Chapter 2, have investigated different techniques for this purpose. These can be broadly classified into in-situ and ex-situ techniques depending on whether or not they can be implemented on an AFM instrument. Studies that reported the implementation of ex-situ techniques, such as those of Bloo *et al.* (1999), Dongmo *et al.* (2000), Chung (2003), Liu *et al.* (2010) and Jacobs *et al.* (2016), rely on the observation of AFM probe tips using electron microscopy instruments. Despite enabling the acquisition of accurate images of tip profiles, such approaches only provide two dimensional (2D) geometry data. In addition, they require the frequent removal of probes from AFM instruments and thus, they are not suited for the true condition monitoring of AFM tips. For the above mentioned reasons, researchers developed other in-situ techniques to overcome these limitations. Some of these techniques enable the acquisition of three dimension (3D) tip

geometry data via the reverse imaging principle through the utilisation of a “special tip characteriser”, which could be commercially available as in the case of Bykov *et al.* (1998), Lucas *et al.* (2008), Calabri *et al.* (2008) and Zhenhua and Bhushan (2006) or custom-made by researchers themselves in the case of Atamny and Baiker (1995), Bao and Li (1998) and Sheiko *et al.* (1994). Such 3D data can also be obtained by scanning the tip under investigation with a sharper AFM probe such as in Gozen and Ozdoganlar (2013;2014) and Zhao *et al.* (2001). A comprehensive critic of existing in-situ and ex-situ techniques will be presented in Chapter 2. The main conclusion from this critical review is that the assessment of the condition of AFM tips remains an area of open research. In particular, it is still of current scientific interest to develop new in-situ tip apex characterisation techniques, which should be conducted on AFM devices in a simple, fast, reliable and repeatable manner.

1.2 Research goals and objectives

In this context, the overall aim of the research reported in this Thesis is to investigate a novel in-situ technique for the assessment of the apex of AFM tips. This technique relies on the analysis of depth-sensing data obtained from the nanoindentation of the probe tip into a soft elastic sample. The theoretical foundations on which this technique is based will be presented in details in Chapter 3. Essentially, it relies on the argument that the current shape of the tip apex in its working position within an AFM device can be approximated as a power-law function and that the exponent of this function can be used as a quantitative measure of the tip bluntness. Based on this approximation, it is possible to extract this bluntness parameter, herein also referred to as the degree of tip bluntness, from AFM nanoindentation data. Indeed, as will be presented in Chapter 3, this approximation enables the utilisation of scaling formulae presented by Borodich *et*

al. (2003) for nanoindentation. These lead to a fundamental relation between the depth of indentation, the load applied and the degree of tip bluntness for the unloading branch of the recorded load-displacement curve.

Thus, the particular objectives of this thesis are:

- To develop an appropriate experimental methodology such that the proposed novel in-situ technique for assessing the bluntness of AFM probe tips can be implemented based on the Borodich rescaling formulae for AFM nanoindentation tests.
- To validate the proposed technique by comparing its results with those obtained when analysing three dimensional geometry data for the AFM tips considered in this research.
- To explore the possibility of proposing additional approaches for assessing the bluntness of AFM tips based on the availability of volumetric measurements for the probes under evaluation.

1.3 Structure of the Thesis

Chapter 2 presents a review and a critical analysis of the different techniques reported in the literature for characterising the condition of the apex of AFM probe tips. Chapter 3 describes the theoretical foundations on which the proposed tip bluntness assessment technique is based. The experimental methodology for implementing this technique in practice is outlined in Chapter 4. Data obtained from nanoindentation experiments carried out on a soft elastic polycarbonate material are reported for set of different non-axisymmetric tips. In the same chapter, these data are also analysed by

applying the Borodich rescaling formulae on the unloading part of the recorded force-displacement curves in order to extract the degree of bluntness for each tip. Chapter 5 focuses on the evaluation of the suitability of this new technique by comparing its outcome with the degree of tip bluntness obtained from the analysis of different cross section profiles extracted from 3D geometry data for all probes considered. Chapter 6 extends the work conducted in Chapter 5 by employing the full set of 3D data available for a given tip, instead of selected cross sections, to perform this comparison. To achieve this, a mathematical model is developed in which the volume of the tip is expressed as a function of its degree of tip bluntness. Based on the experimental knowledge of this volume, the degree of tip bluntness could be calculated using a numerical approach. In the same chapter, an alternative metric is also reported for assessing the condition of the tip apex based on volumetric data only. Finally, Chapter 7 presents a brief summary of the research reported in this Thesis. In particular, the most significant findings and contributions are highlighted. Recommended areas for future work are also given in this chapter.

Chapter Two

Literature Review

2.1 Aim and Objectives

This chapter starts by presenting the basic working principle of an AFM together with the key components, which enable such an instrument to fulfill its range of functions. As already mentioned in Chapter 1, the resolution and accuracy of AFM measurements, and that of derived tip-based fabrication methods on the nano-scale, is critically dependent on the geometry of the probe tip. Thus, for reliability and repeatability purposes in practice and also for theoretical considerations, the accurate knowledge of the shape of the AFM probe tip is critical. For this reason, this chapter also presents a systematic review of different techniques reported in the literature to assess the geometry of the tip of an AFM probe. This review represents the main focus of this chapter and is reported in Section 2.3. The respective advantages and disadvantages are also discussed for each technique. Based on this review, a number of knowledge gaps, which support the motivation for this PhD research, are identified and presented in section 2.4.

2.2 AFM: basic principles

The focus of this section is to introduce the main components of an AFM instrument. Such basic components are required to scan the surface of a sample by enabling the detection and the control of the interaction force between the tip and the surface. They can be grouped into the following three categories, namely force sensing, actuation and feedback mechanism. These are respectively described in the following paragraphs.

The force sensing functionality of an AFM can be described as consisting of two main elements, namely the AFM probe and the instrumentation used to detect the deformation of the probe. Probes are micro-fabricated following a lithography-based process route. An AFM probe can be simply described as a cantilever on which a tip is mounted at its free end. Tips are commonly made of silicon or silicon nitride materials. Also, to increase the accuracy of image obtained by AFM, special probe tips modified to a specific interaction of interest (Medendorp 2011). They can also be coated with a layer of polycrystalline diamond to reduce wear. AFM probe cantilevers may display two different types of geometry, namely rectangular or V-shaped (Cappella and Dietler 1999). Silicon and silicon nitride are also the usual materials that cantilevers are made of. The ability to detect and control the deformation of the cantilever and hence, the force between the tip and the sample, is due to the low force constant that cantilevers possess (Carpick 1997) (Morris *et al.* 2009). In most AFM systems, the cantilever deformation is detected via the optical lever method. As illustrated in Figure 2.1, this method relies on the measurement of the intensity of a laser beam reflected from the back of the cantilever and re-directed onto a photodetector.

The photodetector can basically be considered as a position-sensitive photodiode (PSPD). This is a semiconductor device, which converts the intensity of the received laser beam into a voltage signal. As it can also be seen in Figure 2.1, the PSPD is normally made of four sections. These sections provide the ability to detect both the vertical and torsional deformations of the cantilever. In particular, based on the laser position on the PSPD, the vertical deflection of the cantilever can be determined by the difference in voltage output between the top two and bottom two sections (i.e. the $(A+B)-(C+D)$ signal indicated in Figure 2.1). In addition, changes in the $(A+C)-(B+D)$ signal results from the

voltage difference between the right side and left side of the PSPD and is due to the torsion of the cantilever. This particular output is normally used to study the friction between the tip and the surface. Thus, such a mode of operation is typically referred to as Friction Force Microscopy (FFM) as indicated in Figure 2.1 (Morris *et al.* 2009; H. J. Butt *et al.* 2005; Leite and Herrmann 2005) and (Bhushan 2008).

The second main component of AFM systems are the actuators, which ensure motions along the x , y and z directions with sub-micrometre resolution. These are most commonly made of piezoelectric materials. Thus, such actuators rely on the reverse piezoelectric effect. This means that their dimensions can change in response to an applied voltage. The piezoelectric actuator that controls the vertical displacements of the probe along the z -axis is normally integrated into the head of AFM systems in practice. It is also often referred to as the “Z-scanner”. In Figure 2.1, the motions of the stage along the x and y -axes are induced by a single piezoelectric tube. Such motions can also be realised by two separate linear piezoelectric actuators, one for each axis.

Finally, a feedback mechanism is also required to control the interaction force between the tip and the sample when the probe scans a surface. This is a software component of AFM systems, which relies on a control loop algorithm. Essentially, the principle of such a feedback loop is that it takes into account the signal from the PSPD as an input and it determines the voltage to be supplied to the Z-scanner as an output. In this way, the vertical position of the probe can be constantly adjusted during the scanning of a sample surface.

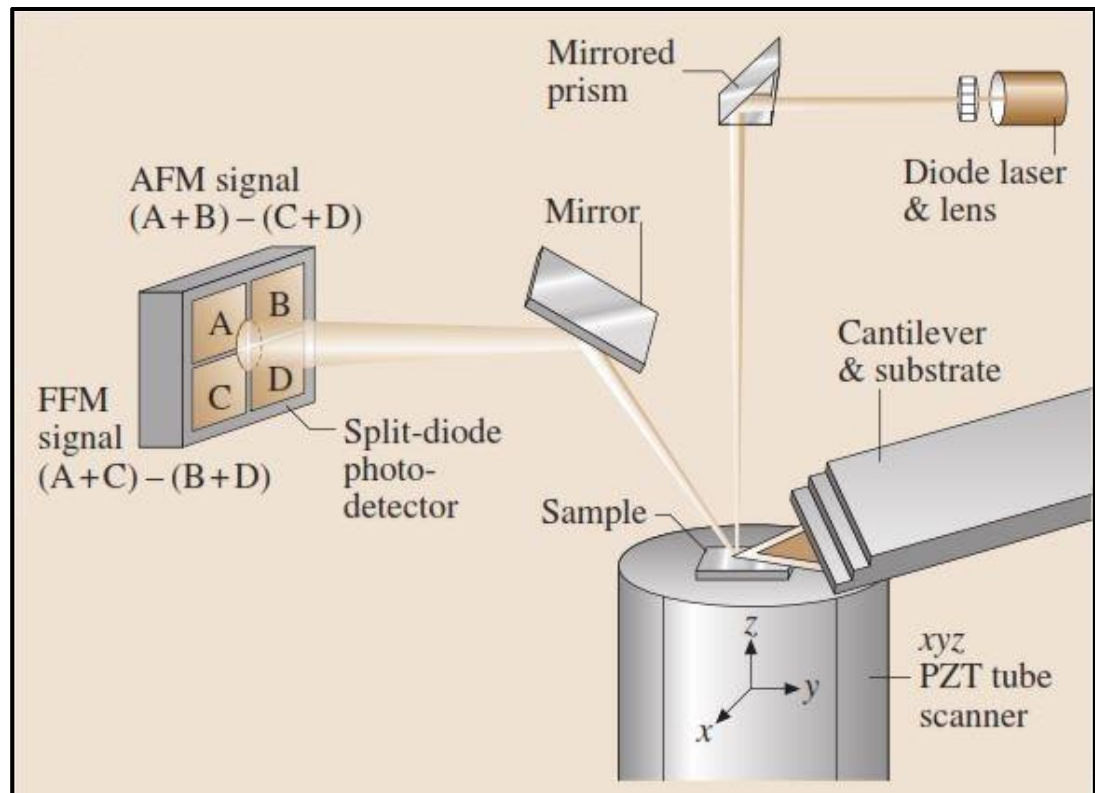


Figure 2.1 Illustration of the main components of an AFM system

(from Bhushan 2011)

2.3 AFM tip characterisation techniques

Depending on the intended AFM application, tips can be used for dimensional metrology, material characterisation or manufacturing purposes. Degradation of the tip condition may introduce important errors in the resulting outcome regardless of whether the probe is utilised as a fabrication or metrology tool (Yan *et al.* 2016) (Ramirez-Aguilar and Rowlen 1998) and (Velegol *et al.* 2003). A single tip may be employed numerous times and scanned over a distance of millimeters to kilometers during its lifetime (Liu *et al.* 2010). Thus, improving the durability of tips and a further understanding of processes that lead to changes in tip geometry have become increasingly important for the research community (Miller *et al.* 1995) (Liu *et al.* 2010). For these reasons, a number of specific

techniques have been reported in the literature over the last 25 years for assessing the geometry of the apex of AFM tips. In this thesis, such techniques are classified as either as in-situ or ex-situ approaches. In particular, an in-situ method is defined as one, which can be conducted on the AFM instrument itself, while an ex-situ technique requires the probe to be physically removed from the AFM and observed using a different microscopy instrument. The literature shows that there is a large variety of in-situ methods. These are presented in the following section. The ex-situ methods essentially consist of various electron microscopy techniques. Some selected examples of studies that employed such ex-situ, electron microscopy techniques, are reported in the subsequent section.

2.3.1 In-situ techniques

The different in-situ techniques could be grouped into four main categories. First, a number of studies have reported the utilisation of a special tip characteriser, which consists of an array of sharp pins or asperities. The second approach groups studies, which employed an alternative sample, which exhibits features that are not necessarily sharp but with a geometry that could still be used to extract tip geometric information. The third group of techniques relies on the processing of AFM scanned data using the mathematical process of dilation and erosion and is normally referred to as the “blind tip estimation” method. The fourth group of in-situ techniques is concerned with utilising an ultra-sharp tip to characterise the probe tip under investigation. Finally, the fifth group of the category relay on assessment of different wear metric.

2.3.1.1 Scan of a tip characteriser made of sharp asperities

Many researchers have used a commercial tip characteriser to extract information about the tip apex geometry. In particular, this is a test structure, which contains an array of sharp asperities. An SEM micrograph of such a test structure is shown in Figure 2.2. In practice, the tip to be assessed is scanned over the tip characteriser. Given that the scanned asperities are much sharper than the tip, the data obtained represents the tip geometry itself. This is due to the convolution effect, which is illustrated in Figure 2.3.

The main advantage of using such a tip characteriser is that it allows the acquisition of three-dimensional (3D) data of the tip geometry. This approach is also referred to as “inverse or reverse imaging” in the literature (Bloo *et al.* 1999) (Bykov *et al.* 1998) and (Jacobs *et al.* 2016). The test structure used as the tip characteriser is normally made from a high-resistivity silicon monocrystalline wafer. Generally, the height of the asperities is around 400-700 nm while their radii are less than 10 nm as shown later on in Bloo *et al.* (1999).

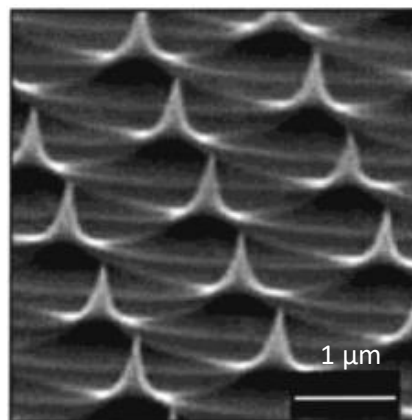


Figure 2.2 An SEM micrograph of a test structure containing an array of sharp asperities
(from Neto and Craig 2001)

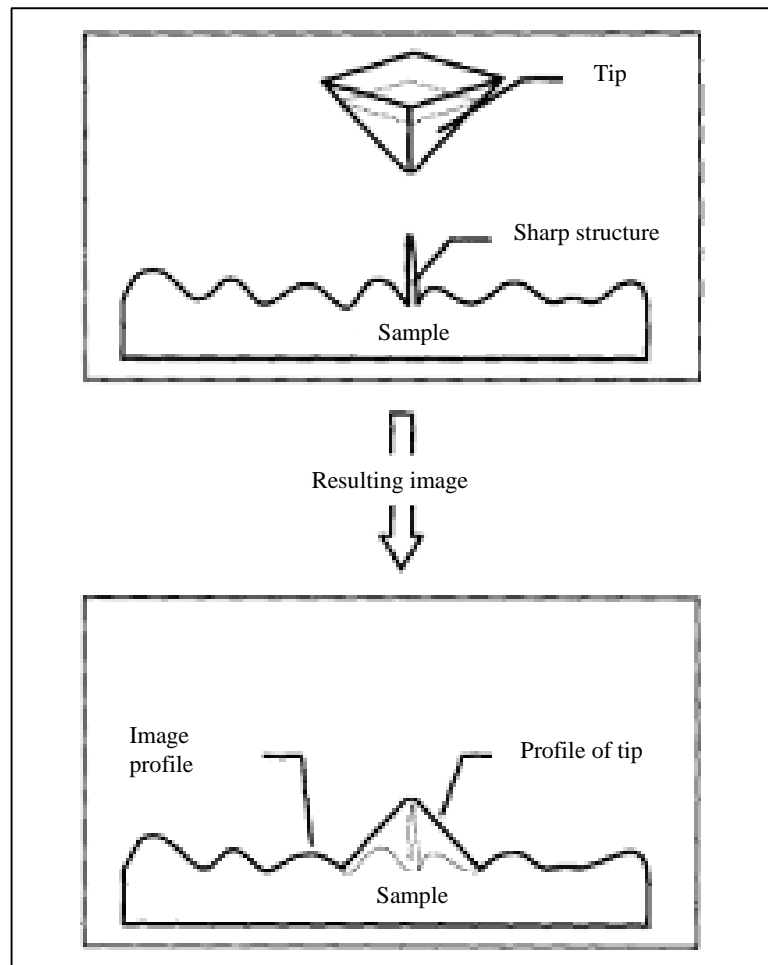


Figure 2.3 Schematic illustration of the convolution principle (adapted from Atamny and Baiker 1995)

It is argued in several studies that most of the image artifacts obtained when using scanning force microscopes (SFM) or AFM are related to the geometrical interaction between the sample being scanned and the probe tip (see e.g. the review from Yacoot and Koenders 2008). This is known as the “convolution effect”. Many research studies explained the origin of this effect which is due to such tip-sample interaction and which induces such artifacts (Schwarz *et al.* 1996) (Markiewicz and Goh 1995) (Odin *et al.* 1994) and (Montelius and Tegenfeldt 1993). In particular, the effect of this interaction on the resulting AFM scan becomes important when a scanned feature has a surface slope, α_{feature} , larger than the slope of the tip face, α_{tip} , which is defined by its acute apex angle.

This effect is also important when the radius of curvature of a scanned feature is similar to or smaller than the radius of the tip (Yacoot and Koenders 2008). The convolution effect is illustrated in Figure 2.4 in the situation where $\alpha_{\text{feature}} > \alpha_{\text{tip}}$.

It is generally accepted that when the scanned sample displays features, which are much sharper or steeper than the tip, such as those present in a tip characteriser, then the convolution effect is such that the obtained AFM image may be considered as an image of the tip rather than of the sample (Keller 1991) (Skårman *et al.* 2000). The process of exploiting this phenomenon for tip characterisation purpose is also known as the reverse, inverse or self-imaging approach. In general, it is also worth noting that for AFM practitioners, the understanding of the tip convolution effect, which due to tip-sample interactions, is critical to realise which part of a scanned image displays the geometry of the tip and which part shows the actual geometry of a scanned surface feature.

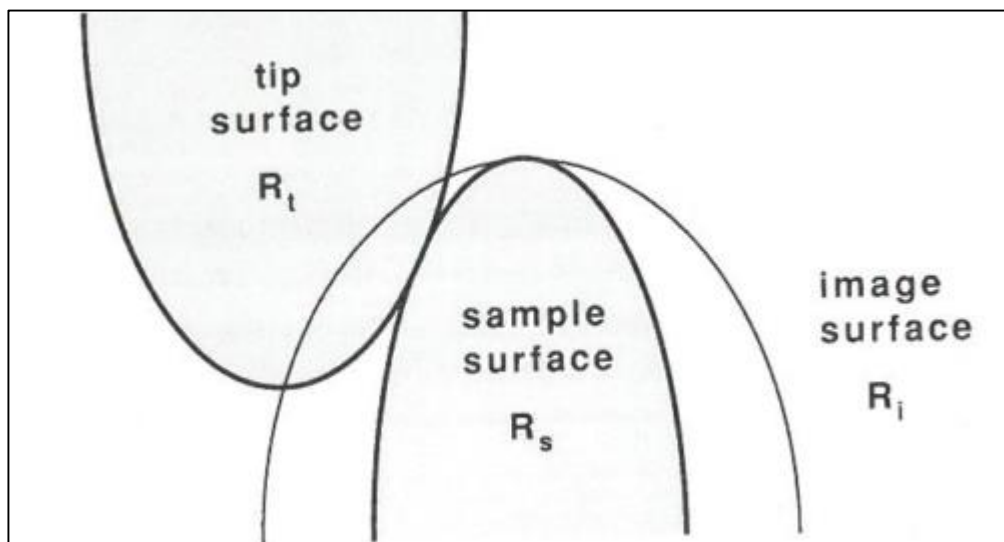


Figure 2.4 Illustration of the convolution effect when the slope of scanned feature is larger than the tip apex angle.

Bykov *et al.* 1998 were the first to report the application of a tip characteriser for the assessment of the apex of AFM probes. These authors noted that scanning such sharp asperities provided a procedure, which could be considered as a mirror transformation of the real probe shape. In this way, the authors assessed different types of tips by comparing their 3D geometry before and after contact-mode scanning experiments.

Soon after, Bloo *et al.* 1999 used the same principle to investigate both the deformation and the wear rate of AFM tips in silicon nitride. The results obtained with the tip characteriser were also validated by inspecting the tips with an SEM instrument. The test structure used as the tip characteriser is illustrated in Figure 2.5. During the experiments, the tips were deliberately subjected to wear for nearly an hour by scanning them on a Si substrate with a contact force of 100 nN. Based on the obtained 3D AFM data for a given tip, the volume loss was estimated by subtracting the volumes of the tip before and after the wear experiment.

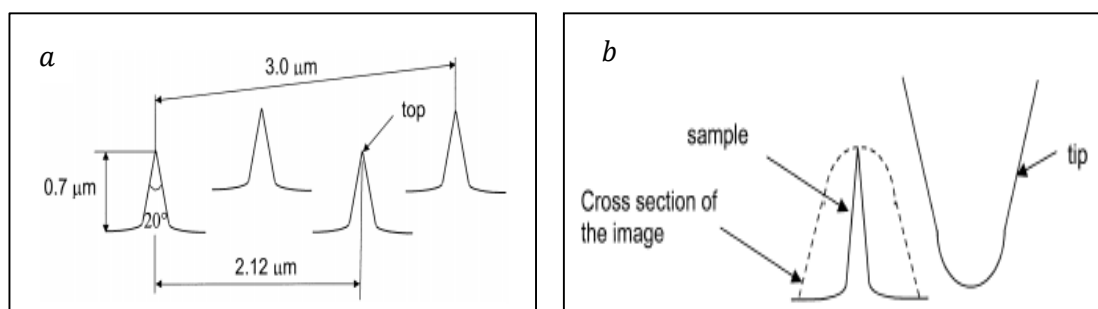


Figure 2.5 (a) Schematic representation of the tip characteriser (b) cross section of the obtained image due to the convolution effect (from Bloo *et al.* 1999)

This technique was also used by Neto and Craig 2001 to characterise colloid probes. Such a probe consists of a tip-less cantilever to which a spherical particle is attached at its free end. The authors scanned a commercial tip characteriser with such probes and

implemented the reverse imaging principle to assess the tip radius, the surface roughness and the profile of the probes, the authors recognised that the method was straightforward and that no further instrument was required to extract the desired data. The tip radius value of a scanned spherical particle was simply calculated from both the width and the height of the imaged tip characteriser.

Maw *et al.* 2002 studied the wear of silicon nitride tips in aqueous solutions as a function of both the applied force and the scanning time using a variety of substrates. For each tip, the wear was assessed at different distances throughout the experiments until a maximum sliding distance of 67.5mm. In this study, the authors also used a commercial tip characteriser made of an array of sharp asperities, which were about 600 nm in height and which had a tip radius less than 10 nm. By scanning the probes over the tip characteriser before and after the wear experiments, it was possible for the authors to compare the change in the tip shape as the example shown in Figure 2.6 illustrates. The obtained AFM scans were subsequently analysed to evaluate the area at the end of worn tips and also to determine the change in tip height as a result of wear.

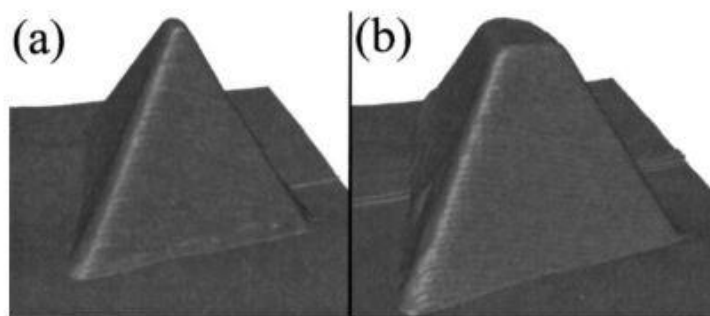


Figure 2.6 AFM image of (a) a unused AFM tip and (b) the same tip after wear (from Maw *et al.* 2002)

Overall, it was noted by researchers such as Odin *et al.* (1994), Montelius and Tegenfeldt (1993) and Keller (1991) that tip characterisers with asperities which are sharper and steeper than the probe tip are the most suitable objects for obtaining the most accurate geometric information about the assessed tip apex. However, it should also be noted that the tip radius of curvature measured from the obtained AFM image is equal to the sum of both radii of the tip and the sharp asperity scanned (Keller 1991). For a given tip, it may be reasonably assumed, as a first approximation, that the contribution from the sharp asperity could be neglected if the radius of the asperity is an order of magnitude smaller than that of the tip.

2.3.1.2 Scan of other specific features

In addition to sharp asperities, other types of features or nanoscale objects have been used by researchers for the purpose of characterising the apex of AFM tips. These represent various alternatives, which are also based on the reverse tip imaging or tip convolution principle. These features includes nanoscale rectangular columns, flat top protrusions with undercuts on the side walls, nanoscale ridge features, colloidal particles, single-wall carbon nanotubes and circular depressions with vertical walls. Studies in which such features were employed are now reported in this section.

Montelius and Tegenfeldt (1993) claimed to report the first study where the implementation of the reverse AFM imaging principle was demonstrated in practice. To achieve this, the authors scanned a V-shaped Si_3Ni_4 tip over a specially fabricated sample that exhibited an array of columns about 60 nm in width and 100 nm in height (see Figure 2.7(a)). These columns were fabricated using dry plasma etching on an InP substrate over which metal particles acting as an etch mask had been previously deposited using an

aerosol-based technique. As explained by the schematics reported in Figure 2.7(b), the obtained AFM images displayed a small plateau on the top of the scanned features, which did not correspond to the actual shape of the tip apex. This artifact was due to the fact that widths of the top part of the columns were blunter than the tip apex of the Si_3Ni_4 probes. Thus, it could be argued that this approach did not represent a suitable method for the accurate data extraction of the shape of the tip apex.

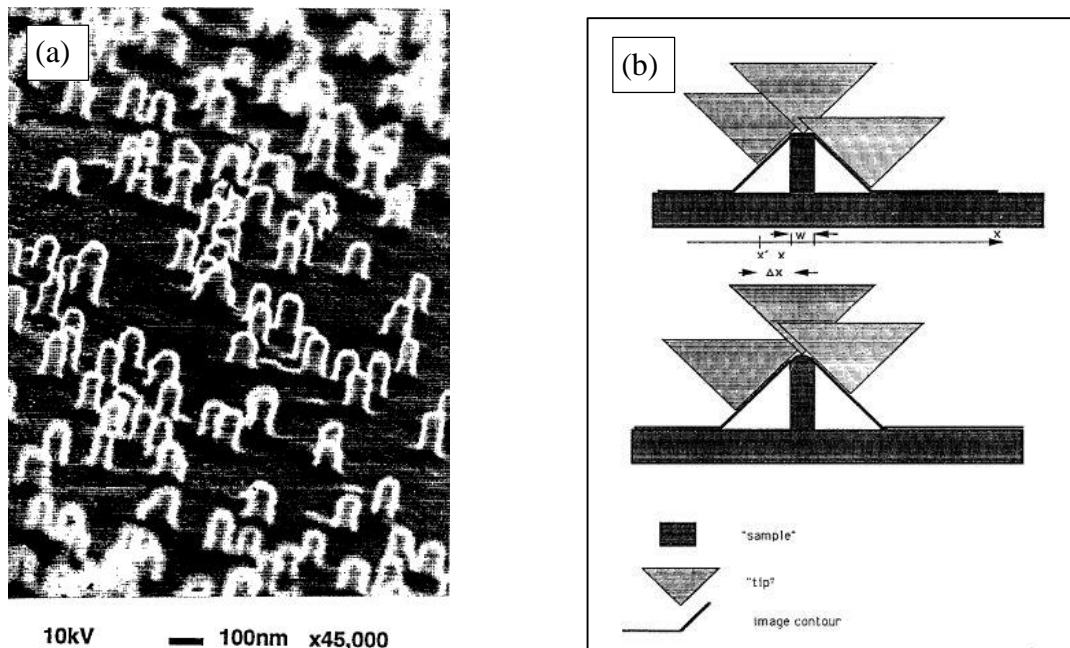


Figure 2.7 (a) SEM micrograph of the arrays of nano-scale columns used by Montelius and Tegenfeldt and (b) schematic representation of the observed tip-sample convolution in the cases of a flat-top column and a column with a top having a parabolic shape (from Montelius and Tegenfeldt 1993)

In the early nineties, Grigg and co-workers presented an in-situ method to characterise AFM probes by scanning pillars exhibiting undercut side walls (Griffith *et al.* 1991) and (Grigg *et al.* 1992). The general concept for extracting the tip shape when employing such structures is illustrated in Figure 2.8(a). Using this method, the obtained profile of the sidewalls reflects the shape of the tip apex as the probe scans the side of the pillars. In order to implement this technique, a rather complex sample preparation process

using special laboratory equipment must be followed. In addition, the width of a scanned pillar must be known a priori and thus, measured using a different method, in order to isolate, and subsequently reconstruct, the profile data, which correspond to the shape of the tip apex. Some sources of error associated with this method may also result from the quality of the pillars, specifically the pillars edge sharpness and pillars size uncertainty. Indeed, the roughness on their top region could produce waviness on the edges of the pillar leading to uncertainties when distinguishing data to be used for reconstructing the tip profile from those that belong to the sample surface. These disadvantages make this technique less suited for practical and accurate tip assessments.

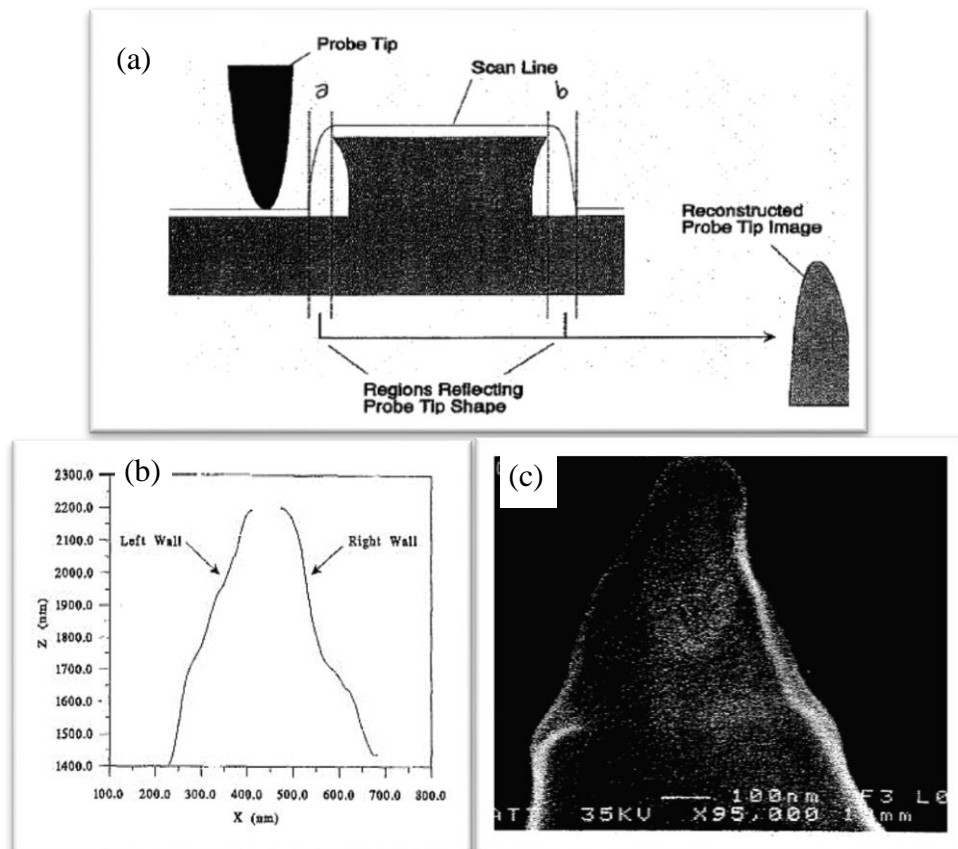


Figure 2.8 (a) Schematic diagram of the method implemented by Grigg *et al.* (1992) for characterising AFM probe tips, (b) reconstructed shape of the tip after scanning two opposing sidewalls and (c) corresponding SEM micrograph of the tip.(from Griffith *et al.* 1991)

The direct imaging approach has also been achieved by Atamny and Baiker (1995) for characterising the apex of Si_3N_4 AFM tips. These authors fabricated their own sharp pin-like protrusions. These were present on copper films when deposited on quartz by metal organic chemical vapour deposition (MOCVD) (see Figure 2.9(a)). These structures exhibited side wall angles that were much steeper than the angle of the probe tip. The lateral dimensions of these pin-like structures were 100 nm, while their height was 300 nm. The authors also reported that the finite size of the top part of such protrusions was about 30 nm, which was of a similar size to that of the inspected tip apex. However, it was not clear to which specific geometric metric this dimension referred. Figure 2.9(b) reports the image of the tip geometry obtained by these researchers. However, similarly to the comment made earlier about the study from Montelius and Tegenfeldt (1993), it is argued that when using this approach, the obtained tip profile around the tip apex region is not imaged correctly due to the column blunted end.

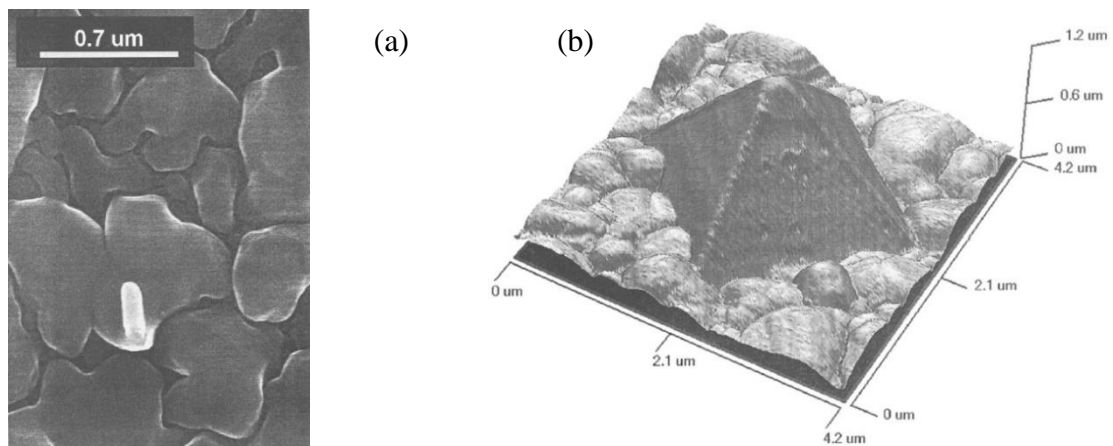


Figure 2.9 (a) SEM micrograph of the structure used by Atamny and Baiker and (b) AFM image obtained following the scan of the tip across this pin-like protrusion (from Atamny and Baiker 1995)

The same reverse imaging principle applied on a purposely-prepared sample was also implemented by Bao and Li (1998). The sample fabricated by the authors consisted

of spike-like crystallites features present on zinc oxide thin films, which had been coated on glass slides by hydrothermal deposition. The radius of the apex of the spike-like crystallites was reported to be less than 30 nm, while the aspect ratio of the spikes was than 1:20. In this study, different types of AFM tips were investigated, namely a Si₃N₄ tip, a broken ultra-sharp silicon tip and a non-contact silicon tip. The authors compared the respective cross-section profiles of different tips based on the obtained AFM scans. However, they did not compare the validity of these results against those which could be acquired using another method such as electron microscopy. In spite of that, the authors concluded that using ZnO crystallites as a sample for AFM tip characterisation was a suitable approach. The authors claimed that a significant advantage of their approach is that the method needed for fabricating the required sample does not require complex chemical laboratory equipment. However, as noted in this study, this method does not guarantee that all such spike-like protrusions could be oriented normal to the plane of the substrate. This drawback is likely to result in uncertainties when analysing an AFM scan as the analysis of the data should be conducted on the scan of a vertical spike.

A CeO₂ thin film grown on a Al₂O₃ substrate was utilised by Skårman *et al.* (2000) to estimate the tip quality of four different Si probes that had been used in tapping mode, i.e. intermittent contact mode. The authors considered this particular sample because the surface of the thin film exhibits sharp crystalline ridges, which are near atomically sharp with only up to three atoms missing at their apex. A high-resolution TEM (HRTEM) instrument was also employed to record the exact geometric profile of these tips with nanoscale resolution before and also after tapping mode imaging operations. Based on the qualitative analysis of the AFM images obtained by scanning the different probes over

the CeO₂ thin film, the authors concluded that this type of substrate could be used successfully to analyse the condition of AFM probe tips.

Iton *et al.* (2006) also prepared their own sample using semiconductor fabrication techniques on a GaAs substrate. This sample consisted of parallel rectangular protrusions with vertical walls while their widths had different values as shown in Figure 2.10(a). The widths of the thinnest structures were measured to be less than 10 nm, while their top surface displayed a rounded shape with a radius of curvature less than 5 nm. The AFM profile obtained when scanning such thin protrusions with the tip of interest enabled the self-imaging of the probe apex (see region C in Figure 2.10 (b) and the extracted profile in Figure 2.10(c)). The protrusions with the larger widths could be used to assess the apex angle of the tip as the gap between them was too small for the tip to access the bottom surface of the substrate. This was done by relating the measured maximum depth of the scanned AFM data between two such protrusions to the width between them, which was a known quantity.

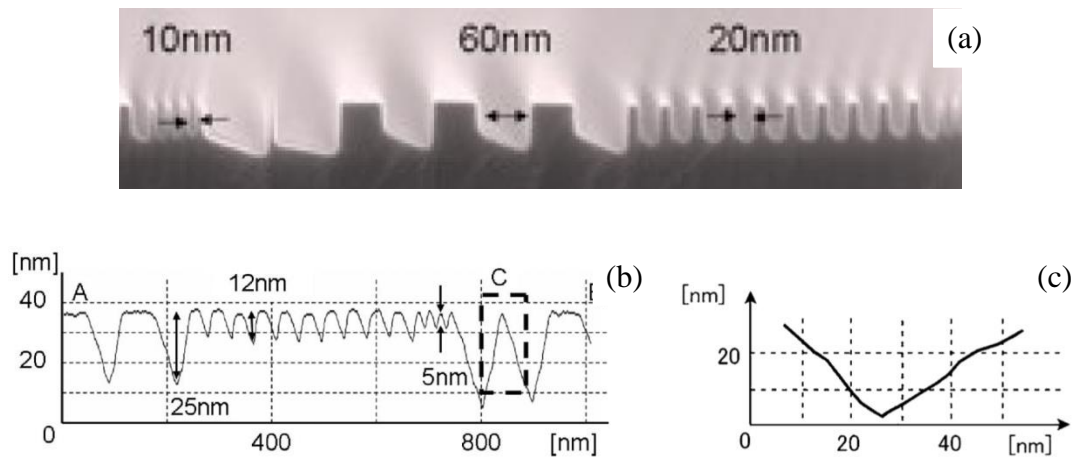


Figure 2.10 (a) SEM micrograph of the cross section of the sample produced by Iton and co-workers; (b) average line profile obtained by scanning the sample with the probe under investigation and (c) tip profile extracted from the AFM data when imaging the thinner structures (from Iton *et al.* 2006)

Vesenka *et al.* 1993 investigated the utilisation colloidal gold particles for implementing the in-situ reverse imaging approach. The authors claimed that the incompressible and spherical nature of such particles could be advantageous when characterising the geometry of AFM tips. The particles used in this study had a nominal diameter between 10 nm and 24 nm. Based on the heights and widths of the particles measured by an AFM scan conducted with the tip under consideration, the radius of its apex was calculated using a simple 2D geometric model. The radius data estimated in this way was then compared against the radius value extracted from the profile of the tip obtained with a TEM instrument. In particular, a sphere was superimposed on the TEM data to evaluate the tip radius. The authors reported that a very good agreement was found between the radius values measured with both techniques. Yet, the evaluation of the actual shape of the probe tip is not straightforward.

In a subsequent study, Miller *et al.* 1995 also employed colloidal gold particles with a diameter almost identical to those utilised by Vesenka *et al.* 1993. These authors developed a mathematical model to reconstruct the three-dimensional geometry of the probe shape based on the AFM scan of such particles. A comparison between the profile of the reconstructed tip and that obtained from a TEM image of the same tip was presented and a good agreement was found to within a few nanometers. The authors noted that several experimental sources of errors could lead to inaccurate tip reconstruction, namely the roundness of the colloidal gold particles and residual material surrounding the gold particles as a result of the sample preparation procedure used.

A similar type of substrate with colloidal particles was considered by Odin and co-worker (Odin *et al.* 1994) to determine the tip apex radius of curvature and its cone angle. In particular, the authors proposed to scan the probe under investigation over a monolayer of rigid latex balls, which had a mean diameter of 176 nm. The analysis presented assumed two possible types of tip geometry, namely a conical tip with a spherical apex and a parabolic tip. It was argued in this study that such particles have the advantage of displaying a well-defined topography and an acceptable degree of symmetry while being considered low cost as their fabrication did not require complex preparation. It was also pointed out by the authors that the obtained radius measurements are influenced by noise errors caused by the quality of the tip and of the scanned image.

Wang and Chen (2007) acknowledged the theoretical benefit of using colloidal particles for characterising the tip of an AFM probe. Indeed, due to their spherical nature, the data processing does not depend on their orientation. However, they pointed out that most colloidal particles utilised in the literature displayed relatively large diameters in comparison with tip radius values, which could be less than 10 nm. This difference could lead to erroneous estimation of the tip radius because relatively large colloidal particles predominantly interact with the walls of a sharp tip rather than its apex. In addition, Markiewicz and Goh (1995) highlighted that the inspection of tips using spheres could be hindered by the fact that the AFM scanning process itself may result in displacing such particles from the sample substrate and lead to their attachment on the surface of the tip.

Based on the limitation related to the size of colloidal particles in practice, Wang and Chen (2007) proposed to employ single-wall carbon nanotubes (SWCNTs) instead.

The authors claimed that the advantage of this approach lied in the fact that the cross section of a SWCNT is circular, similarly to the cross section of a colloidal particle, while at the same time, exhibiting a very small diameter, which was in the range 1 nm to 5 nm in the reported study. Based on the AFM scan of a SWCNT, an example of which is shown in Figure 2.11, a simple geometrical model was applied to relate the measured width and height of the SWCNT to the radius of the tip. It should be noted that possible limitations of the proposed method are that 1) the geometrical model used by the authors to process the data assumed that the tip apex is perfectly spherical and 2) errors could occur from the selection of the cross section on which to apply this model as it should be chosen perfectly perpendicular to the axis of the SWCNT imaged.

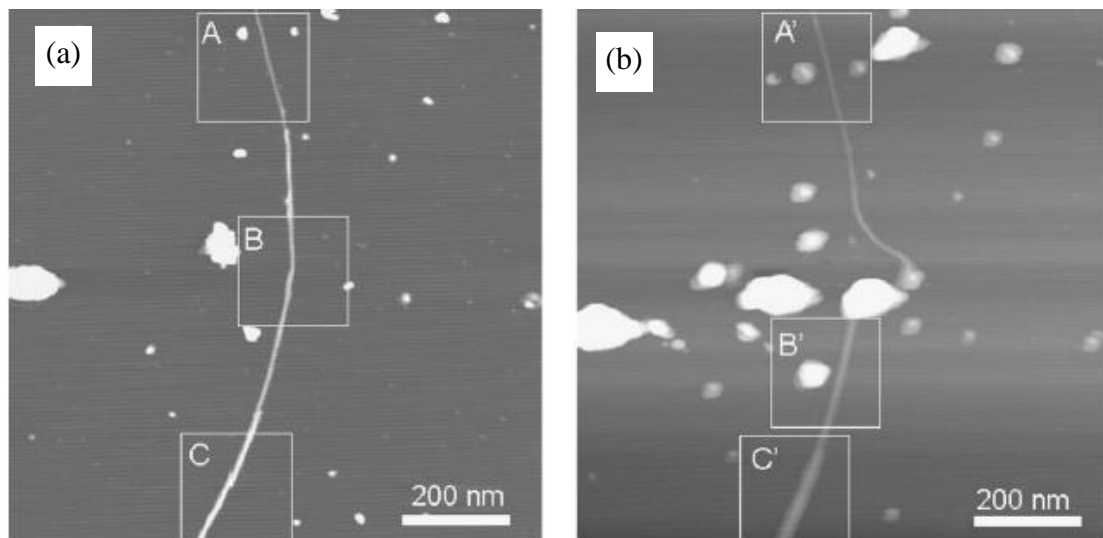


Figure 2.11 (a) AFM image of a SWCNT obtained with a new Si tip and (b) AFM scan of the same region of the SWCNT obtained after purposely blunting the tip (from Wang and Chen 2007)

Substrates containing holes with side walls, which are steeper than the angle of the tip and with an entrance diameter large enough for the tip to reach their bottom surface have also been employed to characterise the apex of AFM probes. This approach was

implemented by Glasby *et al.* 1994 who used samples made of polyethylene glycol methacrylate copolymers, which displayed a wide range of hole dimensions on their surfaces. The depths of these holes ranged from a few tens of nanometres to a few micrometres in depth (see Figure 2.11). The radius of tips could be assessed from the scanned data. The tip angle value was also evaluated by measuring the slope of the scanned hole profiles.

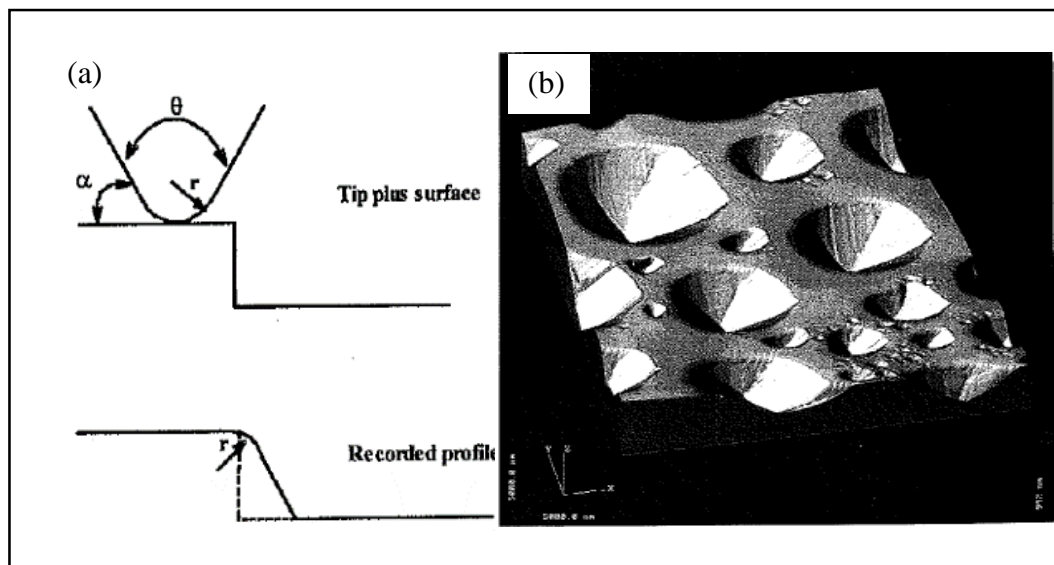


Figure 2.12 (a) Illustration of the origins of the self imaging of an AFM tip and (b) 5 μm by 5 μm image of the surface of the scanned copolymer sample (from Glasby *et al.* 1994)

Markiewicz and Goh (1995) also used the concept of scanning a substrate with circular depressions to characterise the tip apex. In particular, a commercial sample was utilised in this study, which consisted of an array of holes with a diameter of $405 \text{ nm} \pm 25 \text{ nm}$ and a depth of 200 nm. This type of sample, which could be routinely fabricated using semi-conductor fabrication techniques, would otherwise typically be used as a

calibration grid for measuring the motions of piezoelectric actuators. The authors developed a simple deconvolution algorithm to process the AFM data of the circular depressions, which had been obtained by scanning the tip under investigation over this calibration grid. The output of the algorithm, consisted in the 3D reconstruction of the tip shape. Three different types of probes were tested in this study. Based on the obtained results, it was noted by the authors that this approach could not be employed for tips with a square pyramidal shape because the regions on the tip, which did not make contact with the surface of the holes could not be reconstructed. In addition, an important source of errors was due to the relatively large variability in the diameters of the scanned holes as a result of the manufacturing process. For the particular sample used in this study, the uncertainty associated with this dimension was 25 nm. This resulted in an error of up to 25 nm in the radius of the reconstructed tip. In spite of that, the authors recommended that this approach could be suitable to perform a qualitative analysis of the condition of the tip apex.

In comparison with imaging very sharp asperities, employing such alternative nano-scale features or objects for tip characterisation generally require more complex post-processing of the scanned data to extract accurate and relevant geometric data about the tip apex. In addition, most of the approaches belonging to this group of techniques suffer from poor control of the dimensions of the used samples during their fabrication. Also, some of them have limited ability to extract the tip actual shape down to the nanometre scale.

2.3.1.3 Blind tip reconstruction method

Based on the AFM data acquired when scanning the tip under consideration over a surface, the blind tip reconstruction (BTR) is a method that can be applied to reconstruct a 3D image of the tip shape without previous knowledge of the geometry of the scanned surface. The basic principle of the BTR approach, which was established by Villarrubia (see Villarrubia, 1994 and Villarrubia, 1997) is that it allows the derivation of an outer envelope that closely approximate parts of the tip that were in contact with the sample surface during the scanning process. BTR also takes advantage of the convolution effect that is present in AFM scans due to the finite size of the tip. The idea of this technique can be seen in Figure (), more precisely in (a) where a sample surface, a tip and a corresponding image are illustrated, the maximum points of the edge of the image are labeled 1, 2, 3. In (b) two curve are shown (thick and thin black line labeled 1 and 2) referring to regions of the image in the neighborhood of the maximum points 1 and 2. These curves represent the outer bound on the tested tip. Therefore, this technique rule out any tip larger than the intersection of the two independent derived tips. The shaded area in (b) represents this intersection which could considered as a better estimation than either curve taken alone. In (c), an improvement in the image could be seen when the maximum point of curve labeled 3 is included. It was stated by (Dongmo) the following” the extension to additional image maximum follows in similar method, the method is not restricted only to the neighbourhood of the maximum. For each point on the image, even those that are not local maximum, one can derive a corresponding outer bound on the tip”. Dongmo *et al.* (2000)

An experimental investigation was reported also by Dongmo *et al.* (2000) which employed the blind tip reconstruction method to assess the shape of two diamond stylus

profiler tips. The surface scanned by such tips was a commercial roughness calibration specimen.

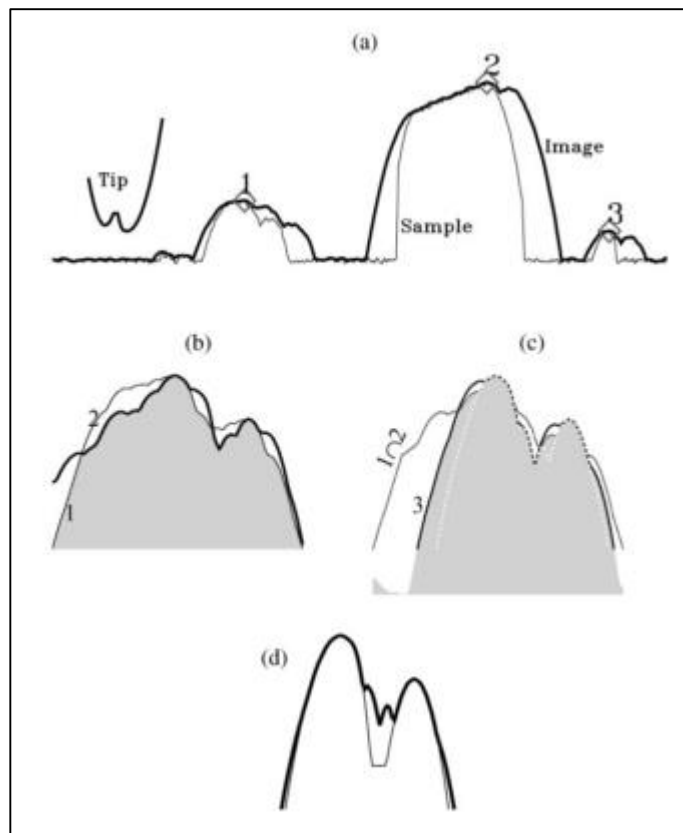


Figure 2.13 illustration of the blind tip reconstruction method. Dongmo *et al.* (2000)

This specimen exhibited a roughness profile along one axis that did not vary along the other axis, which was perpendicular to the first one. One of the tips investigated displayed a relatively smooth shape while the other had a blunter and more complex profile. When comparing the outcome of the BTR method and the profiles of the same tip obtained by scanning electron microscopy, it was shown that a good agreement could be found within about 600 nm from the apex. However, outside this range, the tip envelope reconstructed with the BTR method was overestimated.

Liu also used the BTR method, among others approaches, to investigate the wear of AFM probes (Liu *et al.* 2010). In particular, four types of commercial probes were scanned on the surface of an ultra-nanocrystalline diamond sample in contact mode and solely under adhesion forces. The reconstructed BTR profile of each tips was compared against their profiles obtained with TEM as shown Figure 2.14. Similarly to the observations made in Dongmo *et al.* (2000), a good agreement was found between both techniques only in the region close to the tip apex. In addition to the fact that the application of the BTR method was observed to be restricted to a region close to the tip apex, Wang and Chen (2007) pointed out that, in practice the accuracy of this method is also very sensitive to noise and artefacts that can be present in the analysed AFM data.

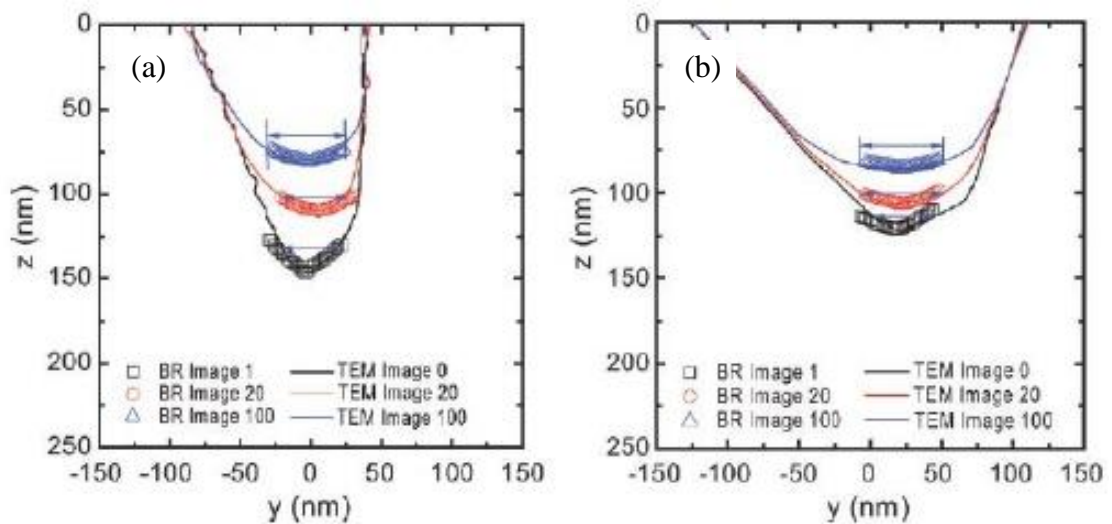


Figure 2.14 Comparison of the tip profiles measured by TEM and blind tip reconstruction for (a) a SiN_x-coated Si probe and (b) a blunter SiN_x tip (from Liu *et al.* 2010)

2.3.1.4 Scan of the tip apex with an ultra-sharp tip

This technique requires the probe to be removed from the head of the AFM instrument first. It is then located on the AFM stage with its tip facing up. In this way, its

apex can be scanned using a sharper tip. Thus, using this technique, the tip to be characterised becomes the sample. Khurshudov and Kato 1995 studied the wear of a Si₃N₄ AFM tip having a nominal radius between 10 nm and 20 nm after scanning it over a smooth Si surface with a small load of 10 nN. These authors showed that a probe of the same type and geometry as the Si₃N₄ AFM tip could be used to provide a direct observation of the tip geometry and thus, of the wear affecting it. It should be noted that this study did not employ a sharper probe to characterise the tip to be inspected. A few years later, the same authors investigated the possibility to use a micro-fabricated Si₃N₄ AFM tip to characterise the wear of an AFM diamond tip, which had a nominal radius about three to four times larger (i.e. 65 nm) than the Si₃N₄ tip (Khurshudov *et al.* 1997). In this second study from these authors, it can be argued that they implemented the “ultra-sharp tip scan” approach.

The same technique was also utilised by Zhao *et al.* (2001) to extract 3 dimensional data of a diamond tip. In this case, the tip was scanned in contact mode by a Si₃N₄ tip, which had a nominal radius about three times smaller. These authors conducted their study in the context of micro/nano machining of a polished single crystal silicon substrate with the diamond tip. In this way, the characterisation of the wear could be performed at different stages of the machining process. Gozen and Ozdoganlar (2013; 2014) also employed the ultra-sharp tip scan approach. Their study was performed in the context of realising so-called “nano-milling” operations. This is a particular process that the authors developed in an earlier study (Gozen and Ozdoganlar, 2012). These machining operations were conducted on single crystal silicon and performed using diamond AFM tips. These tips were characterised through non-contact AFM scanning at various stages of the experimentation using ultra-sharp conical tips. These measurements were used to

determine the progression of the volume of removed material on the tips and the change in the tip radius with increasing the nano-milling distance.

In a recent study conducted in the context of this PhD research, limitations of the ultra-sharp tip scan approach were presented (Alraziqi *et al.* 2016). From a quantitative point of view, it was found to be less accurate than the method relying on scanning a tip characteriser with sharp asperities. From a practical aspect, this study also pointed out that the ultra-sharp tip scan approach increased the likelihood of damaging the tip under investigation as a result of the numerous probe handling cycles, which are required when the tip apex is to be assessed. In addition, the process of precisely locating an ultra-sharp probe over the inspected tip apex proved to be a non-trivial operation, which could also lead to damaging contacts between both tips.

2.3.1.5 Estimation of a wear metric

Other in-situ approaches have been proposed, which rely on the assessment of different wear metrics. The common aspect between these approaches is that they do not lead to the direct extraction of geometric information from the tip. Instead, an indirect wear metric, which is influenced by the degree of bluntness of the tip apex, is used to evaluate the condition of an inspected AFM probe. The studies that fall in this category are now presented below.

Gotsmann and Lantz (2008) performed such as an indirect assessment of sharp silicon tips when sliding them on a polymer surface for loads comprised between 5 nN and 100 nN and over large distances (i.e. up to 750 m). The geometry of a tip was characterised at different stages of the sliding process through the completion of adhesion

tests between the tip and the polymer sample. Given that an increase in adhesion corresponds to an increase in the contact area between the tip and the substrate, measuring the force required to pull the tip off the surface could be used as an indicator of wear. A disadvantage of applying the method proposed by these authors is that a perfect flat punch geometry was assumed to represent the shape of the tip in order to relate the value of the pull-off force measured to its radius. However, in practice, the geometry of AFM tips could be quite varied.

Cheng and co-workers developed an in-situ method, which relied on the use of an acoustic transducer mounted on the top of the AFM tip (Cheng *et al.* 2011). Figure 2.15 illustrates the principle of this approach. The main idea behind it is to transmit and monitor acoustic waves along the length of the tip at GHz frequencies. Detected shifts in the resonance frequency value in comparison with the resonance value of an unworn tip were used to indicate blunting of the apex. The authors showed that their method was sensitive enough to allow the in-situ and non-contact monitoring of nanometre changes in the dimension of the apex. However, in order to implement this approach, the drawback is that the tip should be specially fabricated on a thin film piezoelectric membrane. Therefore, standard commercial AFM probes cannot be used in this case.

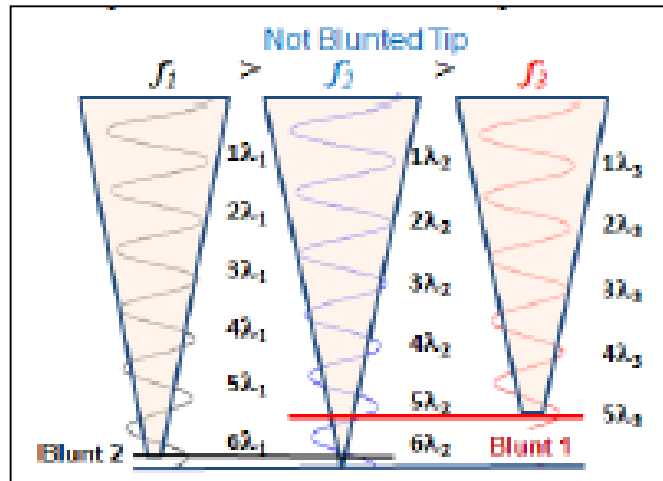


Figure 2.15 Schematic principle of the method proposed by Cheng and co-workers. Various degree of tip bluntness correspond to an increase or a decrease in the resonance frequency of the transmitted acoustic wave (from Cheng *et al.* 2011)

Huang *et al.* (2013) used two different approaches to study the effects of various scanning parameters on tip wear during tapping mode AFM operations. The first approach relied on the BTR method. This method was employed on AFM data obtained when scanning the tip under investigation over a commercially available sample, which displayed shallow but sharp nanostructures on its surface. Extracted BTR data were used to estimate the diameter of the tips. The second approach employed a tip wear metric. In particular, the arithmetical mean roughness, Ra , was also extracted from the AFM data of the sample. In this case, the evolution of the calculated Ra values as a function of the tip scanning time was considered as a tip wear index. A good correlation was found between both approaches when comparing the evolution of the tip diameter to that of the Ra values as a function of the scanning time. In particular, it was observed that the increase of tip wear increased the tip diameter and hence, reduced the measured Ra value. Accordingly, the authors suggested that the Ra metric could be employed as a suitable tip wear index.

Schmutz *et al.* (2010) introduced a technique, which aimed to evaluate changes in the mass of the tip by measuring the change in the resonance frequency of the cantilever (see Figure 2.16). To implement this approach, the authors employed colloid probes, which consisted of small spheres a few micrometres in diameter attached to the tip. Based on the results obtained after conducting wear tests on different combinations of probe and sample materials, it was concluded that the technique was able to detect the increase or decrease of the tip mass down to some picograms. The authors also claimed that the developed technique was at least as precise as a SEM measurements of the tip shape.

Generally, an important limitation associated with the assessment of a wear metric is that it is generally not possible to derive geometric information about the real shape of the tip from the measured physical quantity.

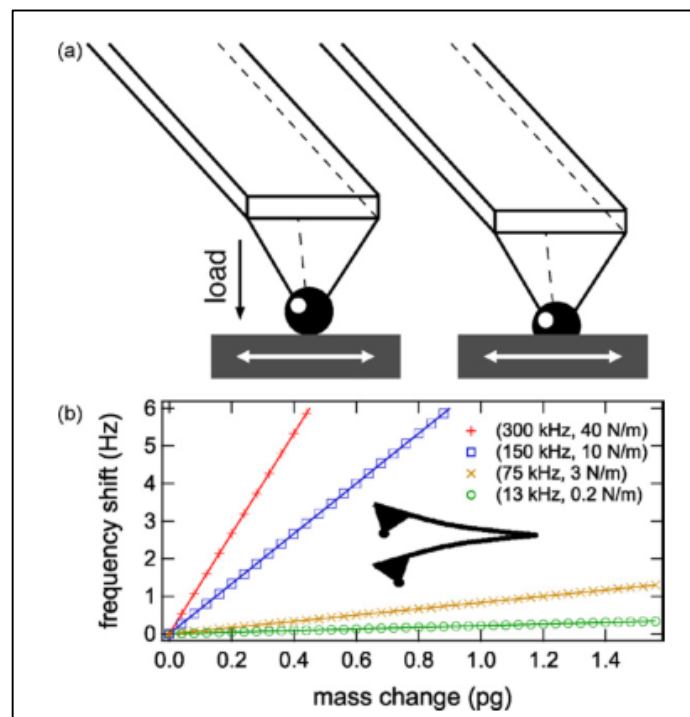


Figure 2.16 Basic principle of the wear measurement procedure introduced by Schmutz and co-workers (a) wear of a colloidal probe and (b) graph showing the linear relationship between the resonance frequency shift and the worn mass for four different types of cantilevers (from Schmutz *et al.* 2010)

2.3.2 Ex-situ techniques

The different approaches in this category include scanning electron microscopy (SEM), transmission electron microscopy (TEM), Scanning TEM (STEM) or High-Resolution TEM (HRTEM). From the literature, it is clear that numerous studies used one or several of these electron microscopy techniques to assess the geometry of AFM tips. Thus, only a few examples of the application of electron microscopy for the purpose of AFM tip characterisation are reported here.

Lantz and co-workers used STEM to image different types of probes (Lantz *et al.* 1998). In particular, the overall objective of this study was to investigate the reliability of semiconductor and metal coated tips when performing conducting AFM experiments. In this context, STEM was used as a tool to assess the tip wear and thus, to support the interpretation of the obtained conductivity data following the AFM experiments. The tested tips were only imaged after the AFM experiments to avoid contamination during the STEM imaging process. It is also worth noting that the authors reported damaging some of the used tips when removing them from the AFM probe holder.

Electron microscopy is also often used following tip sliding tests for investigating the wear process of AFM probes. For example, Chung and Kim analysed the wear of Si and Si₃N₄ tips by observing changes in their geometry from SEM images (Chung and Kim, 2003). The SEM micrographs were obtained before and after sliding tests realised on different substrate materials for a range of applied loads between 10 nN and 800 nN. Bhaskaran *et al.* (2010) used both SEM and TEM data to characterise the geometry of ultra-sharp tips made of diamond-like carbon with silicon before and after sliding tests. In this way, tip wear volume values could be estimated as a function of the sliding distance

on a SiO₂ substrate for applied loads, which were less than 20 nN. Such small loads are typically applied during AFM imaging in contact mode.

A HRTEM instrument was utilised by Chung *et al.* to study the nano-scale wear mechanisms affecting silicon tips when sliding them on diamond-like carbon and silicon substrates for applied loads comprised between 10 nN and 100 nN (Chung *et al.* 2005). In addition to the sliding tests, tip damage was also assessed as a result of the typical tip AFM approach process. Liu *et al.* (2010) reported the utilisation of a TEM instrument to study the nano-scale wear of four types of commercially available AFM tips (i.e. a single crystalline Si tip, a SiN_x-coated Si tip, a sharpened SiN_x tip and an unsharpened SiN_x tip). In this study, the wear tests consisted in scanning the tips on an ultra-nanocrystalline diamond (UNCD) sample surface in contact mode under adhesion forces alone. It was argued by Seah that determining the tip boundary using TEM could be problematic (Seah, 2004). A large scattering was found during the measurement of the thickness of thin SiO₂/Si films via different instrument used by different users. This implies that the detection of the silicon probe tip profile where the thickness is very thin could lead to erroneous results. In addition to that, the evaluation of the diameter of nanoparticles using TEM by different users has been shown to lead to a large range of values (Wang *et al.* 2005; Yacoot and Koenders 2008).

Jacobs reported the design, fabrication and testing of a new fixturing device to help with the handling of AFM probes when these are observed with a TEM instrument (Jacobs *et al.* 2016). The motivation for this research was to overcome issues associated with conventional probe mounting methods for electron microscopy. In particular, such traditional approaches were identified to lead to (1) the inability to reproduce the

alignment between subsequent probe mountings, (2) the possible contamination of tips due to fixation methods such as the usage of carbon tape in some cases and (3) time and material wasting due to low throughput and tip breakage.

• Electron microscopy is also often utilised in tip wear studies as a method to test the validity of alternative in-situ tip assessment techniques. It is argued that the main advantages of this direct approach are that (1) it does not require bringing the tip in contact with any sample surface (Jacobs *et al.* 2016); (2) it is relatively straight forward to implement (Keller and Franke 1993; Wilson *et al.* 1995); (3) in addition to geometric data, qualitative information can also be obtained such as contamination and degradation of tip coatings (Lantz *et al.* 1998). On the other hand, the main drawbacks of electron microscopy for characterising AFM probes are that

- (1) Only two-dimensional (2D) geometry data of the tip apex can be obtained (i.e. only the projected shape of the tip) (De Rose and Revel 1997); For extracting 3D data information, the tip imaging process must be implemented for more than one perspective, indeed that may lead to increase the probability to contaminate or break the tip.
- (2) It can be a time-consuming process and may lead to probe contamination and damage in practice as the probe should be removed from the AFM instrument (Lantz *et al.* 1998);
- (3) It is not suitable for non-conductive tip materials such as Si_3N_4 (Atamny and Baiker 1995; Bao and Li 1998) and
- (4) The assessment of SEM data is generally considered not fully accurate (Cleveland *et al.* 1993). First, this is due to insufficient data resolution if details down to the nanometre level are required. SEM creates an image of the probe

tip region via scanning the surface by a high energy beam of electrons. From this image the profile of the tip can be extracted. Thus, the second reason associated with the limitation in the resulting accuracy could be due to various factors, such as electron beam size, focus, charging beam effect and beam sample interaction and repeatability issues when extracting tip edge from the post processing of SEM micrographs, especially at the nano-scale (Cleveland *et al.* 1993). Finally, another essential issue with electron microscopy, which has been highlighted by other researchers, is that tip data of tip apexes obtained by both SEM and TEM need to be tilted by a specific angle to achieve an accurate profile reconstruction. This is required to take into the cantilever inclination with the sample surface when the probe is mounted in the head of an AFM instrument (Liu *et al.* 2010; Miller *et al.* 1995).

2.4 Summary and identified knowledge gaps

In this chapter, the operating principle of an AFM device was introduced first. Then, based on the body of literature reported by previous researchers, a review of two major types of assessment for characterising AFM probe tips was completed. A brief summary of the main limitations of the different techniques is presented below. This is followed by the description of a number of knowledge gaps, which are identified as the outcome of this review. These knowledge gaps constitute the particular focus of this PhD research.

As reported in this chapter, a number of key issues are faced by researchers when investigating the real shape of the used tip. Currently, most of the presented approaches introduced in the literature depend on the traditional ex-situ measurement of the tip of an AFM probe through the utilisation of electron microscopy systems. As mentioned in the

previous section, these approaches have a number of limitations for assessing the geometry such tips. The most important ones could be briefly summarised as:

- Tip inspection with electron microscopy systems is a slow and time-consuming process.
- Such instruments are limited to providing only 2D data about the tip shape.
- Most reports of implementing this approach do not take into account the fact that when mounted in an AFM device, probes are always oriented at an inclination angle with respect to the surface of a specimen. In other words, this means that the cantilever of an AFM probe is not parallel to the sample surface. This inclination was reported by Liu *et al.* 2010 to be an important factor to be taken into account to evaluate the actual shape of the probe tip effectively, especially for non-axisymmetric tips.

Other researchers tried to extract information about the tip geometry or tip condition via alternative in-situ methods as reported previously. In the table below a list of advantage and disadvantage of the summarised technique in this chapter to identify the need for new approach to characterise the AFM probe tip

Overall, a number of specific difficulties are associated with each of these approaches. These could include:

- Additional cost for special sample preparation,
- Frequent assessments of the reference sample to ensure its integrity,
- Time-consuming procedure,
- The reliance on uncommon and non-commercial probes,
- The lack of any geometry-related metric output.

In this context, it can be said that despite the extensive research efforts that focussed on the characterisation of AFM tips, it is still an area open for further studies. In particular, it is of current scientific interest to propose and investigate new in-situ tip characterisation techniques, which are simple, fast, reliable and repeatable, i.e. without the risk of damaging the apex of an AFM probe. As will be described in details in Chapter 3, it could be possible to use data obtained from completing nano-indentation experiments, with the probe under investigation, for extracting useful information about the shape of its tip apex. To the best of our knowledge, no previous studies have reported this express analysis that study the validity of employing nano-indentation data for this purpose.

Table 2.1: Summary of the technique used to characterise AFM probe tip

Technique	References	Advantages	Disadvantages
Insitu techniques			
Scan of tip characteriser made of sharp asperities	<ul style="list-style-type: none"> • Bykov <i>et al.</i>(1998). • Bloo <i>et al.</i>(1999). • Neto and Craig (2001). • Maw <i>et al.</i>(2002). 	<ul style="list-style-type: none"> • 3 D data is obtained. • Quasi in-situ (sample need to be changed only). • Relatively quick. 	<ul style="list-style-type: none"> • The convolution principle depends on the sharpness of the pin-like structure with respect to the investigated AFM tip. • Because of the convolution effect, in some cases it necessary to know the exact radius of the sharp asperity of the scan is the sum of both. • Relative checking is required due to the fact that the sharp pin used may be broke from previous use.
Scan of other Specific Features	<ul style="list-style-type: none"> • Montellius and Tegenfeld (1993). • Grigg <i>et al.</i>(1992). • Atamny and Baiker (1995). • Bao and Li (1998). • Skarman <i>et al.</i> (2000). • Iton <i>et al.</i>(2006). • Vesenka <i>et al.</i>(1993). • Miller <i>et al.</i> (1995). • Odin <i>et al.</i>(1994). • Wang and Chen (2007). • Glasby <i>et al.</i> (1994). • Markiewicz and Goh (1995). 	<ul style="list-style-type: none"> • Simple. • 3D data considered possible with sharp peaks. • Quasi (In-situ) (doesn't need to take out the tip from AFM). 	<ul style="list-style-type: none"> • More complex sample required (special lab required). • Time consuming • More complex post processing of the scanned data to extract the required geometry data. • Most of these technique suffer from poor control of the dimension of the used sample during the fabrication. • Some of these technique have limited ability to extract the tip actual shape down to nanometre scale.

Blind reconstruction method	<ul style="list-style-type: none"> • Dongmo <i>et al.</i> (2000). • Liu <i>et al.</i> (2010). • Wang and Chen (2007). 	<ul style="list-style-type: none"> • Quasi in-situ (sample need to be changed only). • 3D data is obtained. 	<ul style="list-style-type: none"> • Limited portion of the (tip apex) • Sensitive to selection input of parameters. • Sensitive to high frequency noise in the input data.
Scan of tip apex with an ultra-sharp tip	<ul style="list-style-type: none"> • Khurshudov and Kato (1995). • Kurshudov <i>et al.</i> (1997). • Zhao <i>et al.</i> (2001). • Gozan and Ozdoganlar (2012). 	<ul style="list-style-type: none"> • Can be done on the same AFM equipment. • 3D data is obtained. 	<ul style="list-style-type: none"> • Handling of tips (prone the tip to be damage). • Skilful operator required for the scan itself. • Dependent on the sharpness of ultra-sharp tip used (convolution effect)
Estimation of a wear metric	<ul style="list-style-type: none"> • Gotsmann and Lantz (2008). • Chen <i>et al.</i> (2011). • Huang <i>et al.</i> (2013). • Schmutz <i>et al.</i> (2010). 	<ul style="list-style-type: none"> • In-situ. • No contact with other materials / devices. 	<ul style="list-style-type: none"> • Require specially micro-fabricated tips which increases their cost • Lack of 3D data as output
Exsitu technique			
Electron microscopy SEM/TEM/STEM HRTEM	<ul style="list-style-type: none"> • Lantz <i>et al.</i> (1998). • Chung and kim (2003). • Chung <i>et al.</i> (2005). • Liu <i>et al.</i> (2010). • Jacobs <i>et al.</i> (2016). 	<ul style="list-style-type: none"> • Relatively large portion of the tip (Inspection of the apex and the unworn sides). • HRTEM: Atomic resolution enabling lattice structure to be observed. • Ability to observe different materials which is useful for observing the wear of coated tips and also accumulation of debris of the tips. 	<ul style="list-style-type: none"> • Only 2D data obtained. • Time consuming. • Handling of tips (possibility of tip damage). • Not in-situ (probe under investigation need to be remove from the AFM). • Derived wear volume may not accurate. Because SEM images are only 2D.

Chapter Three

Theoretical fundamentals for express analysis of current bluntness of an AFM tip

3.1 Aim and objective

As it has been explained in the previous chapters, the probe bluntness is one of the crucial parameters that may affect the Atomic Force Microscope tip-based nanomachining. It is clear that the real sharp tips of nanoindenter and AFM probes have deviation from their nominal shapes that are often described as sharp cones. In addition, the indenters used in nano-tests are not axisymmetric, but 3D pyramidal indenters. It is presented here the further application of depth-sensing nanoindentation techniques, however the main object of the investigation is the bluntness of an AFM probe rather than the bluntness of a traditional indenter.

Hence, there is a need in proper estimations of the current bluntness of the probe tip and in the use of appropriate quantitative measures of the tip bluntness. It is suggested

- (i) to approximate the current shape of the probe in its working position as a non-axisymmetric power-law function of degree d ;
- (ii) to use the exponent of the power-law function as the quantitative measure of the degree of the tip bluntness.

It is argued that the results derived for vertical indentation of probes into materials are applicable to problems of indentation by an AFM probe because the lateral displacements of the tip are negligible. Contact problems for indenters of power-law shape are self-similar, one can employ the Borodich scaling approach and the corresponding formulae that are applicable to 3D contact problems (Borodich 1989; Borodich 1993; Borodich 2011; Borodich 2014). The theoretical fundamentals of the method developed for express analysis of bluntness of AFM probes are provided. It is

argued, that the bluntness parameter can be extracted from an express depth-sensing indentation of the probe tip into a soft elastic sample.

The method for express analysis of the current bluntness of an AFM tip is based on a combination of depth-sensing nanoindentation and theoretical formulas of contact theory. Some appropriate information about the depth-sensing nanoindentation techniques and the methods of contact mechanics is provided in this Chapter.

3.2 Depth-sensing nanoindentation

In the last fifty years, instrumented indentation which is capable of probing in the nanometre scale, i.e. nanoindentation, has considered as an essential technique for characterizing mechanical behaviour of materials at small length scales. As Borodich noted in his reviews (Borodich 2011; Borodich 2014), the introduction of the continuous monitoring of the displacement of the indenter using electronic devices was perhaps the most important step in the development of modern materials science. Indeed, the modern load – displacement ($P - \delta$ or $P - h$) diagrams obtained by the depth-sensing indentation technique, are often called the ‘finger-prints’ of materials (see Figure 3.1). Here we denote the load by P , while the letter δ is usually employed in the papers on contact mechanics and the mechanics of adhesive contact to denote the depth of indentation of the indenter, while the materials science community uses mainly the letter h to denote the same variable.

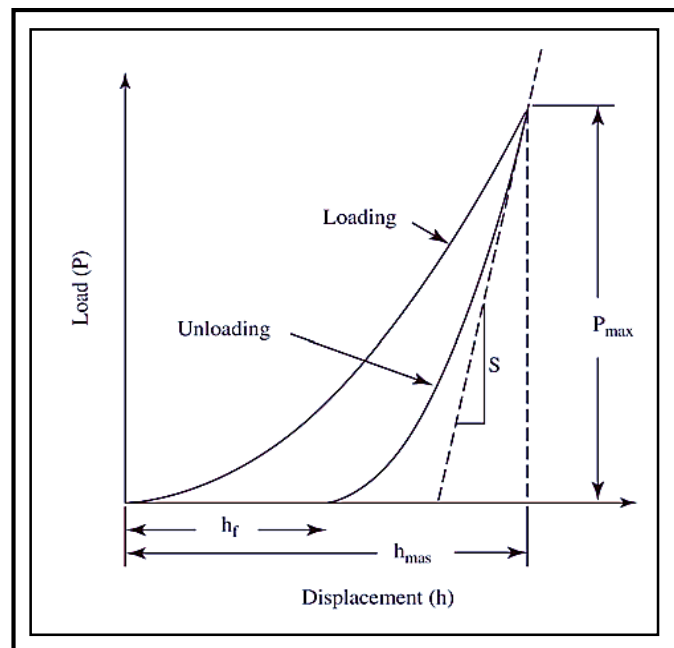


Figure 3.1: Schematic of typical indentation load – displacement data (adopted from (Borodich *et al.* 2003)). Here several important parameters used in the BASH formula and the Oliver and Pharr analysis are described later on.

The first depth-sensing indenter was built by Gennady N. Kalei in 1966 and the techniques used were described in his PhD thesis prepared under the supervision of M.M. Khrushchov and in his paper (Kalei 1968). Originally, Kalei combined a standard microhardness tester PMT-3 introduced by Khrushchov and Berkovich, and a device whose two sensors could be used for recording of two diagrams: the depth of indentation $h(t)$ and the load $P(t)$ as functions of time t . Then Kalei obtained the depth of indentation as the function of the load by superimposing manually these records in order to obtain $P - h$ diagram. Kalei was able to record a diagram of indentation of a chromium film of $1 \mu\text{m}$ thickness when the maximum depth of indentation was just 150 nm. Thus, (Kalei 1968) published the first depth-sensing nanoindentation paper.

The Kalei depth-sensing indentation technique was developed very rapidly. For several years, these revolutionary techniques were known only in the former Soviet Union. However, soon these techniques became known worldwide. In 1982 Newey D., *et al.* (1982) built a nanoindentation machine; and in 1983 Pethica reported that they monitored indentations to depths as low as 20 nm (Pethica *et al.* 1983). Recent studies have used indentation in a variety of environments including in liquid, high and low temperature and high strain rate testing (Bushby *et al.* 2004; Thomas *et al.* 2006; Mayo 1997; Vanlandingham *et al.* 1997; Shen *et al.* 2000; Ho and Marcolongo 2005). Modern sensors can accurately monitor the load and the depth of the indentation in the micro-Newton and nanometre scale, respectively. Nanoindentation system has thus gained enormous popularity as they can be applied to nanoscale specimens.

3.2.1 The BASH (Bulychev-Alekhin-Shorshorov) formula

The crucial step in the development of the depth-sensing nanoindentation techniques was the derivation of the BASH (Bulychev-Alekhin-Shorshorov) formula and was published in several papers with their co-workers (Bulychev, *et al.* 1975; Bulychev, *et al.* 1976). Bulychev and co-worker's presented the elastic contact solution to unloading curve of the load-displacement diagram by assuming that after the plastic deformation the non-homogeneity of the remained stress in the sample may be neglected, see a discussion by Borodich (2014). The BASH-equation presented for stiffness S of the upper portion of indentation load – displacement diagram at unloading is the following (Bulychev, 1975; Shorshorov *et al.* 1981):

$$S = \frac{dP}{dh} = 2aE^* = \frac{2\sqrt{A}}{\sqrt{\pi}} E^* \quad (3-1)$$

$$A = \pi a^2 \quad (3-2)$$

Here P = external load, h is indentation depth of the tip, A is the contact area, a is the radius of the contact region, and E^* is the reduced elastic contact modulus. This modulus can be obtained from the following formula:

$$\frac{1}{E^*} = \frac{1-\nu_1^2}{E_1} + \frac{1-\nu_2^2}{E_2} \quad (3-3)$$

Here E_i and ν_i ($i=1, 2$) are the reduced elastic contact modulus and the Poisson ratio of the first and second solids respectively. It is important to note that BASH relation is an essential relation which can be calculated from the analysis of frictionless contact problems. Also, BASH relation is a valid formula only for a frictionless elastic contact. Noted that BASH relation is valid just for the case of frictionless elastic contact, while the contact problems with friction are more complicated. The last kind of problem were discussed by Borodich and Keer (Borodich and Keer 2004).

3.3 Shape of the nanoindenter probe tip

Usually, the shape of the nanoindenter is described using the approach introduced by Hertz, see for details (Borodich 2014). Let us use both the Cartesian and the cylindrical coordinate frames, namely, $x_1 = x$, $x_2 = y$, $x_3 = z$ and r , φ , z , where $r = \sqrt{x^2 + y^2}$ and $x = r \cos \varphi$, $y = r \sin \varphi$. Let us place the origin O of the Cartesian x_1 , x_2 , x_3^+ and x_1 , x_2 , x_3^- coordinates at the point of initial contact between two bodies, and the axes of x_3^+ and x_3^- are directed along normal to the two bodies drawn toward the inside of each of the solids.

3.3.1. Hertz approximation and General description of the indenter shapes

Let us assume that axis x_1 and axis x_2 are the same for both bodies. The equations of the surfaces of the solids before compression are:

$$z_1 = f_1(x, y), z_2 = -f_2(x, y) \quad (3-4)$$

Let us now consider two surface points situated on the same vertical line A_1 and A_2 of the upper and the lower solids respectively, i.e. the points have the same coordinates (x, y) . If A_1 and A_2 coalesce after compression then following the Hertz assumption one does not consider the lateral displacements in x and y directions. These points had coordinates z_1 and z_2 before compression. Let us denote by w_1 the elastic displacement of the point A_1 and by w_2 the displacement of the point A_2 .

We will also use alternative notations, namely let us denote the quantities referring to the body (probe) $x_3^+ \geq 0$ by a superscript plus sign, and those referring to the second body (sample) by a superscript minus sign. Then the surfaces are described by the shape functions f^+ and f^- , respectively, where the common tangent plane at O is taken as the x_1, x_2 plane. In addition, we have $w_1 = w^+$ and $w_2 = w^-$. Since the coordinates of the points become the same after the contact, we have:

$$w^+ = h^+ - f^+(x_1, x_2), w^- = h^- - f^-(x_1, x_2) \quad (3-5)$$

Or

$$w = h - f(x_1, x_2) \quad (3-6)$$

where $w = w^+ + w^-$, $h = h^+ + h^-$, and $f = f^+ + f^-$.

In addition, the normal pressure P applied to the first solid within the contact region G is equal to the normal pressure applied to the second solid within G .

Let us explain why Hertz (1882) described the general shape of a 3D body as an elliptic paraboloid (Hertz. 1882). It follows from the formulation of the problem that $f(0, 0) = 0$. It is also known that the first derivatives of a smooth function at a maximum or a minimum are zero. If a decomposition of f^+ and f^- into a Taylor series is not degenerative for second terms, then the truncated decomposition can be written as:

$$z^+ = (A^+x_1^2 + B^+x_2^2 + 2C^+x_1x_2), z^- = (A^-x_1^2 + B^-x_2^2 + 2C^-x_1x_2) \quad (3-7)$$

where A_{\pm} , B_{\pm} , and C_{\pm} are constants of the decompositions.

Hertz showed that the contact region for contacting solids whose shape is described by equation (3-4) can be described by:

$$z^+ + z^- = Ax^2 + By^2 = \text{const.} \quad (3-8)$$

and the contact region is an ellipse.

Hertz (1882) assumed that the size of the contact region is small in comparison with the radii of curvature of contacting solids and therefore the linearized boundary-value problem (BVP) for each of the solids can be formulated as a BVP for an elastic half-space (Hertz 1882). Hertz assumed that the shape of a punch can be described by the equation. (3-8), i.e. it is an elliptic paraboloid

$$z = -f(x_1, x_2) = -(Ax_1^2 + Bx_2^2) \quad (3-9)$$

and he proved that the contact region is an ellipse.

3.3.2. Quantitative measure of the tip bluntness

The above discussion has shown that usually contact problems are studied for axisymmetric indenters. Indeed, there is an exact solution to the elastic Hertz-type contact problem for an arbitrary indenter of revolution obtained by Galin (1946) see also (Galín 1953; Galin 2008). For axisymmetric paraboloid of degree, $z = -B_d r^d$, Galin (1946) provided explicit formulae

$$P = \frac{E}{1-\nu^2} B_d \frac{d^2}{d+1} 2^d \frac{[\Gamma(\frac{d}{2})]^2}{\Gamma(d)} a^{d+1}, h = B_d d 2^{d-2} \frac{[\Gamma(\frac{d}{2})]^2}{\Gamma(d)} a^d \quad (3-10)$$

where Γ is the Euler gamma function and a is the radius of the contact region.

Galín's solution includes all classic axisymmetric frictionless contact problems, namely $d=2$ corresponds to sphere (paraboloid of revolution) solved by Hertz (1882), $d=\infty$ corresponds to flat-ended punch solved by Boussinesq (1885), $d=1$ corresponds to cone solved by Love (1939), and $d=2n$ corresponds to monomial punch of integer even degree solved by Shtaerman (1939).

On the other hand, Galanov (1981a,b) and Borodich (1983, 1989) studied contact problems for non-axisymmetric 3D indenters whose shape is described as a homogeneous function of degree d . This statement means that the shape function of the indenter f identically equals h_d , where h_d satisfies the following equation $h_d(\lambda x_1, \lambda x_2) = \lambda^d h_d(x_1, x_2)$ for an arbitrary positive scaling parameter λ . Here d is the degree of the homogeneous function f . It is possible to show that, $d=2$ for the elliptic paraboloids and spheres considered by Hertz and $d=1$ for pyramidal and conical indenters.

Indenters of various shapes are used in modern Materials Science. These include spherical, conical indenters as well as the Vickers four-sided pyramid, Berkovich and

cube-corner three-sided pyramids, and other indenters. Some indenters have special shapes like the Rockwell indenters having a sphere-conical shape. It is clear that the real sharp tips of nanoindenter and AFM probes have a deviation from their nominal shapes that are often described as sharp cones. In addition, the indenters used in nano-tests are not axisymmetric, but 3D pyramidal indenters.

We suggest to describe the indenter shapes as non-axisymmetric power-law functions. This means, that in polar coordinates r, θ , the indenter shape can be described by a monomial function of radius:

$$z = B_d(\theta)r^d \quad (3-11)$$

where $x_1 = r \cos \theta$, $x_2 = r \sin \theta$ and $B_d(\theta)$ is a function of the indenter heights at $r = 1$. The idea to approximate the indenter shape by a power-law function is not new (see a discussion by Borodich (Borodich 1989; Borodich 1993; Borodich 2014) and Borodich *et al.* (2003).

Of course, the above approximation (3-11) is related only to the working part of the indenter. This means that if the tip of an AFM probe used in nanomachining of a surface does not go deeper than 50 nm then the approximation (3-11) is used only to the part of the tip under the cross-section at the height 50 nm. If we are speaking about a nanoindenter that can indent the surface up to 100 nm then this approximation has to be applied to the part of the nanoindenter tip under the cross-section at the height 100 nm.

Let us explain connections between power-law functions and homogeneous functions. Indeed, it follows from the definition of homogeneous functions that

$$h_d(x_1, x_2) = \lambda^{-d}h_d(\lambda x_1, \lambda x_2) = \lambda^{-d}h_d(\lambda r \cos \theta, \lambda r \sin \theta) \quad (3-12)$$

If we take $\lambda = r^{-1}$ then we get that

$$h_d(x_1, x_2) = r^d h_d(\cos \theta, \sin \theta) = r^d B_d(\theta) \quad (3-13)$$

where

$$B_d(\theta) = h_d(\cos \theta, \sin \theta) \quad (3-14)$$

Thus, it is the same to say that the indenter shapes is described by power-law function of power d or the shape of the indenter is described by a homogeneous function of degree, d . It will be assumed in the further analysis that the indenter tip can be described by (3-11). It is shown in Figure 3.2 the shape of a parabola $z = f(r) = r^d$ (power-law function of degree d) changes when d increases.

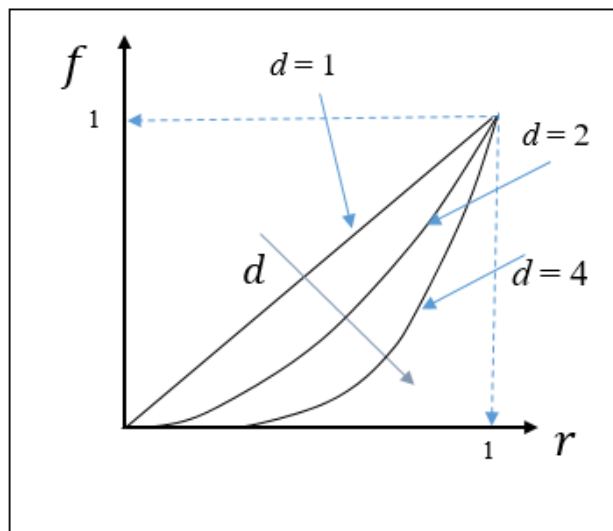


Figure 3.2: The shapes of power-law functions of degree.

It follows from (3-14) that if we describe them as $z(r, \theta) = B_d(\theta) r^d$ then $B_d(\theta)$ is not constant. In fact, $B(\theta)$ describes the height of the indenter at a point (θ, r) on a circle $r = 1$.

3.3.3 Shapes of indenters used in Materials Science

Let us describe the 3D geometry of a three-sided Berkovich and cube corner pyramidal indenters. The Berkovich indenter Figure 3.3 has an angle of 65.3° (115.13° corresponding face angle), while the cube corner indenter (90° face angle) has an angle of 35.26° .

The horizontal cross-sections of both indenters are equilateral triangles. However, if we describe them as $x_3 = B(\theta)$ then $B(\theta)$ is not constant. In fact, $B(\theta)$ describes the height of the indenter at a point (θ, r) on a circle $r=1$.

This formula $B_B(\theta) = \tan \left[90^\circ - \arctan \left(\frac{\tan 65.3^\circ}{\sin(30^\circ + \theta)} \right) \right]$ may be used in the calculation to get the values for cube-corner indenter. It assumed to substitute the respective angle 35.26° instead of 65.3° . This coefficient c could obtained directly as the ratio of tangents of angles in vertical cross-sections $c = \tan 65.3^\circ / \tan 35.26^\circ = 3.075$. So, the values of $B_C(\theta)$ for the cube-corner indenter could obtained from the values for Berkovich indenter $B_B(\theta)$ with $= \frac{B_C(\theta)}{B_B(\theta)} = 3.075$. For a sharper three sided pyramidal indenter, e.g. with an angle of 28.98° (80° corresponding face angle), this coefficient is $c = \tan 65.3^\circ / \tan 28.98^\circ = 3.93$.

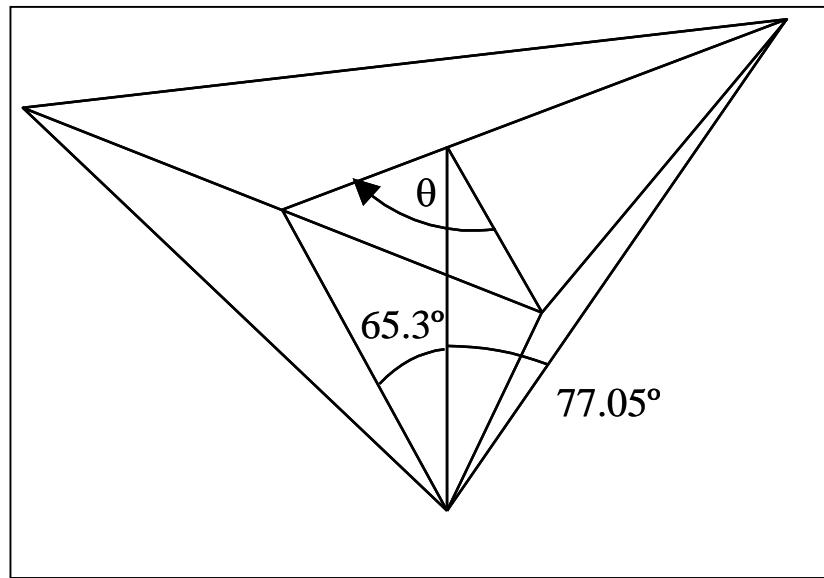


Figure. 3.3: Berkovich indenter geometry (after Borodich *et al.* 2003)

The contact problems for 3D indenters are very difficult or the solution has not been obtained yet. Hence, instead of considering the original 3D shape of the indenter, an effective equivalent cone of revolution is usually considered. It was suggested also to take into account the non-ideal shape of the indenters by the use of equivalent cones connected with spheres or power-law functions of revolution see, e.g., (Lo, R. Y. and Bogy 1999).

One of the main results of this Chapter is the introduction of the quantitative measure of the degree of the tip bluntness, namely the exponent of the shape power-law function. Hence, we need provide a theoretical background and method for fast and reliable extraction of this quantitative measure for the AFM tips in their working positions.

3.4 The shape of an AFM probe tip in its working position

Let us describe the actual shape of the AFM probe tip in its working position shown as in Figure 3.4. It is a general fact that AFM cantilevers are mounted in the AFM head with some initial inclined angle ($\alpha \leq 12^\circ$) from the horizontal axis x (Hutter 2005; Heim *et al.* 2004; Al-Musawi *et al.* 2016). Let α represent the inclined angle of the cantilever as it has been mounted in the AFM head before the test and let φ represent the total inclined angle of the AFM cantilever under the maximum applied load.

We argue that during the shallow nanoindentation test this inclined angle will stay the same. More specifically, during the nanoindentation test $\varphi \cong \alpha$. More theoretical approval regarding this could be found in Chapter 4.

As illustrated in Figure 3.4, once the probe tip is placed in the AFM head, the inclination angle should be taken into account to locate the new centre point of apex coordinate. Then, the new centre point of the tip apex become C rather than C_0 at the vertical position. After applying a low load for the purpose of shallow nanoindentation test, the tip apex centre point become now C' due to elastic deflection of the cantilever. This deflection supposed to cause a reduction in the inclination from α to φ .

Thus, in order to estimate correctly the value of $\Delta\varphi$ we need to use the following equation:

$$\Delta\varphi = \frac{P_{max}L^2}{2EI} \quad (3-15)$$

$$h_{max} = \frac{P_{max}L^3}{2EI} \quad (3-16)$$

Where here $\Delta\varphi$ represents the shifting in the inclination from the initial value φ , P_{max} is the maximum normal load applied, L is length of the cantilever, E is the elastic

contact modulus of the cantilever material, I is the moment of inertia of the cantilever cross section and h_{max} is the maximum depth.

For shallow nanoindentation we assume that the maximum nanoindentation depth h_{max} inside the sample surface $h_{max} \approx 50$. So, using (3-15), (3-16) we could obtain:

$$\Delta\varphi = \frac{3EI h_{max}}{L^3} \frac{L^2}{2EI} \quad (3-17)$$

$$\Delta\varphi = \frac{3}{2} \frac{h_{max}}{L} \quad (3-18)$$

If we assumed $L \approx 100 \mu\text{m}$ (DCP10 from NT-MDT) then we can found the value of $\Delta\varphi = 0.00075 \text{ rad} = 0.043^\circ$ which could consider as negligible. So, for this case to identify the related shifting distance X between C and C' we can use the following equation:

$$X = h_t \cdot \text{Sin } \Delta\varphi \quad (3-19)$$

If we assumed $h_t \approx 10 \mu\text{m}$ then the approximated value of the shifting distance $X = 7.5 \text{ nm}$. Thus, this shift is considered very small and we can employ now the rescaling formulae developed for the case of regular indenter to the AFM probe tips when indent into soft elastic materials.

Usually, at the vertical position when $\alpha = 0$ as in the tip shape could described by a monomial function of radius $z = B_d(\theta) r^d$. We argue here that the probe tip apex at the working position when the new centre of apex is C' could also be describe as this equation $z_1 = B_d(\theta) r^{d_1}$ (as illustrated in Figure 3.4). For non-axisymmetric tip it is clear that d_1 (approximation of the tip bluntness at the maximum depth) is not equal to d of the same tip at the vertical position. Indeed, during the assessment procedure the depth of the nanoindentation does not exceed 50 nm and so it clear that only the apex region is under

investigation. For simplicity, the notation d will be used instead of d_1 for the remainder of this Thesis to express the bluntness of tips in their working position, i.e. when conducting experiments on the AFM device with inclined tips. However, it will be made clear when needed whether the degree of bluntness measured experimentally corresponds to the vertical or the inclined case.

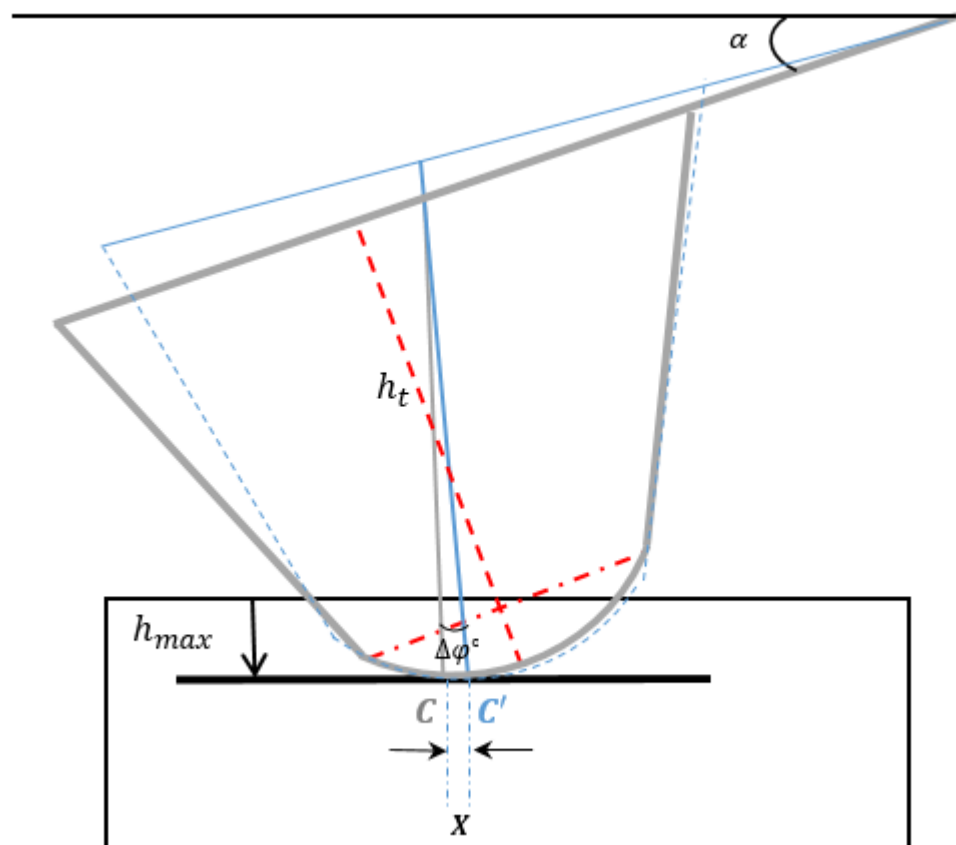


Figure. 3.4: AFM cantilever during the procedure of shallow nanoindentation. where C , represent tip apex centre at working position and C' tip apex centre at the maximum depth.

3.5 Contact problems and nanoindentation

3.5.1 Theoretical analysis of contact problems related to depth-sensing nanoindentation

In addition to the above described BASH formula, there were many other studies on contact problems related to nanoindentation. Let us mention very important results obtained by Galanov and his co-workers on connections between contact mechanics and indentation tests.

In 1983 Galanov published a paper describing influence of lateral displacements that are neglected in the Hertz formulation of contact problems. The Hertz formulation cases incompatibility of the problem, namely, the solution to a problem in Hertz formulation leads to existence of very small fictitious penetration of the elastic half-space into the rigid indenter. Galanov introduced a more precise formulation of the contact problem than the Hertz contact theory and considered not only vertical but also lateral displacements of materials points (Galanov 1983). It was shown that within the framework of this formulation, one can substantially reduce the incompatibility of strains that are observed near the contact zone within the customary formulation. In the problem with Galanov's formulation, the penetration of the elastic half-space into the die is virtually absent. The effects of lateral displacements were discussed later in a number of papers (see, e.g. (Schwarzer. 2006; Kindrachuk *et al.* 2009)).

The Hertz formulation of the contact problem is geometrically linear, i.e. it is assumed that all boundary conditions are formulated on the boundary of an elastic half-space. However, often there are quite large plastic distortions of the specimen surface after indentation. Therefore, formally one cannot use the geometrically linear formulation

of the contact problem. Galanov was the first who showed that one can still use the geometrically linear formulation of the problem at unloading if one considers the actual distance between the indenter surface and the plastically distorted specimen surface. This is the so-called Galanov effect that has to be taken into account for an unloading if after indentation there are large plastic distortions of the specimen surface. In particular Galanov and his co-workers presented models that take into account the plastic deformations of the material surface formed during indentation of pyramidal (Galanov *et al.* 1983), conical and spherical indenters (Galanov *et al.* 1984). These models are based on experimental observations of the shapes of imprints formed in metal samples by spherical and conical indenters: imprints formed by spherical indenters are still spherical Tabor (1948), however with a larger radius of the imprint; the imprints formed by conical indenters are still conical, however with larger included tip angle (Stillwell and Tabor 1961) Although this effect of plastic deformations was discussed in detail by Johanson (1985), Section 6.4), Galanov *et al.* (1983) were there first authors who quantitatively took into account the Galanov effect in their models (see for details (Borodich 2011; Borodich 2014; Borodich *et al.* 2016).

To give more explanation about this issue, we know that the geometry of the Hertz type problem of contact between two axisymmetric elastic solids whose shapes can be described by power-law functions of degree d : $z^+ = B_d^+ r^d$ and $z^- = B_d^- r^d$. So, it is assumed that initially the solids contacted at one point O . Let us fix a point r^* within the contact region. Two point $m^+(r^*)$ and $m^-(r^*)$ coincide after contact. These two points have to go along the z -axis the following distance in order to coincide: $z^+(r^*) + m^+(r^*)$ and $z^+(r^*) + m^-(r^*)$ respectively. Hence, the problem has been reduced to the problem

of contact between a rigid body $z = B_d r^d = (B_d^+ + B_d^-)$ and an elastic half-space. Using Galin's formula, one obtains for a cone ($d=1$) of semi angle $\alpha: z^+ = (\cot\alpha)r$ and conic hole of semi angle $\alpha': z^+ = -(\cot\alpha')r$.

$$P = \frac{2E}{\pi(1-\nu^2)} \frac{1}{[\cot\alpha - \cot\alpha']} h^2 \quad (3-20)$$

In the case of a contact between a sphere ($d = 2$) of radius $R_1: z^+ = \frac{1}{2R_1}r^2$ and a sphere hole $R_1: z^- = -\frac{1}{2R_1}r^2$, one has $z = B_2 r^2 = 0.5(\frac{1}{R_1} - \frac{1}{R_2})r^2$ and therefore, according to the above Galin solution

$$P = \frac{E}{1-\nu^2} \left[\frac{1.4.2}{\frac{1}{2(\frac{1}{R_1} - \frac{1}{R_2})}} \cdot [\Gamma(1)]^{-2} \Gamma(2) \right]^{1/2} \frac{1}{2+1} h^{3/2} = \frac{4}{3} \frac{E}{1-\nu^2} \frac{1}{\sqrt{\frac{1}{R_1} - \frac{1}{R_2}}} h^{3/2} \quad (3-21)$$

If $\alpha'=90^\circ$ then $\cot\alpha - \cot\alpha' = \cot\alpha$ and (3-20) become:

$$P = \frac{2E}{(1-\nu^2)} \pi a^2 \cot\alpha \quad (3-22)$$

The concept of ‘‘effective indenter shape’’ that in fact is the same as the model with the Galanov effect, was introduced later by (Pharr and Bolshakov 2002). The effective indenter shape was discussed also in a number of papers, see, e.g. (Sakai *et al.* 2004; Schwarze and Fuchs 2006).

In 2005 studied has been done by Lim and Chaudhri (Lim and Chaudhri 2005) on experimental indentation of rigid cones into conical holes molded in elastic blocks. In this study they compared the experimental results with the following formula for effective shape of a conical indenter that they adopted from Sakai *et al.* paper (Sakai *et al.* 2004):

$$P = \frac{2E}{\pi(1-\nu^2)} \left[\tan \left\{ \frac{\pi}{2} - (a' - \alpha) \right\} \right] h^2 \quad (3-23)$$

The above formula was not derived from geometrically non-linear formulation of the contact problem. One can see that (3-23) has nothing in common with the Galanov formula (3-20) that follows from the analysis of Hertz type contact problem. Hence, as it was noted by Borodich (2011) the above formula is wrong. It is not a surprise that it does not agree with experiments (Lim and Chaudhri 2005). Further studies by Chaudhri showed that the experimental data is also in disagreement with the Galanov (3-20). However, we need to note that the indenters used by Chaudhri were rather sharp and hence, the geometrically linear formulation was not applicable either in Hertzian model or the model that takes into account the Galanov effect.

Note that we have described some difficulties that could arise from the use of the classic Hertz contact theory when it is applied to nanoindentation tests. In the thesis we concentrate on the problems related to the AFM nanomachining of the surfaces, i.e. problems when the maximum depth of indentation does not exceed 50 nm. For such shallow depths, there is no significant plastic deformations (if any) during vertical indentation. The plasticity arises during horizontal moves of the indenter probes. Thus, we can still use the formulation of the Hertz-type contact problems in our studies.

3.5.2 Scaling transformations and self-similarity of Hertz type contact problems

It is well known that the main feature of the Hertz type contact problems and the main difficulty of solving these problems is that the contact region is not known in advance and it has been found as a part of the solution to the contact problem (Borodich 2014). Therefore, even for linear elastic solids the Hertz type contact problem is non-

linear. However, it was shown by Galanov in many papers (Galanov 1981a; Galanov 1981b; Galanov 1982) for isotropic solids and by Borodich (Borodich 1989; Borodich 1990b) in the general case of anisotropy that the Hertz type contact problems are self-similar and therefore, the non-linear 3D Hertz-type contact problem can be described as steady state. The conditions under which Hertz-type contact are self-similar may be formulated as follows by Borodich see for details (Borodich 1989; Borodich 2011): “The constitutive relationships are homogeneous with respect to the strains or the stresses and the indenter’s shape is described by a homogeneous function whose degree is greater than or equal to unity. It is also assumed that during the contact process, the loading at any point is progressive”.

As it has been mentioned, Galanov (1981b) and Borodich (1983) discovered independently the self-similarity of the 3D Hertz-type contact problems for isotropic linear elastic solid. Galanov (Galanov 1981a; Galanov 1982) discovered also self-similarity of contact problems for non-linear isotropic elastic, visco-elastic and plastic solids. Later Borodich described the general transformations applicable to the 3D Hertz-type contact problems and showed that self-similarity transformations are a particular case of the general case when the shape of the indenter is described by a homogeneous function. He showed also that the self-similar approach is also valid in application to non-linear anisotropic materials in both friction and frictionless boundary conditions.

Thus, to satisfy the conditions of self-similar contact problems, the indenter shape should be described by $f \equiv h_d$, i.e. its shape is described by homogeneous function h_d of degree d . Here, the homogeneity of the indenter shape means that the functions of the

indenter's shape f should satisfy the indenter $f(\lambda x_1, \lambda x_2) = \lambda^d f(x_1, x_2)$ for any arbitrary positive λ . Here, d is the degree of a homogeneous function f .

Furthermore, the operators of constitutive relations F for materials of contacting bodies should be homogeneous functions of degree k with respect to the components of the strain tensor e_{ij} , i.e., $F(\lambda e_{ij}) = \lambda^k F(e_{ij})$, that is mean the stress-strain relation of the tested material has to be of the following type $\sigma \sim \epsilon^k$ where k is the work hardening exponent of the constitutive stress-strain relationship.

The following scaling relations follow from the Borodich two-parameter transformations of the contact problems: if a punch whose shape is described by a homogeneous function h_d of degree d , is loaded by the force P_1 and the size of contact region is known and equal to $l(1, t, P_1)$ and the depth of indentation of the punch is equal to $h(1, t, P_1)$ then for a punch loaded by some force P and whose shape is described by the function $cH_d, c > 0$, the size of contact region and the depth of indentation are defined by the following equalities (Borodich 1989; Borodich 1990b.; Borodich 1993; Borodich 2014)

$$l(c, t, P) = c^{-\frac{k}{[2+k(d-1)]}} \left(\frac{P}{P_1}\right)^{\frac{1}{[2+k(d-1)]}} l(1, t, P_1) \quad (3-24)$$

$$h(c, t, P) = c^{-\frac{(2-k)}{[2+k(d-1)]}} \left(\frac{P}{P_1}\right)^{\frac{d}{[2+k(d-1)]}} h(1, t, P_1) \quad (3-25)$$

Borodich (2014) included time t within the arguments in order to include the creeping and viscoelastic materials. However, in our analysis we will avoid such materials.

The above scaling relations (3-24), (3-25) can be used to re-calculate the results obtained for a sphere of radius R_1 to another sphere of radius R ($d=2, c=R/R_1$).

$$l(R, P) = \left(\frac{R}{R_1}\right)^{-\frac{k}{(2+k)}} \left(\frac{P}{P_1}\right)^{-\frac{1}{(2+k)}} l(R_1, P_1) \quad (3-26)$$

$$h(R, P) = \left(\frac{R}{R_1}\right)^{\frac{2-k}{(2+k)}} \left(\frac{P}{P_1}\right)^{\frac{2}{(2+k)}} h(R_1, P_1) \quad (3-27)$$

Both the famous Meyer scaling law and its modification by Bowden and Tabor (1964) can be theoretically justified by the scaling relations (3-26) and (3-27). The above Borodich scaling formulae (3-24) and (3-25) was later used by Borodich *et al.* (2003) to derive the fundamental relations for nanoindentation tests.

Generally as mentioned previously, the real indenter have some deviation from the normal shape. So if the apex of indenter tip approximated by a monomial function of radius of degree d , ($1 \leq d \leq 2$) then both of the equation (3-24),(3-25) can be used to drive the fundamental relations for depth of indentation, size of contact region, load hardness, and contact area for both elastic and non-elastic, isotropic and anisotropic materials

Let us denote by P_1, A_1, l_1 and by h_1 respectively some initial load, the corresponding contact area, the characteristic size of the contact region and the displacement. Because we consider the same indenter then c in (3-24) and (3-25) can be taken as $c = 1$ and, hence,

$$\frac{l}{l_1} = \left(\frac{P}{P_1}\right)^{\frac{1}{2+k(d-1)}}, \quad \frac{h}{h_1} = \left(\frac{P}{P_1}\right)^{\frac{d}{2+k(d-1)}} \quad (3-28)$$

Galanov (1981b) and Oliver and Pharr (1992) noted that the experimental unloading data for various materials can be described as a power-law function of h , as in the following formula:

$$P = \alpha h^m \quad (3-29)$$

Oliver and Pharr (1992) noted that the exponent m is usually in the range from about 1.25 to 1.51. However, these empirical observations can get a scientific justification if one employs results by Galanov (1981b) and Borodich (1989).

So, loading and unloading curves of $P-h$ relation as a result from the nanoindentation test are not the same as mentioned before. Because loading curve represents both elastic and plastic deformations of the material. On the other hand, the unloading curve may be assumed to be purely elastic. Hence, in an ideal scheme, the whole load-displacement curve can be approximately described as:

$$\frac{P}{P_1} = \left(\frac{h}{h_1}\right)^{\frac{2+k(d-1)}{d}}, \frac{P}{P_{max}} = \left(\frac{h-h_f}{h_{max}-h_f}\right)^{1+\frac{1}{d}} \quad (3-30)$$

respectively for loading and unloading branches of a depth-sensing test. Here, P_{max} , h_{max} are the maximum load and the respective displacement, and h_f is the residual displacement (more details see Figure 3.1)(Borodich *et al.* 2003; Borodich 2011). If plastic distortions are small, i.e. one can neglect the Galanov effect, and the non-homogeneity of the residual stresses can be also neglected, then one can assume for the unloading branch that $\kappa = 1$. Thus, we obtain the main equation for the unloading branch of the $P - h$ curve

$$\log P \sim \log(h - h_f)^m = m \cdot \log(h - h_f), \quad m = (d + 1)/d \quad (3-31)$$

or

$$d = \frac{1}{m-1} \quad (3-32)$$

The very simple equation (3-32) is the fundamental equation for extracting the quantitative measure of the current AFM tip bluntness. Hence, the range the exponent m from 1.25 to 1.51 correspond to d within the range from 1.96 to 4. Evidently, for $d = 4$ the tip is rather flat. It has been derived assuming negligibility of the surface distortions

and using the similarity arguments that are valid for frictionless, frictional and no-slip boundary conditions and for linear elastic behaviour of the tested probe materials at unloading branch.

We will use soft polycarbonate plastic as the tested probe material. A typical $P - h$ curve for a soft polycarbonate plastic obtained by nanoindentation of the AFM tip in its working position is presented in Figure 3.5. Note that the original data (in blue) represents both the indentation data (in red) and the additional displacement of the AFM spring (cantilever) under applied load. Hence, the curve is shifted. We suggest to use the indentation data (in brown) and extract the quantitative measure of the current AFM tip bluntness. Using the experimental $P - h$ curve (Figure 3.5) and employing the fundamental equation (3-32), one can extract the quantitative measure of the current AFM tip bluntness. The methodology of the express analysis is described below.

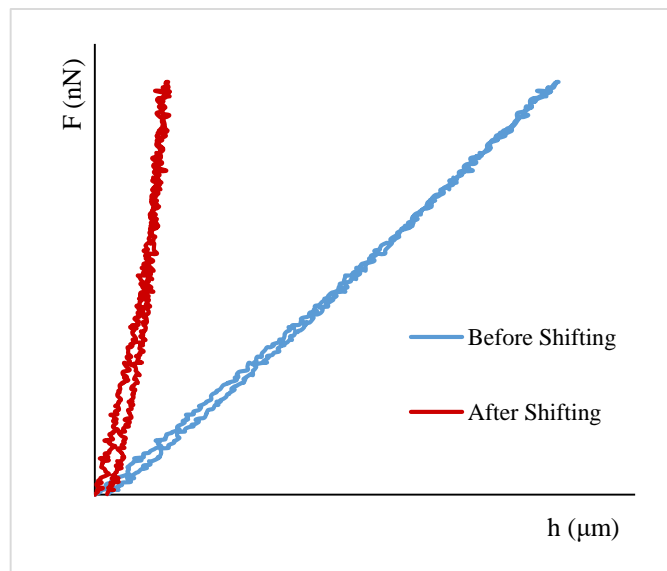


Figure 3.5: A typical $P - h$ curve for a soft polycarbonate plastic obtained by nanoindentation of the AFM tip in its working position. The original data (in blue) and the data obtained after extraction of the AFM beam deflection (in red). Note the plastic imprint is very small, i.e. $h_f \approx 0$ (see Chapter 4 for further details).

3.6 Methodology for the express analysis of actual bluntness of the AFM probe tip.

Based on the above discussion AFM the methodology for the express analysis of actual bluntness of the AFM probe tip may be described as the Figure 3.6.

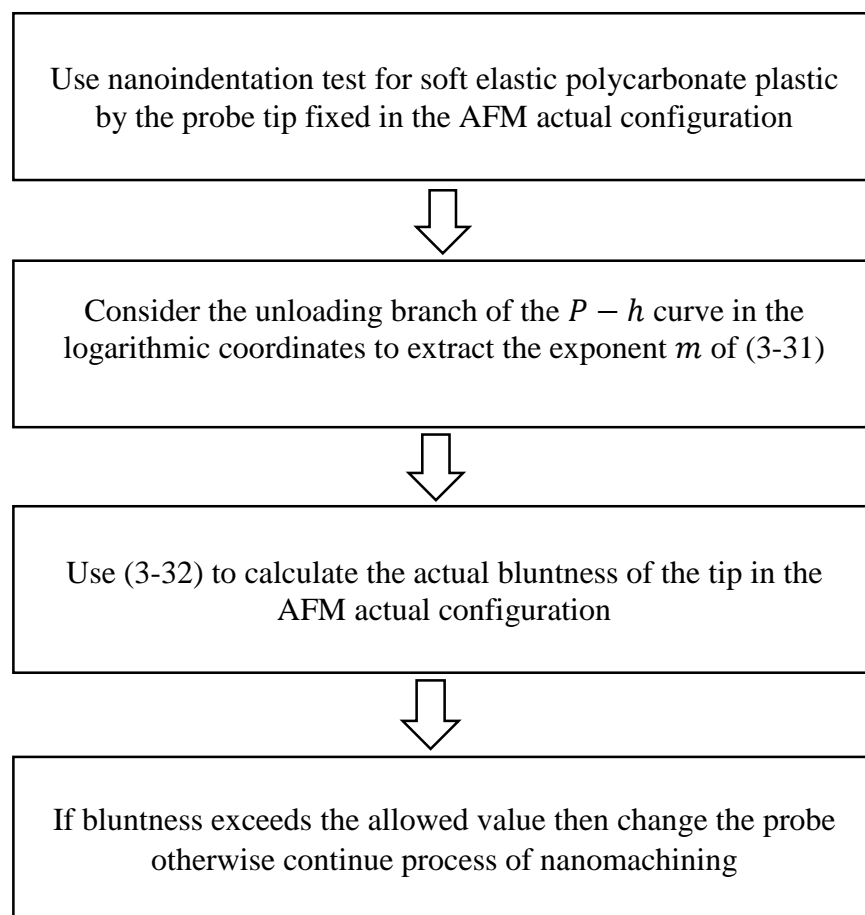


Figure 3.6 methodology for the express analysis of actual
bluntness of the AFM probe tip

3.7 Conclusion

To describe the current shape of the AFM tip in its working position in the range of the possible indentation depth, it is suggested to approximate the shape as a power-law function of degree d .

A quantitative measure of the degree of the tip bluntness has been introduced, namely it is suggested to use the exponent d of the power-law function as the quantitative measure of the bluntness.

It has been shown that the lateral displacements of the AFM tip during its downward motion are negligible. Hence, the approach developed earlier for vertical indentation tests, is also applicable to indentation by an AFM tip attached to the AFM cantilever in its working position. Because the problems of vertical indentation for power-law shaped probes are self-similar, the Borodich scaling arguments for the contact problems have been used to derive fundamental relations (3-30) and (3-32). The relation for the unloading branch of the $P - h$ curve may be used for the quantifying the bluntness of the indenter tip, namely by using the methodology described in Flow chart 3.1.

Although the scaling relations are valid for both elastic and non-elastic, isotropic and anisotropic materials, it is suggested to use an express depth-sensing nanoindentation of a soft elastic isotropic material by an AFM tip. It is suggested to use the soft polycarbonate plastic as the tested probe material.

Thus, it is proposed a method for express analysis of the AFM tip bluntness based on the quantitative measure introduced. One can extract the above quantitative measure

of the bluntness from an express depth-sensing indentation of the probe tip into a soft elastic sample. The theoretical fundamentals of the method are provided. The experimental verification of the method will be presented in the next chapters.

Chapter Four

Implementation of a novel approach for AFM tip characterisation and initial validation

4.1 Aim and objectives

In this chapter, an experimental/analytical procedure is developed to estimate the degree of bluntness of an AFM tip apex “as received from the manufacturer” in its working position in the AFM instrument. This procedure is based on the analysis of the force-displacement curves using the Borodich rescaling formula. The procedure allows to estimate in-situ the actual bluntness of the AFM tip without the use of any additional equipment.

4.2 Introduction

In this chapter, an in-situ method was implemented experimentally to evaluate the AFM tip bluntness degree based on the analysis of nano indentation force-displacement curves. To describe the actual shapes of AFM tips, four different commercially available non-axisymmetric tips coated with diamond have been studied. The specifications of these tips will be presented in Section 4.4. Basically, this method is based on the Borodich rescaling formulae (Borodich 1989; Borodich *et al.* 2003) and his similarity analysis of Hertz-type contact problems. Presenting the force-displacement ($F-h$) as a power law $F \sim h^m$, coordinates $\text{Log } F \sim \text{Log } h$ and using the linear fit of the data, one can estimate the degree (exponent) m . Then, using the rescaling formulae, one can extract the degree d of the shape bluntness. Here and henceforth, it is assumed that the actual shape of AFM tips may be well-fitted at their apexes by non-axisymmetric power-law functions of degree d , $d \geq 1$:

$$f(r, \theta) = B(\theta)r^d \quad (4-1)$$

Here (r, θ) as it was mentioned above, are the polar coordinates in the plane of the sample whose origin is located at the actual apex of the tip. As it was described in details in Chapter 3, Hertz-type contact problems for such punches are self-similar for many constitutive laws (stress-strain) relations.

This chapter is organised as follows. The next section describes in details the basic principle for acquiring force-displacement curves when conducting nanoindentation experiments with an AFM as opposed to a normal vertical indenter. Following this, Section 4.4 describes the experimental set-up used in this study. This includes the microscopy instruments utilised, the probes and the sample material. Then, Section 4.5 presents and discusses the results obtained when assessing the degree of bluntness, d , from AFM nanoindentation tests with the different tips considered. This section also presents an initial validation of these results. More specifically, this was achieved by evaluating d based on the analysis of the two-dimensional profiles of the same tips using SEM micrographs.

4.3 AFM nanoindentation

4.3.1 Force –displacement curve analysis

The application of instrumented indentation tests allows the penetration process of an indenter tip into the sample material to be measured through the control of either a constant loading rate or a constant displacement. In this way, measurements can be recorded for both applied load and penetration depth on the micrometre or nanometre scale (Oliver and Pharr 1992; Doerner and Nix 1986). Figure 4.1 explains the main

concept of the process and the shape of the force-displacement curve expected as a result of this test.

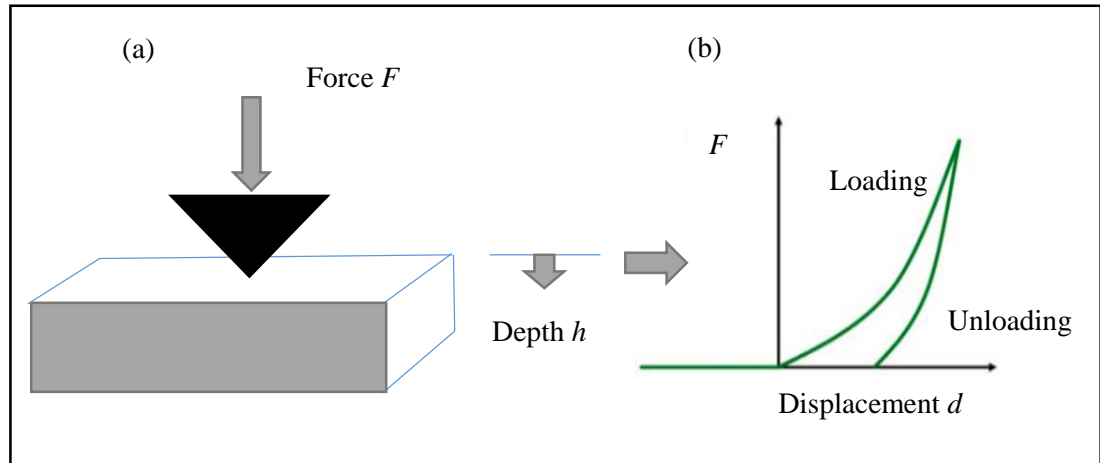


Figure 4.1: (a) Typical concept of instrumented indentation test, (b) the obtained force-displacement curve (adapted from (Bhushan 2008)).

Figure 4.2 illustrates the general shape of the force-displacement curve of the nanoindentation process when conducted on an AFM instrument. In this figure, region I corresponds to the case where the tip is far enough from the sample and thus, there is no interaction force between them. As the tip becomes closer to the sample surface, Van der Waals force effect the tip, which eventually snaps onto the workpiece (region II). Region III presents data when the tip indents the sample to a maximum load causing tip deflection. The last region shows the adhesion area for which the AFM cantilever deflection is affected by the adhesion force before tip finally snaps off from the surface (Borodich *et al.* 2013)

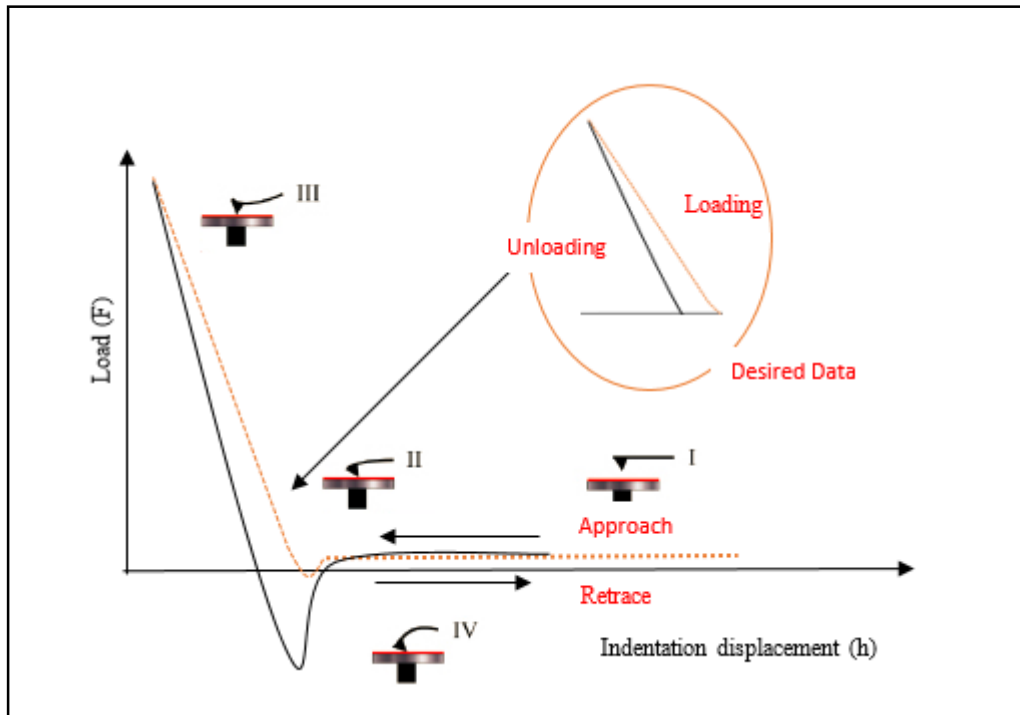


Figure 4.2: General shape of the (F - h) curve for AFM-based nanoindentation, illustrating the different regions of the curve and the specific location of the desired data required for the analysis (adapted from (Butt *et al.* 2005)).

Among the many advantages of using the AFM instead of the standard indenter to apply the nanoindentation test, the fact that AFM tip consists of small radius of curvature rather than the indenter make the interaction between the tip and the surface sample more localized. As a result, a weaker force could be applied, which is a tremendous difference was addressed about 1nN could apply by AFM while the indenters utilized 100nN (Tsukamoto *et al.* 1987).

It is important to consider the fact that AFM cantilevers deflect when applying a specific load at their free end. For this reason, when analysing a force-distance curve obtained with an AFM instrument, the compliance of the probe cantilever should be taken into account. In particular, the deflection of the cantilever, δ , should be subtracted from

the recorded value of the distance coordinates for each point along the loading and unloading branches as given by the AFM instrument (for more details, see Figure 4.3). Therefore, for obtaining an accurate force-displacement curve from this process, data must be measured between the applied load and the actual nanoindentation depth, h , rather than the displacement, z , of the piezoelectric actuator holding the probe. Indeed, the default output of the instrument provides z data rather than h (Jee and Lee 2010; C. a Clifford and Seah 2005; Cappella and Dietler 1999). As a result, a shifting process is an essential step to obtain correct (F - h) curve rather than the original (F - z) curve. This can be implemented using the simple following equation:

$$h = z - \delta \quad (4-2)$$

Due to Hooke's law, one has

$$\delta = \frac{F}{K_n} \quad (4-3)$$

where F and K_n are the recorded applied force and the cantilever normal spring constant respectively. Figure 4.4 illustrates the conversion of the obtained curve from a F vs z curve to a F vs h .

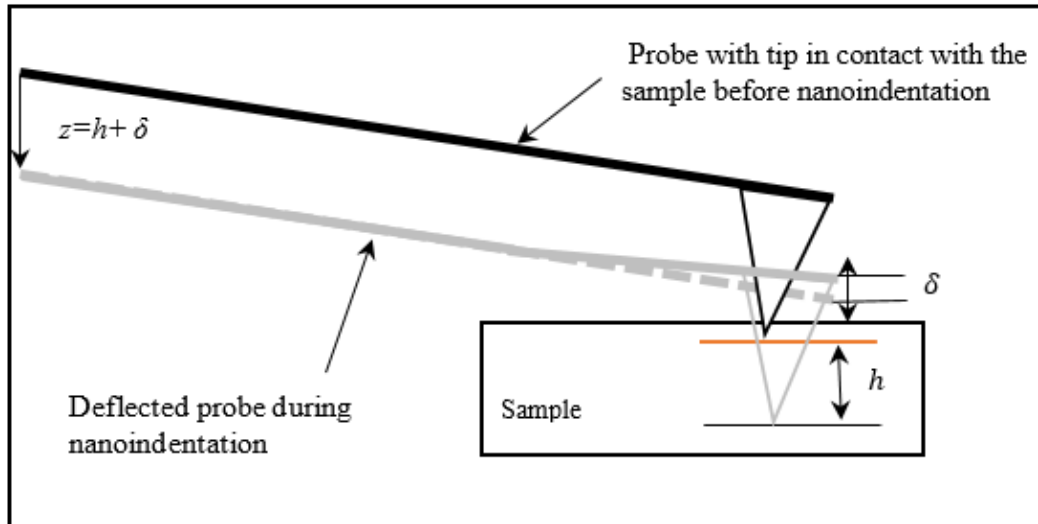


Figure 4.3: Side view of the cantilever during AFM nanoindentation. z is the piezoelectric actuator displacement, h is the indentation depth and δ is the cantilever deflection at its free end.

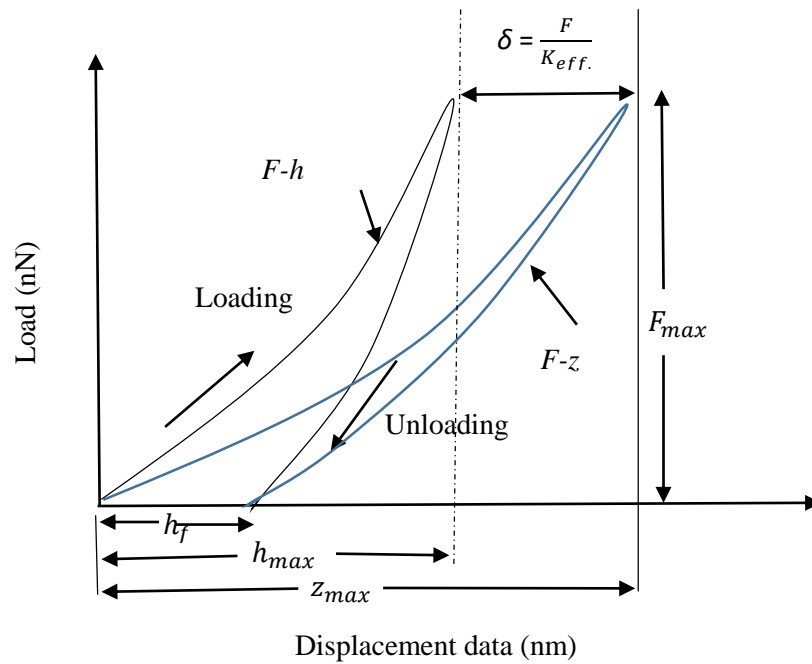


Figure 4.4: Force-displacement curve. The blue curve is the raw data obtained with an AFM instrument. The black curve shows the required data after removing the cantilever deflection, $\delta = F/K_{eff}$ where F is the normal force, K_{eff} is the effective cantilever spring constant (more details about K_{eff} will be explained in section 4.4.3.2)

4.4 Experimental set-up and procedure

For the experimental investigation, a set of techniques were used in this study to quantitatively and qualitatively characterise the tip apex geometry and to extract the bluntness degree d of the investigated probes. Figure 4.5 presents a flow chart, which summarises the experimental procedure followed in this chapter for each probe considered. In particular, a wide range of instruments were employed including an optical microscope, a scanning electron microscope and an Atomic Force Microscope. Full details of each step in this procedure are given in the next sub-sections.

4.4.1 Microscopy equipment

The electron microscopy instrument used in this study was a dual focused ion beam and SEM system from Carl Zeiss (model 1540xB) (see Figure 4.6). This equipment is used to obtain 2D profile data about the real shape of the AFM tips under investigation. An optical microscope was also employed (model DMLM from Leica) to obtain quantitative information about the cantilever dimensions of the probe (see Figure 4.7). In particular, this instrument was utilised to measure the width and length of cantilevers on which tips are mounted. The nanoindentation experiments were carried out on an AFM instrument from Park system (model XE-100). A photograph of this instrument and of its main component are shown in Figure 4.8. This AFM is positioned on an active anti-vibration table (model TS 150 from Table stable) and has three individual piezoelectric actuators (i.e. one for each axis in a Cartesian coordinate system).

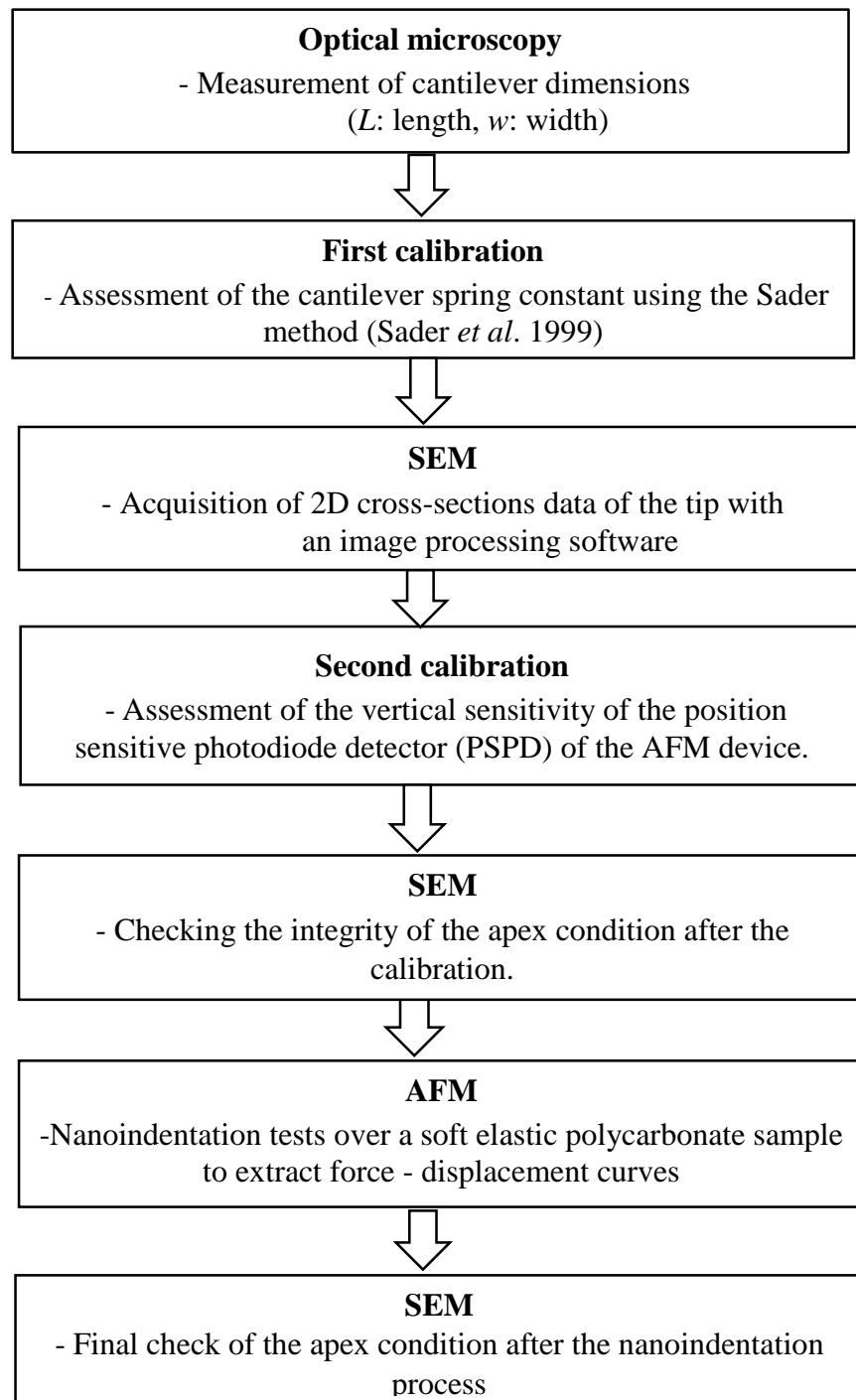


Figure 4.5: Overall experimental procedure followed in Chapter 4



Figure 4.6: The SEM instrument utilised



Figure 4.7: The optical microscope utilised

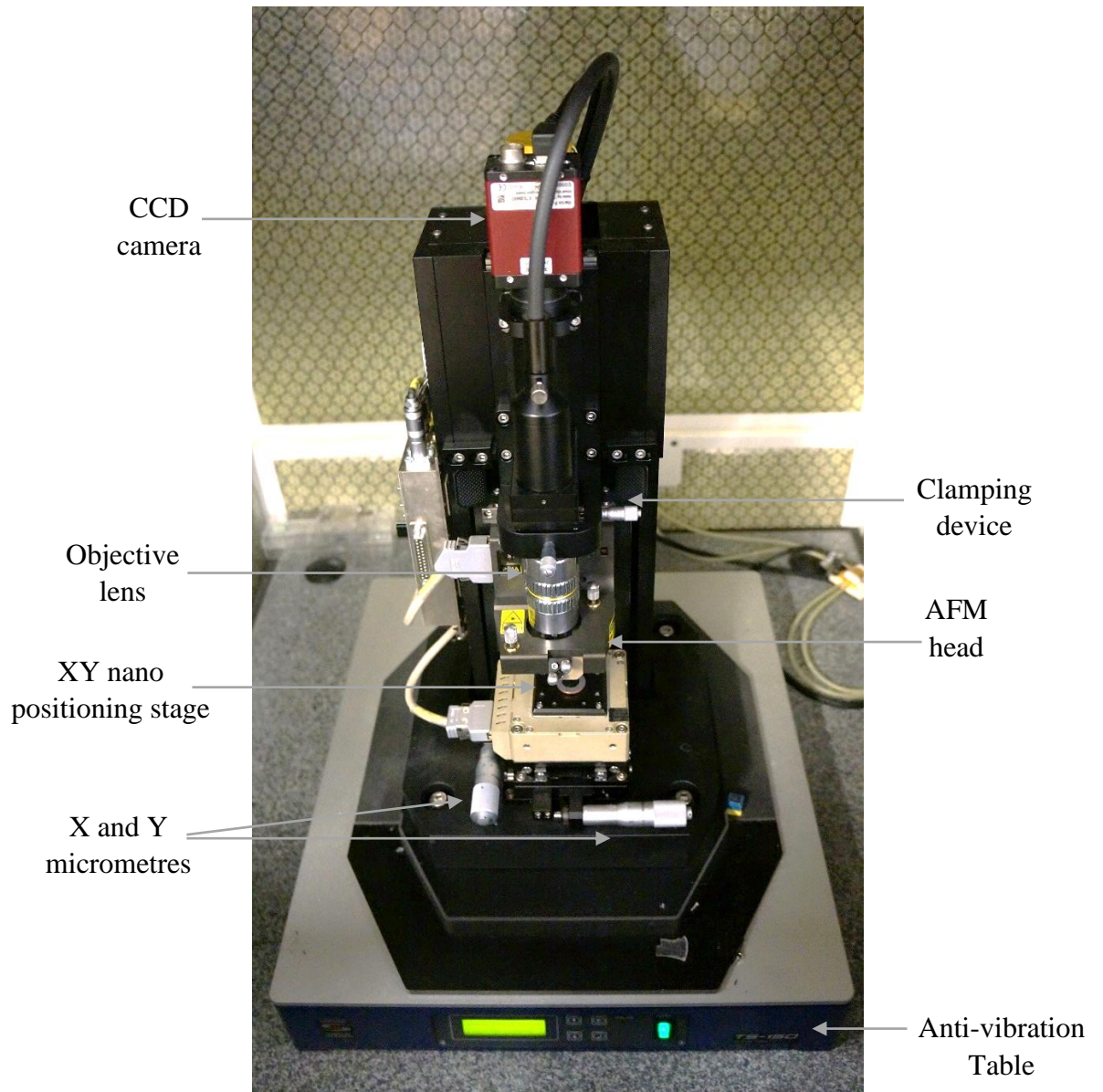


Figure 4.8: XE-100 AFM instrument from Park System.

The X and Y actuators of the AFM instrument generate displacement of the stage along the x and y -axes with sub-micrometre resolution and for a maximum distance of 45 μm . The Z actuator, also referred to the Z-scanner in the thesis, defines the vertical displacement of the fixed end of the AFM probe along the z -axis. The maximum amplitude of the vertical displacement is 7 μm for this particular AFM system. Finally, the “XEI” software from Park Systems was also used to extract nanoindentation curves for further analysis.

4.4.2 AFM probes and sample material

Four non-axisymmetric probes with diamond coated silicon tips (model DCP_10 from NT-MDT) were investigated. The main reason behind the selection of these specific tips was that, in order to apply the rescaling formula we need probe tips with an apex radius in the range between (50-100 nm). Also, during the study the effective spring constant is required for tips calibration process, these tips (referring to DCP_10) are rectangular ones and the direct solution for the rectangular cantilever is already available. The cantilevers of such probes have a rectangular shape with a nominal spring constant given by the manufacturer as 40 N/m. Such probes are mounted on a larger chip which enables their positioning into the head of an AFM device using tweezers. Such a chip has standard dimensions 1.6 x 3.6 x 0.4 mm. In addition, the typical curvature radius of the tip is about 100 nm while the tip height is between 10 - 15 μm according to the manufacturer specifications. Figure 4.9 shows a SEM micrograph of one of the AFM tips studied in this work.

The substrate utilised in this work was made of elastic polycarbonate (PC) material. The particular PC sample used here had lateral dimensions of 30 x 30 mm, while its

thickness was 3 mm. Its arithmetic surface roughness, R_a , was estimated to be 1.9 nm determined from AFM scan of its surface.

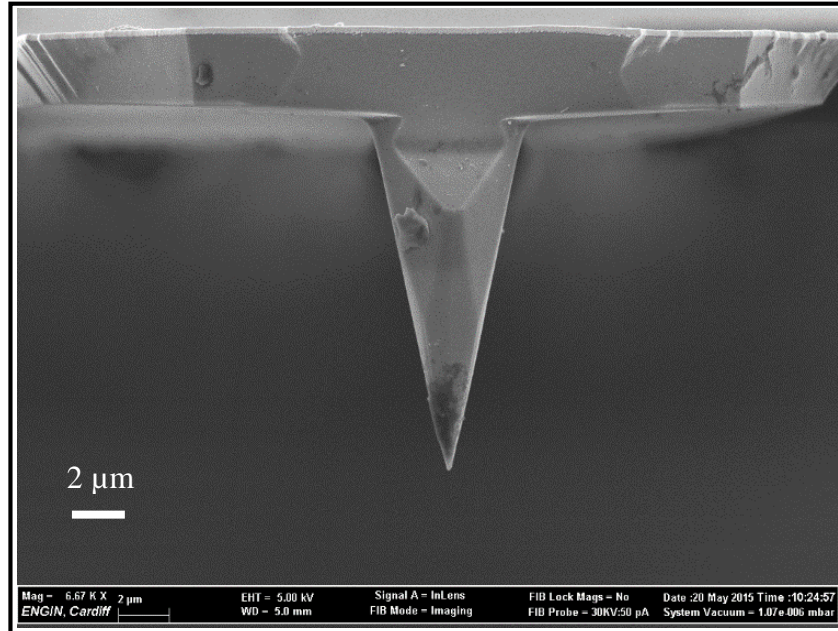


Figure 4.9: SEM micrograph of the tip for one of the AFM probes investigated

4.4.3 Normal force calibration, F

Based on the application of Hooke's law, the accurate determination of the normal force, F , applied by an AFM probe can be obtained from the following expression:

$$F = K_n \times S_n \times V_{A-B} \quad (4-4)$$

where K_n is the normal spring constant of the cantilever, S_n is the normal sensitivity of the PSPD and V_{A-B} is the voltage output of the PSPD corresponding to vertical deflection of the cantilever (Ducker 1992; Butt *et al.* 2005). Thus, when calibrating the applied normal force, it is first required to be correctly evaluate K_n and S_n .

Calibrating the spring constant of used cantilever before the nanoindentation process by AFM is considered an essential process to obtain correct results as mentioned previously by other researchers (Borodich *et al.* 2012; Borodich *et al.* 2013). The nominal value for K_n specified by probe manufacturers is typically comprised within a large range of possible values. Therefore, in order to know the applied load during nanoindentation with good accuracy, the spring constant must be calibrated prior to performing any experiments. In addition, a second calibration step must be done to define S_n such that the voltage measurement V_{A-B} , given by the reflected laser beam from the cantilever into the PSPD of the AFM, can be converted accurately to the actual deflection of the probe (Hutter and Bechhoefer 1993). In this work, these two consecutive calibration steps are completed first in order to reduce the uncertainty for the value of the applied normal force on the sample to a minimum. These steps are described in details in the following subsections.

4.3.3.1 Calibration of the normal spring constant, K_n

The normal spring constant, K_n , of the cantilever can be defined as the ratio of the applied normal force of the cantilever to its deflection in the normal direction at the tip position (Clifford and Seah 2005). Many methods were presented to determine K_n in practice which rely on the determination of a number of geometry characteristics such as length, width and thickness as well as the material properties of the cantilever (see e.g. reports in Clifford and Seah 2005, Neumeister and Ducker 1994, Sader *et al.* 2012). Similar to many studies in the literature, a widespread method was used in this work, which is the so-called the “Sader Method” for assessing the normal spring constant of rectangular probes (Sader *et al.* 1999).

The Sader method suggests determining only the plan view dimensions of the cantilever. i.e. its length and its width. These dimensions can be obtained from optical microscopy as illustrated in Figure 4.10. In addition, measurements of the quality factor of the cantilever, Q , in air and its unloading resonance frequency, f_0 , should be obtained. The quality factor is used in this method to quantify the value of energy dissipated in the fluid (air) due to resonant oscillations. Both quantities can be obtained using the AFM instrument from the analysis of the signal showing the amplitude response of the free end of the cantilever under different excitation frequencies. When implementing this method, both the air density and viscosity are considered constants for a given laboratory environment. The Sader method is generally described as a very convenient method because all the required physical quantities to implement it can be measured accurately without being destructive to the cantilever tip apex.

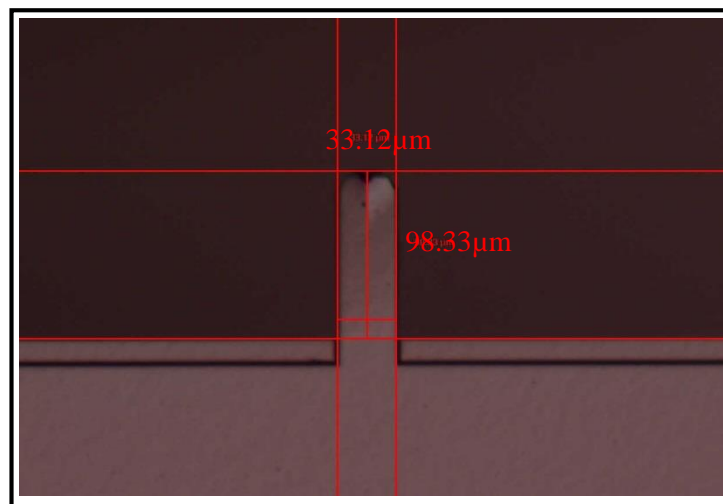


Figure 4.10: Optical microscopy image of one the cantilevers utilised.

In this work, we illustrate the influence of using the correct and a wrong value for the spring constant of the cantilever on the outcome of force-displacement curve obtained from a nanoindentation test. Figure 4.11(a) shows the curve shape when the correct K_n value is used in the analysis. In this case K_n was determined to be $81.2 \text{ N} \cdot \text{m}^{-1}$. Figure

4.11(b) give the curve using an inaccurate value of K_n (i.e. $56.3 \text{ N} \cdot \text{m}^{-1}$). The implication of using a wrong K_n value in this case is that an error of 30% in the normal spring constant measurement brings an error of 76% in the h_{max} value extracted from the force-displacement curve.

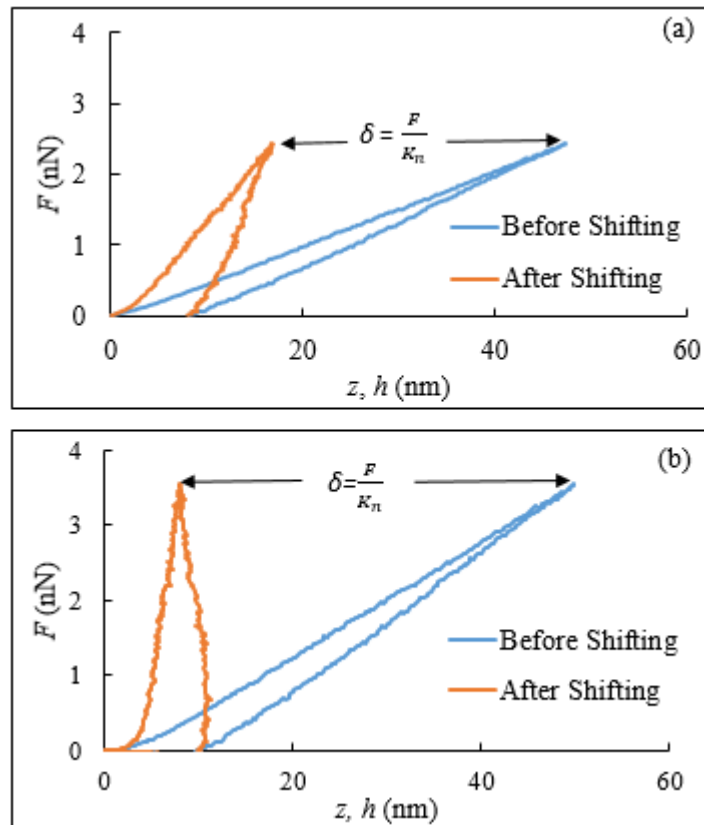


Figure 4.11: Force-displacement curves from an AFM nanoindentation test before and after shifting using $\delta = \frac{F}{K_n}$ based on (a) the correctly measured normal spring constant and (b) a wrong value of the normal spring constant. A 30% error in K_n leads to a 76% error in the value of h_{max} after completing the shifting process.

4.4.3.2 Effective spring constant, K_{eff}

As mentioned previously, it is a common fact that AFM probes are mounted at a slight angle from the horizontal plane that defines the surface of a sample. This is done

on purpose to increase the space between the sample and probe chip. Thus, force measurement errors are expected if a proper correction is not applied due to this inclination (Heim *et al.* 2004, Hutter 2005). In particular, force measurements are overestimated by a factor $\cos^2\alpha$ where α is the mounting angle of the cantilever in the AFM. This angle is generally about 12° . As a result, the normal spring constant is underestimated by this factor if the correction is not applied. Thus, the “effective” spring constant, K_{eff} , of rectangular cantilevers is obtained using of the following equation (Heim *et al.* 2004, Hutter 2005):

$$K_{eff} = \frac{K_n}{\cos^2\alpha} \quad (4-5)$$

In addition, it should be considered that the inclination of the cantilever at its free end is also changed as a result of the nanoindentation process. Thus, the inclination angle in this case is equal to φ which is equal to:

$$\varphi = \alpha - \gamma \quad (4-6)$$

where γ represents the change from the original angle α as a result of the cantilever deflection due to the applied normal force as shown in Figure 4.12. In particular, this figure present in more detail the effect of the inclination process over the required value of φ . The value of γ which represent the change in inclination angle was already calculated in Chapter 3 and was found out to be negligible in this study. Table 4.1 provides the data measured to assess K_n using the Sader method for all the probes investigated. In addition, this table also gives the value of K_{eff} , which are used through the thesis.

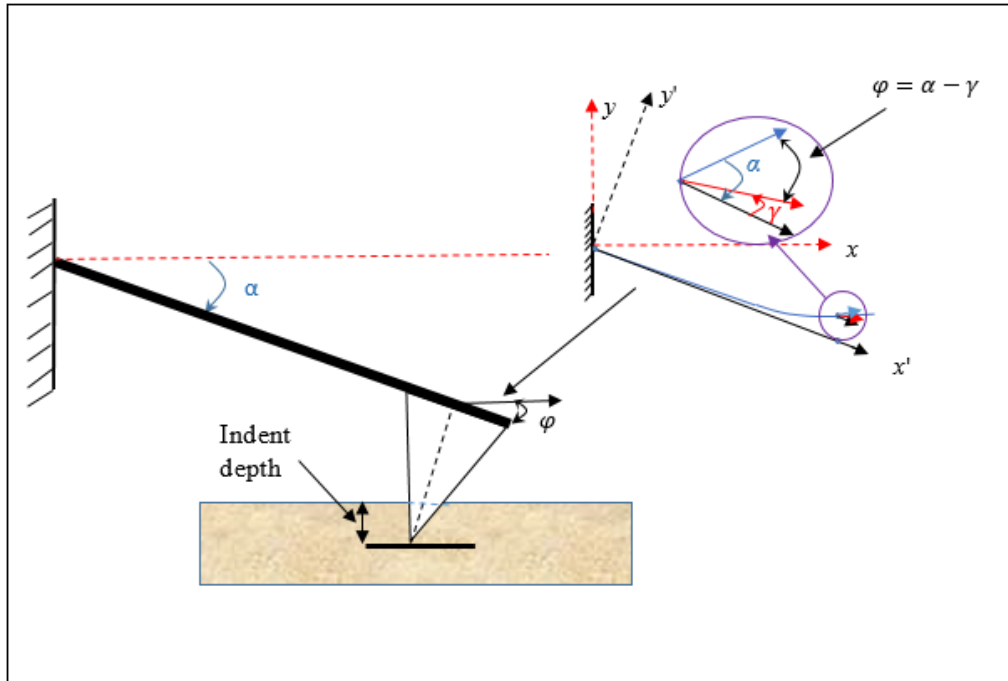


Figure 4.12: Illustration of inclination angles with respect to the tip surface.

Table 4.1: List of calibration parameters value, normal and effective spring constant for the used set of tips.

Tip No.	Probe name	Width (μm)	Length (μm)	Q	Freq. (kHz)	K_n (N/m)	K_{eff} (N/m)
1	DCP_2	33.12	98.33	314	230	9.45	9.93
2	DCP_3	33.12	99.29	369	248	12.50	13.03
3	DCP_4	33.12	98.97	363	224	10.60	11.08
4	DCP_5	33.12	99.94	316	243	10.40	10.87

4.4.3.3 Calibration of the PSPD normal sensitivity, S_n

As mentioned earlier, the accurate measurement of the displacement of the free end of the probe, δ , based on the recorded V_{A-B} signal from the AFM PSPD is very important. Thus, the correct determination of the normal sensitivity of the PSPD, S_n , is also an essential task prior to starting the nanoindentation experiments. This task is presented below and it was applied for each cantilever as recommended by Butt *et al* (2005).

Typically, the calibration of the sensitivity of the PSPD requires bringing the tip in contact with the surface of a hard sample. Then, the cantilever is further brought down towards this sample by a known distance. The fact that a hard sample is used means that there is no penetration from the tip into the sample surface. The output voltage V_{A-B} during this operation is recorded. Thus, based on the following equation:

$$\delta = S_n \times V_{A-B} \quad (4-7)$$

it is obvious that the sensitivity, S_n , is the slope of the displacement, δ , as a function of V_{A-B} .

The impact of this factor calibration on the obtained shape of the loading - unloading curve can be seen in Figure 4.13. In particular, Figure 4.13(a) presents the output curve acquired using the correct calibrated value of the PSPD sensitivity, which was measured to be 69.3 m/V in this case. Figure 4.13(b) shows the distorted loading - unloading curve after using an inaccurate value of S_n (i.e. 84.0 m/V). Overall, it could be seen that an overestimation in the sensitivity value leads to a higher value of the measured deflection δ (see equation 4.10). At the same time, it also results in the underestimation in depth value h (see equation (4.2)), and the overestimation of the normal applied force (see equation (4.3)).

In the present case, the overestimation of the deflection and the normal force brings an obvious measurement error in the shape of the force-displacement curve as shown in Figure 4.13(b). From an 18% change in sensitivity between the correct and inaccurate value, an error of 80% was produced in h_{max} obtained after completing the shifting process. Table 4.2 shows the S_n values measured for all the probes used in this work.

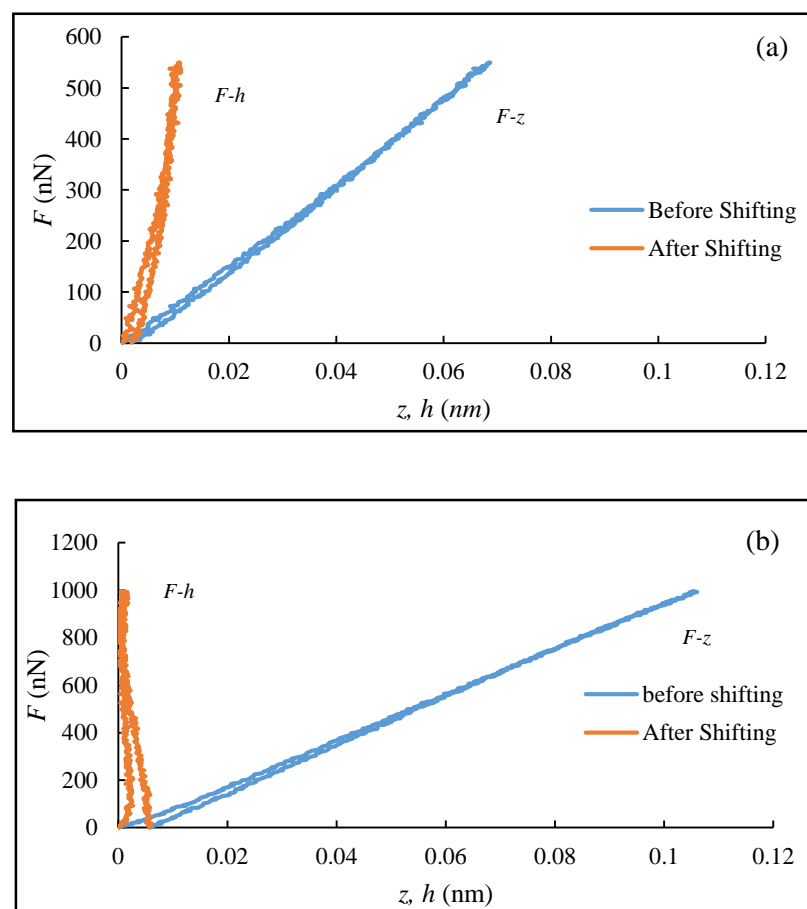


Figure 4.13 The raw force-displacement curve, $F-z$ (blue colour) and the shifted $F-h$ curve (orange colour) based on (a) the correct value of the PSPD sensitivity and (b) a higher and incorrect value for this sensitivity.

Table 4.2: Normal sensitivity S_n associated with each of the probes utilised.

Tip No.	Probe name	Normal sensitivity, S_n (m/V)
1	DCP_2	69.3
2	DCP_3	54.0
3	DCP_4	56.5
4	DCP_5	104.0

4.4.4 Nanoindentation process

The purpose of this section is to present the analytical procedure followed for extracting the average value of d for all the tips used based on the raw (i.e. F - z) nanoindentation data as provided by the AFM instrument. The overview of this procedure is illustrated in Figure 4.14.

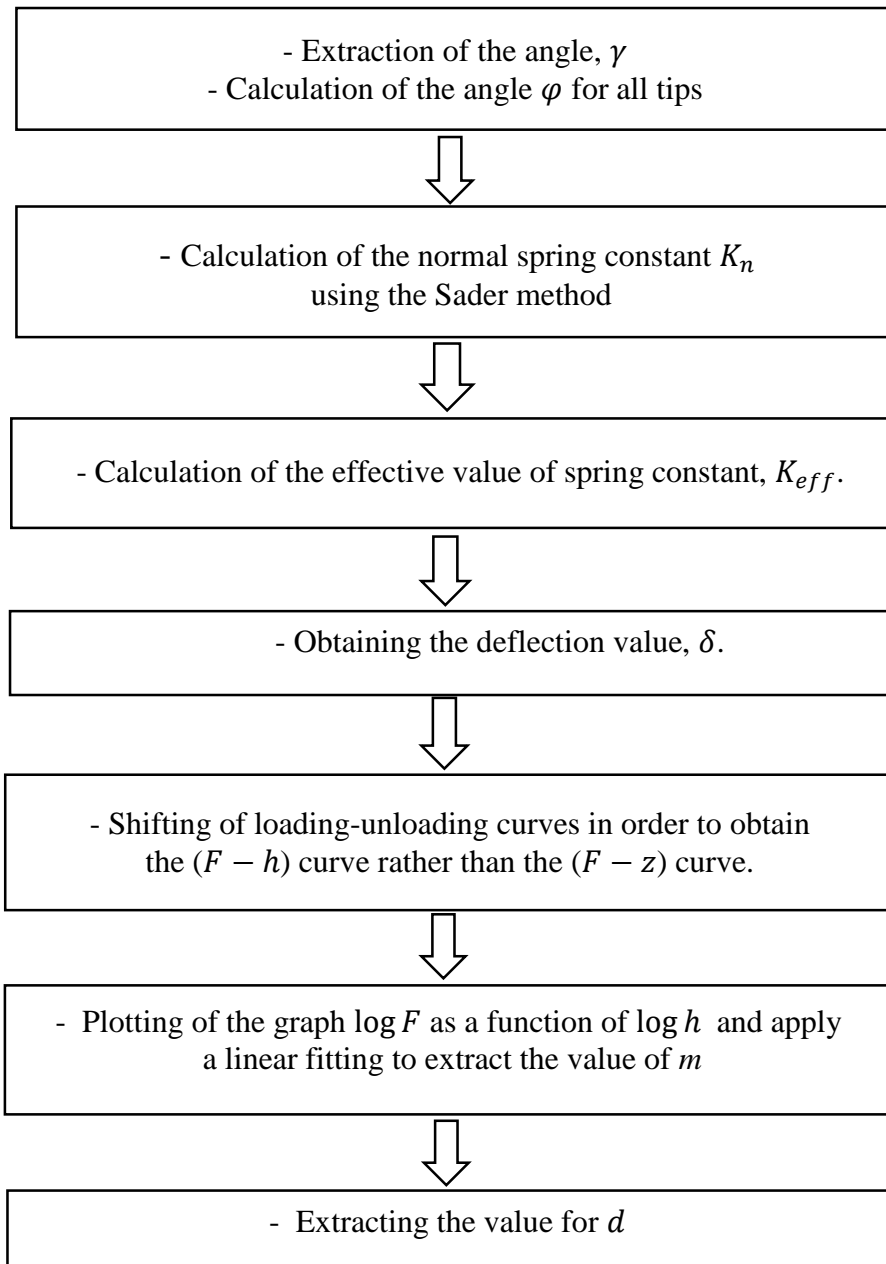


Figure 4.14: Flow chart describing the main analytical steps used to extract the average value of d for a given tip.

However, prior to the start of nanoindentation experiment, a scan of the sample surface is performed in order to locate a suitable position on the surface and to avoid the influence of any possible contamination may exist on the sample which effect the final result. (Young and Budynas 2001; Vanlandingham *et al.* 2001). This is another

procedural difference when conducting the nanoindentation process on an AFM instrument in comparison on a nanoindenter device. In this study, the initial imaging of the sample surface was performed in non-contact mode in order not to damage the tip apex. It should also be noted that, the nanoindentation experiments were realised without holding time between the loading and un-loading processes. This was to avoid the influence of time-dependent deformation mechanisms, such as creep or viscoelastic effect on the results. (Tang and Ngan 2003). The nanoindentation tests were carried out at room temperature. For each tip, a set of 10 nanoindentation cycles were realised on different locations over the surface of the PC sample in order to extract an average value for d . Appendix A1. shows the user interface of the Park Systems software utilised when defining the map of the 10 nanoindentation locations.

For all experiments, the generic set-up was as follows:

- Scan an area 5 μm by 5 μm on the sample in non-contact mode at 0.6 Hz scan rate.
- Approach the tip onto the sample surface until a set normal force of 100 nN is reached.
- Define a map of 10 nanoindentation locations.
- Perform a nanoindentation cycle for a given location through the control of the displacement of the Z-scanner. A vertical motion of 80 nm was applied every time. In addition, the speed of the Z-scanner was 0.20 $\mu\text{m}/\text{sec}$ during both loading and un-loading. This small range of vertical motion ensured that the reflection of the laser beam from the back of the deflected cantilever could always be contained within the working range of the PSDP.

- Move the tip to the next nanoindentation location by using a low applied force of 30 nN between the tip and the sample and repeat the previous step until completion of the 10 cycles. This value of applied force was selected not to wear the tip apex through the movement between the points

The raw force-displacement curve for each indentation point could be visualised with XEI software from Park Systems. This data were then exported into a text file, which could subsequently be processed using the Excel software for further analysis. In particular, the first data processing step before extracting the d value was to perform the shifting process as explained earlier in section (4.3.1).

Finally, as can be seen in Figure 4.14, the last data processing step consisted in plotting the unloading part of the nanoindentation curve using logarithmic coordinates ($\text{Log } F - \text{Log } h$). In particular, according to the similarity approach as explained in detail in Chapter 3, we have:

$$\frac{F}{F_{max}} = \left(\frac{h-h_f}{h_{max}-h_f} \right)^{(1+1/d)} \quad (4-8)$$

which can be re-arranged as follows:

$$F = F_{max} \left(\frac{h-h_f}{h_{max}-h_f} \right)^{(1+1/d)} \quad (4-9)$$

Taking into account that the non-homogeneity of the residual stress is neglected (Borodich *et al.* 2003) and by using logarithmic coordinates, one can extract the value of m based on experimental data as the slope of the ($\text{Log } F - \text{Log } h$) data from the following equation:

$$\text{Log } F = \text{Log } F_{max} + m \text{Log}(h - h_f) \quad (4-10)$$

where m is defined as:

$$m = 1 + \left(1/d\right) \quad (4-11)$$

The value of the exponent m experimentally found in this way is then employed to extract the degree of bluntness d using equation:

$$d = \frac{1}{m-1} \quad (4-12)$$

It should be noted that for shallow indentation depth, vibrations from the environment (kinetic or acoustical vibration) could have a significant effect on the load-displacement curve if they are of the same magnitude. The influence of this vibration noise are the main cause of erroneous results when shifting the force-displacement curve, and data scattering from one test to another. These effects can be reduce by using air damping plates between the tip and sample are necessary (Choi *et al.* 2011). In this work, we have used an anti-vibration table and an acoustic enclosure to minimise such influences.

4.4.5 SEM data processing

2D profiles of each tip were also extracted from SEM micrographs via an image processing software (Image J). These data represent only a cross-section image of the tip, i.e. the cross section facing the incident electron beam during the scanning process. Figure 4.15 presents the SEM image for each of the four tips (see Appendix A1 for more detailed SEM image zoomed to the apex region for all four tips). As stated earlier, these tips are commercially available; they have a non-axisymmetric geometry and are coated with a layer of single crystal diamond. Their dimension and spring constant values were already reported in Table 4.1.

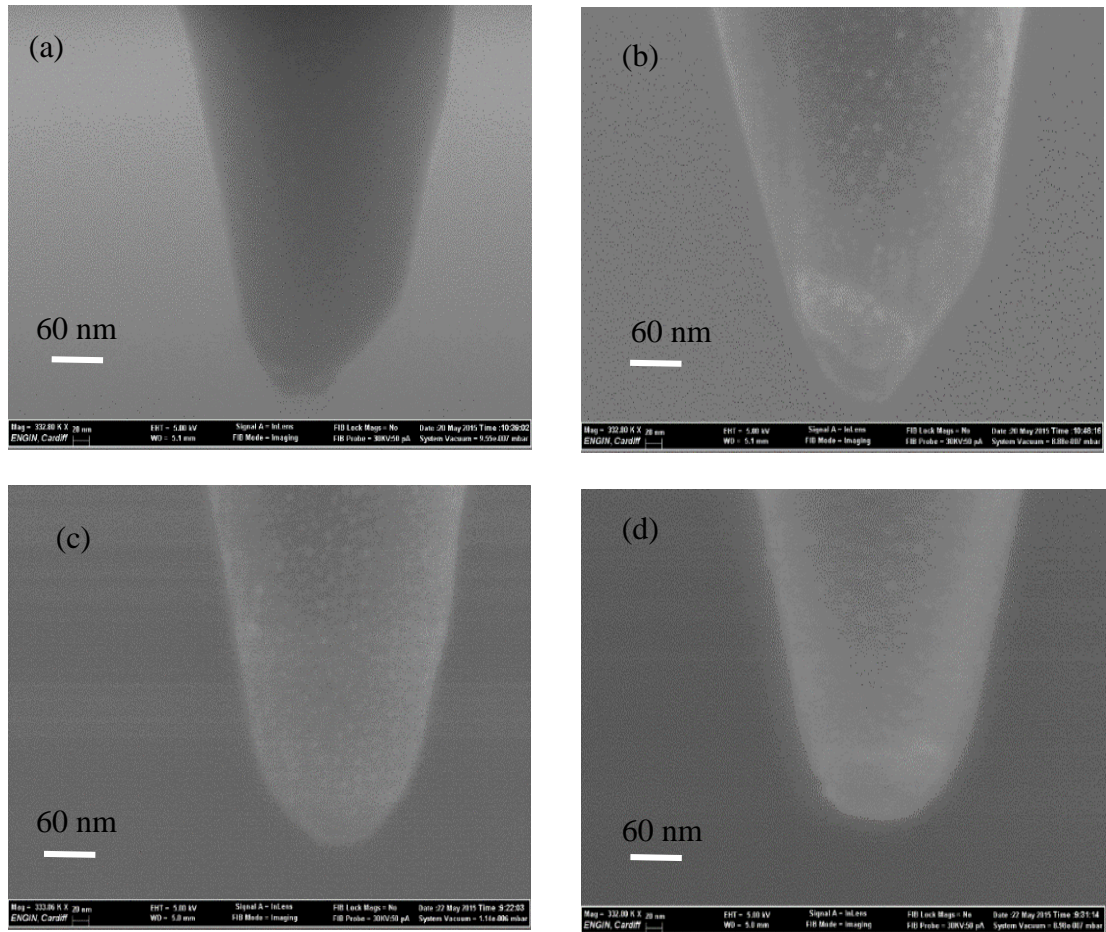


Figure 4.15: SEM image for (a) tip 1, (b) tip 2, (c) tip 3 and (d) tip 4 according to the nomenclature defined in Table 4.1.

One advantage of using the SEM device in this work was to gain more information about the shape of the tip apices before and after each process steps when performing the tip calibration and the indentation tests. In this way, it was possible to make sure that the geometry of each tip apex did not change through the whole procedure. The assessment was done in a qualitative manner as can be seen in Figure 4.16 for one of the used probes. In particular, this figure shows SEM images of tip 1 for a fixed magnification value before and after the tip calibration process and also after the completion of the 10 nanoindentation tests. Based on this data, it could be reasonably assumed that the succession of the steps implemented in the overall procedure could be considered as non-destructive.

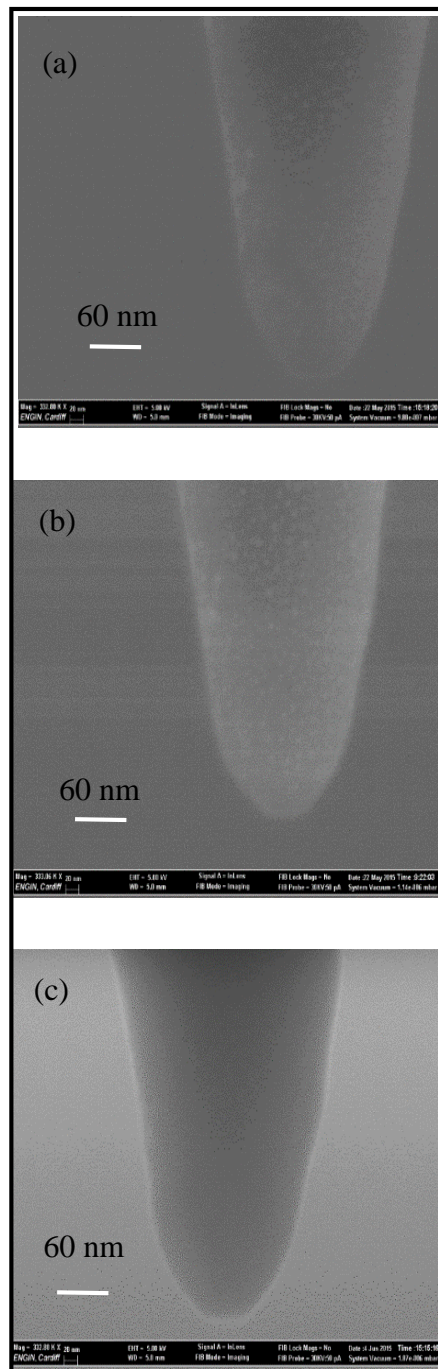


Figure 4.16: SEM micrographs of tip 1 (a) as received from the manufacturer, (b) after calibration and (c) after the nanoindentation tests

4.5 Results and discussion

4.5.1 Nanoindentation

The nanoindentation tests were performed over PC elastic polymer sample for the set of four tips considered under the same experimental conditions to make sure that any discrepancies in the obtained force-displacement curves corresponded to actual difference in tips sharpness. Figure 4.17 shows a typical force-displacement curve acquired from one of the 10 nanoindentation tests for each tip. From this figure, it can be observed that the generic shape of the loading - unloading curve for each tip is consistent. In order to extract the correct data and neglect the impact of the adhesion effect between the tip and the sample in the unloading data, careful selection of the origin point (i.e. when F is considered to be null) of the unloading curve must be carried out. The adhesion region may vary from one indentation location to another in the map and also from one tip to another depending on its composition and surface chemistry. Thus, the origin point was selected when the contact force on the loading curve was at the minimum (Carpick 1997)

From each $F-h$ curve, only the unloading data were of interest. Thus, in each case, a new plot was prepared to show only the unloading part. For each of these new plots, the $F-h$ curve was shifted horizontally toward the origin by a value equals to h_f to ensure that all the unloading data analysed started at the point (0, 0). Also, it should be noted that because of the inhomogeneity of the polymer material used on the nanoscale, data for each unloading curve obtained with the same probe could vary (Borodich *et al.* 2012 ; Sawa and Tanaka 2001). This is why the d value measured here was calculated as an average from 10 nanoindentation experiments.

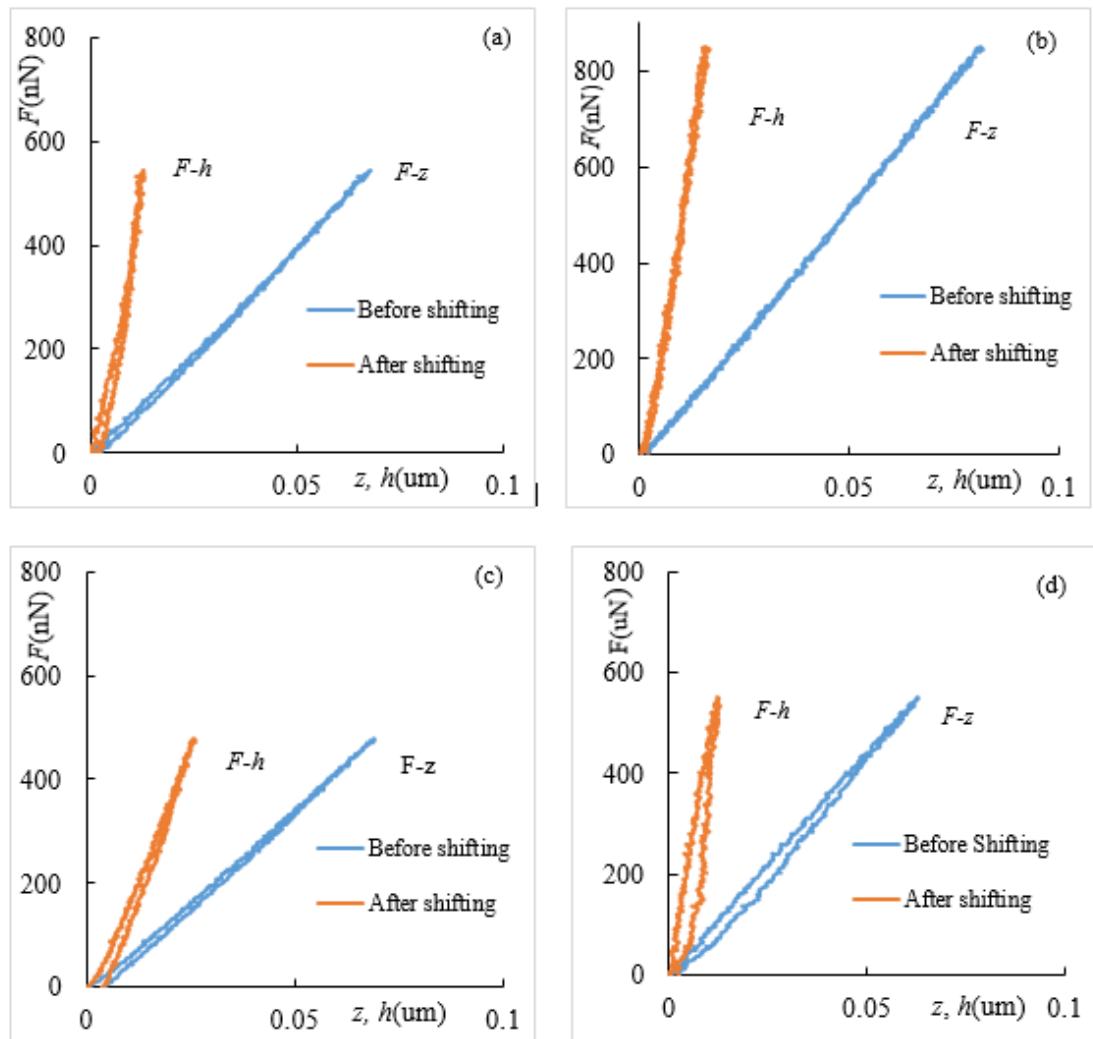


Figure 4.17: Example of the experimentally acquired force-displacement curves from one AFM-based nanoindentation cycle for (a) Tip 1, (b) Tip 2, (c) Tip 3 and (d) Tip 4. The blue curve represents the $F-z$ data while the orange curve shows the $F-h$ data.

A general qualitative observation was made when considering all the loading and unloading curve obtained for the different investigated tips. In particular, tip number 1, 2 and 3 displayed a low amount of fluctuation in the acquired force displacement curve across all 10 nanoindentation tests. However, all the curves for tip 4 exhibited a distinctively higher and level noise, as can be observed in Figure 4.17. The possible explanation for this could be due to the normal sensitivity of the PSPD value measured for each tip. More specifically, the measured magnitude of S_n for the first 3 tips was in the range 54 to 69.3 m/V as reported in Table 4.2, while the value for tip 4 was the highest, i.e. 104 m/V. As expected and also from evidenced in Figure 4.17, the lower the value of S_n measured for the tip, the better performance, i.e. the lower the noise, for the output produced. Thus, it is preferable to use AFM cantilevers with as low a sensitivity as possible in order to reduce the undesirable influence of noise (such as acoustic vibration) that may effect the accuracy of the nanoindentation curves (Binnig *et al.* 1986, Butt *et al.* 2005, Dukic *et al.* 2015).

After careful data processing of all the unloading curves for the tested tips, the values of the power law exponent, m , as well as of the degree of tip bluntness, d , were determined. These results are given in Table 4.3. The variations observed in this table between different nanoindentation tests for the same tip could be the result of:

- The non-ideal geometry of the tip under investigation;
- Vibrations that could not be completely eliminated;
- Non-homogeneity of the surface properties (i.e. nanoscale roughness and local chemical composition) of the used PC sample.

Table 4.3: The experimentally extracted values of parameters m and d as observed in nanoindentation with used tips, the average value of 10 tests after fitting the unloading curve of the used set of tips using the rescaling formula.

Test no.	Tip 1		Tip 2		Tip 3		Tip 4	
	m	d	m	D	m	d	m	d
1	1.80	1.25	1.81	1.23	1.72	1.39	1.50	2.00
2	2.33	0.75	1.54	1.85	1.89	1.12	1.50	2.00
3	1.60	1.66	1.5	2.00	1.86	1.16	2.00	1.00
4	1.71	1.42	1.38	2.60	1.71	1.40	1.70	1.40
5	1.71	1.42	1.67	1.50	1.62	1.61	1.65	1.54
6	1.72	1.38	1.46	2.50	1.96	1.04	2.00	1.00
7	1.71	1.42	1.58	1.72	2.2	0.80	2.10	0.90
8	1.71	1.42	1.47	2.13	2.10	0.90	2.10	0.90
9	1.80	1.25	1.58	1.71	2.3	0.76	2.00	1.00
10	1.71	1.42	1.5	2.00	1.65	1.61	1.50	2.00
Average value	1.78	1.34	1.55	1.92	1.90	1.18	1.81	1.37
Standard deviation		0.22		0.40		0.30		0.46

The experimental data reported in Table 4.3 shows a good agreement with results already published in the literature such as by Oliver and Pharr (1992) and Borodich *et al* (2003). In particular, the average values of the power law exponent, m , measured here vary between 1.55 and 1.90 and the results for d are comprised between 1.92 and 1.18. Thus, the experimental results for m in this work lie between those of a spherical and a conical indenter for which $m = 1.5$ and $m = 2$, respectively. This means that, for the range of nanoindentation depths achieved here (i.e. less than 50 nm from the tip apex), the shape of the tips used can be considered to be between a perfect sphere and an ideal cone.

In addition, it can also be observed from this table that tip 3 is the sharpest tip. Tip 1 and tip 4 exhibits nearly the same degree of tip bluntness d . Lastly, tip 2 displays the highest value for d which means that it more blunt than the others.

As pointed by Briscoe and co-workers, all conical or pyramidal AFM probes may present some sort of defect geometry such as blunting at the tip apex, and thus they cannot be considered perfectly sharp (Briscoe *et al.* 1994; Briscoe and Sebastian 1996; Briscoe, B.J. and Sebastian 1996). This is verified with the results presented here. Indeed, all the tips investigated are new, and of the same model while also being taken from the same box as provided by the manufacturer. In spite of that they show different degrees of bluntness. Such differences in the case of a blunt tip could be due to some small local protrusions at the tip apex, which in practice, may act as the actual sensor for the tip (Skårman *et al.* 2000). This reinforces that fact that it is important to assess the tip apex sharpness at the working position in order to use such probes for further AFM-based fabrication or characterisation on the nanoscale.

The complete set of results when calculating d for each tip and from each nanoindentation test is given with Figures 4.18 to 4.21. These plots provide some indication about the repeatability of the measured value of d . Tip 2 shows generally high values of d , while tip 3 generally presents low values of d . The sources of some discrepancies in the results for a given tip were discussed earlier. Also, it must be stated that a possible (6%) uncertainty in force measurement (Song *et al.* 2015) using AFM could bring about (± 0.22) in d value extracted according to one curve analysis.

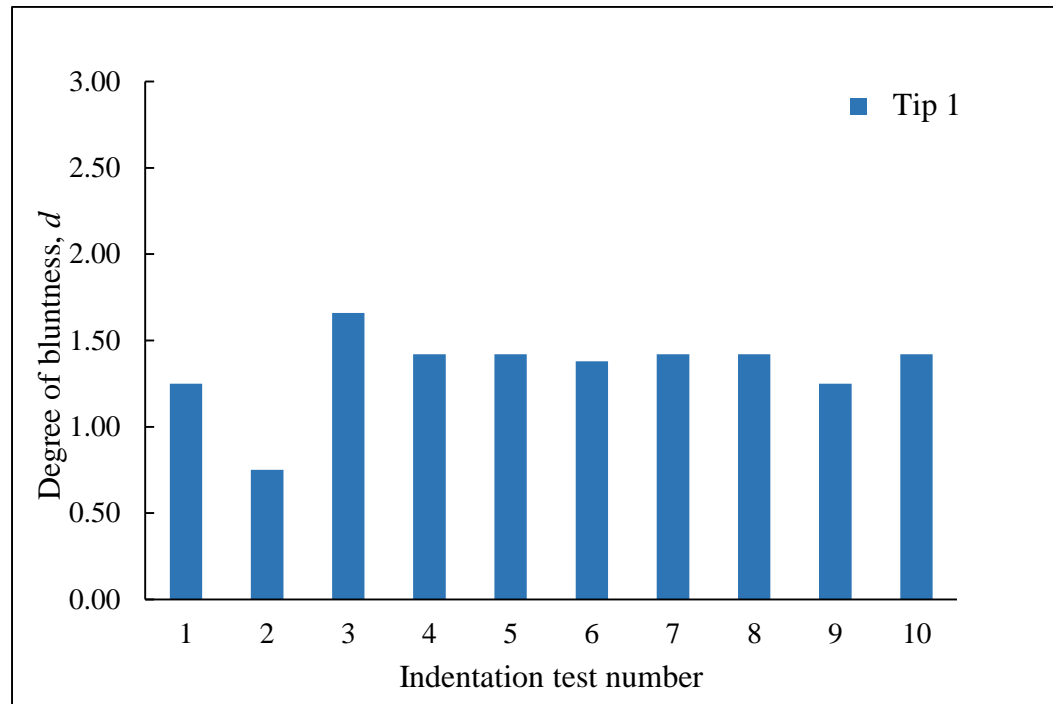


Figure 4.18: Plots of the d value extracted for each of the nanoindentation test for
tip 1

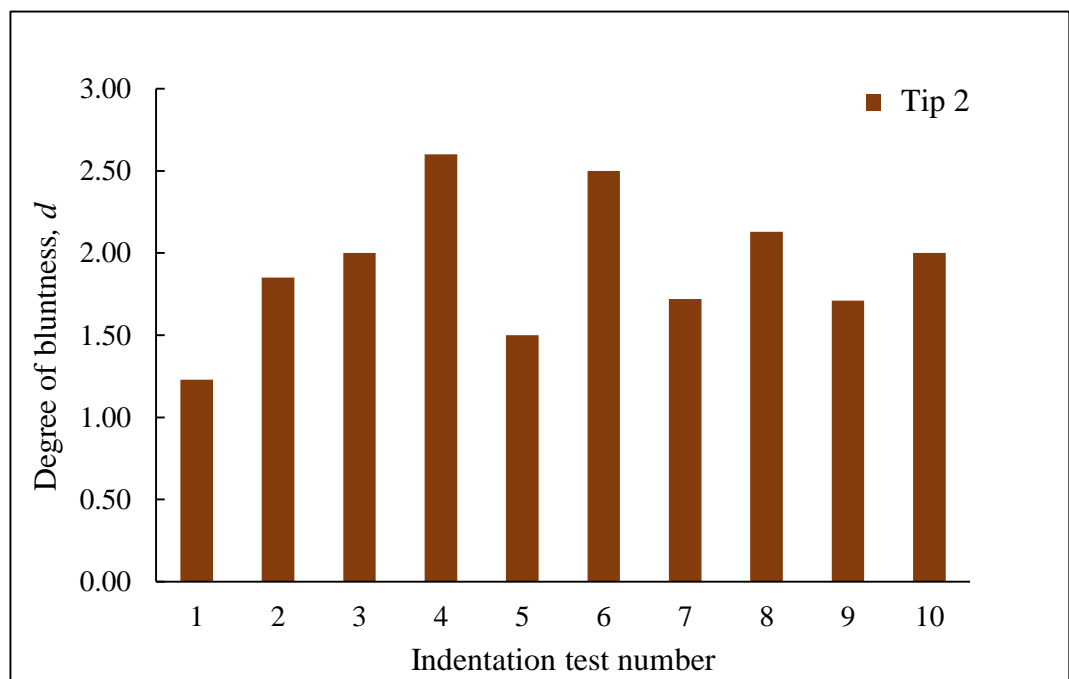


Figure 4.19: Plots of the d value extracted for each of the nanoindentation test for
tip 2

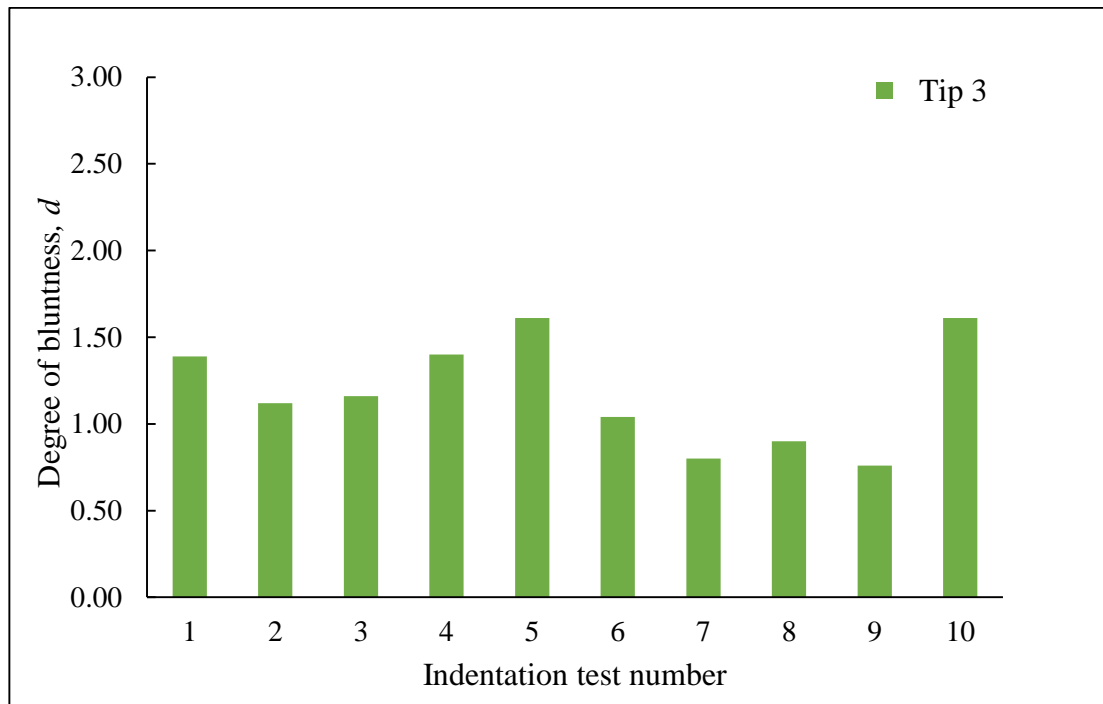


Figure 4.20: Plots of the d value extracted for each of the nanoindentation test for tip 3

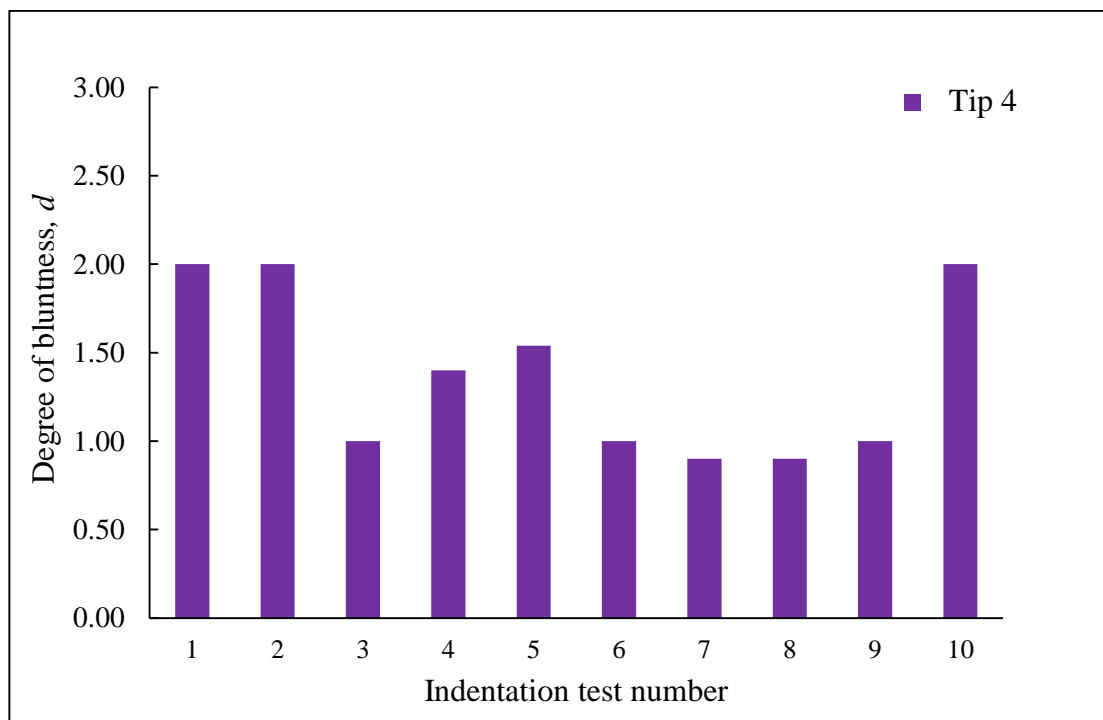


Figure 4.21: Plots of the d value extracted for each of the nanoindentation test for tip 4

4.5.1.1 Further analysis of the proposed method to assess the tip bluntness

Additional analysis can be completed about the extracted value of d for each tip apex by examining the obtained data for both h_{max} and h_f . As introduced earlier in F, these represent the maximum indent depth and the final indent depth, respectively. Both h_{max} and h_f values can be extracted from the force-displacement curve after the shifting operation to output $F-h$ from $F-z$. Figure 4.22 shows the number of times the value of h_{max} was comprised within a given interval for each tip. More specifically, the x -axis shows intervals of length 2 nm (i.e. from 0 to 2 nm, then from 2 nm to 4 nm, etc....) while the y -axis shows the number of nanoindentation tests for which the of h_{max} obtained was within an interval.

From these results, it can be seen that tip 3, which should be the sharpest tip having an average $d = 1.18$, always led to the highest nanoindentation depth, h_{max} , inside the tested sample with an average equals to nearly 30 nm. In contrast, tip 2, which is assumed to be the bluntest tip (i.e. average $d = 1.92$), resulted in the majority of the h_{max} data near 10 nm to 12 nm. These observations are in-line with the assessment of the d values made earlier. Indeed, it is expected that a blunter tip leads to a shallower penetration depth at the maximum load. Regarding the other two tips, i.e. number 1 and number 4, a small differences could be found in the bar graphs of Figure 4.22 although their average degree of bluntness d was found to be nearly the same, i.e. $d = 1.34$ for tip 1 and $d = 1.37$ for tip 4. This could be due to different reasons such as sample properties, technical issue.

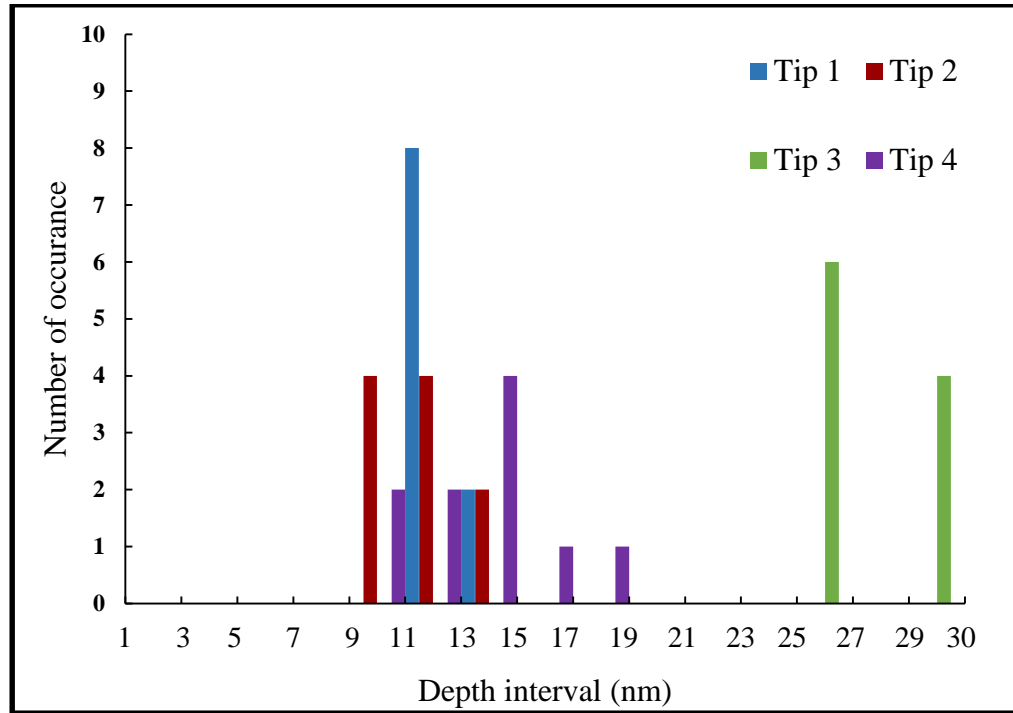


Figure 4.22: Bar graph showing the number of times the measured h_{max} is comprised within a specific interval. The data for tip 3 were taken for a load of 600 nN so for comparison purpose with the other tips

A similar comparison, as has been done with Figure 4.22, was carried out using the results for h_f (see Figure 4.23). This figure presents the number of tests where h_f , i.e. the permanent depth of penetration after the indenter is fully unloaded, is within a specific interval for each tip under investigation. From this figure, it is clearly observed that tip 3 (i.e. the sharpest tip) often results in the maximum h_f value, while tip 2 (i.e. the bluntest) exhibited almost the same value of h_f for every nanoindentation tests which was also the lowest among all tips with an average value about 2 nm.

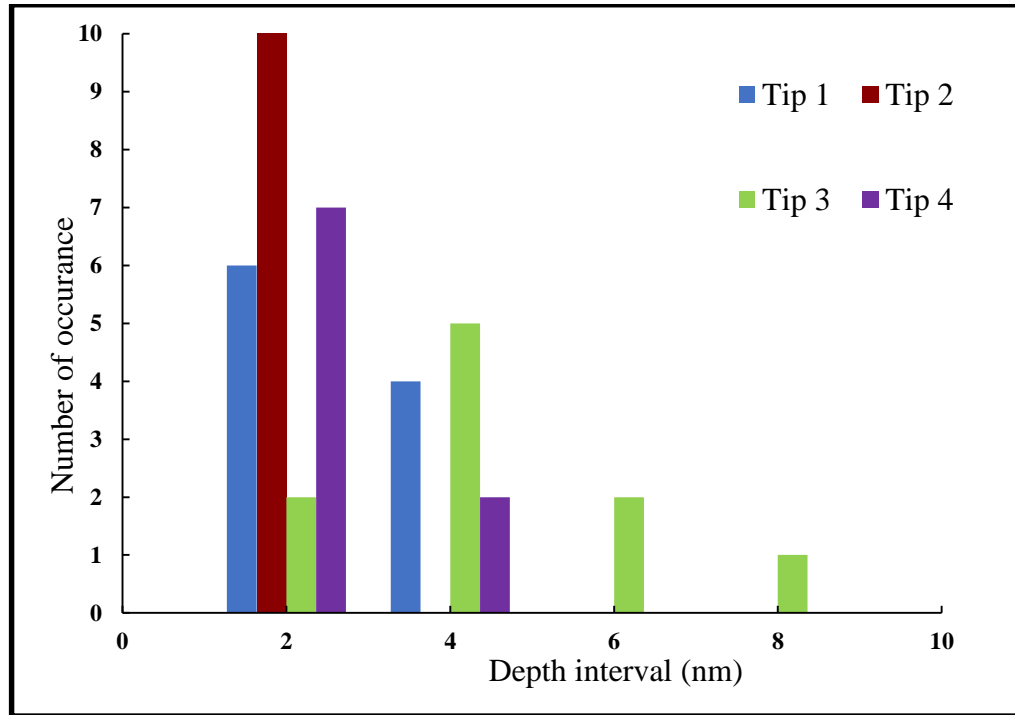


Figure 4.23: Bar graph showing the number of times the measured h_f value is comprised within a specific interval. The data plotted here were extracted considering the actual F_{max} achieved during the experiments.

Finally, the average values for h_{max} and h_f were calculated for each tip. The results were plotted against the average d value assessed earlier for each tip. This relationship between d and h_{max} is illustrated in Figure 4.24. From this figure, it is clear that a smaller d for the investigated tip leads to a higher penetration depth inside the polymer sample. The same behaviour can be seen with the plot of h_f versus d as illustrated in Figure 4.25. Thus, the overall output from force-displacement curves indicates that the smaller the value of d for the tested tip, the higher the result of both h_{max} and h_f under similar test conditions. Table 4.4 provides the actual average values of both h_{max} and h_f used in Figures 4.24 and 4.25. The average degree of bluntness d is also repeated in this table.

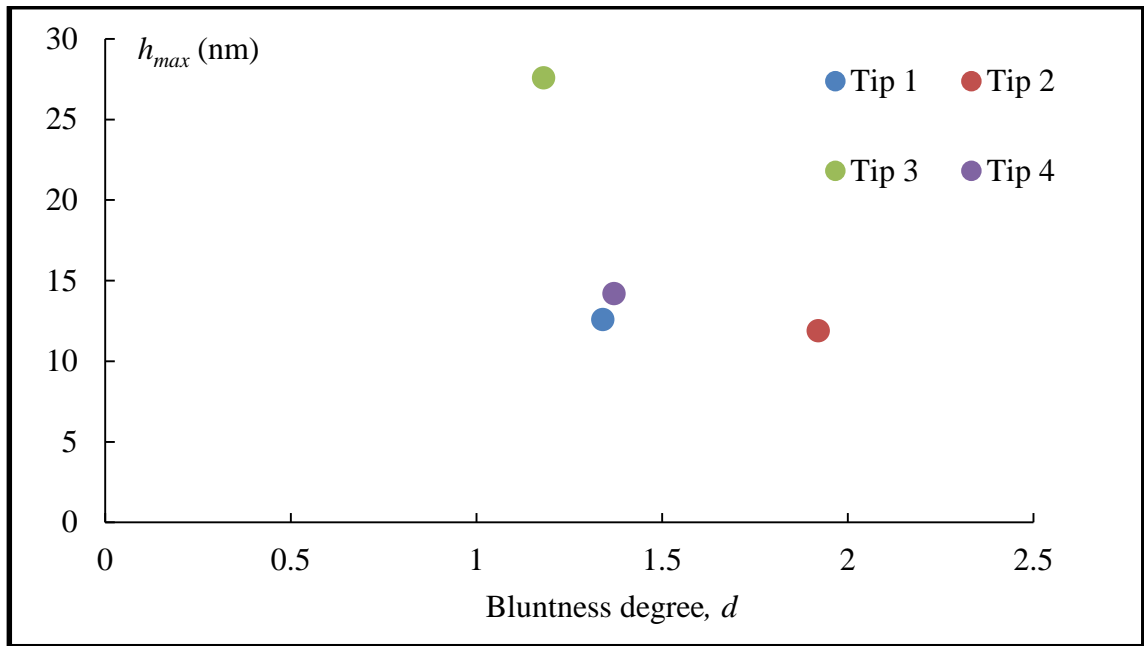


Figure 4.24: Experimental relationship between the average degree of bluntness, d , and the average h_{max} values for each tip.

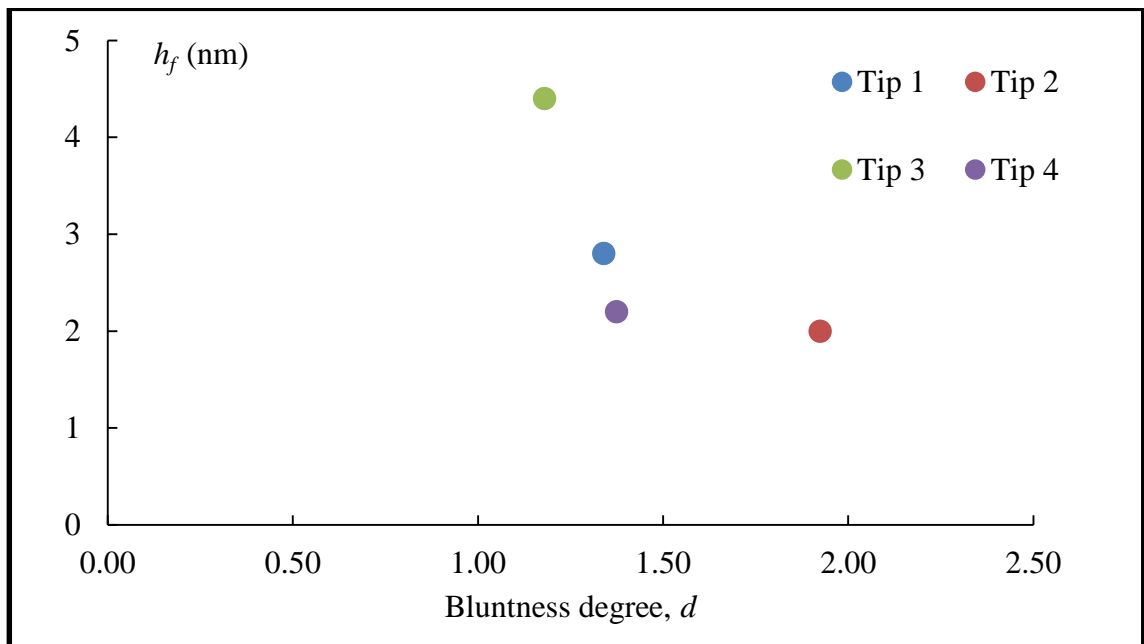


Figure 4.25: Experimental relationship between the average degree of bluntness, d , and the average h_f values for each tip.

Table 4.4: shows the average value of d , h_{max} and h_f for the used sets of tips.

Tip No.	Average h_{max} (nm)	Average h_f (nm)	Average d
1	12.6	2.8	1.34
2	12.0	2.0	1.92
3	27.6	4.4	1.18
4	14.2	2.2	1.37

4.5.2 SEM micrographs

The height, h , of the 2D profiles of each tip extracted from SEM micrographs are given in Figure 4.26 as a function of their width. It is obvious that the tips are neither perfectly sharp, as would be the case for an ideal cone, nor perfectly spherical. Thus, their shape cannot be assumed in advance of experiments. In addition, these 2D profiles present limited details regarding the tip actual shapes because of their non-axisymmetric nature. Thus, the appropriate description of the tip shape differ from one radial cross section to another. Also, a general comparison between the investigated tips is presented in Figure 4.27. In particular, this figure shows all the tip profiles on the same plot for a distance from the tip apex of 50 nm. For both figures, the profiles correspond to a cross section perpendicular to the long axis of the cantilever as a result of the specific orientation of the probe in the SEM instrument.

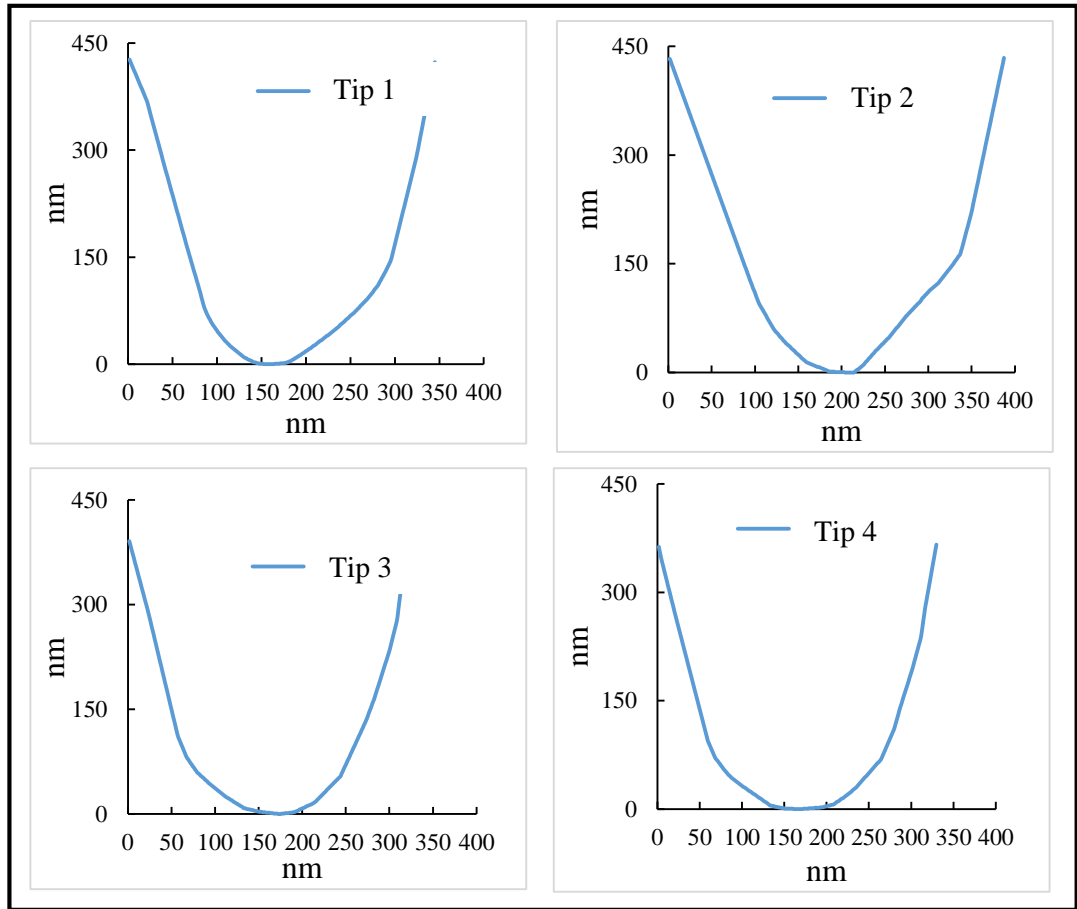


Figure 4.26: Extracted 2D data from SEM profiles for the 4 investigated tips after using image processing software (Image J). The profiles correspond to a cross section perpendicular to the long axis of the cantilever

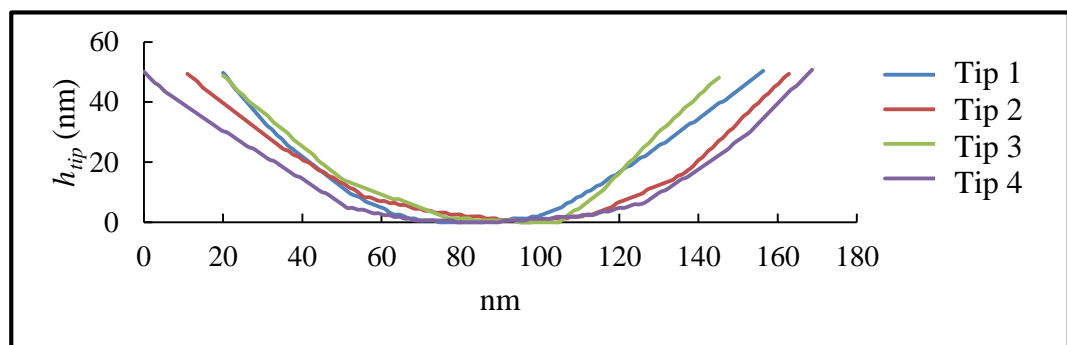


Figure 4.27: AFM tips profiles 2 D for all tips extracted by image j. All tips where superimposed together to show the general geometry of all tips from one perspective up to 50 nm length from the tip apex.

As described in Chapter 3 and based on Borodich *et al.* (2003), it is assumed that using polar coordinates (r, θ) , the shape of the tip apex can be described as a monomial function of degree d as follows:

$$x_3 = B_d(\theta)r^d \quad (4-13)$$

where d is assumed to be the degree of bluntness, B_d is a function of the tip height at $r = 1$. Thus, each SEM profile was further processed to identify the point at its apex. Given that each profile display the tip pointing downward, the apex corresponds to the point on the profile with the lowest value on the y axis. This point was used to split the profile into two parts as shown in Figure 4.28 (a). Then a vertical and horizontal translations were applied in order for this point to become the origin of a new coordinate system to plot the profile as illustrated in Figure 4.28 (b). A mirror transformation about the y axis was applied to the left part of this profile, i.e. the blue profile in Figure 4.28 (b). This resulted in both profiles to be plotted for positive coordinates along the x axis, as shown in Figure 4.28 (c). In addition, the maximum height over which both profiles were considered was taken to be equal to h_{max} for that tip, as reported in Table 4.4. In this way, it was possible to fit a power law function, $h_{tip}(r)$, to each profile with two unknown parameter, B_d and d as follows:

$$h_{tip}(r) = B_d r^d \quad (4-14)$$

where r represent the radial length the profile. Figure 4.28(c) shows the fitted function for both profiles considered. The results obtained when assessing d from the SEM data for all tips are given in Table 4.5.

As mentioned above, the d value determined represents the average value obtained from two parts of the profile for each tip. As mentioned above, the height of this profile was equal to the maximum depth obtained for this tip during the nanoindentation test, h_{max} . These results can now be compared with the d values obtained earlier from the nanoindentation approach. These values are also included in Table 4.5. Finally, this table also presents the percentage error between both approaches implemented to assess the degree of bluntness, d . Finally, Figure 4.29 presents a plot for the values of d extracted from two approaches, in addition to showing the final value of h_{max} for each tip.

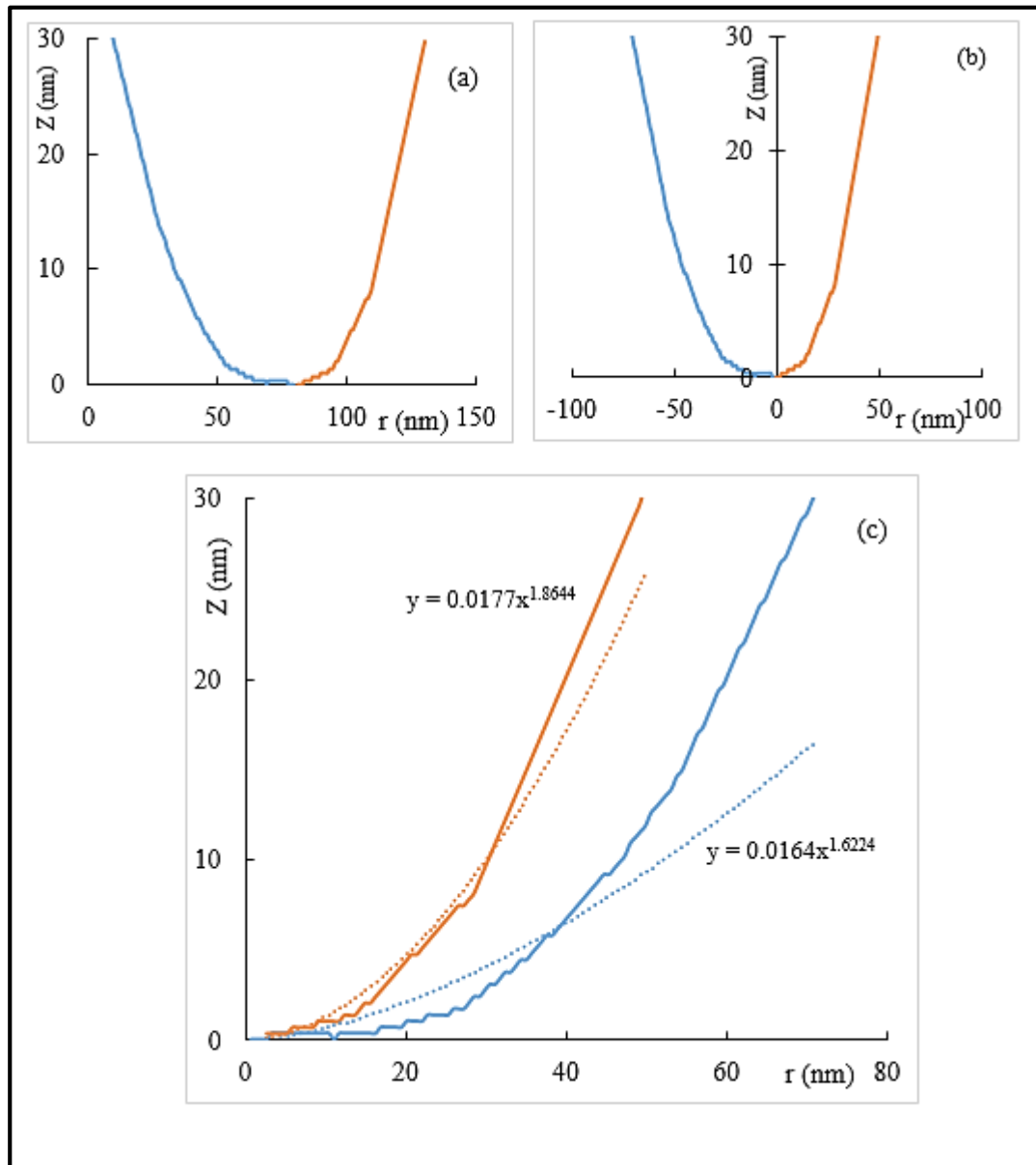


Figure 4.28: Illustration of the steps used to extract the d value from SEM 2D data for one tip (Tip 4). The vertical interval considered, i.e. 30 nm, corresponds the average h_{\max} value obtained during the nanoindentation experiments. The average value of d calculated from the two profiles plotted here was 1.74 as also indicated in Table 4.5.

Table 4.5: Assessment of the degree of bluntness, d , obtained from nanoindentation tests with the rescaling formula and with the 2D profiles extracted from SEM micrographs.

Tip number	d from nanoindentation tests	d from SEM (2D) data	Percentage error
1	1.34	1.45	7.59 %
2	1.92	1.33	30.72 %
3	1.18	1.74	32.18 %
4	1.37	1.57	12.47 %

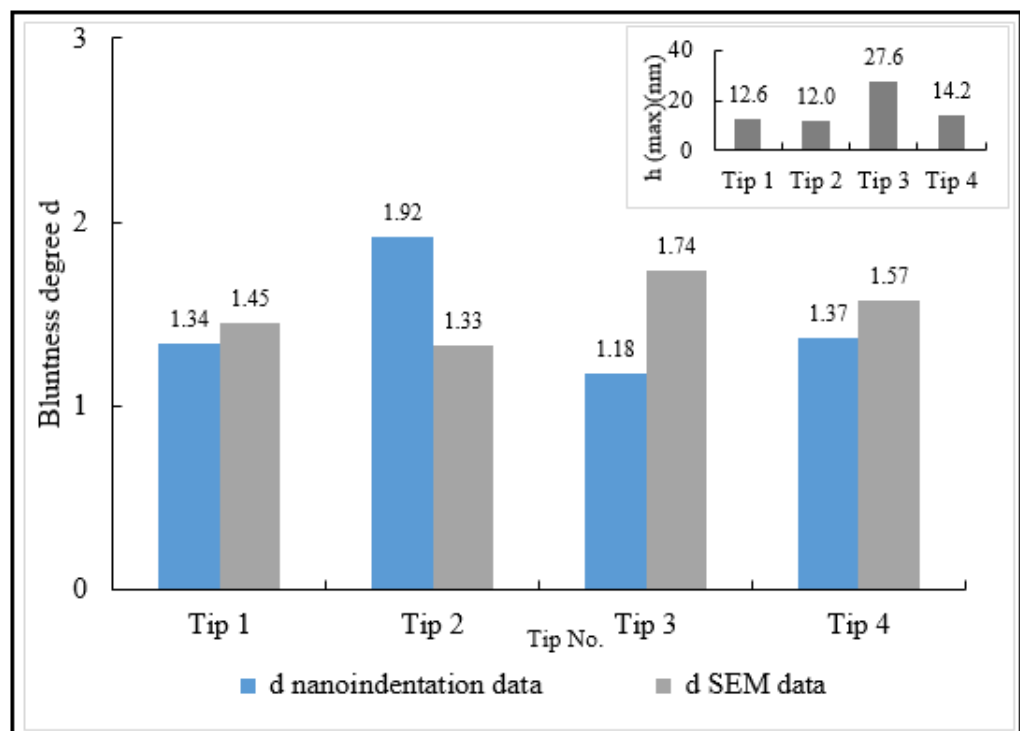


Figure 4.29: degree of bluntness, d , obtained by nanoindentation tests with the rescaling formula and via 2D profile from SEM micrographs. The inset plot shows the average value of h_{max} extracted for the same set of tips

From the results presented in Table 4.5 and Figure 4.29, it is clear that there is a significant difference between the outcome of the two methods when assessing d . Indeed, the percentage error is comprised between 7.6% and 32.18%. This observed discrepancy could be due to many reasons, the most important are:

First, the SEM data only represent a 2D evaluation of the tip shape while nanoindentation tests take into account their 3D geometry. Therefore, the comparison between one cross section of the tip profile to another may differ because of the non-axisymmetric nature of the tip apex.

Second, using the SEM the tip is inspected in its vertical position while it is inclined at an angle when the tip performs AFM nanoindentation tests. This suggests that the bluntness of an AFM tip differs significantly depending on its consideration: in its vertical position or in its working position at an AFM head.

In addition, from Figure 4.29, it can be seen that the smallest value of d (i.e. for Tip 3) as extracted from the nanoindentation tests also corresponds to the higher value of h_{max} . Alternatively, the highest d value, obtained for Tip 2, corresponds to the lower indentation depth measured. This observation is in-line with what would be expected because a sharper tip should lead to a deeper indentation depth.

Finally, using the analysis of the SEM micrographs only, it could be said that Tip 2 is the sharpest of the four tips investigated. However, this does not agree with the results obtained based on the nanoindentation tests. This discrepancy will be further studied in details in Chapter 5.

4.6 Summary

In this work, we reported an experimental/analytical procedure to estimate the degree of bluntness of non-axisymmetric tip apex of AFM probes “as received from the manufacturer”. In particular, this procedure relies on nanoindentation experiments which enable the analysis of the force-displacement curves using the Borodich rescaling formula. Thus, it allows to estimate in-situ the actual bluntness of the AFM tip without the use of any additional equipment. In addition, this evaluation is conducted when AFM probe are in their working position in the AFM instrument. Four commonly used, commercially available AFM probes were considered to implement this approach. These probes were made of single crystalline silicon tips coated with diamond and they displayed different spring constant. The nanoindentation tests were performed over a polycarbonate sample.

Based on the results obtained in this chapter, the following conclusions could be made:

- The data obtained in this study to evaluate the degree of tip bluntness, d , for the different tips investigated are in agreement with the experimental results reported in the literature. In particular, the average values of d ranged from 1.18 to 1.92, which correspond to m values in the range between 1.90 and 1.58. As explained in this chapter, m is the slope of the unloading force displacement curve ($F-h$) when plotted on a logarithmic scale $\text{Log } F \sim \text{Log } h$.
- The observed degree of tip bluntness, d , for the all tips investigated show that the shape of all the assessed tips could considered to be between a spherical and a conical shape approximation, i.e. $d=2$ and $d=1$, respectively. This clearly shows that, when only a shallow distance from the tip apex is effectively used for the study of nanoscale

phenomena, it is not correct to assume that such AFM probe tips have semi-spherical shape at the apex region.

- In this work, it was found that the result of both the maximum nanoindentation depth and the residual indent depth were in-line with the degree of tip bluntness evaluated. Overall, the lower the degree of tip bluntness tended to yield the maximum nanoindentation depth and the highest resulting indent.
- As evidenced with SEM micrographs of the tips at different stages of the process, it could be stated that the proposed procedure is a non-destructive method for determining the tip apex shape when using a polymer material.
- A significant difference, i.e. between 8% and 32%, was found when assessing the degree of tip bluntness from nanoindentation tests and from SEM micrographs of the tip profiles. This discrepancy should be the result of the non-axisymmetric and the non-spherical nature of the used tips. Indeed, the lack of axisymmetry means that the analysis conducted on a 2D profile as obtained with the SEM should not be reliable. More specifically, such 2D data corresponds only to a particular cross-section of a tip and thus, it is not representative of its 3D shape. In addition, the SEM-based analysis does not take into account the tip inclination when the probe is in its working position.
- The study also revealed the significance effect of the calibration of both the cantilever spring constant and the sensitivity PSD to obtain an accurate and a reliable force-displacement curve.

Due to the inherent limitation of using 2D data from the tip apex, the validity of this nano-indentation approach to assess the tip shape is further studied in the next chapter. In this case, 3D data about the tip apex will be used instead of 2D data from SEM micrograph.

Chapter Five

Analysis of the AFM nanoindentation approach for tip shape characterisation using 3D geometry data

5.1 Aim and objectives.

The bluntness degree d was characterised in the previous chapter for four different tips using the AFM nanoindentation test. In this chapter, it is our objective to further assess the suitability of this in-situ technique for the tip bluntness assessment. This is achieved by comparing its outcome with that obtained from the analysis of the three dimensional (3D) geometry of the real tip shape. In particular, the 3D data for the tip geometry is obtained by scanning the four probes investigated over a special tip characteriser as described in Chapter 2. A power law value of d for each tip was obtained from the extracted 3D data. In addition, based on the experimental data obtained in this chapter, an assessment is also made to evaluate the suitability of approximating the tip shape with a perfect spherical cap geometry.

5.2 Introduction

In order to achieve the overall objective of this chapter, 3D geometry data of the tested tips were required. These were obtained by implementing the reverse imaging approach where the AFM tips were used to image a tip characteriser, which is a special test structure consisting of an array of silicon sharp pin-like tips. This technique is considered here as an in-situ direct approach while the nanoindentation-based technique investigated in this Thesis can be seen as an in-situ indirect assessment.

Based on the 3D tip profiles obtained with the tip characteriser, first radius of curvature measurement were carried out using two different methods in 2D and 3D data. More specifically, this was done to identify discrepancies when using these different dimensional measurement and also, to use more accurate radius of curvature value for

further analysis. Second, an analysis of four cross sectional profiles extracted from the 3D data was performed by fitting a power law function over each experimental profile. In this way, an average value of the power law exponent d was obtained for each tip. This provided a validation process to compare the values of d obtained by two different approaches, i.e. the indirect and the direct techniques. Ultimately, further comparison was presented between the probe tip profiles extracted by these two approaches in addition to the theoretical assumption of perfect spherical apex. This was achieved to gain more understanding about the general description of the tip geometry using these different approaches at the apex region.

This chapter is organised as follows: first, a summary flow chart of both the experimental set-up and the analysis of the results is presented in the next section. This is followed by a section that explains the experimental procedure applied to extract the 3D data of the used set of tips. The next section presents the procedure followed to obtain radius measurements from the extracted tip profiles until specific length from the tip apex. Then, Section 5.6 demonstrates the procedure applied to obtain the d value from the fitting of a power law function on different tip profiles based on 3D data. Following this, in Section 5.7 starts by comparing the obtained degree of tip bluntness based on the nanoindentation and power law approaches using 2D and 3D data. In the same section, the validity of approximating the tip shape as a spherical cap is also made. Finally, the last section summaries the main findings and conclusions of the work reported in this chapter.

5.3 Experimental setup and methodology

Figure 5.1 provides a graphical summary of the overall work conducted in this chapter.

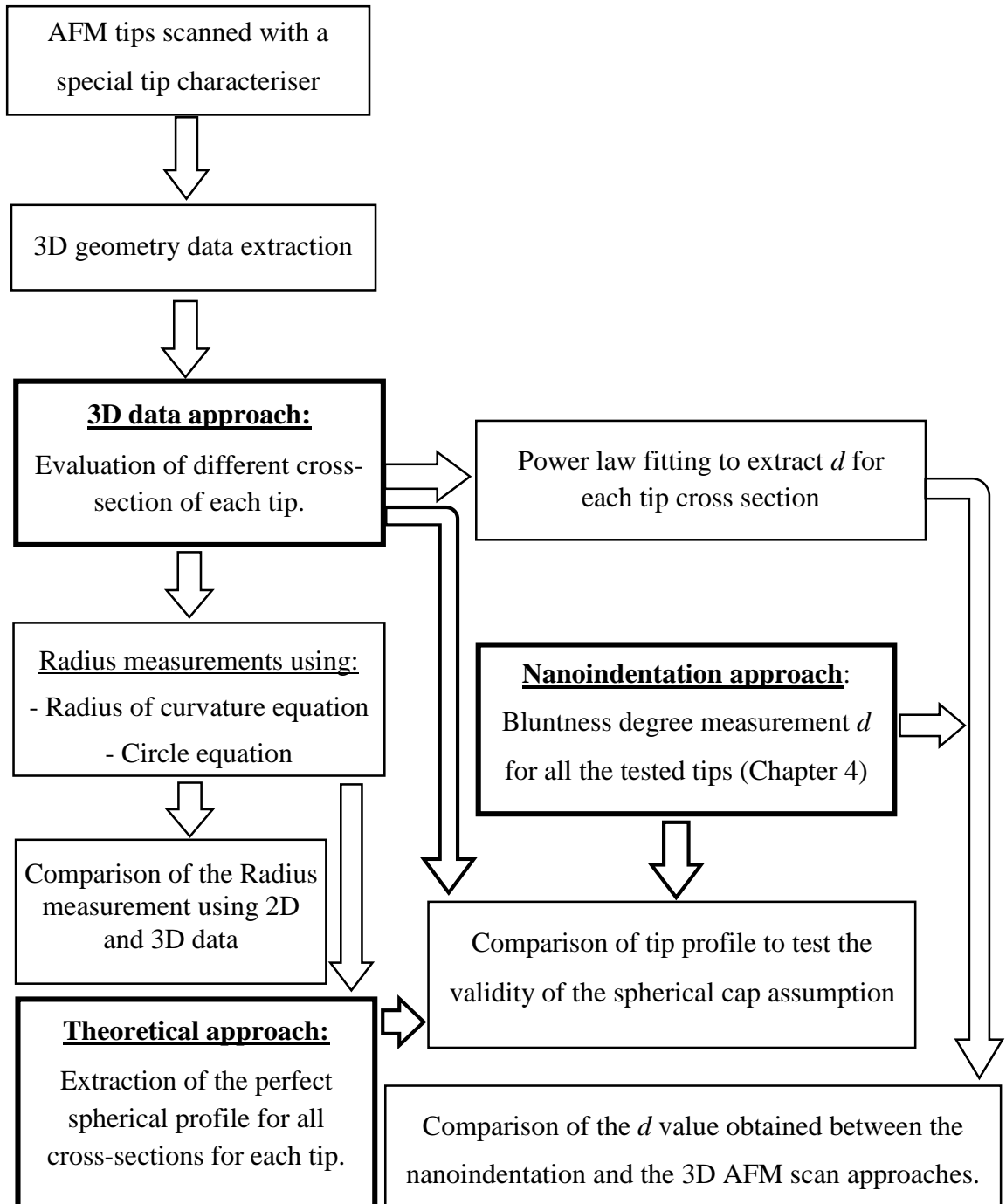


Figure 5.1: Flow chart representing a schematic of the experimental and analytical procedures implemented in this chapter.

5.4. Extraction of three-dimensional tip geometry

5.4.1 Methodology

As reported in Chapter 2, various techniques exist to obtain 3D geometry data of the apex of an AFM tip. Among these, the two approaches that rely on scanning a tip characteriser and on using an ultra-sharp probe to directly image the considered tip are of interest. Indeed, they do not require for the user to fabricate a his/her own lab-made sample and also, they do not need further post-processing once the data have been obtained. A specific study was conducted by the author and co-workers (Alraziqi *et al.* 2016) for comparing the accuracy of both the tip characteriser and the ultra-sharp tip approaches. In this study, SEM profiles were used as a reference to evaluate the reliability of these two techniques. The combination of the achieved qualitative and quantitative results showed that employing the reverse imaging method with a tip characteriser was the most accurate technique for obtaining 3D geometry data, especially within a distance of 100 nm below the tip apex. In addition, as mentioned in Alraziqi *et al.* 2016, in practice, this technique is also more straight-forward to implement as there is no need to remove the tip under investigation from the AFM head. Finally, an important drawback with the ultra-sharp tip scan approach is that it could sometimes lead to damaging contacts between both tips. This is due to the fact that precisely locating an ultra-sharp probe over the inspected tip apex can be a non-trivial process.

For these reasons, the tip characteriser approach is also adopted in this work to extract the required 3D geometry data of the apex for the four tips investigated. The tip characteriser employed here is commercially available (model TGT01) from the company NT-MDT. It consists of an array of silicon sharp pin-like asperities as shown in Figure

5.2. Other researchers also used the same tip characteriser (e.g. Bykov *et al.* 1998, Bloo *et al.* 1999, Zhenhua and Bhushan 2006 and Neto and Craig 2001) for their studies.

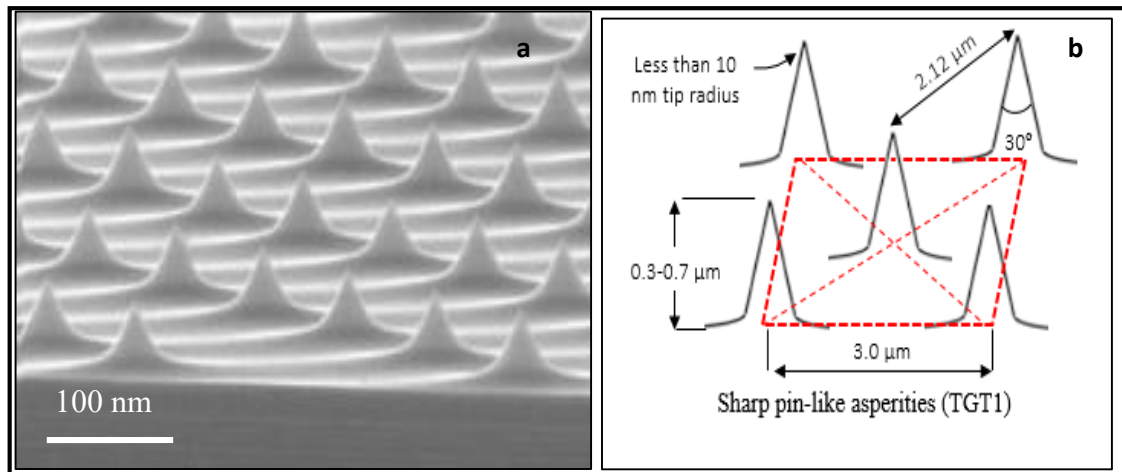


Figure 5.2: (a) SEM image of silicon TGT01 grating sample (from NT-MDT 2017) (b) sketch of the nominal geometry between the features according to the manufacturer (adapted from Bloo *et al.* 1999)

The procedure implemented in this study to obtain the 3D geometry data of the tips was as follows. First, the TGT01 specimen was positioned on the stage of the AFM instrument. Next, it was scanned by the tips under investigation in non-contact mode with a scan rate of 0.6 Hz over an area of $5\ \mu\text{m}$ by $5\ \mu\text{m}$. An example of such a scan is given in Figure 5.3. Then, two sharp asperities were selected and scanned individually using the same scanning parameter. However, in this case, the scanned area was $1.5\ \mu\text{m}$ by $1.5\ \mu\text{m}$ (see Figure 5.3). Two asperities were examined for each tip in order to take the average of the quantities extracted later on from such 3D data. This should minimise measurements errors. Each AFM image were obtained using a resolution of 512 lines with 512 pixels per line.

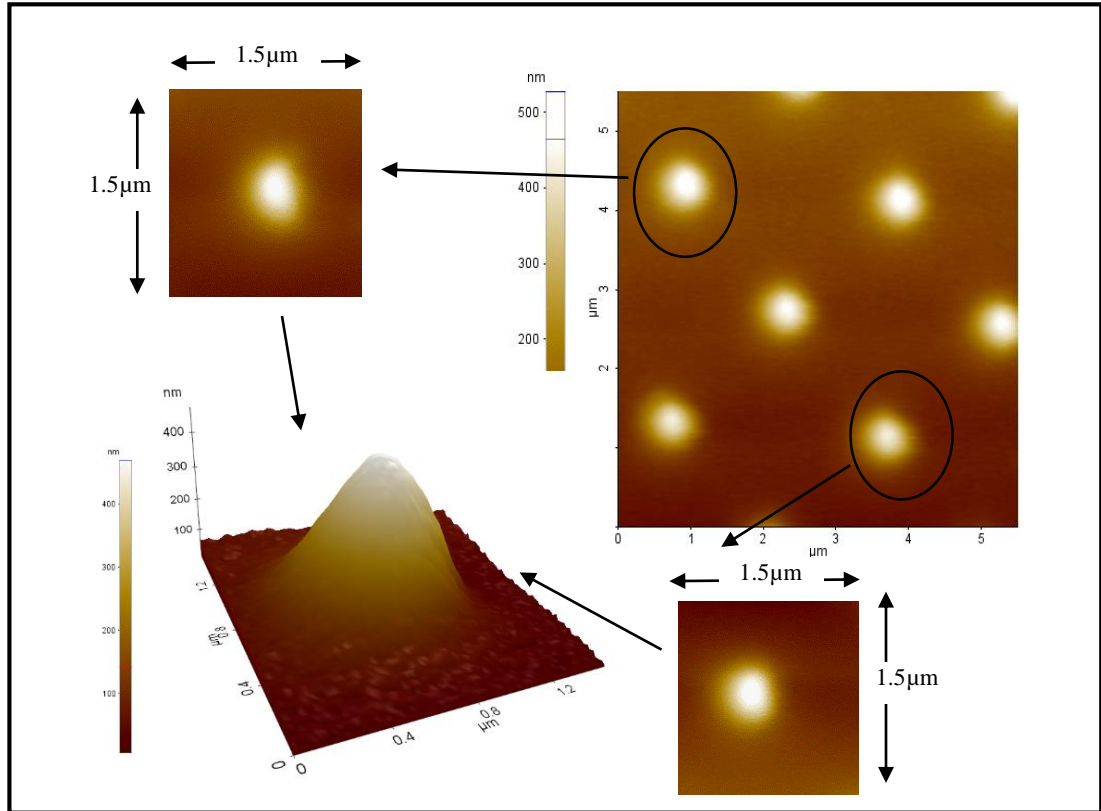


Figure 5.3: Example of an AFM image of the TGT01 tip characteriser scanned by one of the tested tips, including two scans of sharp asperities and one typical example of the 3D view of one of them.

From the 3D geometry data contained in the AFM scan of one asperity, different profile cross sections can be obtained. To achieve this, the scan 3D AFM image is processed in a software package (XEI from Park Systems). This software allows the easy extraction of many cross section profiles with respect to different angles. As illustrated in Figure 5.4, in this study, four profile cross sections were selected, namely along an horizontal orientation (hereafter referred to as the 0° - 180° axis), a vertical orientation (i.e. the 90° - 270° axis) and two diagonal orientations (i.e. the 45° - 225° and 135° - 315° axes). Both diagonals were oriented at 45° with respect to the horizontal and the vertical axes. In addition, when processing such AFM an image, the highest point on the tip is found to

define the centre of all the axes as also shown in Figure 5.4. The 2D coordinates for a cross section are recorded in an ASCII file for further analysis. In addition, in order to assess the degree of bluntness by fitting a power law function later on, it is necessary to define two separate profiles, where the position of the tip apex is at the origin (i.e. at the position (0, 0)). This step is conducted with the Excel software. In summary, following this procedure for one AFM scan of a sharp asperity, it is possible to extract 8 profiles in total (i.e. 2 per cross section). As shown in Figure 5.4, the respective 8 profiles are referred to as 0° , 45° , 90° , 135° , 180° , 225° , 270° and 315° . The advantage of this procedure in comparison with that followed in the previous chapter is that it enables the analysis of a set of profiles which are representative of the 3D geometry of the tip apex. This should be particularly important when working with non-axisymmetric tips, as this is the case in this work, to minimise the measurement error when assessing the tip shape.

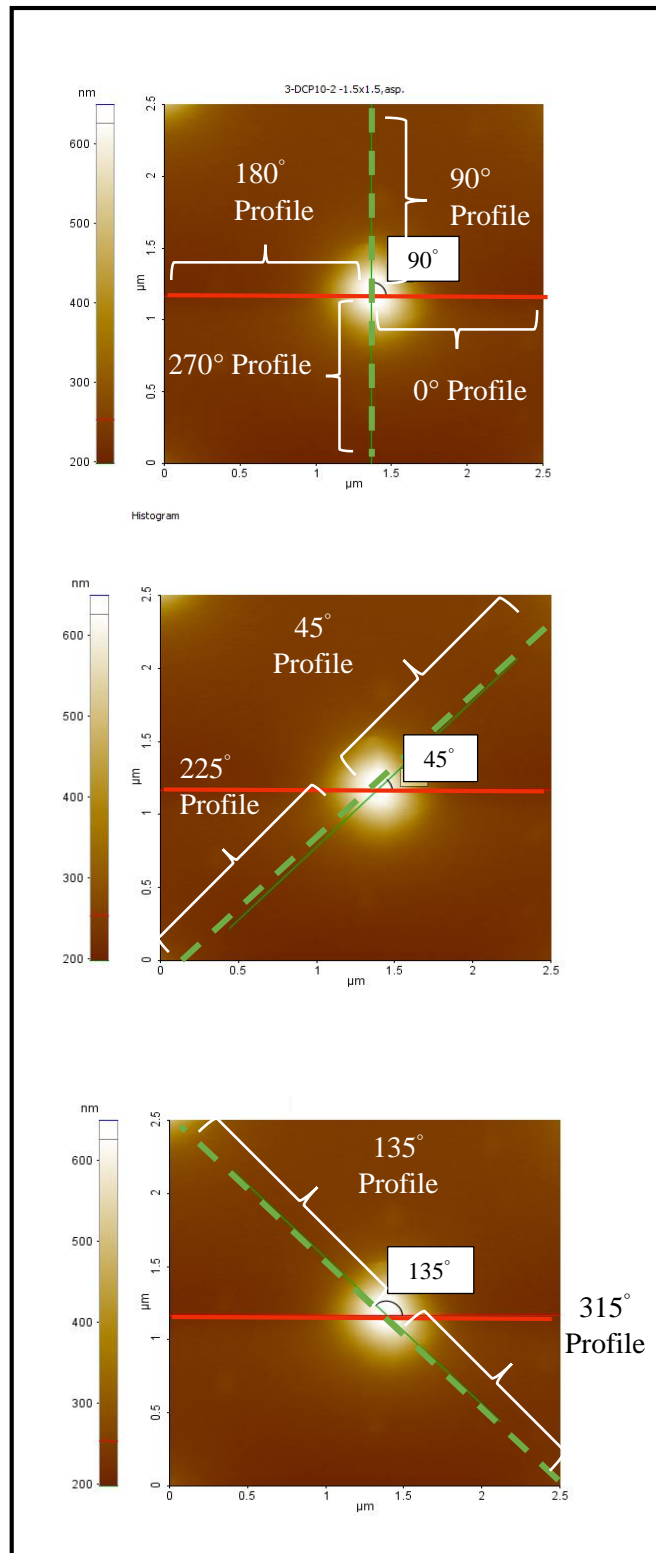


Figure 5.4: Illustration of the selection of the (0°-180°), (90°-270°), (45°-225°), (135°-315°) profile cross sections for Tip 1. In this figure, the horizontal red line is always along the (0°-180°) axis and the green dashed lines represent the other 3 profiles.4

5.4.2: Results and analysis

Two 3D AFM images were obtained for all used tips following the procedure explained in the previous section, Figure 5.5 presents one of the 3D AFM images for each tested tips.

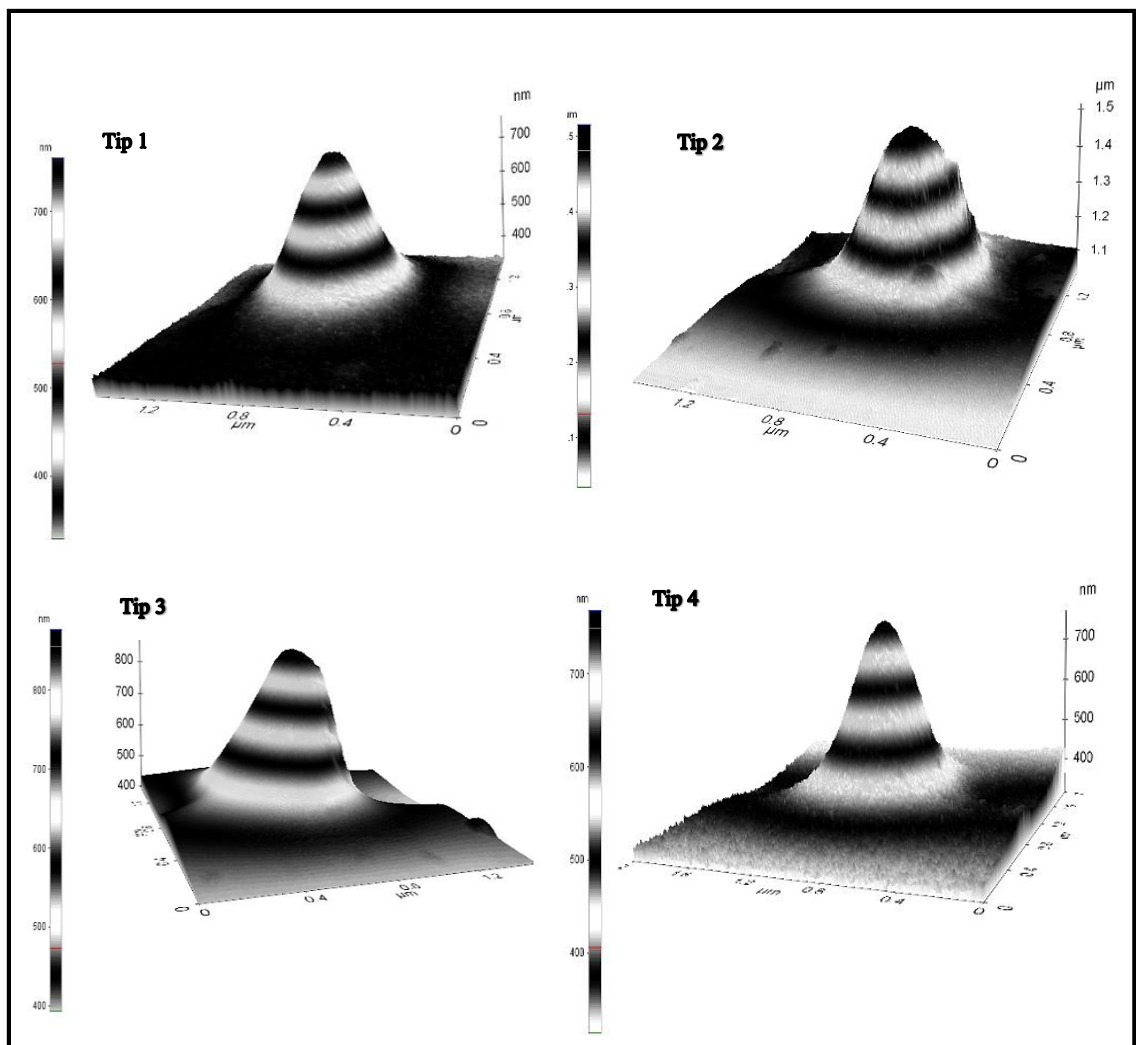


Figure 5.5: 3D AFM images for the four tested tips after scanning the TGT01 tip characteriser

Figures 5.6, 5.7, 5.8, 5.9 show the different profiles extracted for the 4 investigated tips along each cross section. The qualitative analysis of these profiles can give an initial indication about the geometry of tip apex, especially for such non-ideal tip shapes. It is clear from these figures that, for each tip, there is an obvious difference between the different profiles obtained as a function of the orientation of the selected cross section. This implies that the shape of such tips cannot be assessed according to the analysis of one profile only such as the 2D assessment which was realised in the previous chapter and which is a conventional practice in the literature. Thus, it is noticed that what may look like a sharp tip when working with a 2D profile extracted from a SEM micrograph, could in reality consist of defects or irregularities along other cross sections, which the SEM cannot distinguish. For example, this is obvious when one compares Figure 4.26 with Figure 5.6 for Tip 1. The further qualitative observation of figures 5.6 to 5.9 also reveals that, for a given cross section, the agreement between the profiles obtained from the scan of two different asperities is generally good. The discrepancy observed in this case, can be due to the expected experimental error and also due to the possible difference between the sharpness of individual asperities. Indeed, a blunter asperity would result in a slight overestimation of the tip investigated and also, it would tend to detect less nano-scale irregularities on the tip apex region.

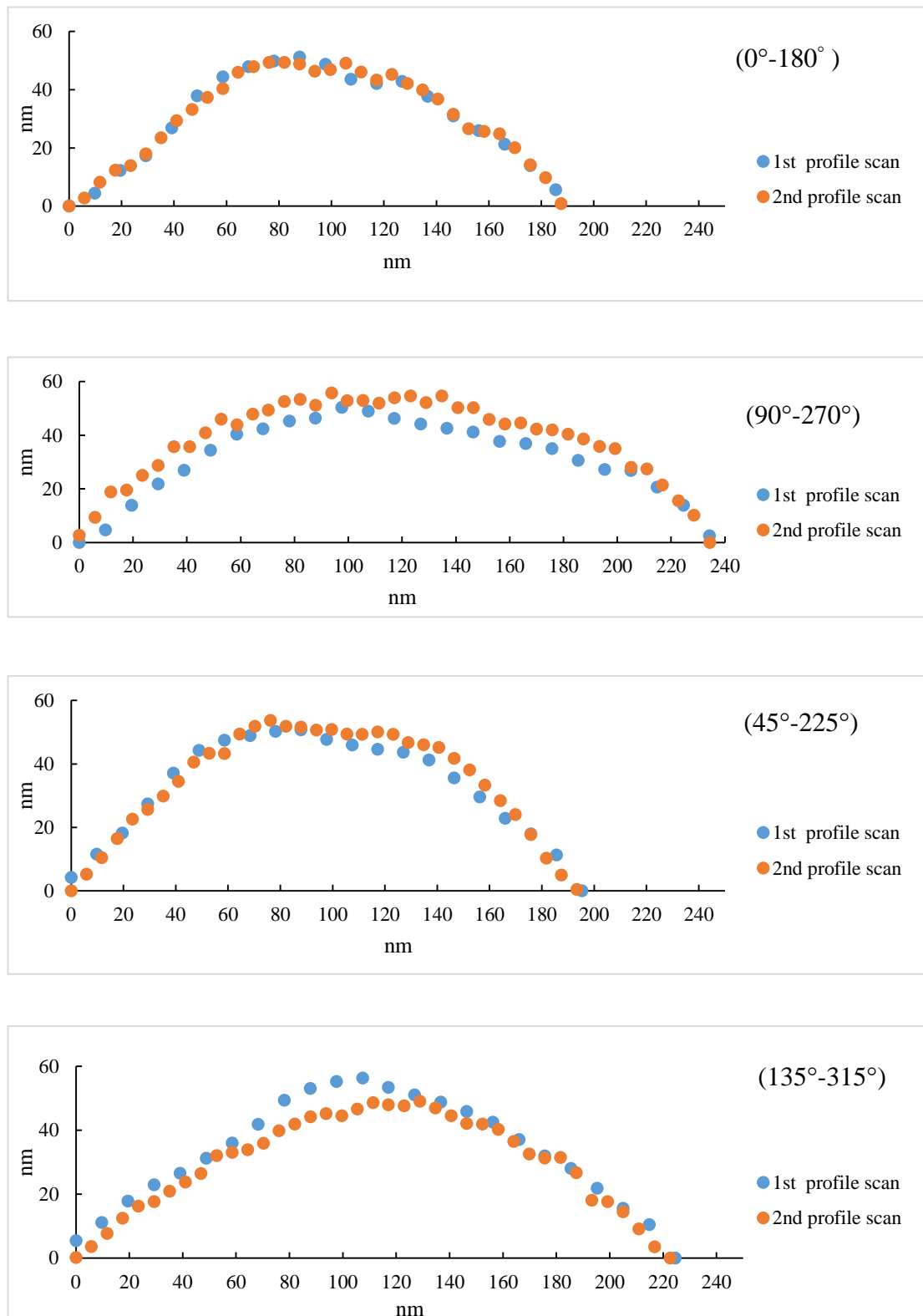


Figure 5.6: The obtained four different profiles cross section for Tip 1.

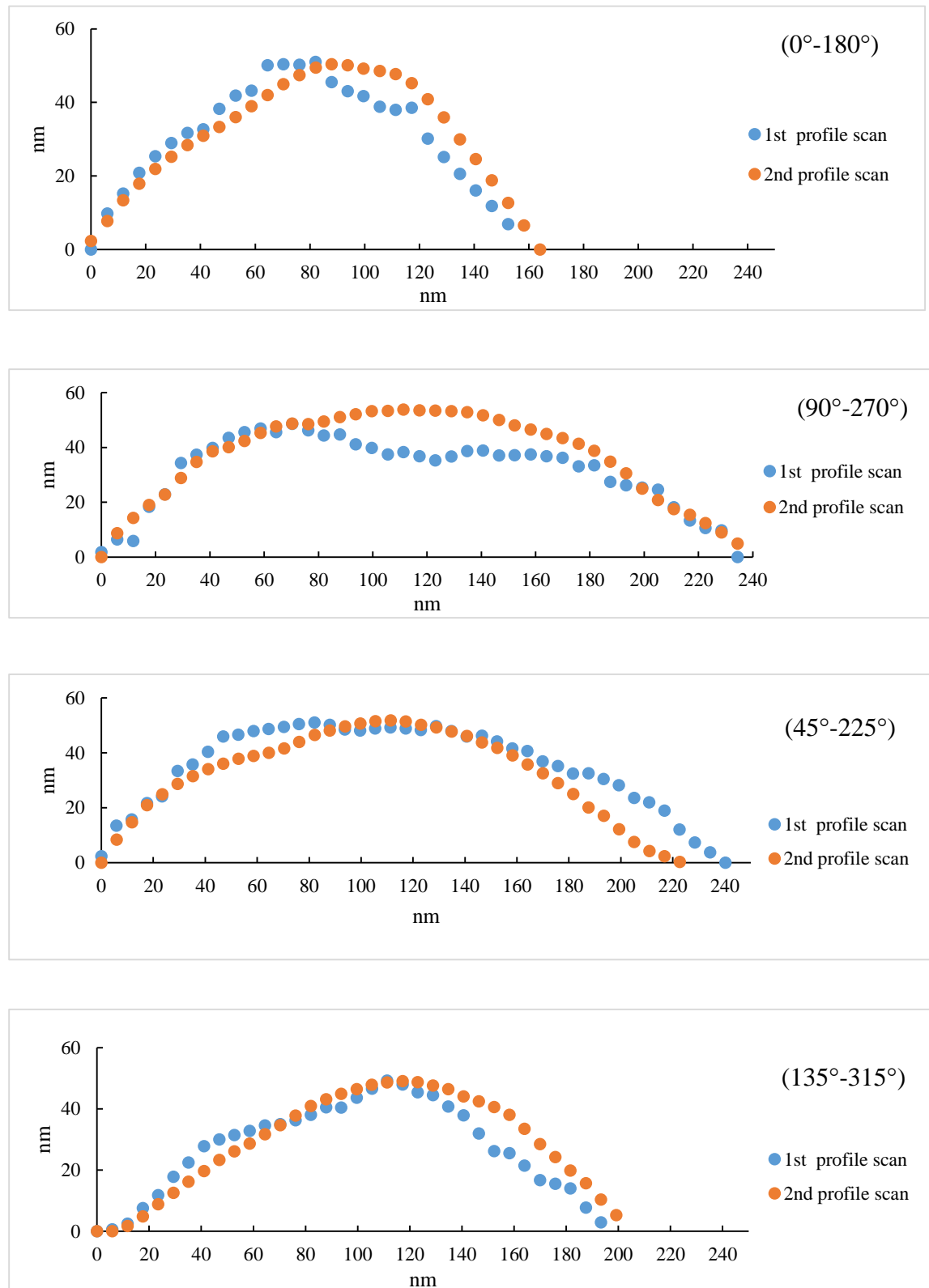


Figure 5.7: The obtained four different profiles cross section for Tip 2.

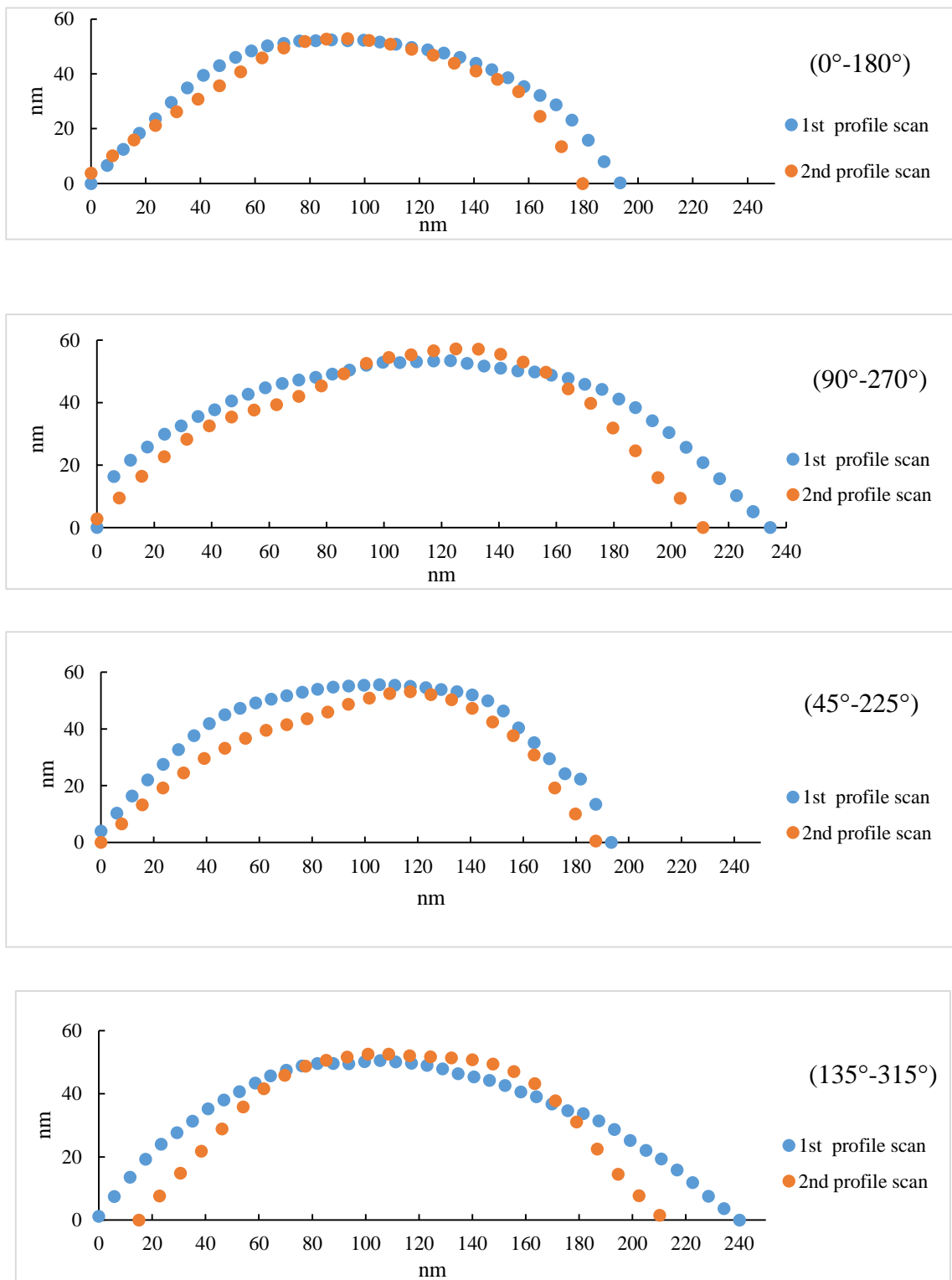


Figure 5.8: The obtained four different profiles cross section for Tip 3.

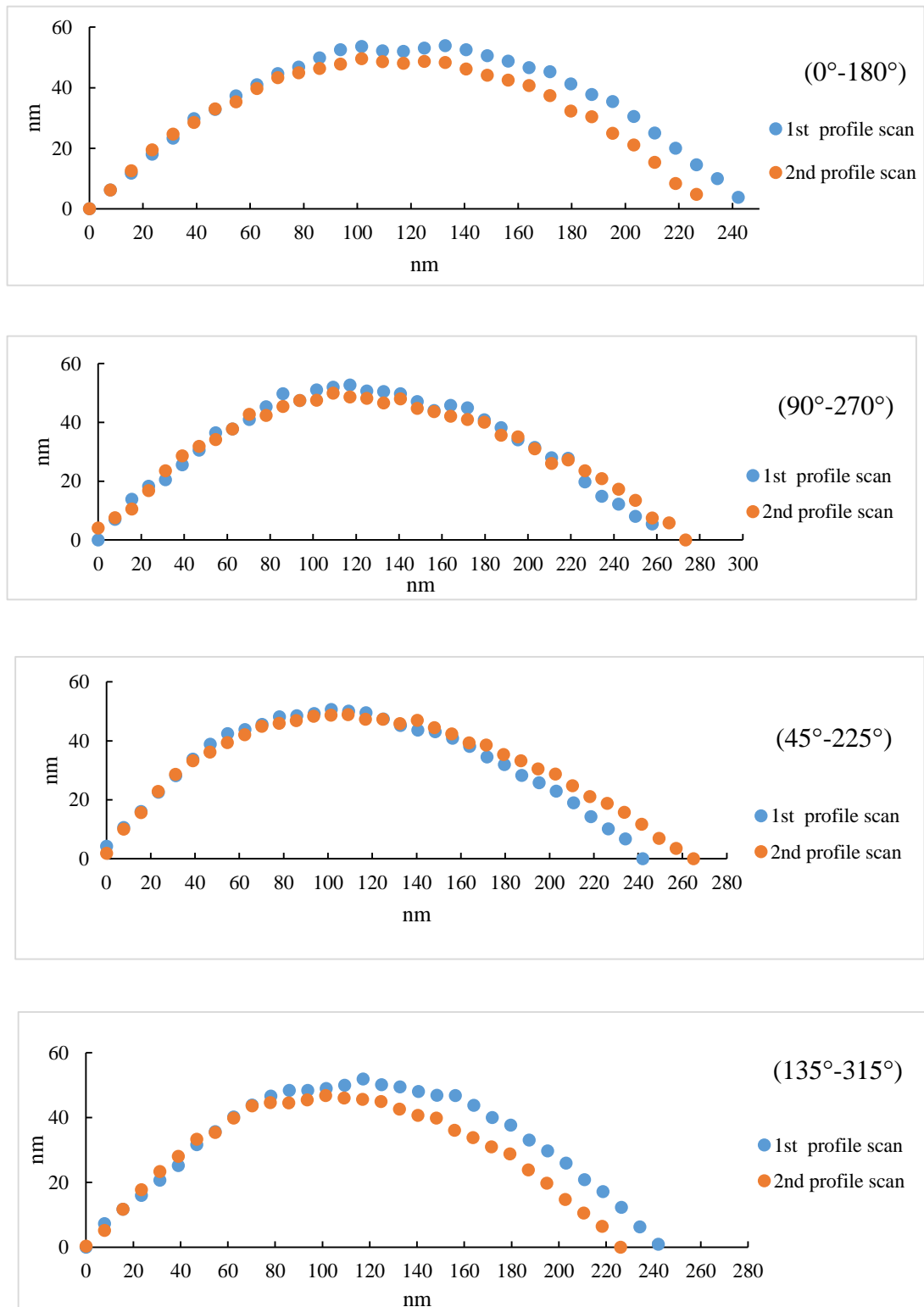


Figure 5.9: The obtained four different profiles cross section for Tip 4.

5.5 Tip apex radius measurements

In addition to the degree of bluntness, d , another parameter has been studied in this Chapter for the same set of probes, which is the radius of curvature at the tip apex. It is necessary to correctly obtain this parameter to have a better understanding of the tip shape. Indeed, the imaging quality of AFM could be affected by changing the radius value of the non-ideal used tip. In addition, this parameter can also be used to provide an approximate knowledge about the tip geometry under investigation if its apex was assumed to be a perfect spherical cap (Calabri *et al.* 2008). In this study, this parameter is also considered as a required factor in order to assess the suitability of the nanoindentation result (in situ-indirect method), by comparing to other available technique as will be described later in section 5.7.

Two different methods were studied for assessing the radius. The first one relied on fitting a polynomial to the extracted profile data over a specific tip height first and then by calculating the radius of curvature at the inflection point on the fitted profile. The second method was applied according to the assumption that the shape of the tip ended by spherical cap. In this case, a circle equation was used to find the radius value for the used profile. Both methods were applied to 2D data obtained from the SEM images of all tips first and then to 3D data of all tips after scanning them over the tip characteriser.

5.5.1 Radius measurements applied on 2D SEM data

The 2D profile of the probe tips was obtained from the post-processing of SEM micrographs as presented in the previous chapter. Using such SEM profiles, the extracted 2D geometry data of the used tips corresponds to the cross-section oriented along the 0°-

180° axis. Thus, the result achieved in this way does not represent the actual 3D geometry but only a planar view of the tips. The value of the tip apex radius was evaluated at a specific height of 50 nm from the tip apex for the sake of comparison.

5.5.1.1 Methodology

For the first method, a polynomial, $f(x)$, must be fitted first to the apex profile data. Next, the radius of curvature, $R_{cu}(x)$, was obtained at the maximum point of the polynomial (i.e. at the tip apex) according to the following formula:

$$R_{cu}(x) = \frac{[1+f'(x)^2]^{3/2}}{f''(x)} \quad (5-1)$$

where $f'(x)$ and $f''(x)$ represent the first and second derivative of $f(x)$, respectively.

The second method for determining the radius of our tip apexes used the circle equation. The principle of this method is illustrated in Figure 5.10. It relies on fitting a circle over the tip profile first. The equation of a circle is given below:

$$R_{ci}^2 = (x - a)^2 + (y - b)^2 \quad (5-2)$$

where R_{ci} is the radius of the circle, and a and b are the coordinates of the centre of the circle on the x and the y axes, respectively.

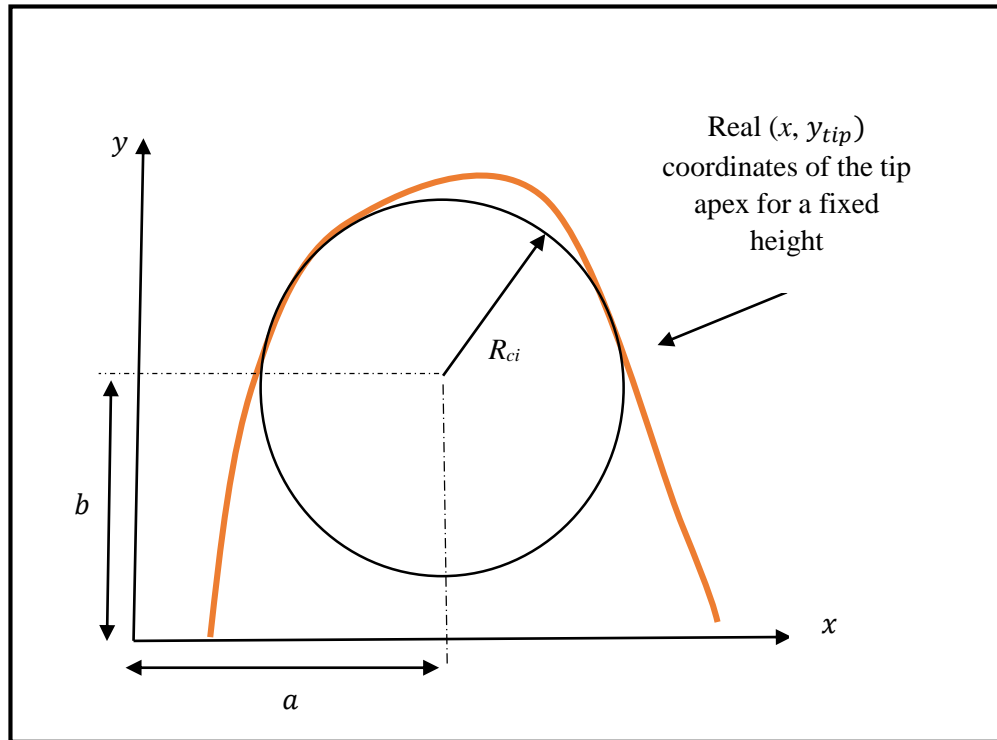


Figure 5.10: Schematic illustration of the second method for determining the radius, R_{ci} , of a circle fitted to the profile data of a tip apex.

The y coordinates of the points on the fitted circle along can be expressed as follows:

$$y_{ci} = \sqrt{(R_{ci})^2 - (x - a)^2} + b \quad (5-3)$$

Thus, the best fitted circle could be obtained by finding the set of values for a , b and R_{ci} which minimising the following *error* function:

$$error = \sum_1^n (y_{ci} - y_{tip})^2 \quad (5-4)$$

where n is the number of profile point on the x axis and y_{tip} is the real y coordinate on the profile of the tip apex for a given point on the x axis.

Minimising of this *error* function was achieved using the so-called “solver” function of the Excel programme. As a result, a reliable measurement of the tip apex radius could be estimated taking into account the optimum value of a , b and R_{ci} which represent the best fit to the experimental profile data as they minimise the *error* function defined above.

5.5.1.2 Results and analysis

The fitted polynomial, as required for first method, and the fitted circle, required for the second method, are plotted in Figure 5.11 for the four investigated tips. It was decided that the polynomial should be of order six when implementing the first method as it gave a reasonable fit to the profile data. Also, in this figure the probe tip apex profile obtained experimentally is shown until 50 nm from the tip apex for each tip. Based on this data and on the methodology presented earlier, the different radius values could be obtained for each tip. These are presented in Table 5.1. From this table, it can be seen that the extracted radius values showed acceptable agreement between the two methods. More specifically, Tip 1 and Tip 2 have the lowest radius while Tip 3 and Tip 4 show the highest values. Finally, circles with the radius values obtained by both methods were plotted directly above the SEM image for the sake of comparison between the results (see Figure 5.12). This was done to support our previous results and to show the compatibility of the obtained value with the real tip image.

These results now need to be compared with radius calculations completed on the 3D data for further understanding of the estimation of the real shape of tip apexes. This is the purpose on the next section.

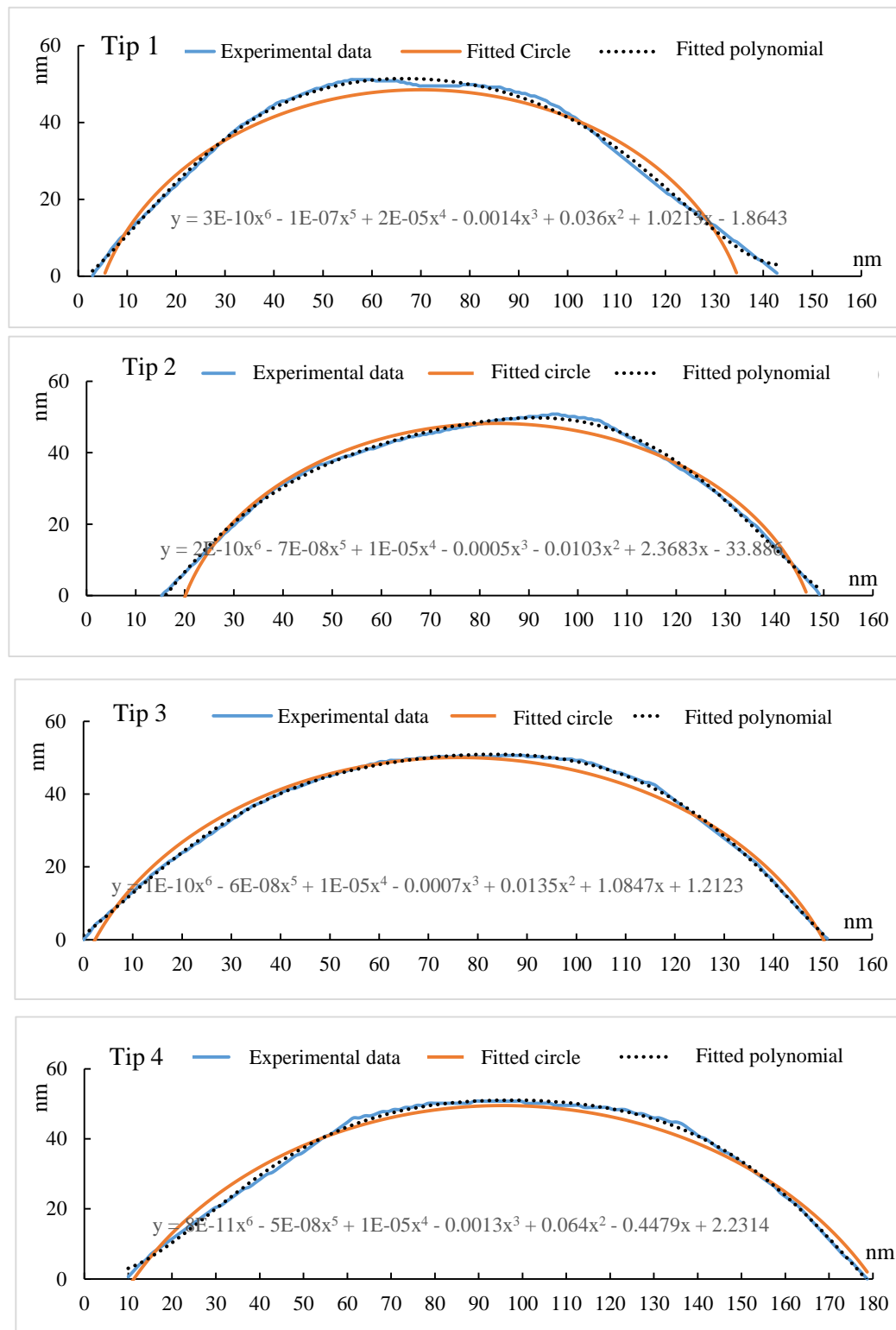


Figure 5.11: Plots showing the experimental 2D profile, the fitted polynomial and the fitted circle for the four tips investigated which used in the two methods to calculate R value.

Table 5.1: Tip radius values obtained using the different methods.

Probe number	Radius (nm)	
	Method 1: polynomial fitting	Method 2: circle fitting
Tip 1	52.0	67.15
Tip 2	56.0	64.0
Tip 3	75.8	79.8
Tip 4	106.4	96.3

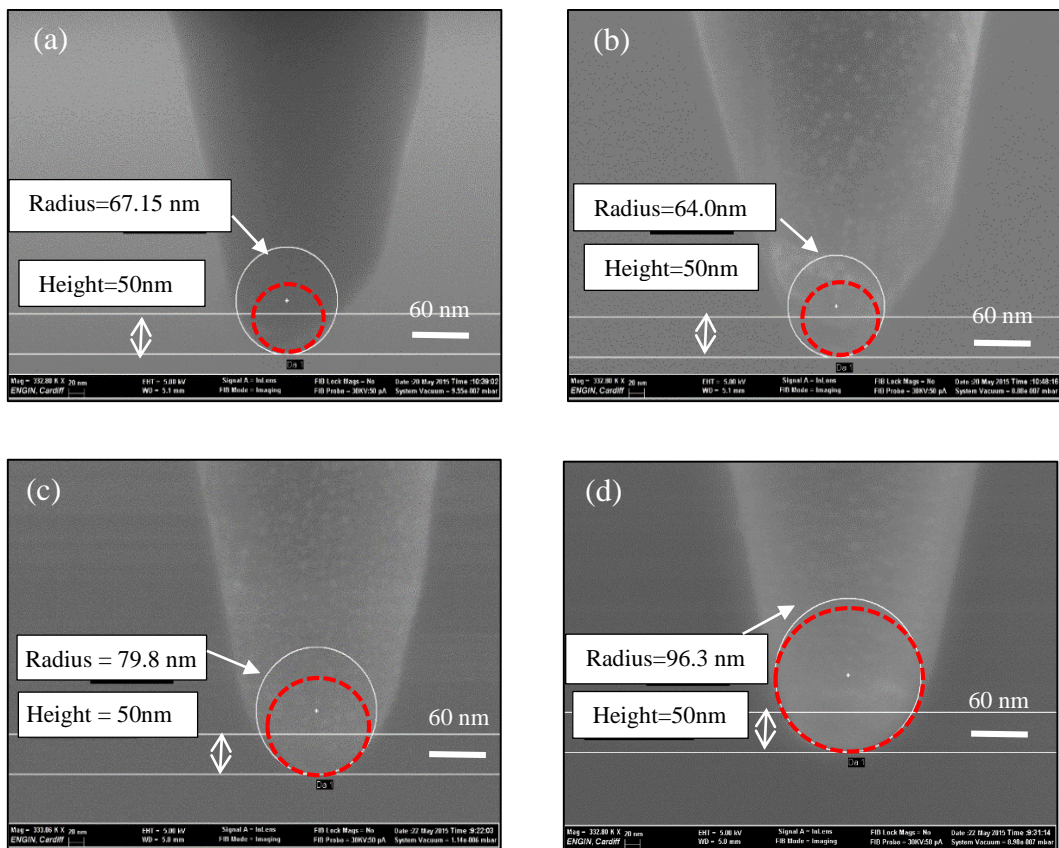


Figure 5.12: SEM micrographs of the apices for (a) Tip 1, (b) Tip 2, (c) Tip 3, and (d) Tip 4. Circles were superimposed on the micrographs using the radius value obtained by the polynomial fitting (red dashed line) and by the circle fitting method (white line).

5.5.2 Radius measurements applied on 3D AFM data

5.5.2.1 Methodology

In this section, the two methods presented in the previous section to calculate the radius of the tip apexes were now implemented on the cross sections obtained from 3D AFM data after scanning the tip characteriser. In particular, the cross sections used were those already reported in Figures 5.6 to 5.9. In this way, it is expected that the uncertainty of the tip radius calculation should be more accurate.

5.5.2.2. Results and analysis

Tables 5.2 and 5.3 present the radius calculated using the polynomial and the circle fitting method, respectively. In particular, these tables include the results for each of the considered four profile cross sections, namely 0° - 180° , 90° - 270° , 45° - 225° and 135° - 315° for a given tip and for each of the two asperities scan in each case. In this way, an average value for the radius could be considered as shown in the last column for each table. It is obvious from these results that consistent radius values were found using both methods. More specifically, Tip 3 always exhibits the smallest radius, which is then followed by Tip 1, Tip 2 and Tip 4 when considering increasing radius values. In addition, it could be said that the first method (i.e. the polynomial fitting) always results in a lower estimation of the radius than the second method (i.e. the circle fitting). This is due to the fact that the fit with the first method is better as the polynomial order is relatively high (i.e. order six) and also, it considers a more local radius compared to the circle fitting. Finally, it could

be seen from both tables that there is a good consistency between the radius value obtained from the two different scanned asperities for each cross-section.

Table 5.2: Values for R_{cu} obtained with the polynomial fitting method based on two asperities scan and the average value for each tip

Tip number	Cross-section name	Radius (nm) from polynomial fitting		Average radius for 1 st asperity (nm)	Average radius for 2 nd asperity (nm)	Average radius for both asperities (nm)
		1 st asperity	2 nd asperity			
Tip 1	0°-180°	90.4	96.4	117.2	116.3	116.8
	90°-270°	152.6	143.4			
	45°-225°	100.7	94.6			
	135°-315°	125.1	130.9			
Tip 2	0°-180°	66.2	70.7	128.4	108.8	118.6
	90°-270°	185.2	135.2			
	45°-225°	156.6	122.3			
	135°-315°	105.6	107.2			
Tip 3	0°-180°	92.4	81.9	121.1	93.7	107.4
	90°-270°	148.2	108.0			
	45°-225°	91.7	94.5			
	135°-315°	152.1	90.3			
Tip 4	0°-180°	143.6	137.0	180.6	168.8	174.7
	90°-270°	273.3	203.1			
	45°-225°	162.6	195.4			
	135°-315°	142.9	139.8			

Based on such data sets calculated by different methods, we can assess which methods should be considered most valid and more accurate for further analysis which will be conducted in the next section. For this reason, a systematic comparison between both methods is presented with Figure 5.13 and Figure 5.14. In these two figure, the radius values measured along the cross section 0°-180° are plotted using both 2D data from SEM micrographs and 3D AFM scans. More specifically, this process consists of first obtaining the average radius value from the two asperities scan for each tip as indicated in Table

5.2 for the first method and Table 5.3 for the second method. Secondly, for a given radius assessment technique, the difference in radius value obtained between both 2D and the 3D approach are plotted. For this particular analysis, the radius assessed from a 2D SEM profile can be considered as a reference. It is clear from both Figures 5.13 and 5.14 that first method (i.e. the polynomial fitting) shows a better agreement between both the 2D and 3D approaches.

Table 5.3: Values for R_{ci} obtained with the circle fitting method based on two asperities scan and the average value for each tip

Tip number	Cross-section name	Radius (nm) from circle fitting		Average radius for 1 st asperity (nm)	Average radius for 2 nd asperity (nm)	Average radius for both asperities (nm)
		1 st asperity	2 nd asperity			
Tip 1	0°-180°	114.0	115.0	139.3	132.3	135.8
	90°-270°	172.0	150.0			
	45°-225°	122.0	112.0			
	135°-315°	149.0	152.0			
Tip 2	0°-180°	86.0	85.0	145.6	124.9	135.3
	90°-270°	197.0	158.0			
	45°-225°	167.0	130.0			
	135°-315°	132.4	126.6			
Tip 3	0°-180°	113.9	106.7	141.9	115.5	128.7
	90°-270°	167.1	130.0			
	45°-225°	113.5	113.8			
	135°-315°	173.1	111.6			
Tip 4	0°-180°	164.0	159.0	176.7	190.0	183.3
	90°-270°	192.6	224.0			
	45°-225°	182.0	217.0			
	135°-315°	168.0	160.0			

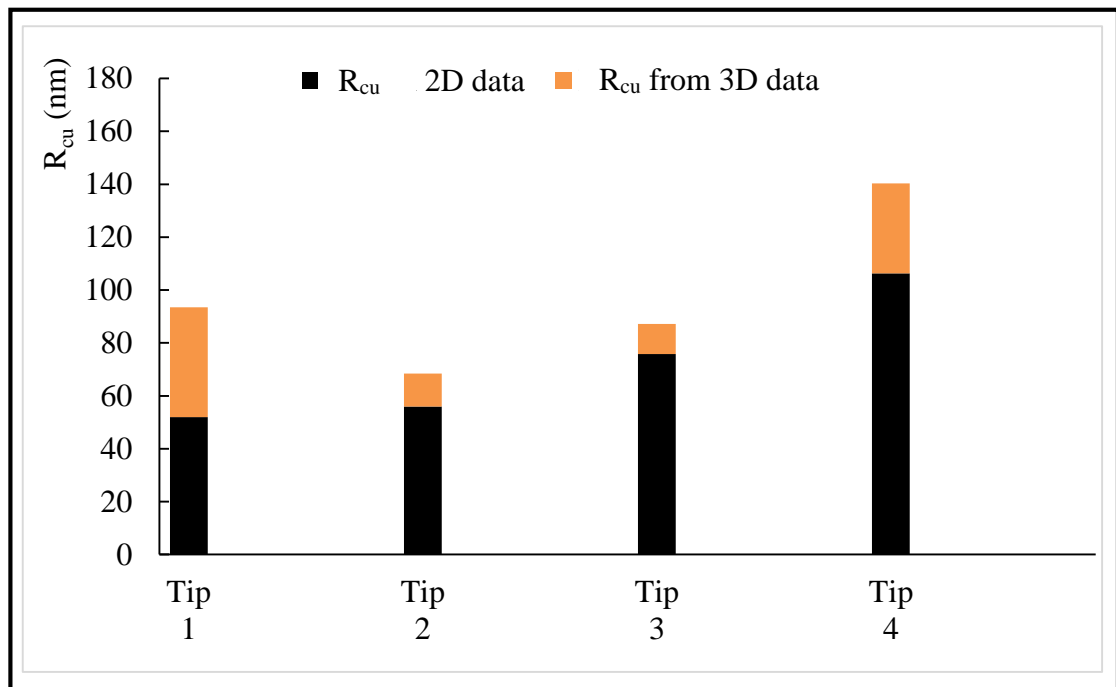


Figure 5.13: Plot of R_{cu} values for each tip apex along the 0° - 180° profile cross section obtained with both SEM and AFM data based on the polynomial fitting

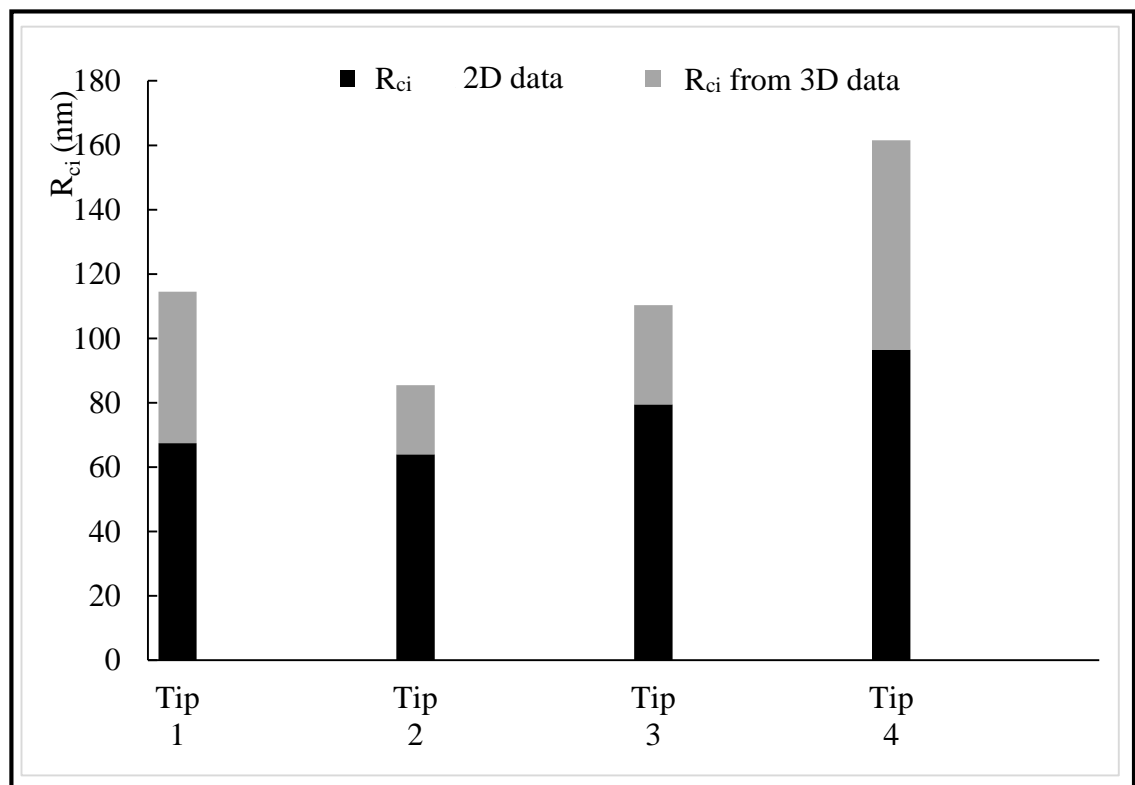


Figure 5.14: Plot of R_{ci} values for each tip apex along the 0° - 180° profile cross section obtained with both SEM and AFM data based on the circle fitting method

In addition, from Figure 5.15, it is also obvious that the total average difference in radius measurement obtained between the 2D and the 3D data when analysed with the polynomial fitting method is lower than when processed with the circle fitting method. Besides, the standard error obtained is also lower in this case as illustrated also in Figure 5.15. So, based on the quantitative analysis conducted here, it can be said that the polynomial fitting method provides more reliable radius values in comparison to than the circle fitting method. However, one of the sources of the slight deviation between both set of methods in radius measurement is identified as follows. The results presented here also imply that the used tips should not be consider to exhibit a perfect spherical shape even in a region as small as 50 nm from the tip apex.

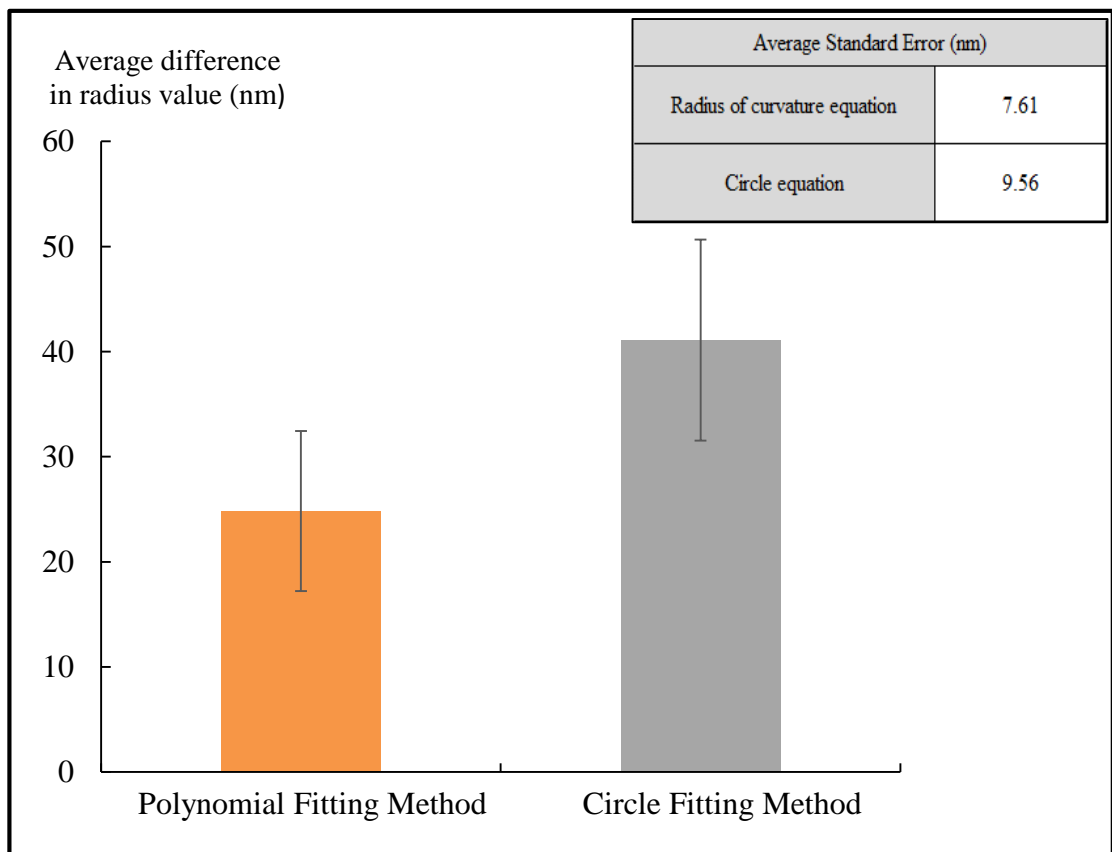


Figure 5.15: Plot for the total average difference in radius value between the 2D and the 3D data for both the polynomial and circle fitting method.

5.5.3 Comparison the radius measurements between the 2D and the 3D data

As was discussed in Section 4.5.2, it is expected that there should be a discrepancy between the assessments of the tip bluntness when the analysis is conducted on 3D data or on 2D data only. Table 5.4 shows that this is also the case when the quantity under investigation is the radius of the tip apex. In particular, Table 5.4 presents the total percentage error in radius values between the 2D and the 3D data when using both the polynomial and the circle fitting method. It can be seen from this table that analysing the 2D data leads to a consistent underestimation of the radius measurement. Overall, the percentage error obtained with the polynomial fitting method was measured to be between 30-55%, while this value was between 38-53% in case of the circle fitting evaluation.

Table 5.4: Percentage error in the radius assessment between 2D SEM data and 3D AFM data for both the polynomial and the circle fitting method

Probe number	Radius, R_{cu} , (nm) from polynomial fitting		% difference	Radius, R_{ci} , (nm) from circle fitting		% difference
	2D SEM data	3D AFM data		2D SEM data	3D AFM data	
Tip 1	52.0	116.8	55%	67.2	135.8	51%
Tip 2	56.0	118.6	53%	64.0	135.3	53%
Tip 3	75.8	107.4	30%	79.8	128.7	38%
Tip 4	106.4	174.7	39%	96.3	183.3	48%

5.6 Assessment of the degree of tip bluntness from power law fitting on 3D data

In this section, the focus is on estimating the degree of tip bluntness, d , from profile data similar to the work conducted in Chapter 4. However, this time, the tip profiles are obtained from the 3D AFM scans of the tip characteriser instead of from the 2D SEM data as was the case in Chapter 4. Thus, the procedure followed is the same as that explained in section 4.5.2 and already illustrated with Figure 4.28. More specifically, this procedure is now applied on the four different profile cross-sections extracted for each tip (see Figures 5.6 to 5.9). For each profile, a power law function was fitted on the data to extract the power law exponent, d , which describes the profile geometry of the indenter tip. Basically, the value of d was estimated for two profiles extracted from one cross-section as a function of radial distance from the tip apex (see Figure 4.28 for a reminder of the procedure followed). Thus, by fitting the following equation:

$$h_{tip}(r) = B_d r^d \quad (5-5)$$

which was already described in Chapter 4, both value of B_d and d could be obtained for all the probes tip profiles. As mentioned previously, in order to minimize the error, this analysis was carried out from the 3D AFM scans of two asperities for each tip. Tables 5.5 and 5.6 summarise the results for each of the two asperity scans while Table 5.7 provides the average d value obtained from the two asperities scan for all tips.

Table 5.5: Assessment of the degree of bluntness, d , obtained from 3D scans of the first asperity using power law fitting on the extracted profiles

Tip profile	Tip 1	Tip 2	Tip 3	Tip 4
0°	1.40	1.87	1.42	2.30
180°	1.45	2.20	1.44	1.22
90°	1.92	1.88	1.30	1.21
270°	1.82	2.18	1.44	1.46
45°	0.82	1.70	1.30	2.10
225°	0.80	1.77	1.60	1.70
135°	1.62	1.77	1.49	0.75
315°	1.60	1.90	1.30	1.60
Average	1.43	1.91	1.41	1.54

Table 5.6: Assessment of the degree of bluntness, d , obtained from 3D scans of the second asperity using power law fitting on the extracted profiles

Tip profile	Tip 1	Tip 2	Tip 3	Tip 4
0°	1.50	2.23	1.41	1.12
180°	1.60	1.95	1.60	2.27
90°	1.60	2.20	1.24	1.12
270°	2.25	2.10	1.50	1.28
45°	0.85	1.73	1.11	1.72
225°	0.71	2.04	1.40	2.56
135°	1.65	1.76	1.80	1.45
315°	2.53	1.63	1.85	2.20
Average	1.59	1.96	1.49	1.72

Table 5.7: Average value of the degree of bluntness, d , for all tips from data in Tables 5.5 and 5.6

Tip profile	Tip 1	Tip 2	Tip 3	Tip 4
Average	1.51	1.93	1.45	1.63

From Tables 5.5 and 5.6, it can be noted that a small variation in the d values assessed could be found for one specific profile when comparing two scanned asperities. The possible explanation for this issue is due to the fact that: (a) the geometry (height and radius) of the asperities present of the used tip characteriser (i.e. TGT01 sample) from the manufacturer is not perfectly consistent and (b) slightly different scanning parameters were used during the imaging process for the feedback loop that controls the height of the probe.

Overall, the average results presented in Table 5.7 gives a range of d values of the bluntness degree which are comprised between 1.45 and 1.93. From this data, it can be inferred that the order of the tips from the sharpest to the bluntest is as follows: Tip 3, Tip 1, Tip 4 and Tip 2. It is worth mentioning that this order is matching the order already found in Chapter 4 when the degree of bluntness, d , was extracted from the nanoindentation approach. It is also worth recalling that this agreement was not found, in the previous Chapter, when comparing the results obtained from the nanoindentation data and the 2D SEM data.

5.7 Comparison and validation of different tip shape assessment approaches

5.7.1 Nanoindentation and power law approaches using 2D and 3D data

The main objective of this chapter was to further assess the suitability of the proposed in-situ technique for tip bluntness assessment using the AFM nanoindentation approach by comparing its outcome presented in Chapter 4 with that obtained from the analysis of the 3D geometry of the real tip shape. Table 5.8 gives a summary of the

average value of the degree of tip bluntness, d , obtained using the three different approaches, namely the application of (1) the rescaling formula on nanoindentation data, (2) the power law function on 3D geometry data and (3) the power law function on 2D geometry data. The table also presents the percentage error between the nanoindentation approach and the power law approximation from both 2D and 3D data. The value of d described by the 3D data approach presented a good consistency in the approximation of tip order comparing to value of d obtained with the nanoindentation approach. It is clear from this table that a better agreement was found in this Chapter between the nanoindentation and the power law approaches when 3D data are considered. This result increases the confidence in the fact that the tip characterisation technique proposed in this Thesis could be considered as a reliable approach for the in-situ assessment of AFM probes.

It is worth noticing that the degree of tip bluntness extracted from the 3D AFM scan via the power law fitting is always slightly larger than obtained from the nanoindentation tests. As discussed in Chapter 2 and observed in Alraziqi *et al.* (2016) and in Mukhtar (2017) for instance, the characterisation of the tip shape via the inverse imaging method using a tip characteriser may lead to a small overestimation of the volume of the tip investigated. In addition, it should be mentioned that when applying the power law approximation on 3D data, the manual selection of the tip profile should be considered as a factor which may affect the error between the nanoindentation-based and the AFM scan-based approaches. This issue should be especially important for such non-ideal tip apexes at such small scale. Addressing this potential issue is the focus of the next chapter. Finally, such comparison is also inevitably affected by minor errors associated with each experiment circumstances (acoustic vibration and sample roughness).

Table 5.8: Bluntness degree, d , obtained for the four tips considered using different approaches and the error percentage between them

Tip No.	d from nanoindentation tests (Chapter 4)	d from 3D (AFM) data (Chapter 5)	Percentage difference between nanoindentation and 3D data	d from 2D (SEM) data (Chapter 4)	Percentage difference between nanoindentation and 2D data
1	1.34	1.51	11.3%	1.45	7.59 %
2	1.92	1.93	0.5%	1.33	30.73 %
3	1.18	1.45	18.6%	1.74	32.18 %
4	1.37	1.63	16.0%	1.57	12.74 %

5.7.2 Assessment of the tip shape when approximated as a spherical cap

Conical indenter probes are considered by some researcher as a cone that is ended with rounded apex (Van Landingham *et al.* 2005; Burnham and Colton 1989; Ma *et al.* 2012; Chiu and Ngan 2002). More specifically, this rounded apex is described as a spherical cap and the transition from this geometry to the full conical shape is defined with a height limit. In this study, we would like to check to which extent this assumption agrees with our experimental data. Therefore, the height limit for the spherical cap geometry is taken to be equal to h_{max} from the tip apex, as illustrated in Figure 5.16. It is recalled that h_{max} is the maximum depth that each tip achieved during the nanoindentation test results. The selection of h_{max} for this purpose was necessary such that a valid comparison could be made with our experimental data.

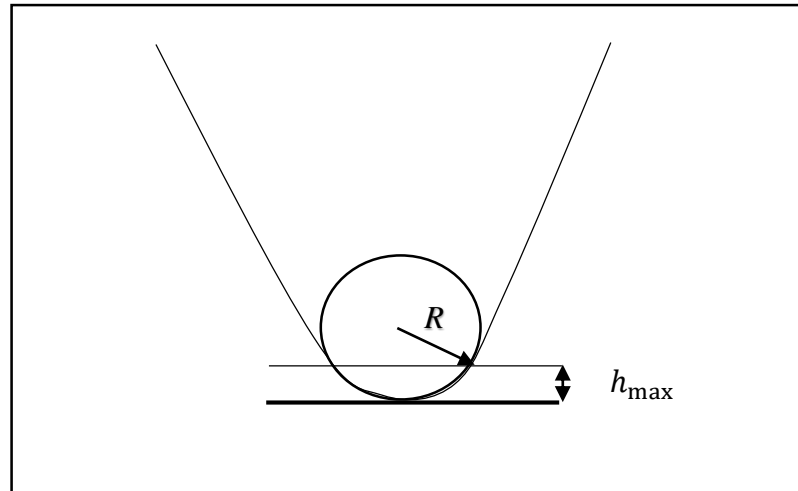


Figure 5.16: Schematic of the profile of a conical tip ended with a spherical cap of radius R . h_{max} represents the height limit for the tip apex at which the probe geometry transitions from a spherical to a conical shape.

In reality, the case of AFM conical tips at a small depth from the apex region should exhibit some differences from the ideal spherical geometry, since they do not possess perfect axisymmetric body shape. To check the validity of the spherical cap assumed by some researchers against the results of the bluntness degree d obtained in Chapter 4, the following comparison should be made:

- First: the error between the experimental profile data along different tip cross sections and the corresponding theoretical profile when it is assumed to be described by the cross section of a spherical cap. In this case, this means that d is equal to 2. In Cartesian coordinates, for a spherical indenter, the profile of the apex is described by $y = \frac{x^2}{2R}$ (Hertz 1896), where R is the radius of the sphere. In this work, R was obtained for each tip cross section by applying the approach described in Section 5.5 and taking into account the value of h_{max} for each tip.

-
- Second: the error between the experimental profile data along different tip cross sections and the corresponding profile when it is assumed to be described by a power law function where d is that obtained from the nanoindentation approach.

In this research, these comparisons are carried out along the different cross sections already defined earlier using 3D AFM data. In this case, four different cross sections were used for each tip. In addition, each cross section was split into a left and right profile as discussed earlier in Section 5.6. For the sake of brevity, Figures 5.17 until 5.20 present the different profile data extracted as described above for Tip 1 only. Each plot includes the tip profile from the experimental 3D data, the theoretical profile for the case of a perfect spherical cap tip (i.e. when $d=2$) and also for the case of the power law fitting when d is equal to that obtained from the nanoindentation tests. The value of both axes on these plots have also been rescaled, such that the maximum value on an axis is 1, in order to ease the qualitative comparison between the different plots. Appendix A2 provides the same plots in the case of Tip 2, Tip 3 and Tip 4 (see Figures A2.1–A2.12). According to Figures 5.17 until 5.20, which represent a qualitative comparison, it is clearly shown that there is an overall good agreement between the tip profiles plotted with these three approaches. Finally, Figure 5.21 presents a quantitative comparison of the accuracy between the theoretical profiles obtained with the spherical cap assumption against the real profiles extracted from the reverse imaging method (i.e. from the 3D AFM scan of the tip characteriser). In addition, this figure shows the same quantitative comparison when profiles are reconstructed based on the bluntness degree d obtained in Chapter 4. Specifically, the error bars plotted in this figure represent the sum of the errors between the y coordinate (i.e. the height) of the experimental profile and that obtained with both profile reconstruction approaches for the four cross sections considered for each

tip. It is clear from this figure that for all tips, the spherical assumption led to the largest error from the experimental data.

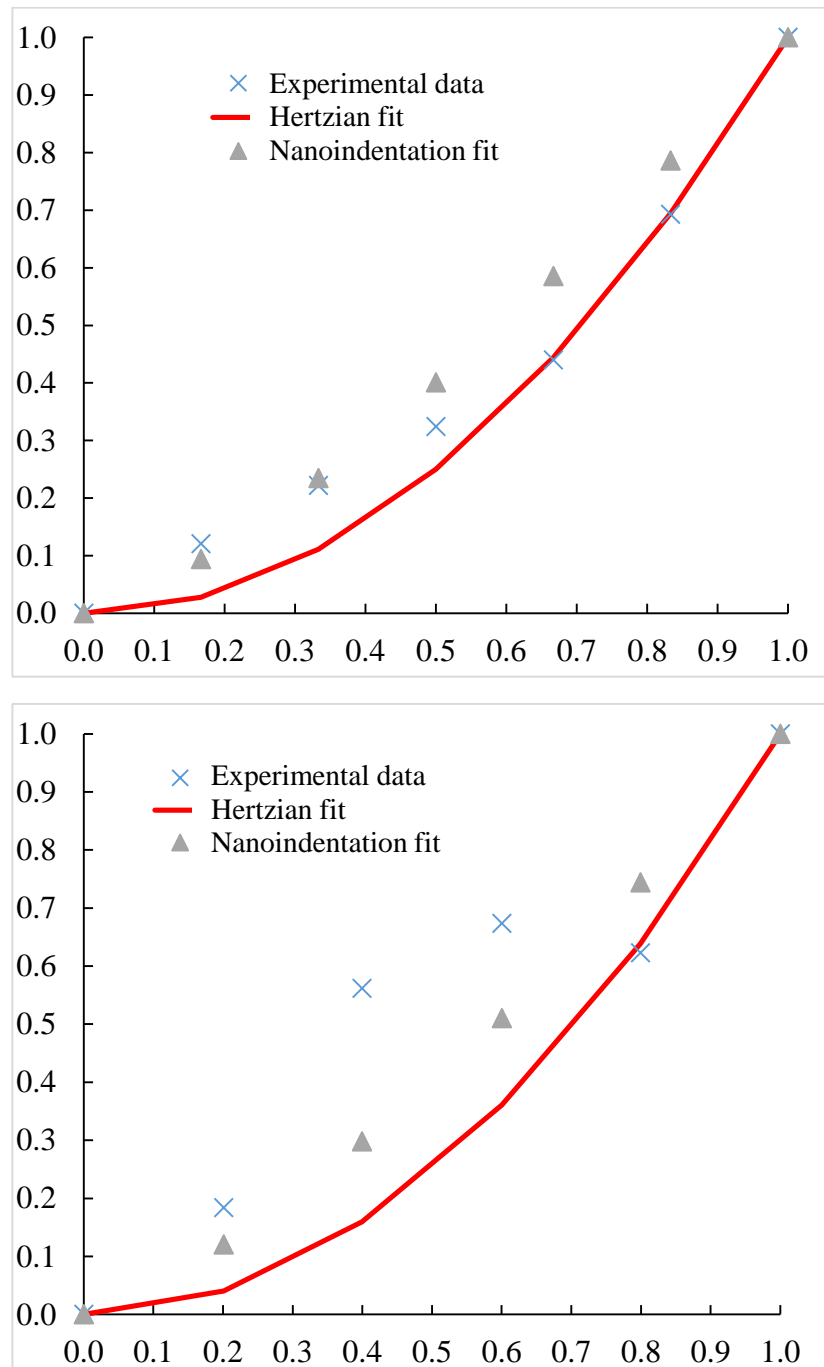


Figure 5.17: Qualitative comparison, for Tip 1 along the 0° - 180° profile cross section, of the experimental profile obtained with the reverse imaging method, the profile reconstructed with the spherical assumption (i.e. Hertzian fit) and that reconstructed by considering the d value of the power law function equal to that obtained from the nanoindentation tests.

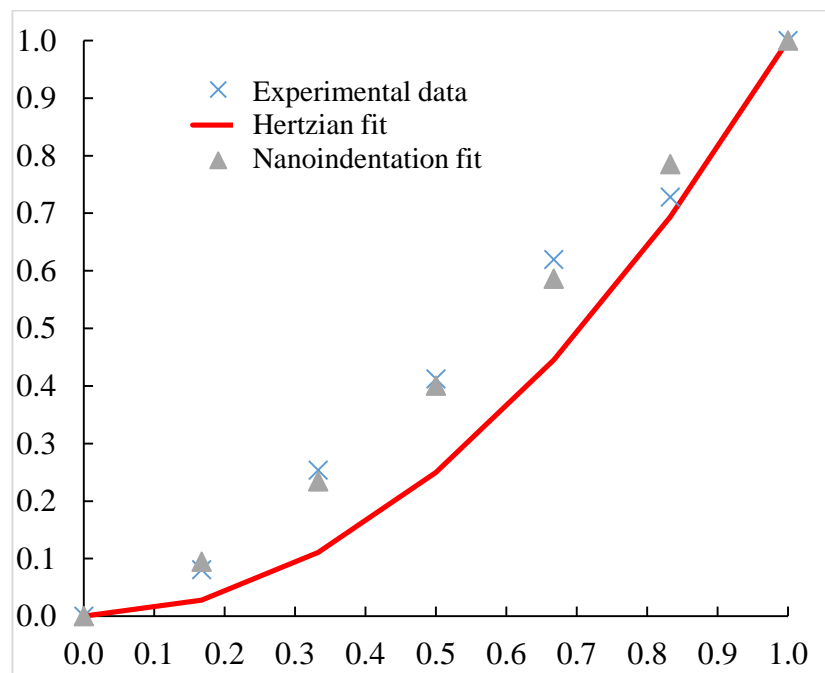
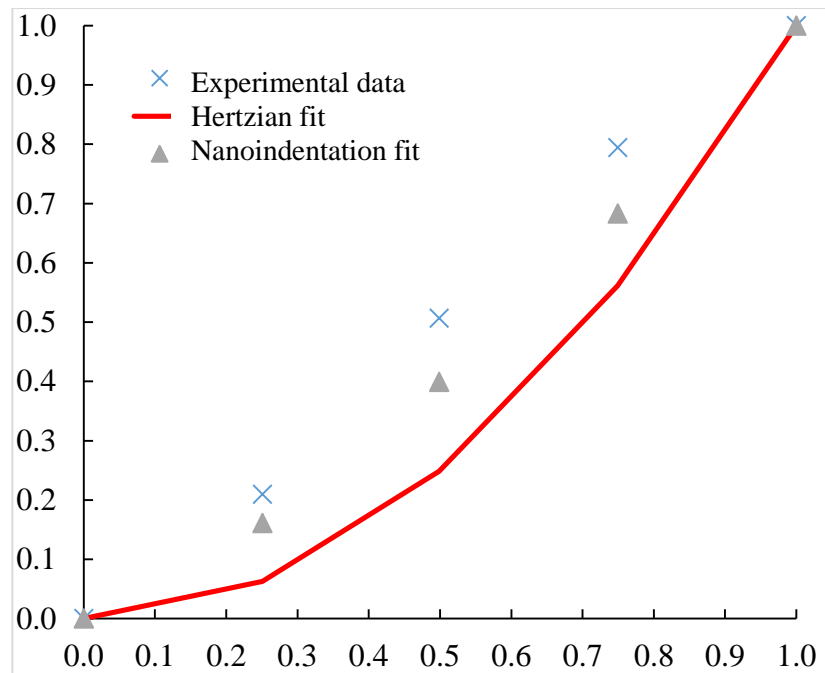


Figure 5.18: Qualitative comparison, for Tip 1 along the 90°-270° profile cross section, of the experimental profile obtained with the reverse imaging method, the profile reconstructed with the spherical assumption (i.e. Hertzian fit) and that reconstructed by considering the d value of the power law function equal to that obtained from the nanoindentation tests.

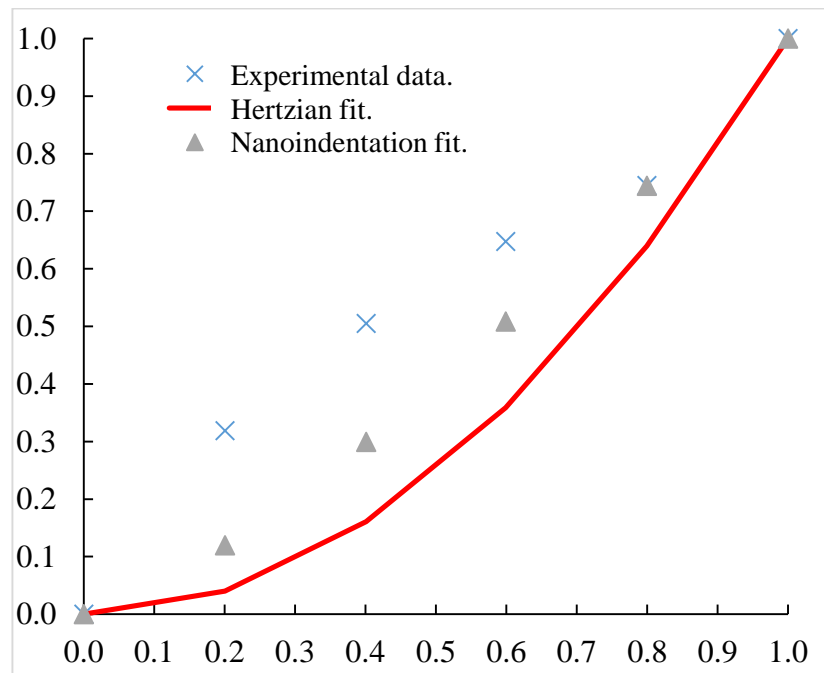
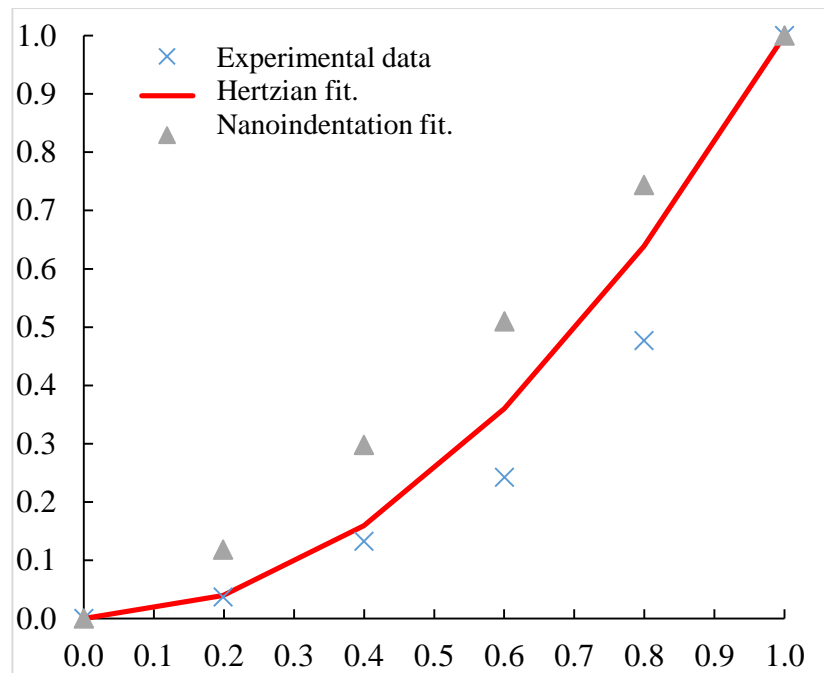


Figure 5.19: Qualitative comparison, for Tip 1 along the 45°-225° profile cross section, of the experimental profile obtained with the reverse imaging method, the profile reconstructed with the spherical assumption (i.e. Hertzian fit) and that reconstructed by considering the d value of the power law function equal to that obtained from the nanoindentation tests.

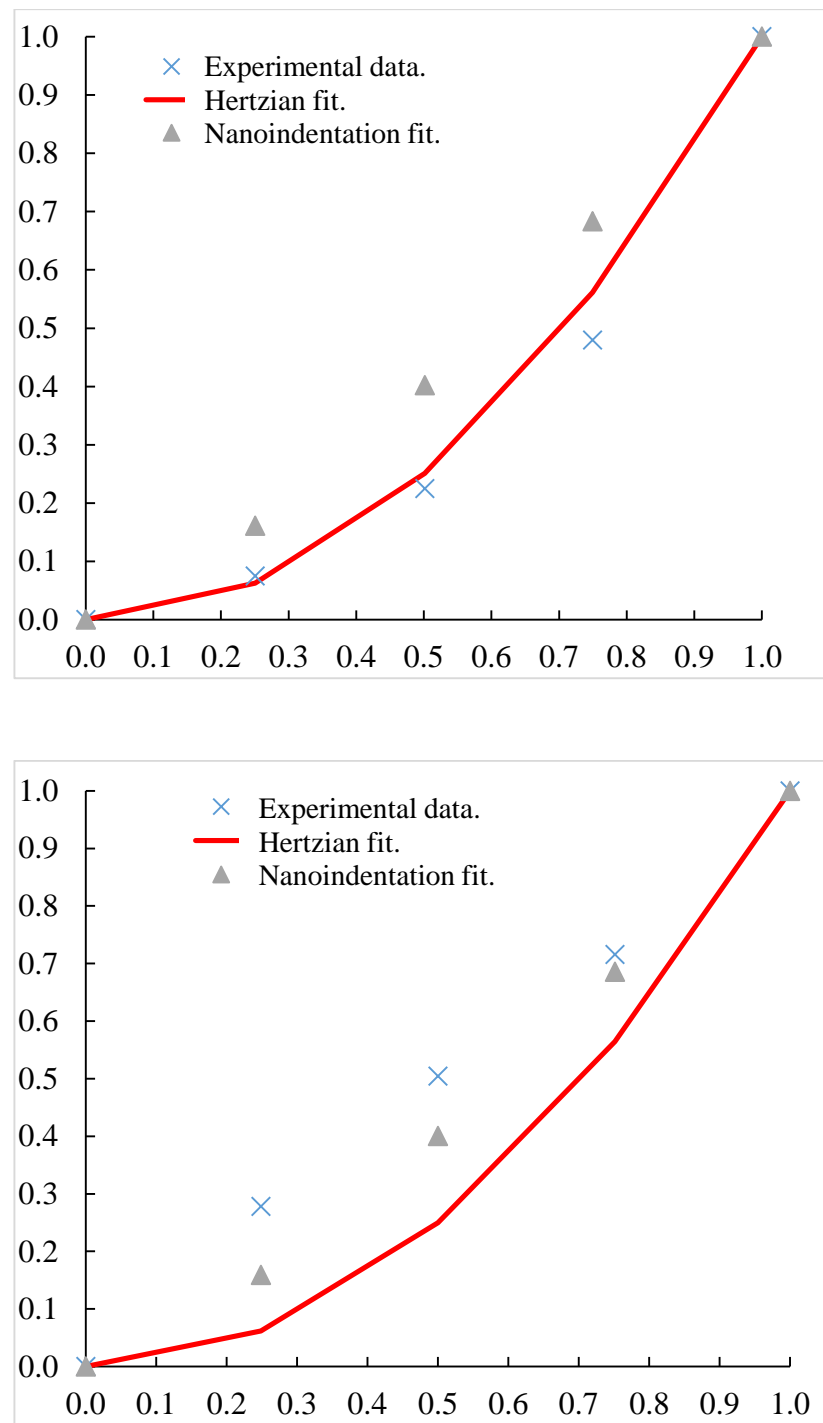


Figure 5.20: Qualitative comparison, for Tip 1 along the 135°-315° profile cross section, of the experimental profile obtained with the reverse imaging method, the profile reconstructed with the spherical assumption (i.e. Hertzian fit) and that reconstructed by considering the d value of the power law function equal to that obtained from the nanoindentation tests.

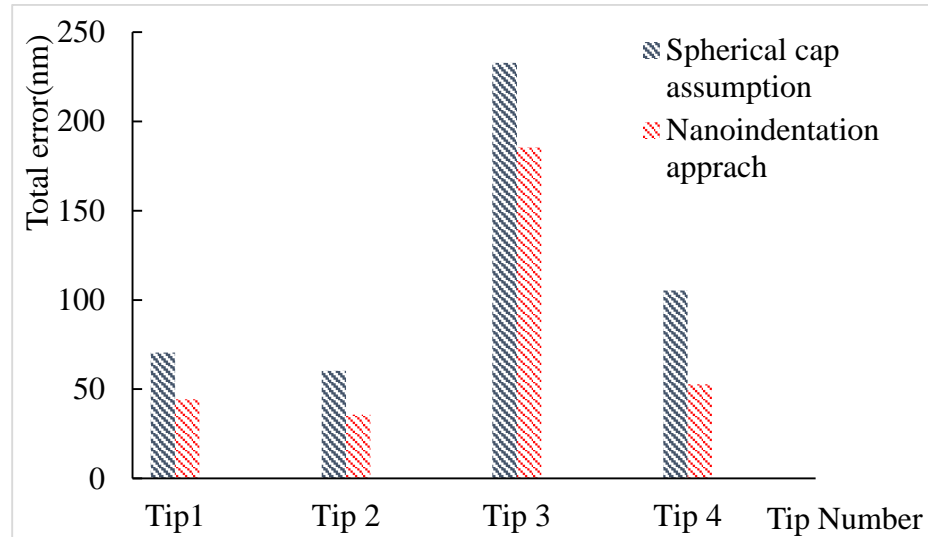


Figure 5.21: Total difference between the experimental data and the spherical cap assumption (i.e. $d=2$) and the nanoindentation tests (i.e. d obtained from the nanoindentation tests) for each tip.

5.8 Summary

In this chapter, the reverse imaging technique was used to obtain the 3D geometry data for all the used tips in the Chapter 4. In particular, a tip characteriser consisting of an array of sharp-pin like asperities was employed. The rationale behind the selection of this technique was based on the results of a former study made by the author when assessing the reliability of different 3D characterisation technique for AFM tips. Based on these data, the tip radius values were evaluated according to fixed length of 50 nm from the tip apex. These values were obtained using two different methods, firstly by performing a “polynomial fitting” and secondly a “circle fitting” on the experimental data obtained with the reverse imaging technique. It was observed that both methods agreed when ordering the tips from the lower to the higher tip radius values. However, it was also noted that a slight overestimation when applying the “circle fitting” method.

In addition, the degree of tip bluntness, d , was also measured for each tip using the power law fitting on 3D AFM data. More specifically, an average d values was obtained from profiles extracted along more four cross-sections taking into account data which corresponded to the maximum penetration depth, i.e. h_{max} , recorded for each tip in Chapter four. Based on the observed results, it could be said that a better agreement was found in this Chapter between the nanoindentation and the power law approaches when 3D data are considered.

The most important findings from this chapter are as follows:

- Assessing the radius value of non-axisymmetric tips should require the analysis of 3D data describing the geometry of the apex rather than 2D data only. Indeed, based on the radius assessments of the four tips considered in this research, it was found that the discrepancy between both approaches was always over 30%, which should not be considered insignificant.
- The nanoindentation-based and in-situ tip characterisation technique proposed in this Thesis was further validated. This is due to the fact that a good agreement was found between this technique and the power law fitting approach applied on 3D data for evaluating the degree of tip bluntness. In fact, and as one could expect, a better agreement was achieved here when the power law fitting is carried out on 3D data rather than on 2D data only as reported in Chapter 4.

- Despite being a common assumption in some of the literature, it was found that approximating the tips considered in this work as having an apex described with spherical cap was less accurate than describing them with a power law function with a degree smaller than two.

Chapter Six

Theoretical investigations using volumetric measurements to estimate the shape of AFM tips

6.1 Aim and objectives:

The main goal of this chapter is to investigate the possibility of using a mathematical model that could estimate the actual shape of an AFM tip apex in term of the degree of bluntness, d , described in previous chapters. The specific motivation here is that the complete set of 3D data should be used instead of selected cross sections as was the case in Chapter 5. Also, the developed model can also be employed to validate the results obtained in both Chapter 4 and Chapter 5. Based on a simple mathematical assumption, two new analytical methods were proposed for this purpose.

6.2 Introduction

As it was presented in Chapter 5, the actual shape of the tested tips were assessed by the selection of some tip profile cross-section to extract average value of the power law exponent d . This power law exponent is considered as a key parameter to describe the AFM tip real shape. In the previous chapter, more than one profile cross-sections were utilised (specifically eight such profiles for each tip). It was shown that this led to a better agreement with the results obtained in Chapter 4 (i.e. from the nanoindentation approach) in comparison with using 2D SEM data only. This is due to the non-axisymmetric characteristic that these kind of commercial tips exhibit. Thus, it is essential to understand whether the tip shape assessment conducted from the selection of a few orthogonal cross-sections may bring an erroneous approximation of the real tip shape.

In order to address this potential issue, two novel methods have been proposed in this chapter. More specifically, these methods rely on analysis the full set of volumetric

data until a specific length limit from the tip apex. There is clear evidence from the literature that the true volume measurement of an AFM tip could provide an accurate information about the apex geometry (Bloo *et al.* 1999, Maw *et al.* 2002, Chung *et al.* 2005, Bhushan and Kwak 2007, Gozen and Ozdoganlar 2013 and Liu *et al.* 2010). The first method consists in evaluating a simple measure define as a “volumetric ratio”. The second method relies on a simple double integral to extract the main parameters (i.e. B_d and d) that are used to describe the 3D shape of the tip with an homogenous function as already explained in Chapter 3.

This chapter is organised as follows. The next section is concerned with the description of the mathematical model assumed to evaluate tip real shape. In practice, the 3D geometry for the same set of tips that were used in both Chapter 4 and 5 was processed further to obtain volumetric measurements. This procedure is outlined in Section 4. These volumetric values were finally utilised in Section 5 to present two novel methods for assessing the geometry of the probe tip. Finally, based on the results obtained for both methods implemented in this chapter, a comparison was made to validate the different approaches presented in the Chapters 4, 5 and 6 of this Thesis when assessing the degree of tip bluntness, d . The last section presents the main conclusions and findings from this chapter.

6.3 Mathematical approach

At low load and shallow nanoindentation, which is the case for the experimental work completed in this Thesis, it is not possible to assess the volume of the tip based on the dimensions of the imprint left after completing the unloading process. This is due to the expected influence of the elastic recovery of the indented material. For this reason, the nanoscale volume of the tip apex that penetrated inside the sample during

nanoindentation tests was measured experimentally using an alternative approach as follows:

a) The 3D geometry data of the AFM tip was obtained first via scanning it over the tip characteriser as described in Chapter 5. It was suggested that this technique provided the most accurate 3D data about the apex geometry (Alraziqi *et al.* 2016).

b) The depth-sensing nanoindentation curves were used to provide the specific value of h_{max} that each tip penetrated inside the sample. This value was then employed as the specific length limit from the tip apex over which the 3D geometry data could be analysed.

The above experimental information provides the main data required to establish our proposed mathematical model to assess the bluntness of AFM tips. Based on these data, two novel mathematical models could be investigated. First, it is proposed to calculate the ratio of the volume of the tip, V_{tip} , to the volume of an imaginary cylinder, V_{cy} , in which the tip is contained. Second, a numerical method is proposed based on describing the tip volume with a double integral and solving this integral as a function d such that the calculated volume agrees closely with the experimental 3D data. Figure 6.1 illustrates the different basic volumetric data utilised to implement the proposed models. In addition, Figure 6.2 shows the flow chart of all the procedures conducted in this chapter.

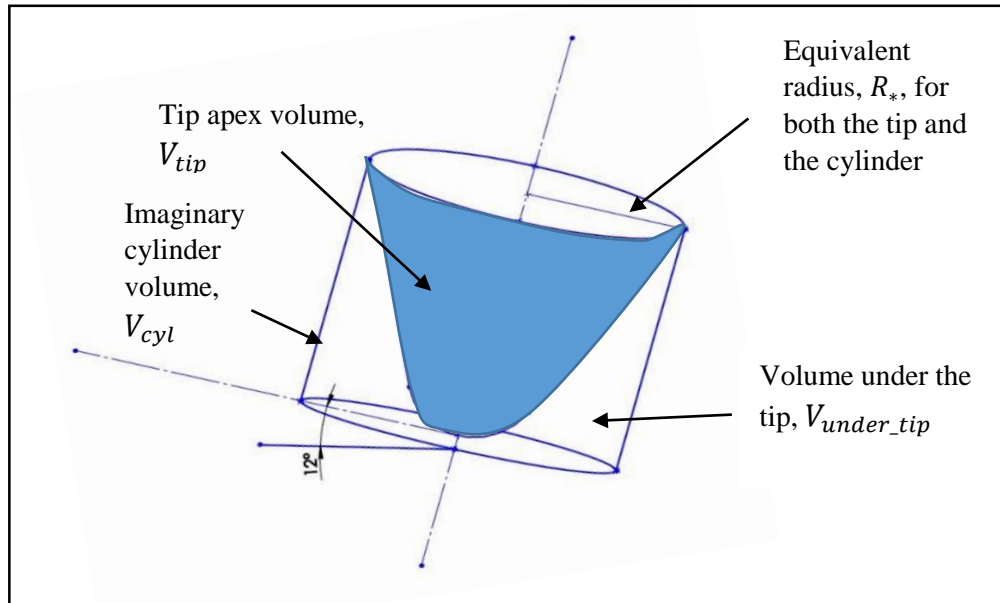


Figure 6.1: Illustration of the concept of the volume occupied by the tip and that of the imaginary cylinder in the working position

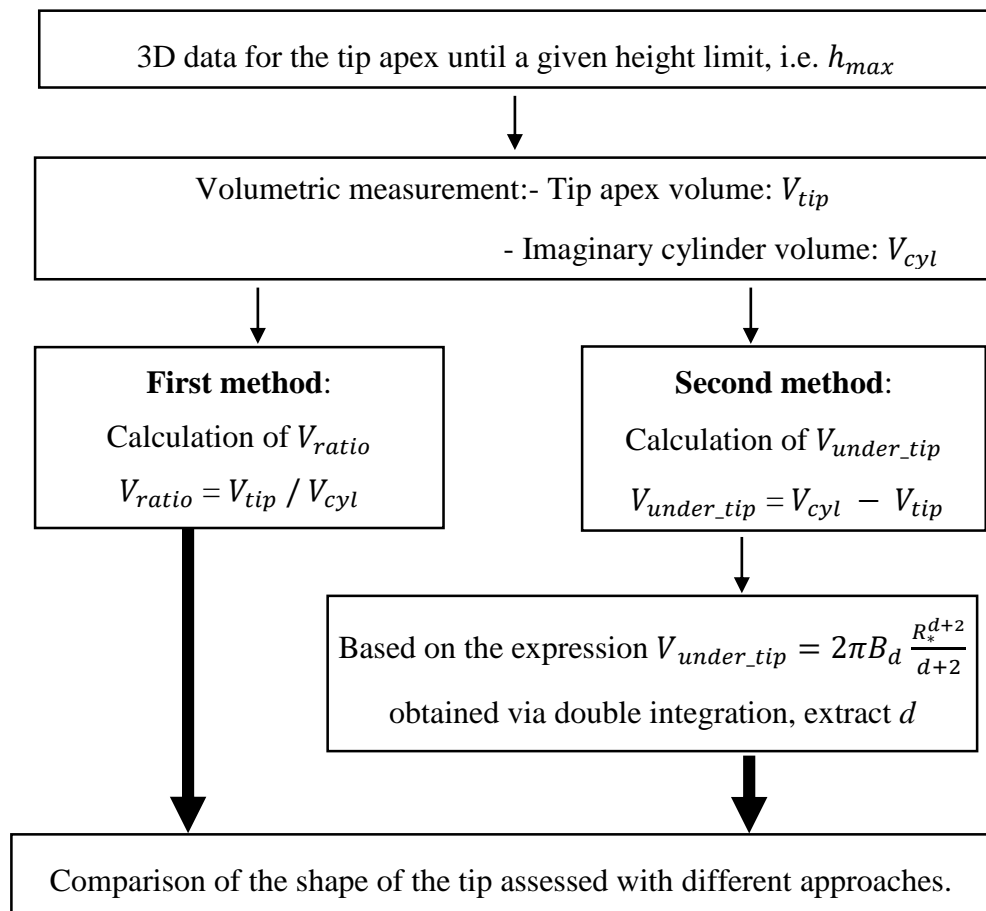


Figure 6.2: Overview of proposed procedure followed in this chapter.

6.4 Volumetric data

6.4.1 Tip volume measurement

In this section, a description of the process used to measure the tip apex volume, V_{tip} , is provided. The 3D data about the tip geometry were considered until a specific height limit which correspond to the maximum penetration depth of the tip into the material during nanoindentation, i.e. h_{max} . This means that the same height limit was used here and in both former chapters (i.e. Chapters 4 and 5). In this way, a valid comparison could be conducted later on. According to the 3D data provided for each tip and the information regarding each tip height limit, we can estimate precisely the volume of each tip apex.

From the AFM data, a two-step process was followed to identify the relevant set of 3D points which belonged to the height interval between the tip apex and h_{max} . This set of points are then used to calculate V_{tip} . The first step, which is illustrated with Figure 6.3, is a coarse selection where a “boundary region” around the tip apex is defined. This region contains all the relevant points but also some which are outside the height interval between the tip apex and h_{max} and which will be discarded during the second step. Figure 6.3(a) shows the 3D AFM image for a given tip (i.e. Tip 1 in this example). Figure 6.3(b) gives the SEM image of the tip apex. Figure 6.3(c) shows the selected boundary region. This coarse selection relied on analysing two perpendicular cross sections. In particular, in this figure, the line (A-A) represents the 0° - 180° cross section while (B-B) is the 90° - 270° cross section. Comparing the different cross section data with the 3D AFM image shown in Figure 6.3(c) confirms once more that SEM data provide limited information

for the purpose of assessing the shape of AFM probe tips, as discussed in previous chapters.

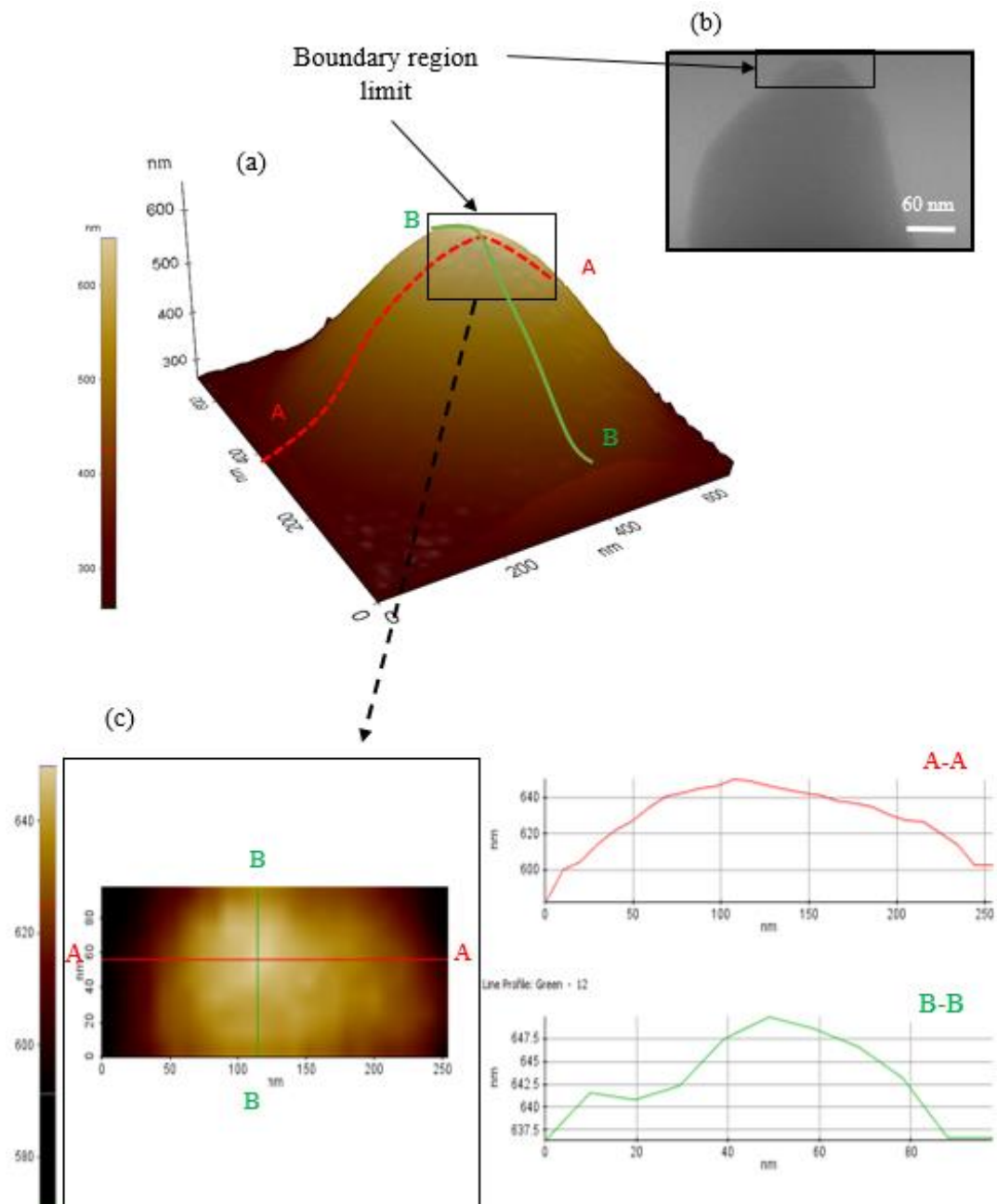


Figure 6.3: (a) 3D AFM image (area: 650 nm x 650 nm) around of the tip apex corresponding to a total height of about 350 nm (b) SEM image of the corresponding tip (i.e. Tip 1) and (c) identification of the apex region inside the boundary limit with the analysed cross sections.

An AFM image contains a set of 3D points described by their x , y , z coordinates. The x and y data are generated by the x -scanner and y -scanner movements of the stage, respectively. The z -scanner operates the vertical motion of the AFM probe through the close feedback loop. In this way, the z coordinates can be recorded for each data points. During the acquisition of an AFM image, the raster scan strategy is employed. This means that the data are recorded line by line and that all points along one line have a fixed y coordinate. Based on the data contained in the “boundary region”, a fine selection step is performed to make sure that only the relevant points are subsequently used in the calculation of V_{tip} . In particular, within this region, the point with the highest z coordinate is identified first. Then, the difference between the z coordinate of each point within this region and that of the highest point is evaluated. In this way, any point which does not belong the height interval of interest, h_{max} , is discarded. Figure 6.4 plots all the profiles within the “boundary region” for Tip 1. It is obvious that in this case only 10 profiles were detected inside this region. The higher the value of h_{max} obtained for a tip means the bigger the boundary region and thus, the higher the number of profiles.

Then, the required value of V_{tip} was simply measured by multiplying the sum of the measured height for each data point by an elementary area. More specifically, the elementary area used here was defined as the product of the distances between two data points in both planar coordinates. So, after extracting the relevant 3D data as describe above, V_{tip} was calculated using the following equation:

$$V_{tip} = \sum_{k=1}^{k=n} z_k \cdot \Delta x \cdot \Delta y \quad (6-1)$$

where n is the total number of relevant points selected, z_k is the height of the tip for the k^{th} point, while Δx and Δy represent the resolution of the AFM scan. More specifically, Δx is the distance between two pixels along the x axis and Δy is the distance between two pixels along the y axis.

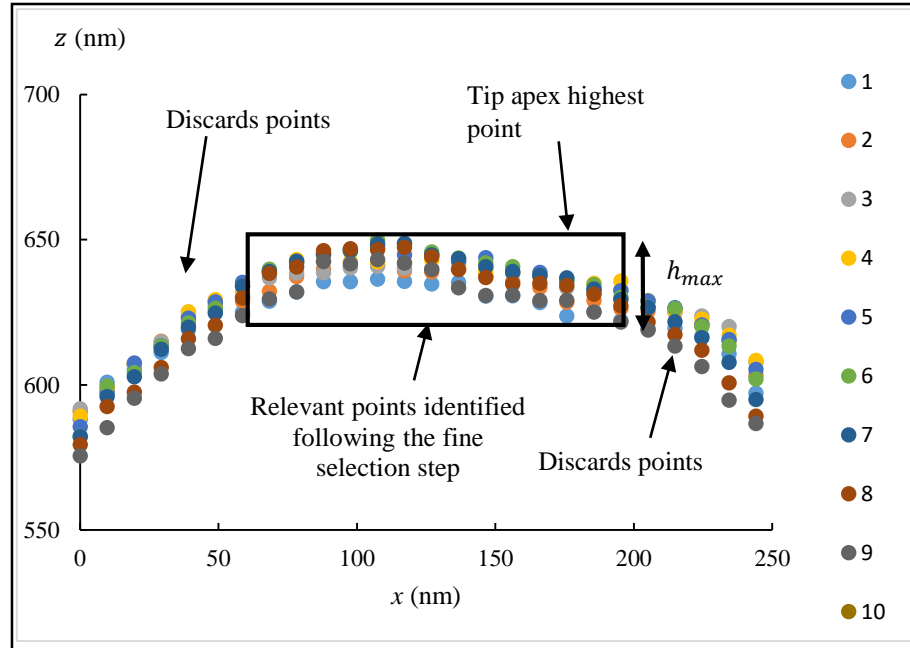


Figure 6.4: Plot of the cross-section profiles for Tip 1 contained within the “boundary region” and illustration of the fine selection step.

6.4.2 Imaginary cylinder volume measurement

The concept of the imaginary cylinder was already explained in section 6.3 and illustrated with Figure 6.1. Based on the 3D AFM data, the volume of the outer imaginary cylinder can be estimated by:

$$V = \pi \times R_*^2 \times h_{max} \quad (6-2)$$

where R_* is the radius of the base of the imaginary cylinder. In order to estimate R_* , the following equation was used

$$R_* = \frac{R_{(0^\circ-180^\circ)} + R_{(90^\circ-270^\circ)}}{2} \quad (6-3)$$

where $R_{(0^\circ-180^\circ)}$ and $R_{(90^\circ-270^\circ)}$ represent half of the length of the $0^\circ-180^\circ$ profile cross section along the horizontal axis and along the $90^\circ-270^\circ$ cross section, respectively. The procedure was adopted because of the fact that all the tested tips in this work had a non-perfect circular base. Thus, an average radius estimated from two cross section is assumed to be sufficient to minimise the error when estimating R_* , as illustrated in Figure 6.5.

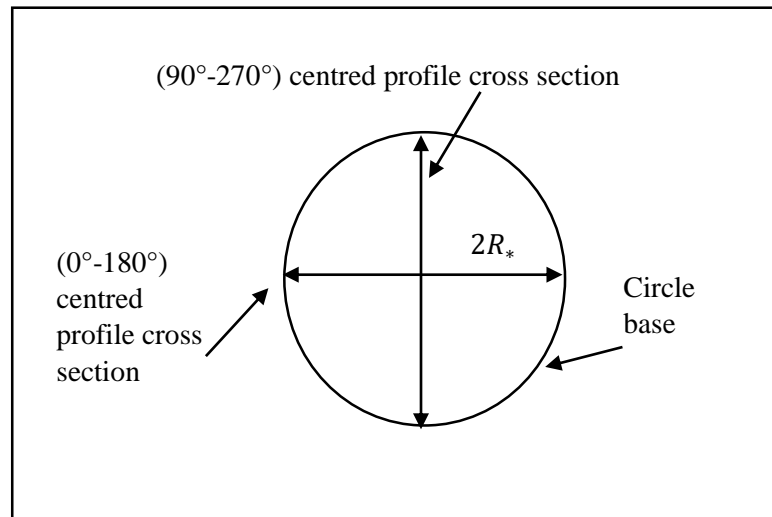


Figure 6.5: Top view illustration of the concept used to estimate the radius of the imaginary cylinder.

6.4.3 Numerical analysis for tip geometry assessment

In this section, we propose a new analysis to assess the tip shape according to a simple volumetric measurement. Basically, a numerical equation is established to express the tip volume. This equation is a function of B_d and d . Thus, based on the experimental knowledge of the tip volume, which was achieved in section 6.4.1, these two parameters can be found numerically. Practically, the experimentally value of each tip apex volume until a specific length limit h_{max} should be utilised to achieve this analysis. A number of

stages are involved in deriving this equation. First, the volume of the tip at a given height from the tip apex is expressed as follows:

$$V_{tip} = V_{cyl} - V_{under_tip} \quad (6-4)$$

where V_{cyl} is the volume of the imaginary cylinder, as presented in section 6.4.2 and V_{under_tip} is the volume within the imaginary cylinder which is under the tip region. All of these volumetric measurements have already been estimated from experimental data (c.f. Table 6.1). Here, the quantity V_{under_tip} is now also expressed theoretically, using double integration, as a function B_d and d . Figure 6.6 shows a schematic to illustrate the principle for calculating the volume of the region under the tip. In particular using polar coordinate and the elementary volume represented by the shaded region in Figure 6.6, this volume can be expressed as follows:

$$V_{under_tip} = \int_0^{2\pi} \int_0^{R_*} B_d r^d r dr d\theta \quad (6-5)$$

Solving the inner integral gives:

$$V_{under_tip} = \int_0^{2\pi} B_d \frac{R_*^{d+2}}{d+2} d\theta \quad (6-6)$$

Finally, we obtain the following expression to describe V_{under_tip} as a function B_d and d :

$$V_{under_tip} = 2\pi B_d \frac{R_*^{d+2}}{d+2} \quad (6-7)$$

Equation (6-6) can now be re-written as follows:

$$V_{tip} = \pi R_*^2 h_{max} - 2\pi B_d \frac{R_*^{d+2}}{d+2} \quad (6-8)$$

where R_* and h_{max} are a specific measured experimentally extracted for each tip. The only unknown quantities in equation (6-8) are B_d and d . These two quantities can be extracted by establishing a numerical method to solve this equation. Thus, this provides another route to estimate the required parameters to describe the actual shape of AFM tips. The implementation of this numerical analysis will be explained in more details in section 6.5.2.

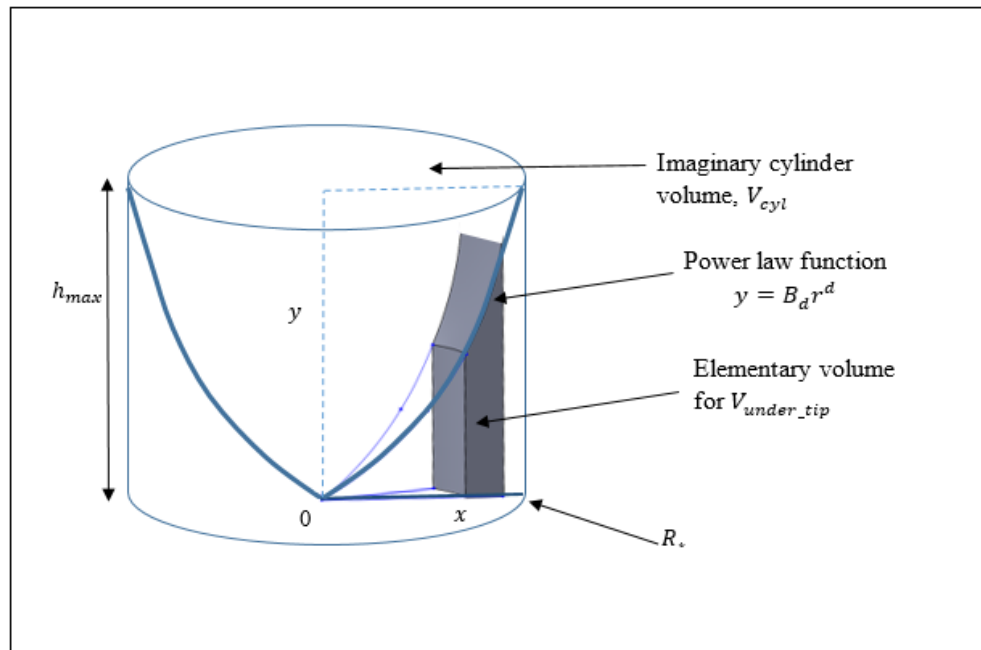


Figure 6.6: Schematic illustration of the elementary volume for V_{under_tip} .

6.5 Results and discussion

6.5.1 A new tip shape assessment metric: the volumetric ratio

For each of the four considered tips, the volumes V_{tip} and V_{cyl} were calculated based on the methodology presented in the previous section. This enabled the calculation of a new tip characterisation metric, V_{ratio} , using a simple expression:

$$V_{ratio} = V_{tip} / V_{cyl} \quad (6-9)$$

It is suggested that V_{ratio} may be considered as a possible metric to approximate the tip bluntness. Indeed, it should be expected that the blunter the tip then, the higher should be its V_{ratio} . Table 6.1 presents the results obtained when assessing V_{tip} , V_{cyl} and V_{ratio} for all four tips. The volume under the tip, V_{under_tip} , is also provided in each case. In addition, the theoretical V_{ratio} is also reported for the hypothetical cases where the tip would be a perfect cone (PC) or a perfect spherical cap (PSC).

Table 6.1: Experimental results for the tip volume, the imaginary cylinder volume, the volume under the tip and the volumetric ratio metric for each tip. This metric is also given for the theoretical cases of a perfect conical tip and of a tip described as a spherical cap.

Tip Number	V_{tip} (nm^3)	V_{cyl} (nm^3)	V_{under_tip} (nm^3)	V_{ratio}	Theoretical V_{ratio} for a perfect cone	Theoretical V_{ratio} for a perfect spherical cap
1	50076.7	107523.3	57446.6	0.47	0.33	0.51
2	45596.0	86413.2	40817.2	0.53	0.33	0.51
3	271929.4	699616.5	427687.2	0.39	0.33	0.51
4	58,082.4	122200.7	64118.3	0.48	0.33	0.51

As it can be seen from this table, Tip 3 presents the lowest V_{ratio} value, i.e. 0.39. This should indicate that it is the sharpest among the four tips considered. In addition, the tip bluntness increases in the following order: Tip 1, Tip 4 and finally, Tip 2. This result agrees with the findings presented in the previous Chapter. A more detailed comparison will be provided later on in section 6.5.1.2. In addition, Figure 6.7 plots the measured V_{ratio} for each together with the theoretical value of this metric for the hypothetical PC

and PSC cases. It is clear from this figure that the V_{ratio} estimated for Tips 1,2 and 4 approximate that of a PSC. On the other hand, the V_{ratio} for Tip 3 was found to approximate the geometry of a PC rather than that of a PSC. A possible theoretical explanation for this result is now be discussed in the next sub-section. The work done in this subsection has been published in (Alraziqi *et al.* 2016).

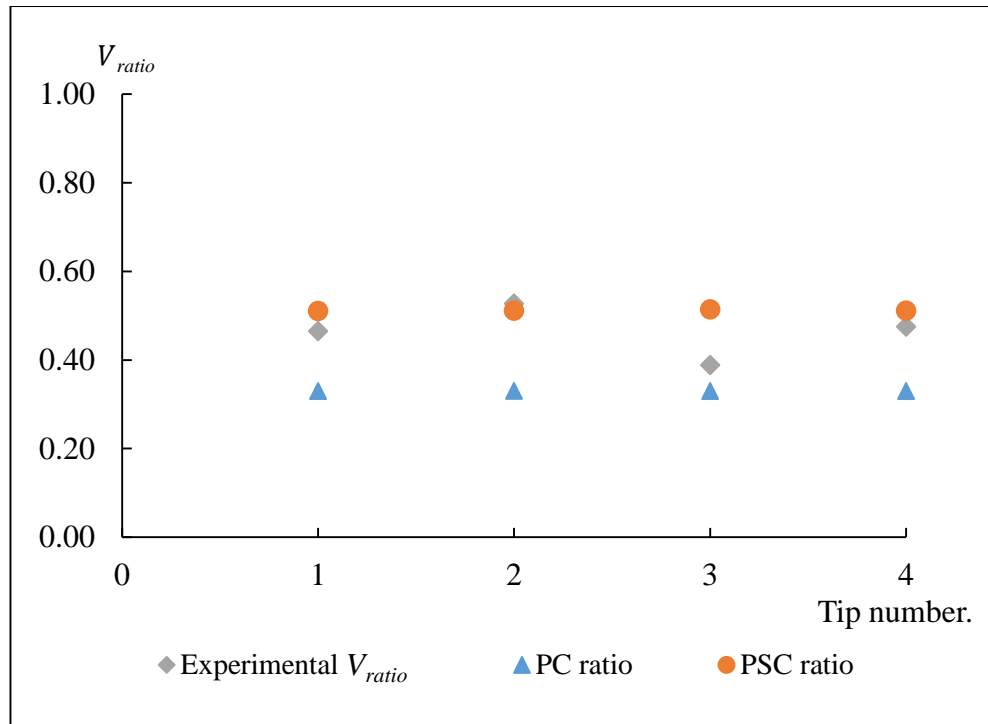


Figure 6.7: Comparison of the plots of the experimental V_{ratio} for each tip against the theoretical V_{ratio} for a PC and a PSC.

6.5.1.1. Influence of tip linear portions on the V_{ratio} metric

The above result for Tip 3 may be explained as follows. Although it is not possible to assume that in practice, this tip is not ideally sharp, and thus should not lead to a V_{ratio} equal to that of a perfect cone, it is possible that a horizontal layer of its 3D volume displayed flat surfaces. In this case, it could be theoretically assumed that the profile of such a tip presents a spherical portion and a linear portion, as illustrated in Figure 6.8, for

the sake of the argumentation presented here. In particular, this figure shows a schematic of a hypothetical tip profile plot for a total height, $h_2 = 40$ nm, and a total radius, $r_2 = 40$ nm. This figure shows how the different portions of an apex profile (i.e. the profile from the spherical cap portion and that from a linear portion) contribute the value of V_{tip} and ultimately, to that of the V_{ratio} . Based on the theoretical profile shown in this figure, we can calculate the V_{ratio} as a function of the length of the linear portion. This is now explained below.

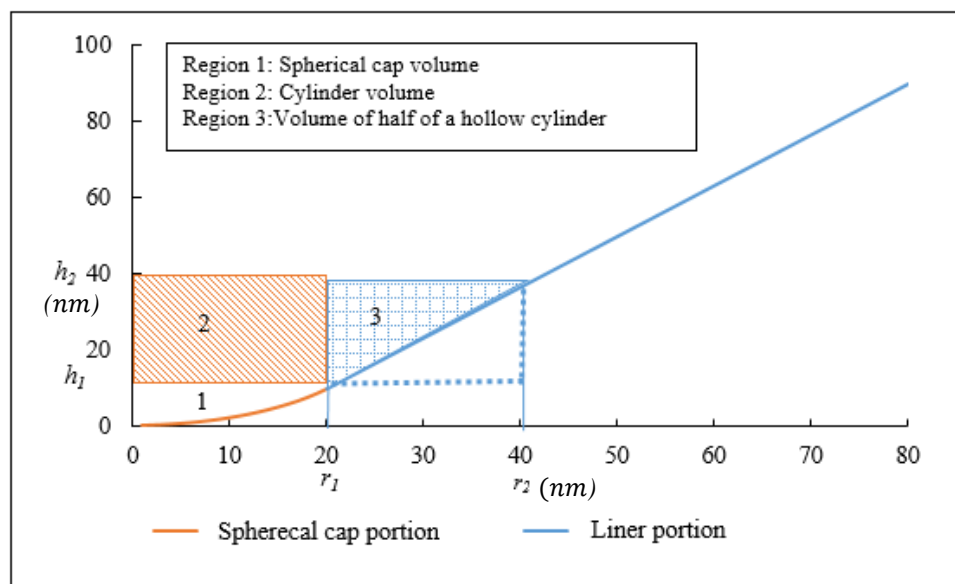


Figure 6.8: Schematic description of the geometry of a hypothetical tip profile for a total radius, $r_2 = 40$ nm, and a total height, $h_2 = 40$ nm.

As illustrated in the schematic of Figure 6.8, the total value of the tip volume can be calculated by adding the volumes of the all the portions present in its geometry. Portions 1, 2 and 3 respectively represent the volumes of a spherical cap, V_1 , of an inner cylinder, V_2 , and that of half of a hollow cylinder, V_3 , which has a height equal to $h_2 - h_1$ and a thickness equals to $r_2 - r_1$. Based on these different portions, the theoretical V_{ratio} can be calculated using the following equation:

$$V_{ratio} = (V_1 + V_2 + V_3) / V_{cyl} \quad (6-10)$$

Figure 6.9 plots the theoretical V_{ratio} as a function of the length of the linear portion. All the calculations and equations used to prepare this plot based on equation (6-10) are given in the Appendix A3 (see equations A3.1-A3.5) in addition to further 3D description of the different portions that the tip apex consists of for this specific theoretical case. From Figure 6.9, it could be said that as the straight line portion increases, the calculated V_{ratio} value decreases. In particular, it can be seen from this figure that the highest values for the V_{ratio} are located in the spherical cap region (i.e. region A). Once tip starts exhibited a linear portion (i.e. Region B), this ratio start to reduce.

Based on these theoretical results, it may be said that the reduced V_{ratio} value for Tip 3, which was reported in Figure 6.7, could be due to a relatively large contribution of the linear portion to its geometry in comparison with other tips.

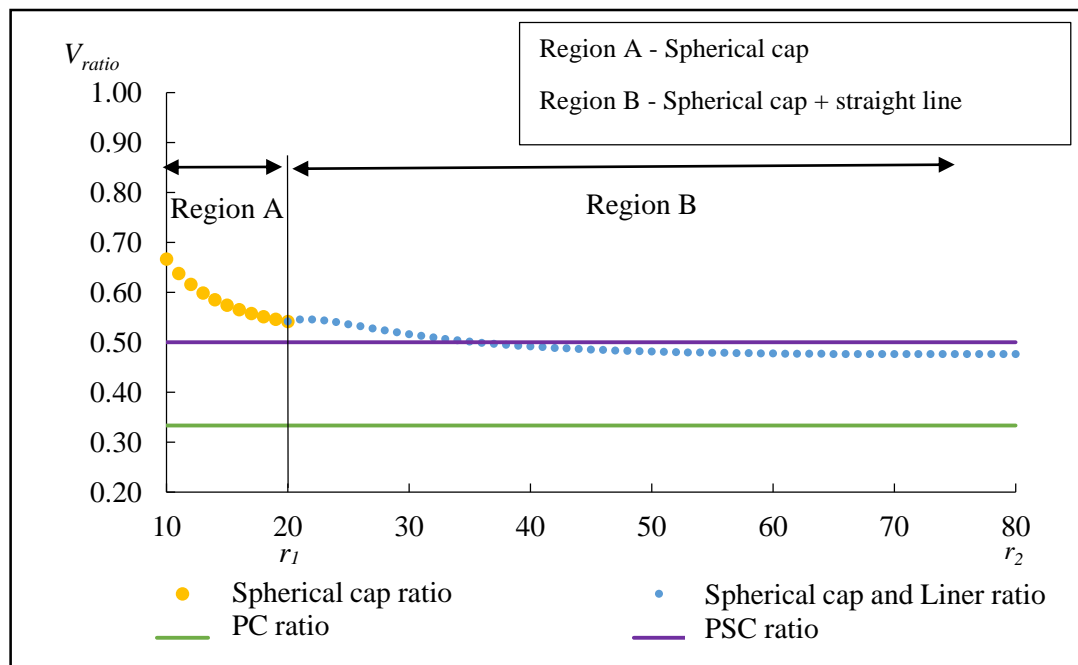


Figure 6.9: Theoretical V_{ratio} as a function of the contribution of a linear portion in the geometry of a tip profile.

6.5.1.2. Method validation

To check the validity of this new metric, the V_{ratio} value for two different distances from the tip apex were also evaluated in addition to the values already calculated for each tip case until h_{max} , as reported earlier. More specifically, these two distances corresponded to a height limit of 10 nm and 20 nm from the tip apex. These additional calculations of the V_{ratio} corresponding to these two different heights were conducted to check the consistency of the results obtained with this new metric. In particular, it is expected that the further this distance is from each tip apex, then the lower will be the value of the V_{ratio} . Figure 6.10 shows the results for the V_{ratio} for each of these different distances from the apex for all the tested tips.

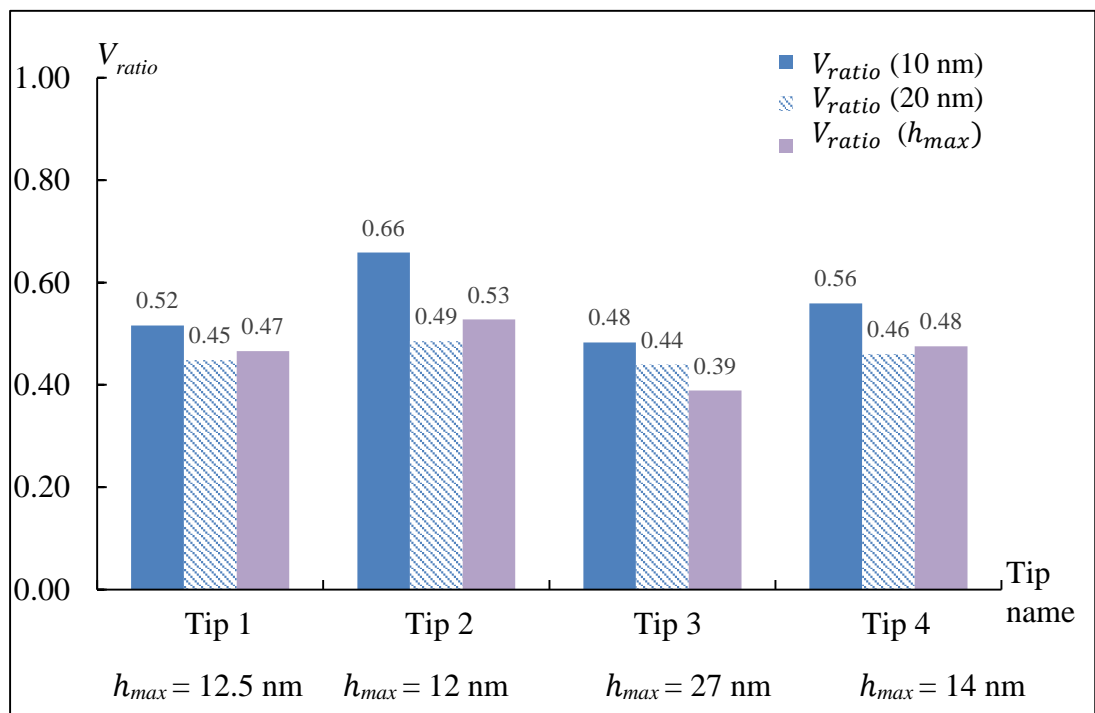


Figure 6.10 Variation of V_{ratio} measurement when estimated at different distances from the tip apex, namely 10 nm, 20 nm and h_{max} for each tip.

From Figure 6.10, Tip 3 presents the lowest V_{ratio} regardless of the distance considered from the apex. This was an expected result because Tip 3 was previously found to be the sharpest tip among the group of probes investigated. On the other hand, Tip 2, which was identified earlier as the bluntest, exhibits the highest V_{ratio} . In addition, it should be noted from this figure that for each tip, the V_{ratio} decreases when the considered distance from the apex increases. As mentioned earlier in section 6.5.1.1, this should be due to the contribution of the linear portion of the tip geometry. Overall, it could be said that this new metric, which based on simple volumetric measurement, could bring an acceptable description of a tip bluntness condition, which takes into account its 3D geometry rather than just a selected cross section.

Furthermore, for the purpose of validating this new metric, the V_{ratio} results were also compared with those obtained using the nanoindentation test to evaluate the degree of tip bluntness. d . This comparison is shown in Figure 6.11. The value of V_{ratio} of each tip are in good agreement with the results obtained in Chapter 4 when estimating d . Indeed, this comparison highlights that both approaches provide identical results with respect to ordering the tips as a function of their bluntness (always tip 3 with low V_{ratio} means (sharper), while tip 2 always with higher V_{ratio} means (blunter)).

As it was mentioned in Chapter 5, it is possible that the reverse imaging method leads to a minor overestimation of the actual tip volume at the apex. This experimental uncertainty would affect the determination R_* when estimating the V_{ratio} . This is probably the reason why the V_{ratio} for Tip 2 (i.e. 0.53) was found to be slightly higher than that of

a perfect spherical cap (i.e. 0.51) in spite of the fact that its degree of tip bluntness (i.e. $d = 1.92$) indicated that its shape should be sharper than a perfect sphere (i.e. $d = 2$). Also, experimental errors associated with other parameters such as sample roughness, thermal stability, acoustic vibration should contribute to the discrepancy between the theory and the results obtained from experiments.

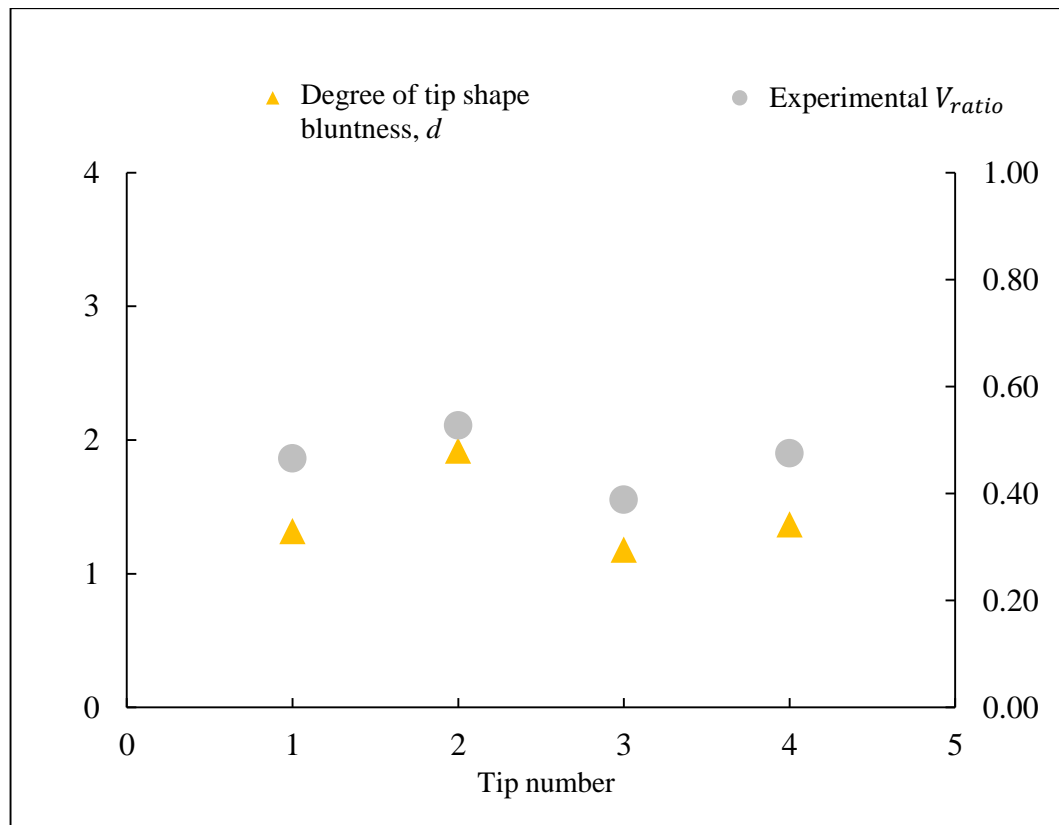


Figure 6.11 a comparison between V_{ratio} and the degree d of the shape bluntness for each tip.

6.5.2 Numerical determination of the degree of tip bluntness

The main idea for the numerical method implemented on this work was to extract the optimum value for B_d and d such that equation (6-8) agrees with experimental volume data as closely as possible. The numerical determination of the optimum values for both

B_d and d , that fit the measured V_{tip} for each tip case, was achieved in this study by utilising a special optimisation tool, called “Solver”, available within the Excel software. This tool employs the generalized reduced gradient method (Fylstra *et al.*1998) to solve non-linear optimisation problems, which is the case for our work (c.f. equation (6-8)). The objective, when using this optimisation tool for each tip, is to minimise the difference between the V_{tip} value found experimentally and that calculated with equation (6-8).

In practice, to implement our model with the Excel Solver, we need first to define the relationship between our mathematical expression represented by equation (6-8) and one or more “input variables”. The “input variables” introduced in this proposed model are R_* , h_{max} and V_{tip} for each tip case. Finally, the two factors B_d and d are the “decision variables” that we need obtained. The calculated difference between V_{tip} found experimentally and that calculated with equation (6-8) is called the “set objective”. The d values calculated in this way are presented in Table 6.2 for each tip.

Table 6.2: Numerically extracted d values for each tip

Tip name	d value calculated numerically
Tip 1	1.53
Tip 2	1.98
Tip 3	1.46
Tip 4	1.64

6.5.3 Comparison of the degree of tip bluntness obtained with different methods

The values of degree of tip bluntness, d , obtained with all the different methods studied throughout this Thesis are presented in Table 6.3 as well as in Figure 6.12. From Table 6.3, it can be seen that the percentage difference between the results extracted with the nanoindentation and the numerical approaches is nearly the same as the percentage error already calculated in Chapter 5. Thus, it can be said that assessing the tip shape from the selection of a few orthogonal cross-sections (as was the case for Chapter 5) does not bring any substantial error when approximating the real tip shape.

Table 6.3: Degree of tip bluntness, d , obtained with four different techniques

Tip number	d from the nanoindentation test (Chapter 4)	d from the numerical analysis (Chapter 6)	Percentage difference	d from 3D (AFM) data (Chapter 5)	d from 2D (SEM) data (Chapter 4)
1	1.34	1.53	12.42%	1.51	1.45
2	1.92	1.98	3.03%	1.93	1.33
3	1.18	1.46	19.18%	1.45	1.74
4	1.37	1.64	16.46%	1.63	1.57

In Figure 6.12, the degree of tip bluntness assessed from these different approaches is also summarised graphically for each tip with a bar chart. The value for d produced from the nanoindentation tests using the rescaling formula in Chapter 4 is given with a blue bar. The value measured using the power law fitting (i.e. $z = B r^d$) on a 2D profile cross-section extracted from SEM images is given in green. Using power law fitting, the value for d extracted from the analysis of the 3D tip apex data as an average of two scans

of the tip characteriser asperities is also given in black. Finally, the results for d evaluated through the numerical analysis, which includes the power exponent d in a double integral, is provided in red. In addition, the inset bar chart in this figure presents the average penetration depth for each tip during the nanoindentation tests. This additional bar chart provides interesting comparative data because the higher the value of d , then the less value of h_{max} is expected.

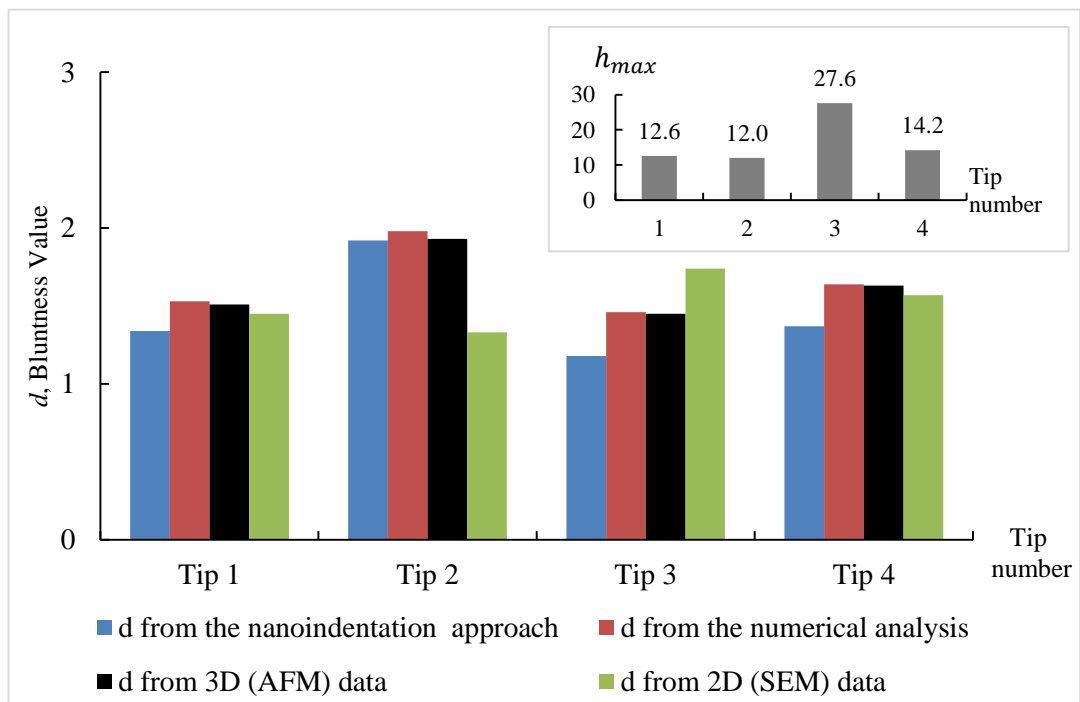


Figure 6.12: Degree of tip bluntness, d , obtained with four different techniques, namely with the nanoindentation approach, the numerical analysis, the 3D AFM data and the 2D SEM data.

It can be seen clearly from Figure 6.12, that a reasonable agreement is found between the values of d when extracted with the different approaches except when obtained with the SEM-based technique. In addition, when these SEM-based results are not considered, it can be said that each of the other approach provides consistent results with respect to the ordering of the tips as a function of their bluntness. Indeed, Tip 3 is

always assessed as the sharpest in the group, while Tip 2 always presents the highest value of d (i.e. it is the blunter). It is also interesting to notice that the tip shape bluntness extracted from the nanoindentation tests always present a slightly lower estimation of d in comparison with the other two 3D-based approaches.

The sources of discrepancy between the results from the nanoindentation and the 3D-based approaches were already mentioned in Chapter 5. Further work should be required to quantify the sources of errors. In addition, as pointed out by Vanlandingham *et al.* 2000, generally, it can be expected that the variation in size of sharp features on a tip characteriser and their susceptibility to damage during imaging would contribute to this uncertainty. Another possible factor would be the particular choice of parameters used to control the feedback loop during scanning, which depends on the AFM user experience.

The larger discrepancy with the 2D-based approach was expected as mentioned in Chapter 4. Thus, it can be said that assessing the degree of tip bluntness from SEM data is not a reliable method. This should be due to the fact that SEM data do not provide true 3D information as such data are limited to only one cross section. In addition, the inclination of the cantilever when mounted on the AFM device is not taken into account in this case, which does not represent the working condition of an AFM tip.

6.6 Summary

In this chapter, two novel mathematical approaches were proposed to characterise the bluntness of AFM probe tips. This could be achieved by the use of 3D geometry data about the apex obtained by scanning the AFM tip over a special tip characteriser. This

work was motivated from the experimental finding obtained in Chapter 5, which brought the question of whether there was any influence from the selection of a few cross-sections on the approximation of the degree of tip bluntness. Therefore, complete sets of 3D data were used in this chapter for each tips.

The proposed methods consist in determining the volumetric information of the tip apex region taking into account a specific height limit, which corresponds to the maximum penetration depth during nanoindentation. The first method is based on the calculation of the volumetric ratio between the tip apex volume and the volume of an imaginary cylinder in which the tip is contained. The second method employed a new numerical analysis that relies on experimental volume data value to assess the degree of tip bluntness. When comparing the results obtained with both methods, a good qualitative agreement was found with respect to identifying which tips were the sharpest and which were blunter. These results were also found to be in-line with those found in Chapter 4 and Chapter 5.

When comparing all the different approaches used to estimate the degree of tip bluntness, the data obtained show a good agreement between the nanoindentation-based results and the 3D-based results achieved with two different methods. In addition, it was also found that using 2D data to assess the tip shape bluntness led to a non-reliable assessment in the case of non-axisymmetric tips.

The main conclusions, which can be made from the study reported in this chapter are:

- A new metric was successfully proposed to characterise the AFM tip bluntness condition using simple volumetric measurements.

-
- A new numerical approach was achieved to extract the degree of bluntness, d , of AFM probe tip based on volumetric measurements.
 - The selection of a few orthogonal cross sections from the complete description of the 3D geometry of the tip appears to be sufficient to extract reliable values for the degree of tip bluntness.
 - The analysis of only a cross section profile based on the SEM micrograph of the tip apex to assess the degree of tip bluntness should be avoided

Chapter Seven

Contributions, Conclusions and Future work

Contributions, Conclusions and Future work

The main goal of this research was to propose and validate a novel in-situ technique to characterise the degree of bluntness of AFM probe tips. Based on the literature review presented in Chapter 2, it was argued that there is still a need to develop such a technique, which could be simple, fast, reliable and repeatable and which can effectively support AFM practitioners in deciding when an AFM probe should be changed. The particular technique investigated in this Thesis relies on the analysis of depth-sensing data obtained from the nanoindentation of the probe tip into a soft elastic sample. This chapter summarises the main contributions of this research. It also presents the most important conclusions achieved. Finally, suggestions for future work are also outlined.

7.1 Contributions

The following original contributions were made:

- To estimate the current bluntness of AFM probe tips, we developed a new experimental procedure based on analytical treatment of experimental results of depth-sensing indentation into a soft elastic substrate. We proposed to assume that the AFM probe may be approximated by a non-axisymmetric power-law function and to use the exponent of the power-law as a quantitative measure of the bluntness.
- We showed that the lateral displacements of an AFM tip at shallow indentations can be neglected, therefore, the scaling approach to the indentation results is applicable.
- To evaluate the accuracy of the results obtained by the use of the self-similar (scaling) approach to depth-sensing indentation, we also performed experimental studies

of the actual shape of several AFM tips using the reverse imaging method. This conventional method is more sophisticated and time consuming, hence cannot be used for the express analysis of the bluntness of AFM tips. In this case, we also approximated the tip shape as a power-law function and extracted an effective bluntness as the exponent of the fitted power-law function on 3D geometry data. Given that the exponent is not the same at different cross-sections, we used an effective exponent.

- There is a good agreement between values of the bluntness parameter evaluated by the express analysis using depth-sensing indentation and the effective bluntness obtained by power-law approximation of the actual shapes of AFM tips.

- Experiments showed that the utilisation of SEM data to determine both the tip radius of curvature and the bluntness degree were inaccurate. In fact, this also suggests the bluntness of an AFM tip differs significantly depending on its consideration: in its vertical position or in its working position at an AFM head.

- We also explored the utilisation of a novel metric (i.e. the V_{ratio}) to assess the AFM tip bluntness condition using simple volumetric measurements. Based on such data, we also implemented a numerical approach to extract the degree of bluntness.

-

7.2 Conclusions

Based on the results obtained during this research, the following conclusions can also be drawn:

- The provided experimental results when assessing the degree of bluntness of commercial AFM probes showed that the approximation of the spherical cap near the

apex region is not correct. In fact, different values were obtained using four tips from the same box.

- Both the maximum nanoindentation depth and the residual indent depth were in-line with the degree of tip bluntness evaluated using all approaches except from the 2D (i.e. SEM) approach.

- Based on the SEM micrographs for all tips obtained before and after the nanoindentation tests, it can be said that the nanoindentation-based technique proposed in this work could be considered as a non-destructive method.

- It was found that the percentage difference between the evaluation of the tip bluntness using 2D (SEM) data and nanoindentation test data ranged between 8% and 32%.

- A significant effect was found of the calibration of both the cantilever spring constant and the sensitivity of the PSPD to obtain an accurate and a reliable force-displacement curve. For the experimental conditions used here, it was noted that an error of 30% in the normal spring constant led to an error of 76% in the maximum indentation depth. While an under-estimation of 80% in the maximum indentation depth could result from an 18% change in the sensitivity of the PSPD.

- The implemented numerical approach to extract the degree of tip bluntness showed a good consistency with the nanoindentation-based approach. The discrepancy between both methods ranged from 3% to 19%.

- It was found that there was only slight change in the degree of bluntness estimated from 3D geometry data when extracted from a few selected cross sections or from the complete set of 3D data.

- Overall, all 3D-based tip assessment approaches investigated to estimate the degree of tip bluntness presented a good consistency with respect to ordering the tips as a function of their bluntness.

7.3 Future work and recommendations

This research has produced some original contributions and findings in the field of the AFM probe tip characterisation. However, the following research lines are still worth of future investigations in this area:

- Experimental investigations of the AFM tip wear using the proposed nanoindentation-based in the context of AFM probe-based nanomachining.
- Experimental investigations using a wider range of probe types and geometries.
- Further investigation to study the suitability of using the proposed simple volumetric measurement, i.e. the V_{ratio} , to evaluate the tip wear as a function of the tip bluntness.

References

- Al-Musawi, R.S.J., Brousseau, E.B., Geng, Y. and Borodich, F.M., 2016. Insight into mechanics of AFM tip-based nanomachining: bending of cantilevers and machined grooves. *Nanotechnology*, 27(38), p.385302.
- Alraziqi Z. Mukhtar N.F.H. and Brousseau E., 2016. Comparison of two AFM probe inspection techniques for three-dimensional tip characterisation. In euspen's 16th International Conference and Exhibition Nottingham, UK, May 30 - June 03. pp. 59–60.
- Alraziqi Z. , Brousseau E. and Borodich F. 2016. A new metric to assess the tip shape condition of AFM probes based on three-dimensional data. The international conference for students on applied engineering, Newcastle, UK, October. pp.24-29. IEEE Conference Publication.
- Atamny, F. and Baiker, A., 1995. Direct imaging of the tip shape by AFM. *Surface science*, 323(3), pp.L314-L318.
- Bao, G.W. and Li, S.F.Y., 1998. Characterization of atomic force microscopy (AFM) tip shapes by scanning hydrothermally deposited ZnO thin films. *Talanta*, 45(4), pp.751-757.
- Bhaskaran, H., Gotsmann, B., Sebastian, A., Drechsler, U., Lantz, M.A., Despont, M., Jaroenapibal, P., Carpick, R.W., Chen, Y. and Sridharan, K., 2010. Ultralow nanoscale wear through atom-by-atom attrition in silicon-containing diamond-like carbon. *Nature nanotechnology*, 5(3), pp.181-185.
- Bhushan, B., 2011. *Hand book of Nano-technology* 3rd editio., Springer-Verlag Berlin Heideiberg 2010.
- Bhushan, B., 2008. *Nanotribology and nanomechanics: An introduction*, Springer-Verlag Berlin Heideiberg.
- Bhushan, B. and Kwak, K.J., 2007. Platinum-coated probes sliding at up to 100 mm s⁻¹ against coated silicon wafers for AFM probe-based recording technology. *Nanotechnology*, 18(34), p.345504.
- Binnig, G., Rohrer, H., Gerber, C. and Weibel, E., 1982. Surface studies by scanning tunneling microscopy. *Physical review letters*, 49(1), p.57.
- Binnig, G., Quate, C.F. and Gerber, C., 1986. Atomic force microscope. *Physical review*

References

- letters*, 56(9), p.930.
- Bloo, M.L., Haitjema, H. and Pril, W.O., 1999. Deformation and wear of pyramidal, silicon-nitride AFM tips scanning micrometre-size features in contact mode. *Measurement*, 25(3), pp.203-211.
- Borodich, F.M. and Keer, L.M., 2004. Contact problems and depth-sensing nanoindentation for frictionless and frictional boundary conditions. *International Journal of Solids and Structures*, 41(9), pp.2479-2499.
- Borodich, F.M., 2011. Contact problems at nano/microscale and depth sensing indentation techniques. In *Materials Science Forum* (Vol. 662, pp. 53-76). Trans Tech Publications.
- Borodich, F.M., Galanov, B.A., Gorb, S.N., Prostov, M.Y., Prostov, Y.I. and Suarez-Alvarez, M.M., 2012. Evaluation of adhesive and elastic properties of materials by depth-sensing indentation of spheres. *Applied Physics A*, 108(1), pp.13-18.
- Borodich, F.M., Galanov, B.A., Gorb, S.N., Prostov, M.Y., Prostov, Y.I. and Suarez-Alvarez, M.M., 2013. Evaluation of adhesive and elastic properties of polymers by the BG method. *Macromolecular Reaction Engineering*, 7(10), pp.555-563.
- Borodich, F.M., 1989. Hertz contact problems for an anisotropic physically nonlinear elastic medium. *Strength of Materials*, 21(12), pp.1668-1676.
- Borodich, F.M., 1990b. On the three-dimensional contact problems of the anisotropic theories of plasticity and creep. In *In Proceedings of All-Union Institute on Light Alloy, Moscow*. pp. 1–8.
- Borodich, F.M., 1983. Similarity in the problem of contact between elastic bodies. *Journal of Applied Mathematics and Mechanics*, 47(3), pp.440-442.
- Borodich, F.M., 1983. Similarity in the problem of contact between elastic bodies. *Journal of Applied Mathematics and Mechanics*, 47(3), pp.440-442.
- Borodich, F.M., 2014. The Hertz-type and adhesive contact problems for depth-sensing indentation. *Adv. Appl. Mech*, 47, pp.225-366.
- Borodich, F.M., Keer, L.M. and Korach, C.S., 2003. Analytical study of fundamental nanoindentation test relations for indenters of non-ideal

References

- shapes. *Nanotechnology*, 14(7), p.803.
- Borodich, F.M., Pepelyshev, A. and Savencu, O., 2016. Statistical approaches to description of rough engineering surfaces at nano and microscales. *Tribology International*, 103, pp.197-207.
- Boussinesq, J., 1885. *Applications des potentiels "à l'Étude de l'équilibre et du Mouvement des Solides Élastique*, Paris: Gauthier-Villars.
- Bowden, F. P. and Tabor, D., 1964. The friction and lubrication of solids. *Part II. Oxford: Clarendon Press*.
- Briscoe, B.J., Sebastian, K.S. and Sinha, S.K., 1996. Application of the compliance method to microhardness measurements of organic polymers. *Philosophical Magazine A*, 74(5), pp.1159-1169.
- Briscoe, B.J. and Sebastian, K.S., 1996, March. The elastoplastic response of poly (methyl methacrylate) to indentation. In *Proceedings of the Royal Society of London A: Mathematical, Physical and Engineering Sciences* (Vol. 452, No. 1946, pp. 439-457). The Royal Society.
- Briscoe, B.J., Sebastian, K.S. and Adams, M.J., 1994. The effect of indenter geometry on the elastic response to indentation. *Journal of Physics D: Applied Physics*, 27(6), p.1156.
- Bulychev, S. I., Alekhin, V. P., Shorshorov, M. K., Ternovskii, A. P., and Shnyrev, G. D., 1975. Determination of Young's modulus according to indentation diagram. *Industrial Laboratory*, 41, 1409–1412.
- Bulychev, S. I., Alekhin, V. P., Shorshorov, M. Kh. and Ternovskii, A.P., 1976. Mechanical Properties of Materials Studied from Kinetic Diagrams of Load Versus Depth of Impression During Microimpression. *Strength of material*, 8(9), pp.1084–1089.
- Burnham, N.A. and Colton, R.J., 1989. Measuring the nanomechanical properties and surface forces of materials using an atomic force microscope. *Journal of Vacuum Science & Technology A: Vacuum, Surfaces, and Films*, 7(4), pp.2906-2913.
- Bushby, A.J., Ferguson, V.L. and Boyde, A., 2004. Nanoindentation of bone: Comparison of specimens tested in liquid and embedded in polymethylmethacrylate. *Journal of*

References

- Materials Research*, 19(01), pp.249-259.
- Butt, H.J., Cappella, B. and Kappl, M., 2005. Force measurements with the atomic force microscope: Technique, interpretation and applications. *Surface science reports*, 59(1), pp.1-152.
- Bykov, V., Gologanov, A. and Shevyakov, V., 1998. Test structure for SPM tip shape deconvolution. *Applied Physics A: Materials Science & Processing*, 66(5), pp.499-502.
- Odin, C., Aime, J.P., El Kaakour, Z. and Bouhacina, T., 1994. Tip's finite size effects on atomic force microscopy in the contact mode: simple geometrical considerations for rapid estimation of apex radius and tip angle based on the study of polystyrene latex balls. *Surface Science*, 317(3), pp.321-340.
- Calabri, L., Pugno, N., Menozzi, C. and Valeri, S., 2008. AFM nanoindentation: tip shape and tip radius of curvature effect on the hardness measurement. *Journal of Physics: Condensed Matter*, 20(47), p.474208.
- Cappella, B. and Dietler, G., 1999. Force-distance curves by atomic force microscopy. *Surface science reports*, 34(1-3), pp.15-3104.
- Carpick, R.W. and Salmeron, M., 1997. Scratching the surface: fundamental investigations of tribology with atomic force microscopy. *Chemical Reviews*, 97(4), pp.1163-1194.
- Cheng, T.J., Han, J.H., Ziwicki, M., Lee, C.H. and Bhave, S.A., 2011, January. 6.4 GHz acoustic sensor for in-situ monitoring of AFM tip wear. In *Micro Electro Mechanical Systems (MEMS), 2011 IEEE 24th International Conference on* (pp. 521-524). IEEE.
- Chiu, Y.L. and Ngan, A.H.W., 2002. A TEM investigation on indentation plastic zones in Ni₃Al (Cr, B) single crystals. *Acta material*, 50(10), pp.2677-2691.
- Choi, J.H. and Korach, C.S., 2011. Tip bluntness transition measured with atomic force microscopy and the effect on hardness variation with depth in silicon dioxide nanoindentation. *International Journal of Precision Engineering and Manufacturing*, 12(2), pp.345-354.

References

- Chung, K.H. and Kim, D.E., 2003. Fundamental investigation of micro wear rate using an atomic force microscope. *Tribology Letters*, 15(2), pp.135-144..
- Chung, K.H., Lee, Y.H. and Kim, D.E., 2005. Characteristics of fracture during the approach process and wear mechanism of a silicon AFM tip. *Ultramicroscopy*, 102(2), pp.161-171.
- Cleveland, J.P., Manne, S., Bocek, D. and Hansma, P.K., 1993. A nondestructive method for determining the spring constant of cantilevers for scanning force microscopy. *Review of Scientific Instruments*, 64(2), pp.403-405.
- Clifford, C.A. and Seah, M.P., 2005. The determination of atomic force microscope cantilever spring constants via dimensional methods for nanomechanical analysis. *Nanotechnology*, 16(9), p.1666.
- Clifford, C.A. and Seah, M.P., 2005. Quantification issues in the identification of nanoscale regions of homopolymers using modulus measurement via AFM nanoindentation. *Applied surface science*, 252(5), pp.1915-1933.
- Doerner, M.F. and Nix, W.D., 1986. A method for interpreting the data from depth-sensing indentation instruments. *Journal of Materials research*, 1(04), pp.601-609.
- Dongmo, L.S., Villarrubia, J.S., Jones, S.N., Renegar, T.B., Postek, M.T. and Song, J.F., 2000. Experimental test of blind tip reconstruction for scanning probe microscopy. *Ultramicroscopy*, 85(3), pp.141-153.
- Ducker, W.A., Senden, T.J. and Pashley, R.M., 1992. Measurement of forces in liquids using a force microscope. *Langmuir*, 8(7), pp.1831-1836.
- Dukic, M., Adams, J.D. and Fantner, G.E., 2015. Piezoresistive AFM cantilevers surpassing standard optical beam deflection in low noise topography imaging. *Scientific reports*, 5, p.16393.
- Fylstra, D., Lasdon, L., Watson, J. and Waren, A., 1998. Design and use of the Microsoft Excel Solver. *Interfaces*, 28(5), pp.29-55.
- GALANOV, B., 1981a. Approximate solution of some contact problems with unknown contact area under conditions of power-law hardening of the material. *Akademiia Nauk Ukrains' koi RSR, Dopovidi, Seriia A-Fiziko-Matematichni ta Tekhnichni Nauki*, pp.35-40.

References

- Galanov, B.A., 1981. The approximate solution of certain problems of the elastic contact of two bodies. *Akademiia Nauk SSSR, Izvestiia, Mekhanika Tverdogo Tela*, pp.61-67.
- Galanov, B.A., 1983. *Mechanics of Solids.* , Vol.18, p.51.
- Galanov, B. A., Grigorev, O. N., Milman, Y. V., and Ragozin, I. P. (1983). Determination of the hardness and Young's modulus from the depth of penetration of a pyramidal indenter. *Strength of Materials*, 15, 1624–1628.
- Galanov, B.A., Grigor'ev, O.N., Mil'man, Yu.V., Ragozin, I.P. and Trefilov, V.I. 1984. Determination of the hardness and Young's modulus with elastoplastic penetration of indentors into materials, *Soviet Physics Doklady*, Vol. 29, p. 146
- Galanov, B.A., 1982. An approximate method for the solution of some two-body contact problems with creep in the case of an unknown contact area. *International Applied Mechanics*, 18(8), pp.711-718.
- Galin, L. A., 1953. *Contact problems in the theory of elasticity*. Moscow-Leningrad: Gostekhizdat.(Russian).
- Galin, L. A., 2008. Contact problems: The legacy of L.A. Galin. In G. L. Gladwell (Ed.), Springer.
- Galin, L. A., 1946. Spatial contact problems of the theory of elasticity for punches of circular shape in planar projection. *PMM Journal of Applied Mathematics and Mechanics*, 10, 425–448. (Russian).
- Glasbey, T.O., Batts, G.N., Davies, M.C., Jackson, D.E., Nicholas, C.V., Purbrick, M.D., Roberts, C.J., Tendler, S.J.B. and Williams, P.M., 1994. The use of a polymer film to estimate AFM probe profile. *Surface science*, 318(3), pp.L1219-L1224.
- Gotsmann, B. and Lantz, M.A., 2008. Atomistic wear in a single asperity sliding contact. *Physical review letters*, 101(12), p.125501.
- Gozen, B.A. and Ozdoganlar, B., 2013. "An Experimental Analysis of Diamond Tip Wear During Nano- milling of Single Crystal Silicon". Proceedings of the 8th International Conference on MicroManufacturing. Canada, March 25-28, 2013, pp.507-513.
- Gozen B. A. and Ozdoganlar B., 2014, "Wear of Ultrananocrystalline Diamond AFM Tips during Mechanical Nano-Manufacturing by Nano-Milling", *Wear*, Vol. 317,

References

- Issues 1-2, pp. 39-55.
- Galanov, B.A., 1982. An approximate method for the solution of some two-body contact problems with creep in the case of an unknown contact area. *International Applied Mechanics*, 18(8), pp.711-718.
- Griffith, J.E., Grigg, D.A., Vasile, M.J., Russell, P.E. and Fitzgerald, E.A., 1991. Characterization of scanning probe microscope tips for linewidth measurement. *Journal of Vacuum Science and Technology B: Microelectronics and Nanometer Structures Processing, Measurement, and Phenomena*, 9(6), pp.3586-3589.
- Grigg D. A., Russell J. E., Griffith, Vasile M. J. and Fitzgerald E. A., 1992, "Probe Characterization for Scanning Probe Metrology", *Ultramicroscopy*, Vol. 42-44, Part 2, pp. 1616-1620.
- Hertz, H., 1882a. Ueber die Berührung fester elastischer Körper. *Journal für die reine und angewandte Mathematik*, 92, 156–171. (English transl. Hertz, H. (1896). On the contact of elastic solids. In D. E. Jones & G. A. Schott (Eds.), *MiscellaneouspapersbyH.Hertz*. London: Macmillan, pp. (146–162).
- Heim, L., Kappl, M. and Butt, H.-J., 2004. Tilt of Atomic Force Microscope Cantilevers: Effect on Friction Measurements. *Langmuir*, 20(6), pp.2760–2764.
- Hertz H., 1896. *Miscellaneous Papers*, New York: MacMillan and Co., Ltd.
- Ho, E. and Marcolongo, M., 2005. Effect of coupling agents on the local mechanical properties of bioactive dental composites by the nano-indentation technique. *Dental materials*, 21(7), pp.656-664.
- Huang, Y.P., Lin, S.C. and Lin, V.T.Y., 2013. Effects of system parameters on tip-wear in tapping mode atomic force microscopy. *Surface Topography: Metrology and Properties*, 1(1), p.015003.
- Hutter, J.L. and Bechhoefer, J., 1993. Calibration of atomic-force microscope tips. *Review of Scientific Instruments*, 64(7), pp.1868-1873.
- Hutter, J.L., 2005. Comment on tilt of atomic force microscope cantilevers: effect on spring constant and adhesion measurements. *Langmuir*, 21(6), pp.2630-2632.

References

- Itoh, H., Fujimoto, T. and Ichimura, S., 2006. Tip characterizer for atomic force microscopy. *Review of scientific instruments*, 77(10), p.103704.
- Jacobs, T.D., Wabiszewski, G.E., Goodman, A.J. and Carpick, R.W., 2016. Characterizing nanoscale scanning probes using electron microscopy: A novel fixture and a practical guide. *Review of Scientific Instruments*, 87(1), p.013703.
- Jee, A.Y. and Lee, M., 2010. Comparative analysis on the nanoindentation of polymers using atomic force microscopy. *Polymer Testing*, 29(1), pp.95-99.
- Johanson, K.L., 1985. *Contact Mechanics*, Cambridge, England: Cambridge University Press.
- Kalei, G.N., 1968. Some results of microhardness test using the depth of impression. *Mashinovedenie*, 4(3), pp.105–107.
- Keller, D., 1991. Reconstruction of STM and AFM images distorted by finite-size tips. *Surface Science*, 253(1-3), pp.353-364.
- Keller, D.J. and Franke, F.S., 1993. Envelope reconstruction of probe microscope images. *Surface Science*, 294(3), pp.409-419.
- Khurshudov, A. and Kato, K., 1995. Wear of the atomic force microscope tip under light load, studied by atomic force microscopy. *Ultramicroscopy*, 60(1), pp.11-16.
- Khurshudov, A.G., Kato, K. and Koide, H., 1997. Wear of the AFM diamond tip sliding against silicon. *Wear*, 203, pp.22-27.
- Kindrachuk, V.M., Galanov, B.A., Kartuzov, V.V. and Dub, S.N., 2009. Refined model of elastic nanoindentation of a half-space by the blunted Berkovich indenter accounting for tangential displacements on the contact surface. *Journal of materials science*, 44(10), pp.2599-2609.
- Lantz, M.A., O'Shea, S.J. and Welland, M.E., 1998. Characterization of tips for conducting atomic force microscopy in ultrahigh vacuum. *Review of scientific instruments*, 69(4), pp.1757-1764.
- Leite, F.L. and Herrmann, P.S.P., 2005. Application of atomic force spectroscopy (AFS) to studies of adhesion phenomena: a review. *Journal of adhesion science and technology*, 19(3-5), pp.365-405.

References

- Liu, J., Notbohm, J.K., Carpick, R.W. and Turner, K.T., 2010. Method for characterizing nanoscale wear of atomic force microscope tips. *ACS nano*, 4(7), pp.3763-3772.
- Lo, R.Y. and Bogy, D.B., 1999. Compensating for elastic deformation of the indenter in hardness tests of very hard materials. *Journal of materials research*, 14(6), pp.2276-2282.
- Love, A.E.H., 1939. Boussinesq's problem for a rigid cone. *The Quarterly Journal of Mathematics*, 10, pp.161–175.
- Lucas, M., Gall, K. and Riedo, E., 2008. Tip size effects on atomic force microscopy nanoindentation of a gold single crystal. *Journal of Applied Physics*, 104(11), p.113515.
- Ma, L., Levine, L., Dixson, R., Smith, D. and Bahr, D., 2012. Effect of the spherical indenter tip assumption on the initial plastic yield stress. In *Nanoindentation in Materials Science*, 22 (6), pp.1656-1661
- Markiewicz, P. and Goh, M.C., 1995. Atomic force microscope tip deconvolution using calibration arrays. *Review of scientific instruments*, 66(5), pp.3186-3190.
- Maw, W., Stevens, F., Langford, S.C. and Dickinson, J.T., 2002. Single asperity tribochemical wear of silicon nitride studied by atomic force microscopy. *Journal of Applied Physics*, 92(9), pp.5103-5109.
- Mayo, M.J., 1997. High and low temperature superplasticity in nanocrystalline materials. *Nanostructured materials*, 9(1-8), pp.717-726.
- Medendorp, C.A., 2011. Atomic force microscopy method development for surface energy analysis.
- Miller, R., Vesenka, J. and Henderson, E., 1995. Tip reconstruction for the atomic force microscope. *SIAM Journal on Applied Mathematics*, 55(5), pp.1362-1371.
- Montelius, L. and Tegenfeldt, J.O., 1993. Direct observation of the tip shape in scanning probe microscopy. *Applied physics letters*, 62(21), pp.2628-2630.
- Morris, V.J., Kirby, A.R. and Gunning, A.P., 2009. *Atomic force microscopy for biologists*. World Scientific.
- Mukhtar, N.F.H., 2017. *Characterisation of Tip Wear during AFM Probe-Based*

References

- Nanomachining* (Doctoral dissertation, Cardiff University).
- Schwarzer, N., 2006. Effect of lateral displacement on the surface stress distribution for cone and sphere contact. *Philosophical Magazine*, 86(33-35), pp.5231-5237.
- Neto, C. and Craig, V.S., 2001. Colloid probe characterization: radius and roughness determination. *Langmuir*, 17(7), pp.2097-2099.
- Neumeister, J.M. and Ducker, W.A., 1994. Lateral, normal, and longitudinal spring constants of atomic force microscopy cantilevers. *Review of Scientific Instruments*, 65(8), pp.2527-2531.
- Newey, D.M.A.H.M., Wilkins, M.A. and Pollock, H.M., 1982. An ultra-low-load penetration hardness tester. *Journal of Physics E: Scientific Instruments*, 15(1), p.119.
- Oliver, W.C. and Pharr, G.M., 1992. An improved technique for determining hardness and elastic modulus using load and displacement sensing indentation experiments. *Journal of materials research*, 7(06), pp.1564-1583.
- Pethica, J.B., Hutchings, R. and Oliver, W.C., 1983. Hardness measurement at penetration depths as small as 20 nm. *Philosophical Magazine A*, 48(4), pp.593-606.
- Pharr, G.M. and Bolshakov, A., 2002. Understanding nanoindentation unloading curves. *Journal of Materials Research*, 17(10), pp.2660-2671.
- Ramirez-Aguilar, K.A. and Rowlen, K.L., 1998. Tip characterization from AFM images of nanometric spherical particles. *Langmuir*, 14(9), pp.2562-2566.
- De Rose, J.A. and Revel, J.P., 1997. Examination of atomic scanning force microscopy probe tips with the transmission electron microscopy. *Microsc.Microanal*, 3(3), pp.203-213.
- Sader, J.E., Sanelli, J.A., Adamson, B.D., Monty, J.P., Wei, X., Crawford, S.A., Friend, J.R., Marusic, I., Mulvaney, P. and Bieske, E.J., 2012. Spring constant calibration of atomic force microscope cantilevers of arbitrary shape. *Review of Scientific Instruments*, 83(10), p.103705.
- Sader, J.E., Chon, J.W. and Mulvaney, P., 1999. Calibration of rectangular atomic force microscope cantilevers. *Review of Scientific Instruments*, 70(10), pp.3967-3969.
- Sakai, M. Akatsu, T. and Numata, S., 2004. Finite element analysis for conical

References

- indentation unloading of elastoplastic materials with strain hardening. *Acta Material*, Vol. 52, p. 2359
- Sawa, T. and Tanaka, K., 2001. Simplified method for analyzing nanoindentation data and evaluating performance of nanoindentation instruments. *Journal of Materials Research*, 16(11), pp.3084-3096.
- Schmutz, J.E., Fuchs, H. and Hölscher, H., 2010. Measuring wear by combining friction force and dynamic force microscopy. *Wear*, 268(3), pp.526-532.
- Schwarz, U.D., Köster, P. and Wiesendanger, R., 1996. Quantitative analysis of lateral force microscopy experiments. *Review of scientific instruments*, 67(7), pp.2560-2567.
- Schwarzer, N. and Fuchs, M., 2006. Comprehensive analysis of thin film nanoindentation data via internetportal—A principal feasibility study. *Thin solid films*, 515(3), pp.1080-1086.
- Seah, M.P., 2004. Intercomparison of silicon dioxide thickness measurements made by multiple techniques: the route to accuracy. *Journal of vacuum science & technology A: vacuum, surfaces, and films*, 22(4), pp.1564-1571.
- Sheiko, S.S., Möller, M., Reuvekamp, E.M.C.M. and Zandbergen, H.W., 1994. Evaluation of the probing profile of scanning force microscopy tips. *Ultramicroscopy*, 53(4), pp.371-380.
- Shen, W., Jiang, B., Han, B.S. and Xie, S.S., 2000. Investigation of the radial compression of carbon nanotubes with a scanning probe microscope. *Physical review letters*, 84(16), p.3634.
- Shorshorov, M. K., Bulychev, S. I., and Alekhin, V. P. (1981). Work of plastic and elastic deformation during indenter indentation. *Soviet Physics—Doklady*, 26, 769–771.
- Shtaerman, I.Y., 1939. On the Hertz theory of local deformations resulting from the pressure of elastic solids. *Doklady Akademii Nauk SSSR*, 25, pp.360–362.
- Skårman, B., Wallenberg, L.R., Jacobsen, S.N., Helmersson, U. and Thelanders, C., 2000. Evaluation of intermittent contact mode AFM probes by HREM and using atomically sharp CeO₂ ridges as tip characterizer. *Langmuir*, 16(15), pp.6267-6277.
- Stilwell, N.A. and Tabor, D., 1961. Elastic recovery of conical indentations. *Proceedings*

References

- of the Physical Society*, 78(2), p.169.
- Song, Y., Wu, S., Xu, L. and Fu, X., 2015. Accurate calibration and uncertainty estimation of the normal spring constant of various AFM cantilevers. *Sensors*, 15(3), pp.5865-5883.
- Tabor, D., 1948, February. A simple theory of static and dynamic hardness. In *Proceedings of the Royal Society of London A: Mathematical, Physical and Engineering Sciences* (Vol. 192, No. 1029, pp. 247-274). The Royal Society.
- Tang, B. and Ngan, A.H.W., 2003. Accurate measurement of tip-sample contact size during nanoindentation of viscoelastic materials. *Journal of Materials Research*, 18(05), pp.1141-1148.
- Rabiei, A., Thomas, B., Jin, C., Narayan, R., Cuomo, J., Yang, Y. and Ong, J.L., 2006. A study on functionally graded HA coatings processed using ion beam assisted deposition with in situ heat treatment. *Surface and Coatings Technology*, 200(20), pp.6111-6116.
- Thurn, J. and Cook, R.F., 2002. Simplified area function for sharp indenter tips in depth-sensing indentation. *Journal of Materials Research*, 17(05), pp.1143-1146.
- Tseng, A.A., Notargiacomo, A. and Chen, T.P., 2005. Nanofabrication by scanning probe microscope lithography: A review. *Journal of Vacuum Science & Technology B: Microelectronics and Nanometer Structures Processing, Measurement, and Phenomena*, 23(3), pp.877-894.
- Tsukamoto, Y., Yamaguchi, H. and Yanagisawa, M., 1987. Mechanical properties of thin films: Measurements of ultramicroindentation hardness, Young's modulus and internal stress. *Thin Solid Films*, 154(1-2), pp.171-181.
- VanLandingham, M.R., Villarrubia, J.S., Guthrie, W.F. and Meyers, G.F., 2001, March. Nanoindentation of polymers: an overview. In *Macromolecular symposia* (Vol. 167, No. 1, pp. 15-44). Wiley-Blackwell, 111 River Street Hoboken NJ 07030-5774 USA.
- Vanlandingham, M.R., McKnight, S.H., Palmese, G.R., Elings, J.R., Huang, X., Bogetti, T.A., Eduljee, R.F. and Gillespie Jr, J.W., 1997. Nanoscale indentation of polymer systems using the atomic force microscope. *The Journal of Adhesion*, 64(1-4), pp.31-59.

References

- VanLandingham, M.R., Juliano, T.F. and Hagon, M.J., 2005. Measuring tip shape for instrumented indentation using atomic force microscopy. *Measurement Science and Technology*, 16(11), p.2173.
- Velegol, S.B., Pardi, S., Li, X., Velegol, D. and Logan, B.E., 2003. AFM imaging artifacts due to bacterial cell height and AFM tip geometry. *Langmuir*, 19(3), pp.851-857.
- Vesenka, J., Manne, S., Giberson, R., Marsh, T. and Henderson, E., 1993. Colloidal gold particles as an incompressible atomic force microscope imaging standard for assessing the compressibility of biomolecules. *Biophysical journal*, 65(3), pp.992-997.
- Villarrubia, J.S., 1997. Algorithms for scanned probe microscope image simulation, surface reconstruction, and tip estimation. *Journal of research of the National Institute of Standards and Technology*, 102(4), p.425.
- Villarrubia, J.S., 1994. Morphological estimation of tip geometry for scanned probe microscopy. *Surface science*, 321(3), pp.287-300.
- Wang, C.Y., Pan S.P., Peng a G.S., Tsai J. 2005. A comparison study on the measurement of nanoparticles. In *SPIE conference 5879*. pp. 298–303.
- Wang, Y. and Chen, X., 2007. Carbon nanotubes: A promising standard for quantitative evaluation of AFM tip apex geometry. *Ultramicroscopy*, 107(4), pp.293-298.
- Wilson, D.L., Kump, K.S., Eppell, S.J., Marchant, R.E., 1995. Morphological Restoration of Atomic Force Microscopy Images. *Langmuir* 11, p.265.
- Yacoot, A. and Koenders, L., 2008. Aspects of scanning force microscope probes and their effects on dimensional measurement. *Journal of Physics D: Applied Physics*, 41(10), p.103001.
- Yan, Y., Xue, B., Hu, Z. and Zhao, X., 2016. AFM tip characterization by using FFT filtered images of step structures. *Ultramicroscopy*, 160, pp.155-162.
- Young, W.C. and Budynas, R.G., 2002. *Roark's formulas for stress and strain* (Vol. 7). New York: McGraw-Hill.
- Zhao, Q.L., Dong, S. and Sun, T., 2001. Investigation of an atomic force microscope diamond tip wear in micro/nano-machining. In *Key Engineering Materials* (Vol. 202, pp. 315-320). Trans Tech Publications.

References

Zhenhua, T. and Bhushan, B., 2006. Wetting properties of AFM probes by mean of contact angle measurment. *Journal of physics D:Applied Physics*, 39 (17) P. 3858.

APPENDIX A1

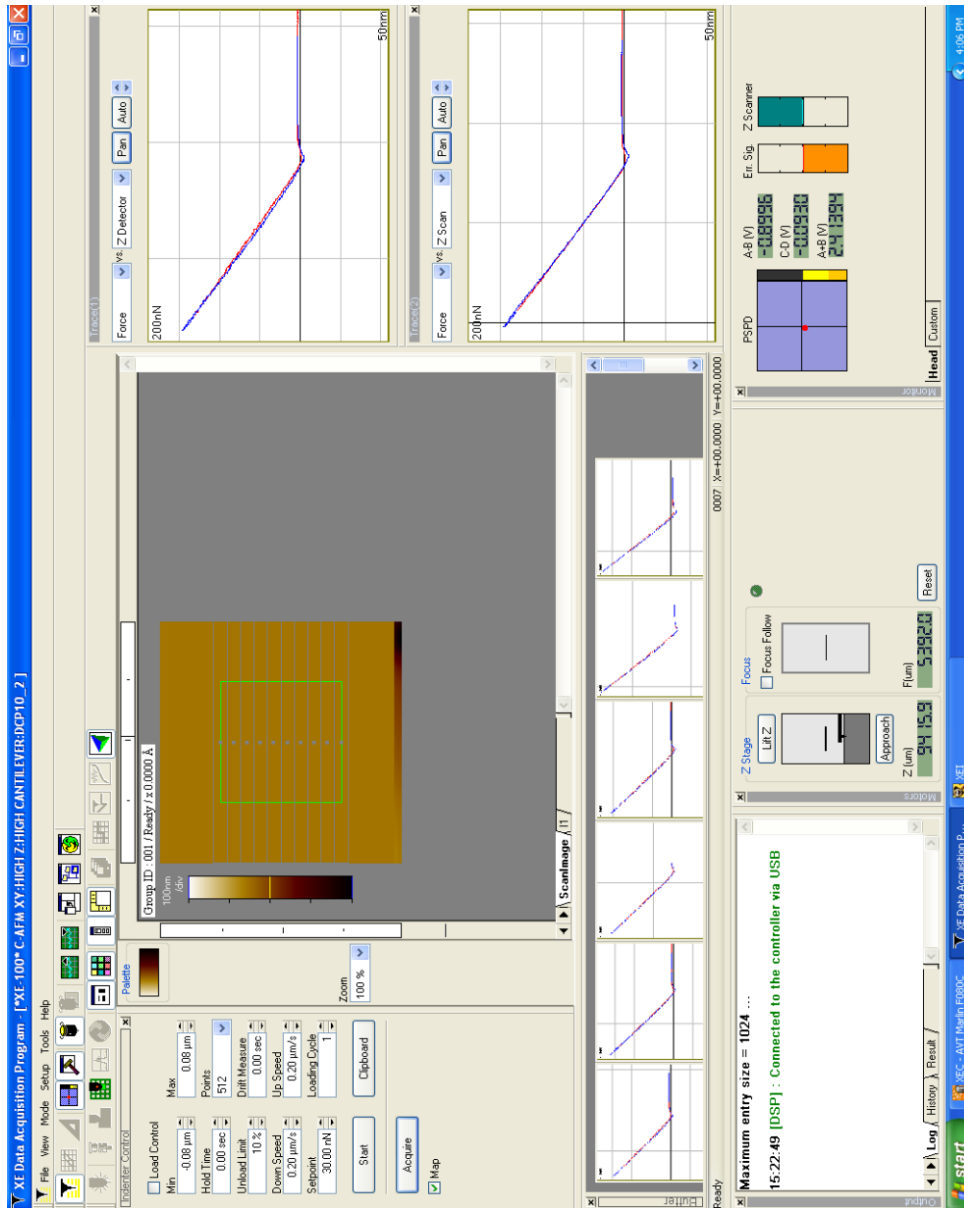


Figure A1.1: Indenter control window

APPENDIX A1

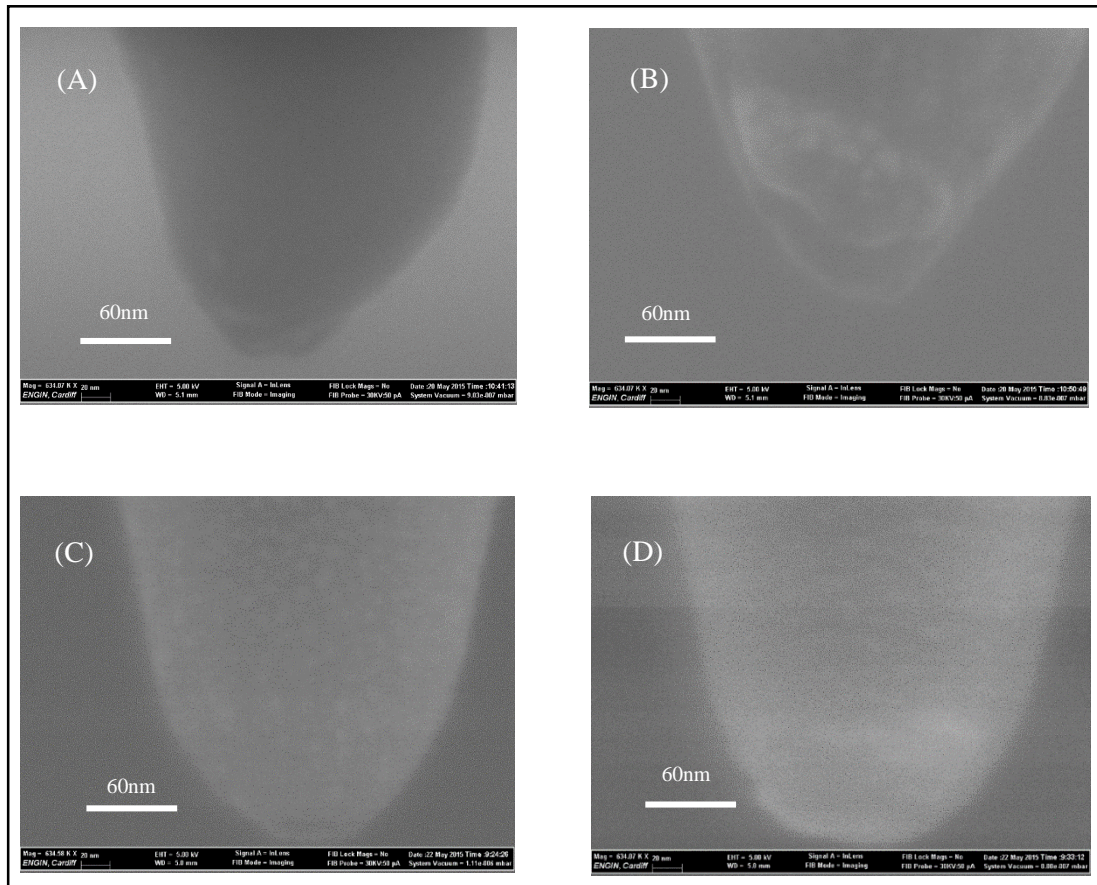


Figure A1.2: SEM image for (A) tip 1, (B) tip 2, (C) tip 3 and (D) tip 4 according to the nomenclature defined in Table 4.1

APPENDEIX A2

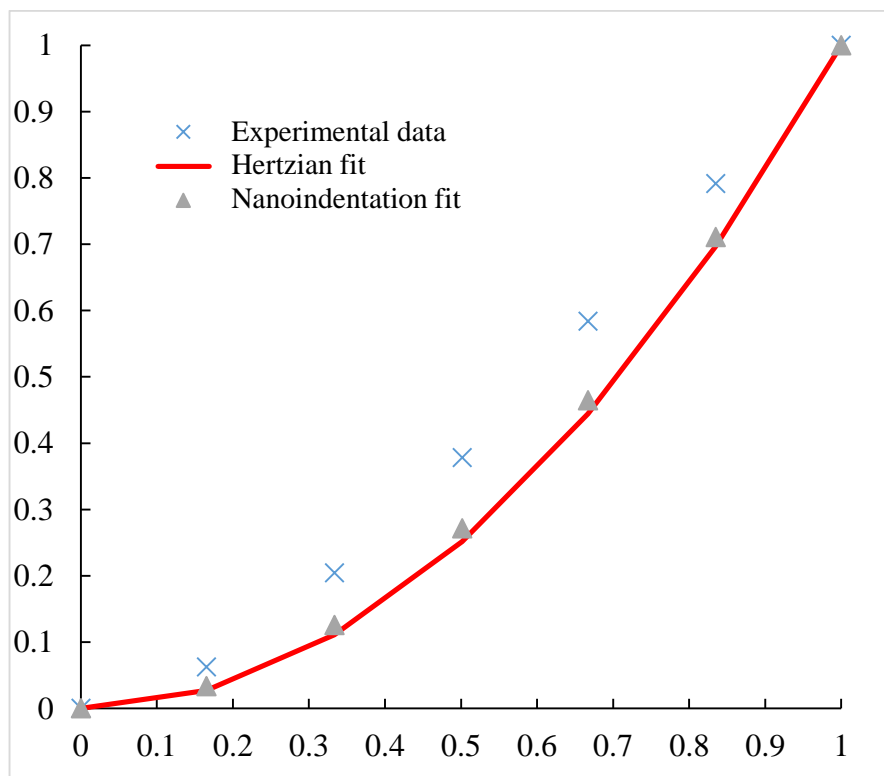
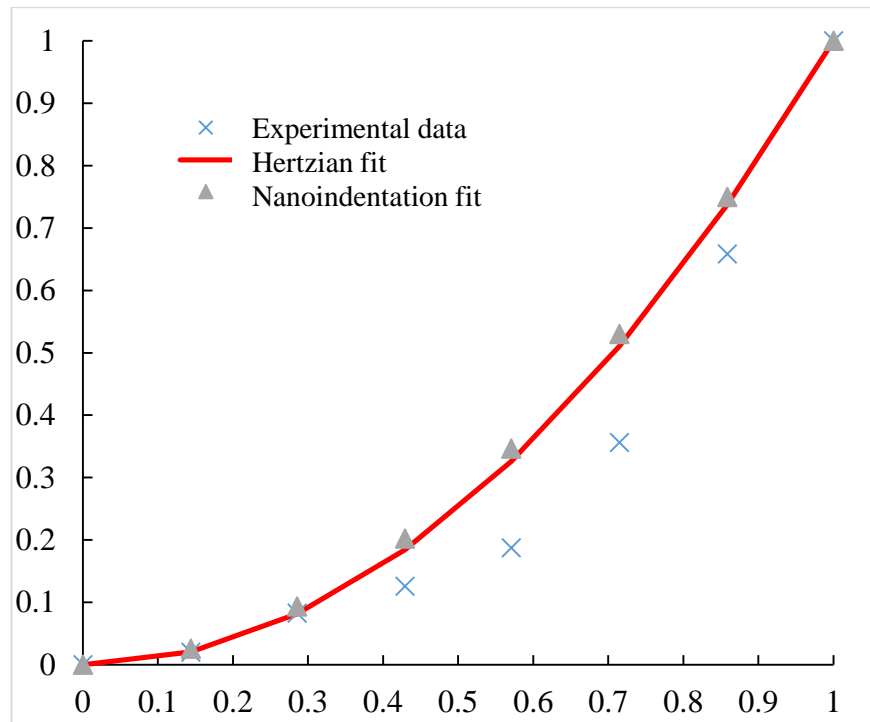


Figure A2.1: Qualitative comparison, for Tip 2 along the 0°-180° profile cross section, of the experimental profile obtained with the reverse imaging method, the profile reconstructed with the spherical assumption (i.e. Hertzian fit) and that reconstructed by considering the d value of the power law function equal to that obtained from the nanoindentation tests.

APPENDEIX A2

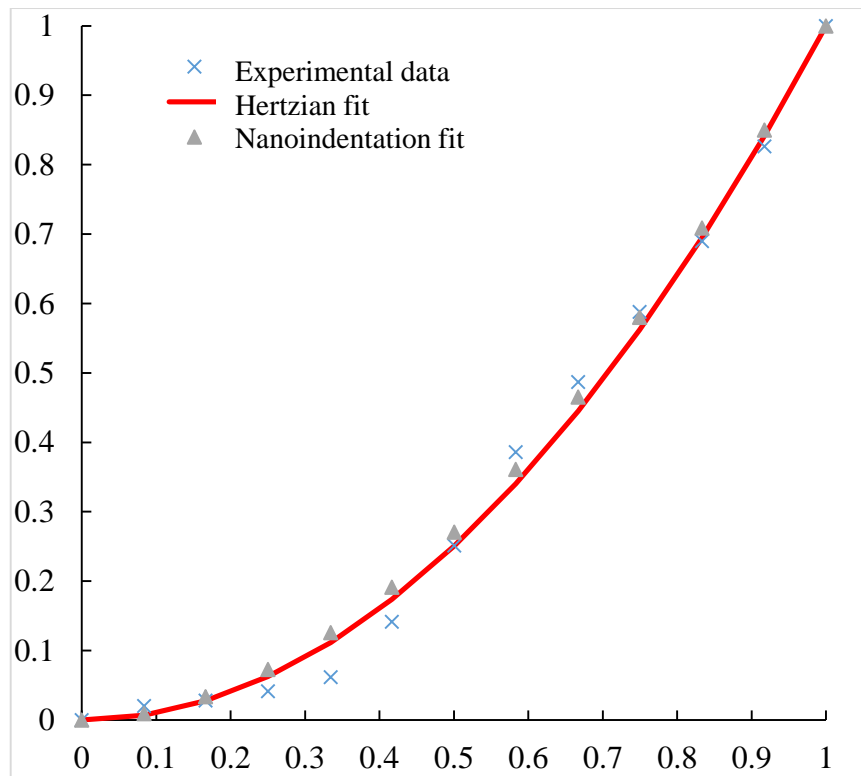
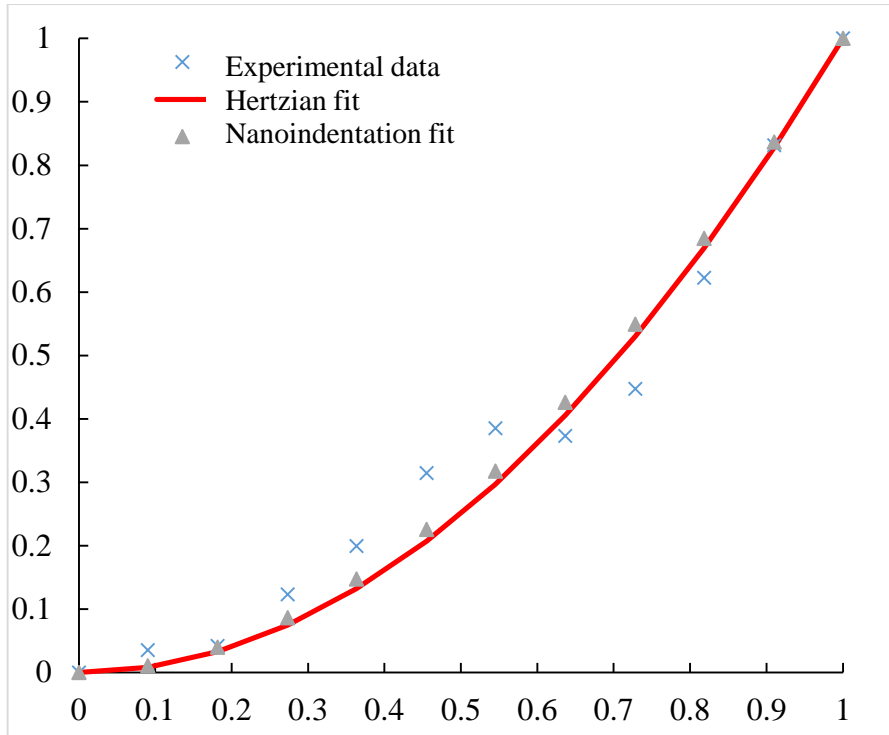


Figure A2.2: Qualitative comparison, for Tip 2 along the 90°-270° profile cross section, of the experimental profile obtained with the reverse imaging method, the profile reconstructed with the spherical assumption (i.e. Hertzian fit) and that reconstructed by considering the d value of the power law function equal to that obtained from the nanoindentation tests.

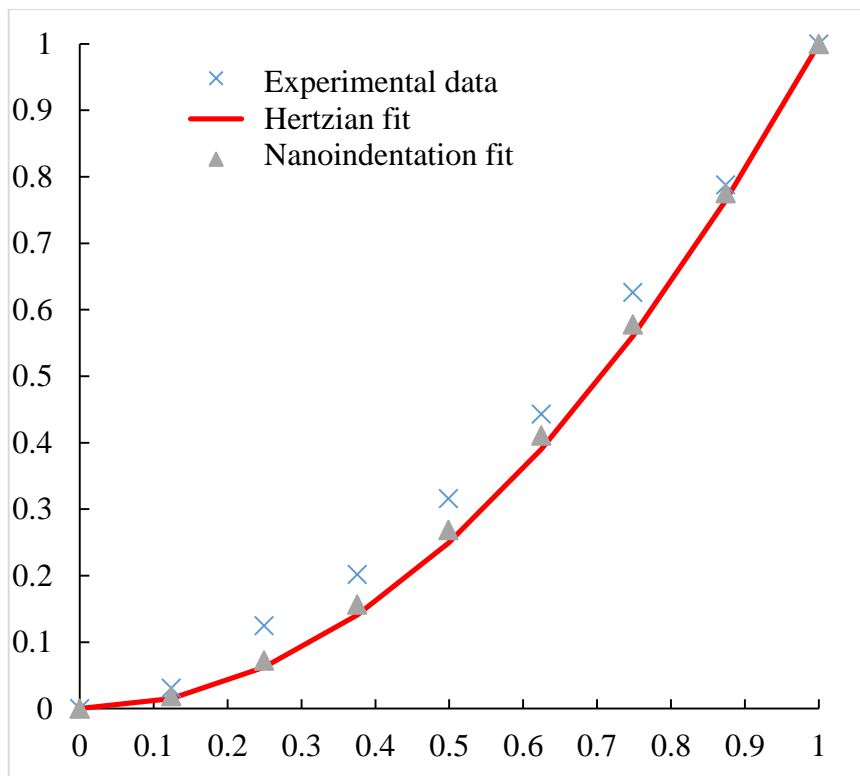
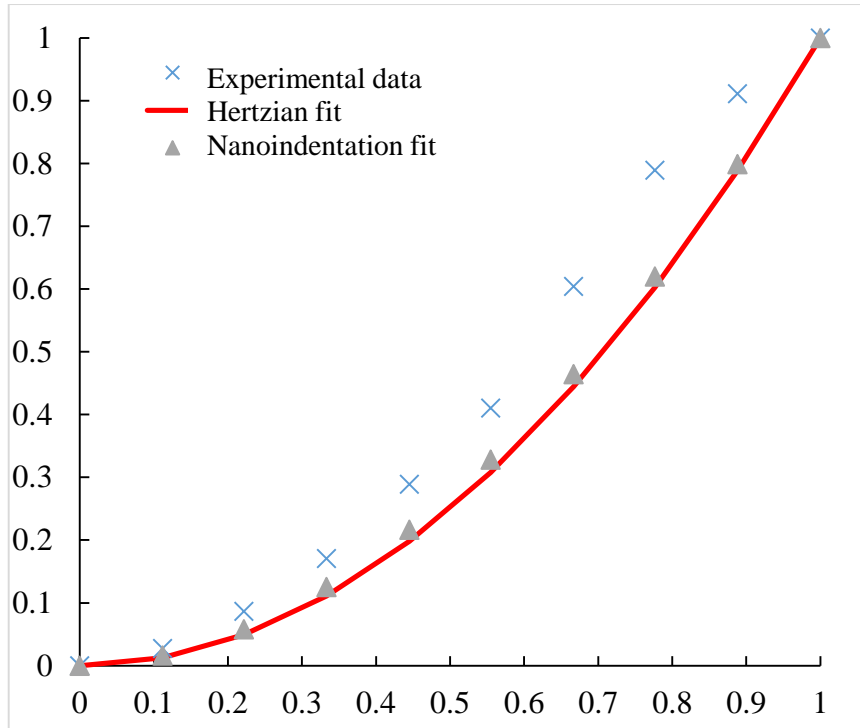


Figure A2.3: Qualitative comparison, for Tip 2 along the 45°-225° profile cross section, of the experimental profile obtained with the reverse imaging method, the profile reconstructed with the spherical assumption (i.e. Hertzian fit) and that reconstructed by considering the d value of the power law function equal to that obtained from the nanoindentation tests.

APPENDEIX A2

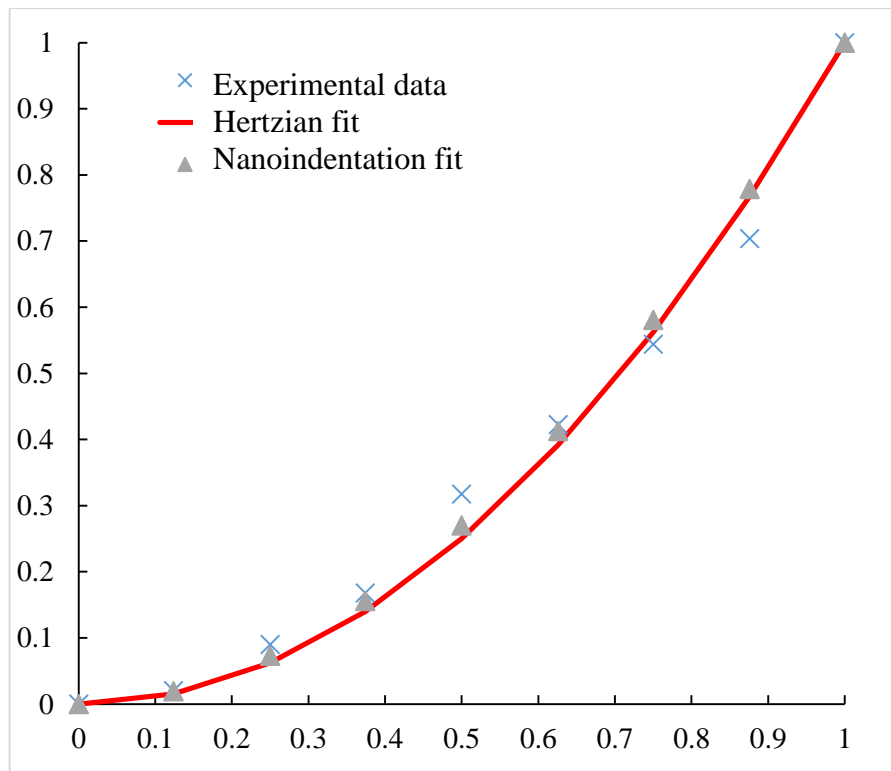
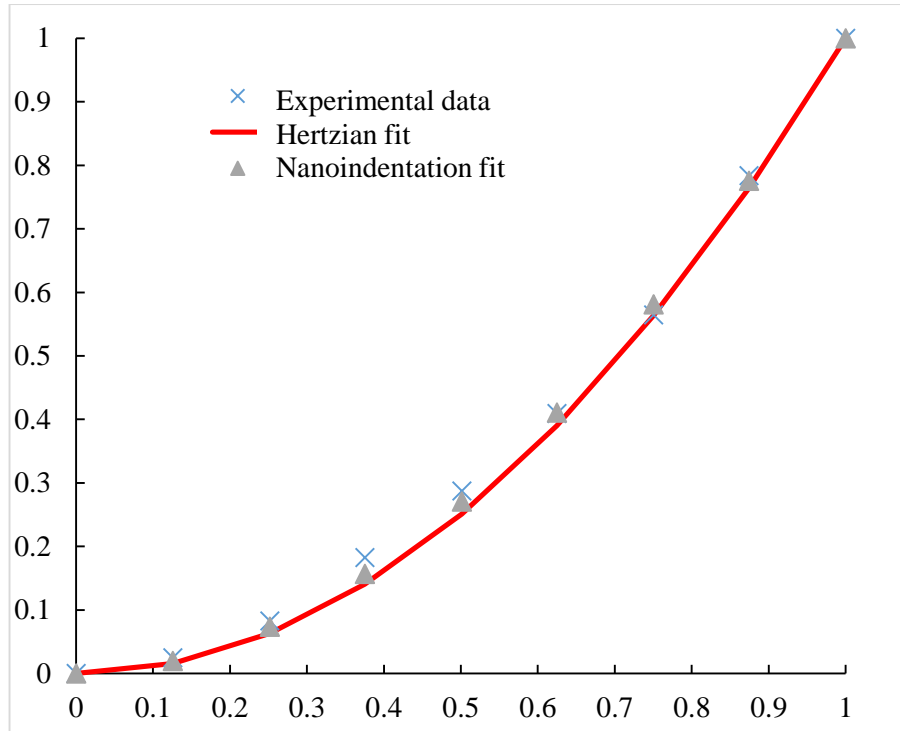


Figure A2.4: Qualitative comparison, for Tip 2 along the 135°-315° profile cross section, of the experimental profile obtained with the reverse imaging method, the profile reconstructed with the spherical assumption (i.e. Hertzian fit) and that reconstructed by considering the d value of the power law function equal to that obtained from the nanoindentation tests.

APPENDEIX A2

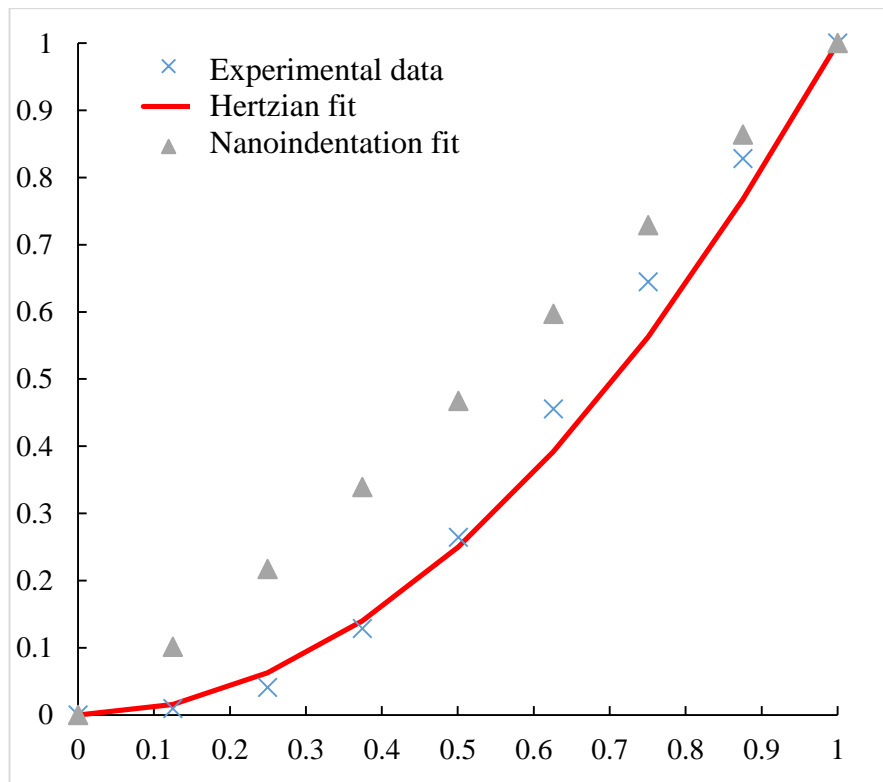
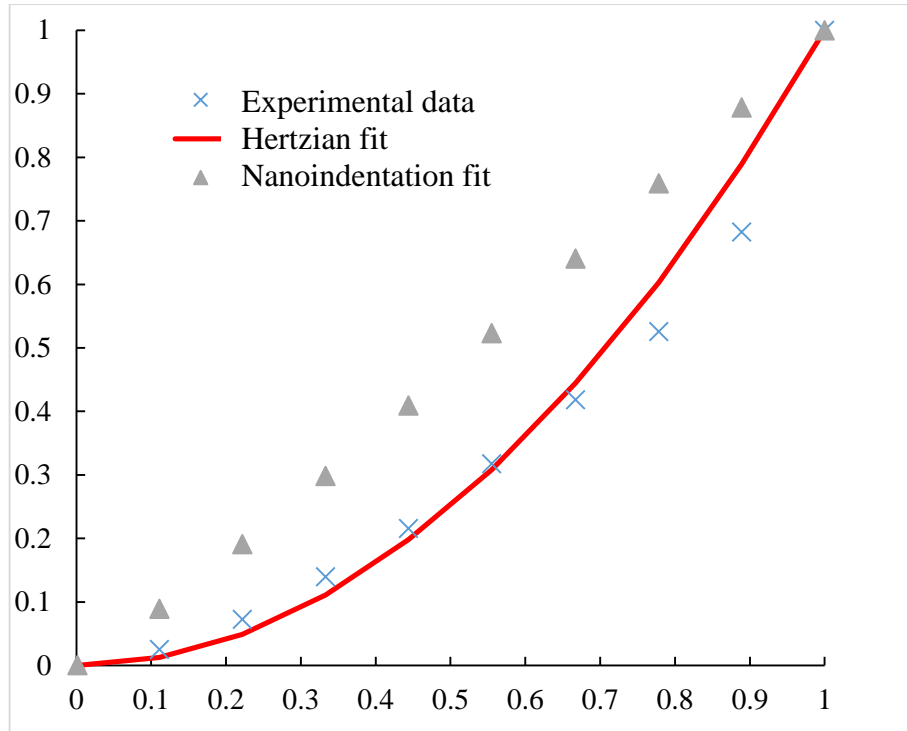


Figure A2.5: Qualitative comparison, for Tip 3 along the 0°-180° profile cross section, of the experimental profile obtained with the reverse imaging method, the profile reconstructed with the spherical assumption (i.e. Hertzian fit) and that reconstructed by considering the d value of the power law function equal to that obtained from the nanoindentation tests.

APPENDEIX A2

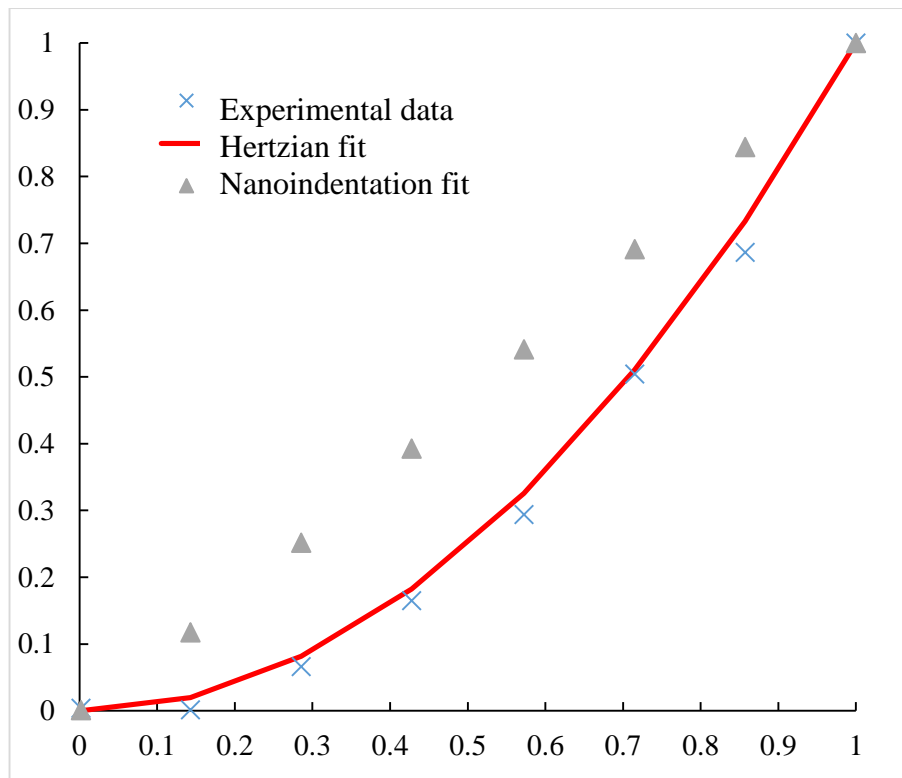
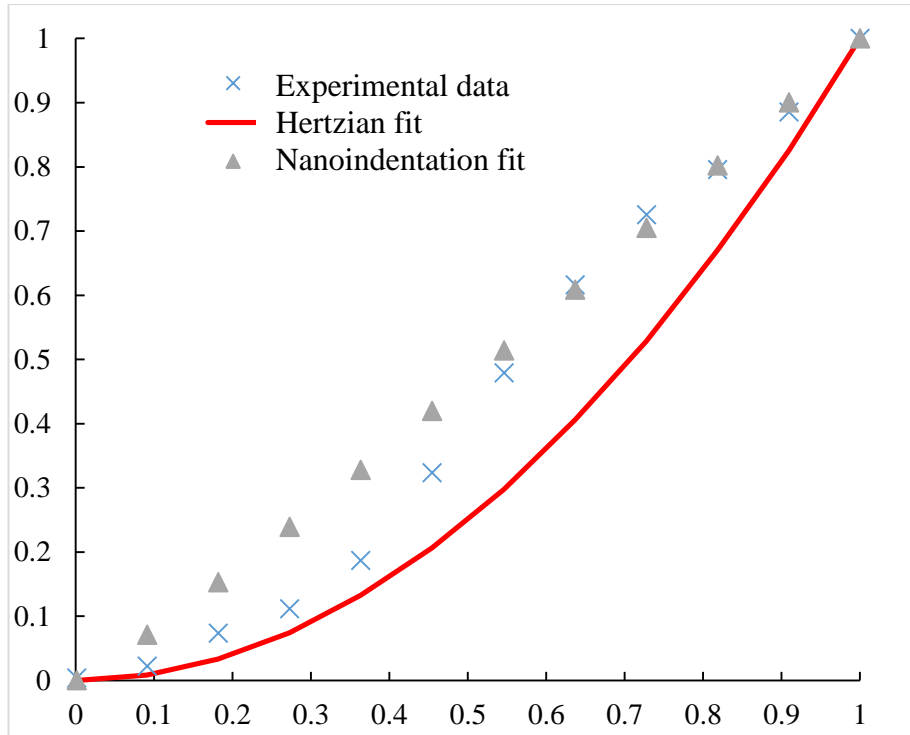


Figure A2.6: Qualitative comparison, for Tip 3 along the 90°-270° profile cross section, of the experimental profile obtained with the reverse imaging method, the profile reconstructed with the spherical assumption (i.e. Hertzian fit) and that reconstructed by considering the d value of the power law function equal to that obtained from the nanoindentation tests.

APPENDEIX A2

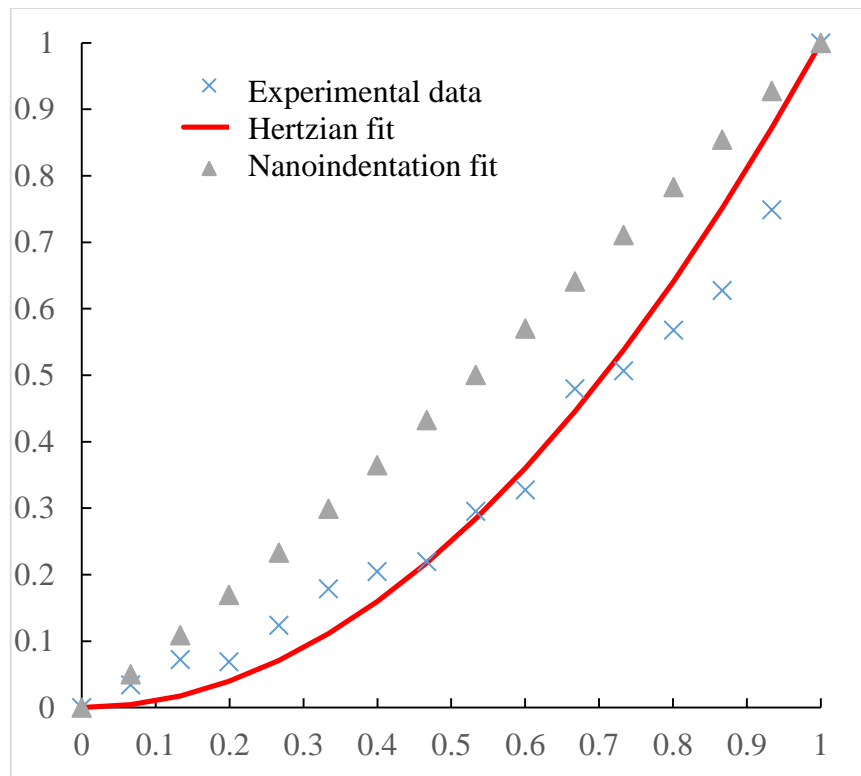
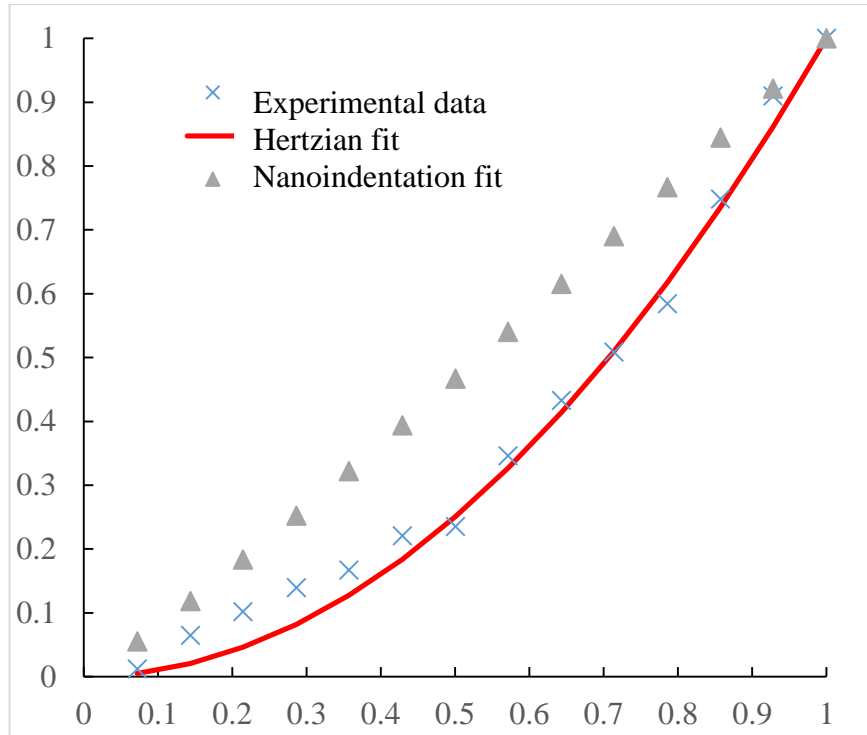


Figure A2.7: Qualitative comparison, for Tip 3 along the 45°-225° profile cross section, of the experimental profile obtained with the reverse imaging method, the profile reconstructed with the spherical assumption (i.e. Hertzian fit) and that reconstructed by considering the d value of the power law function equal to that obtained from the nanoindentation tests.

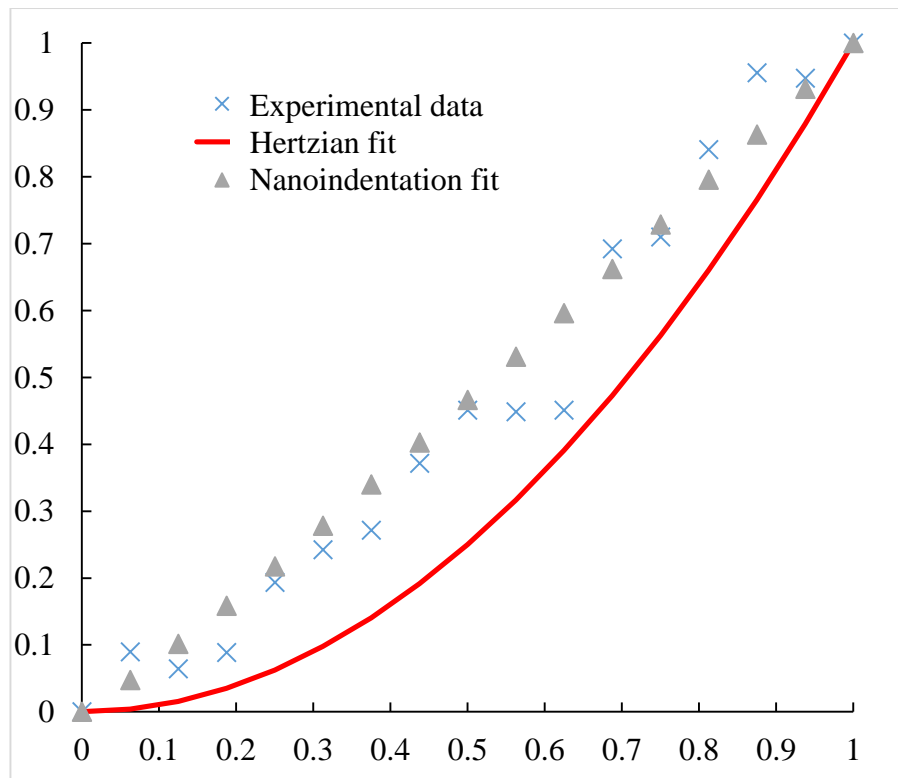
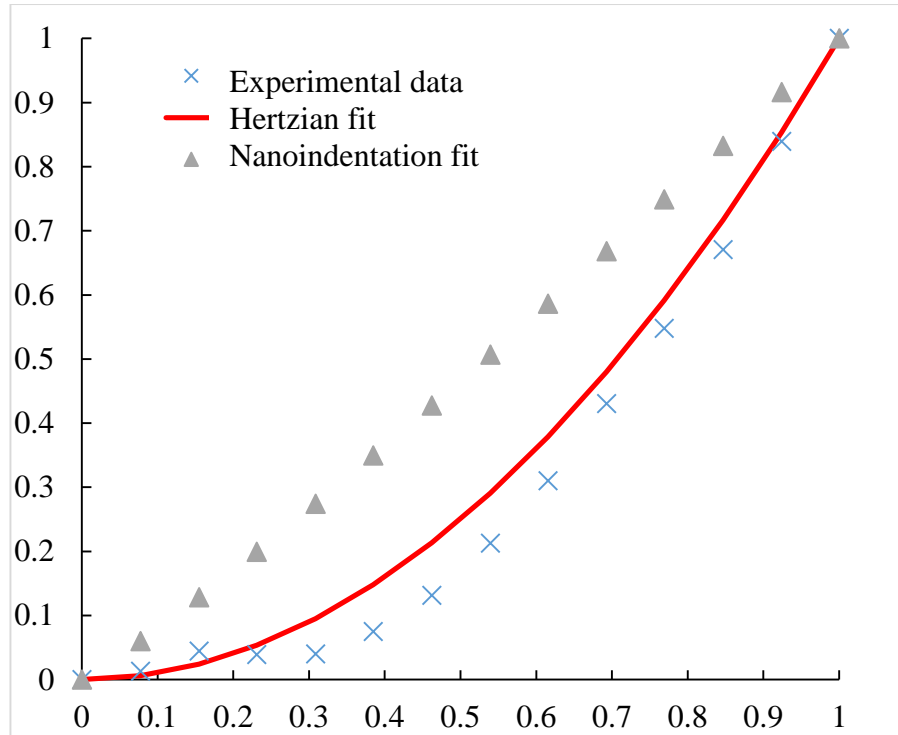


Figure A2.8: Qualitative comparison, for Tip 3 along the 135°-315° profile cross section, of the experimental profile obtained with the reverse imaging method, the profile reconstructed with the spherical assumption (i.e. Hertzian fit) and that reconstructed by considering the d value of the power law function equal to that obtained from the nanoindentation tests.

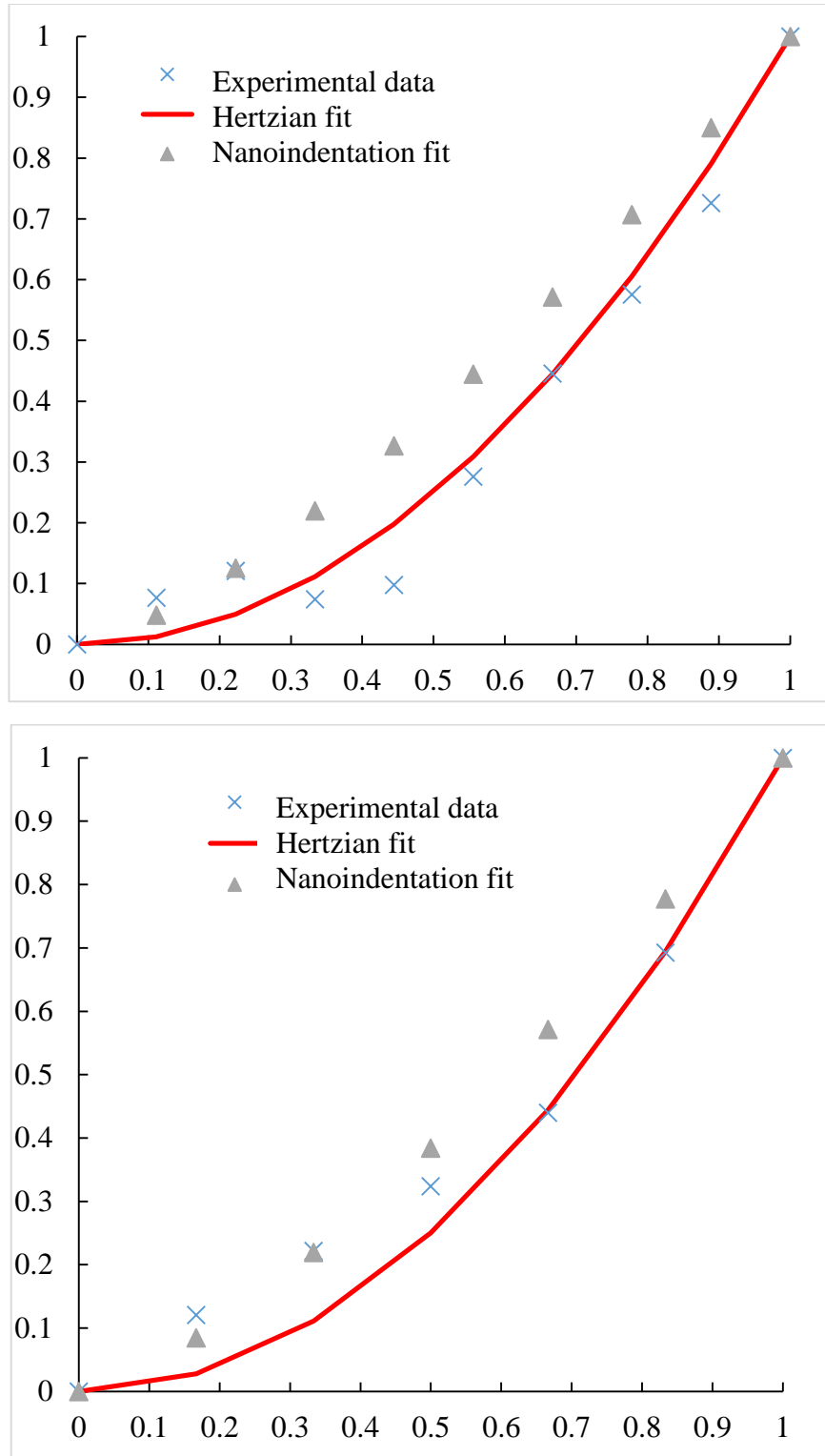


Figure A2.9: Qualitative comparison, for Tip 4 along the 0°-180° profile cross section, of the experimental profile obtained with the reverse imaging method, the profile reconstructed with the spherical assumption (i.e. Hertzian fit) and that reconstructed by considering the d value of the power law function equal to that obtained from the nanoindentation tests.

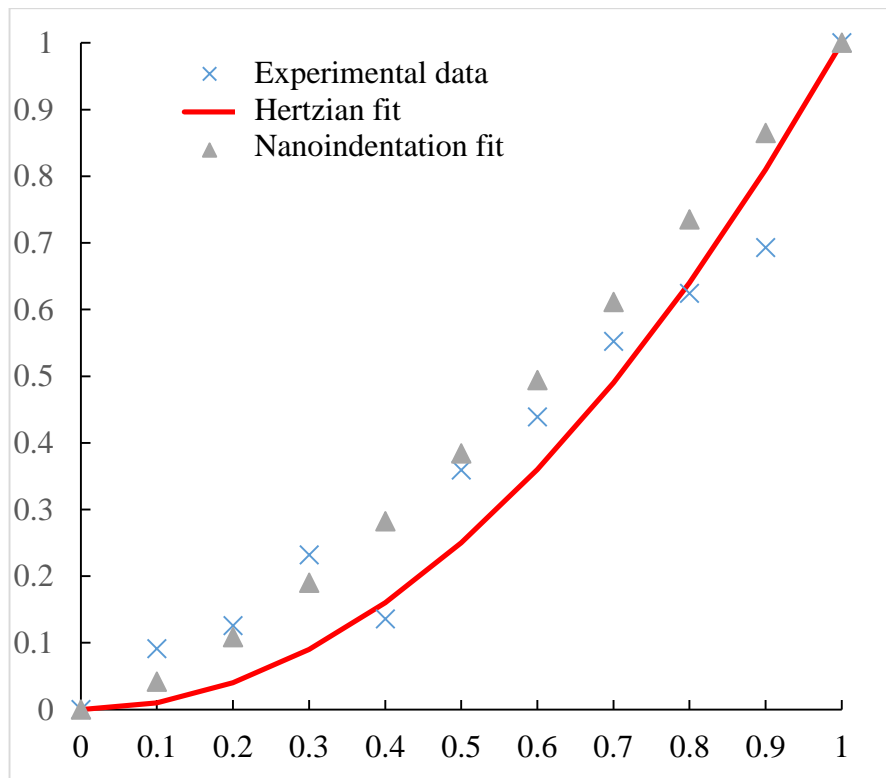
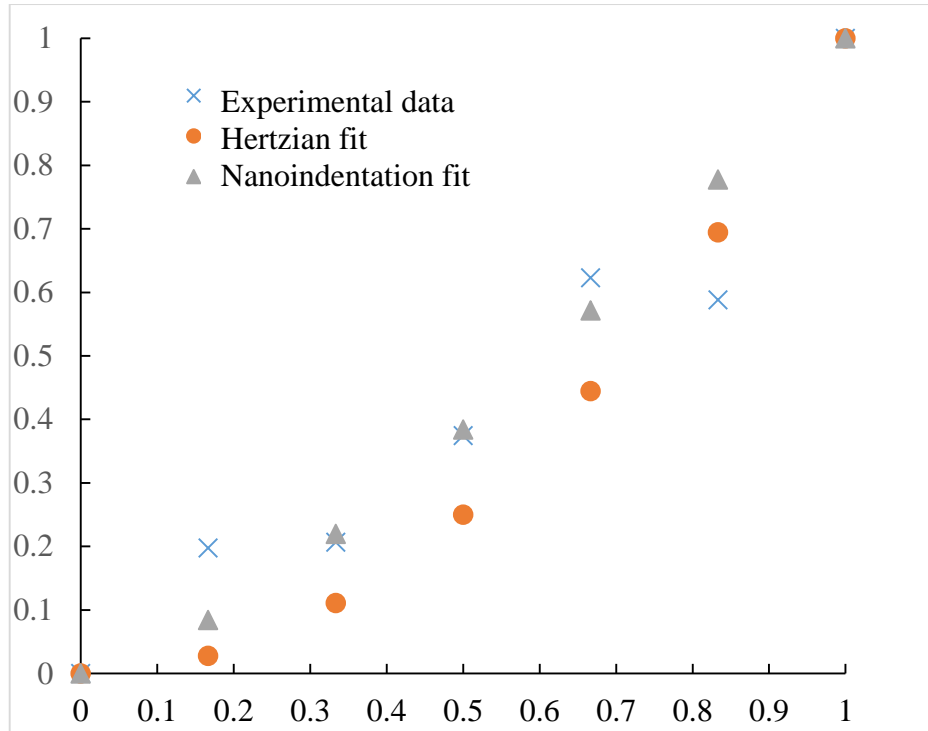


Figure A2.10: Qualitative comparison, for Tip 4 along the 90°-270° profile cross section, of the experimental profile obtained with the reverse imaging method, the profile reconstructed with the spherical assumption (i.e. Hertzian fit) and that reconstructed by considering the d value of the power law function equal to that obtained from the nanoindentation tests.

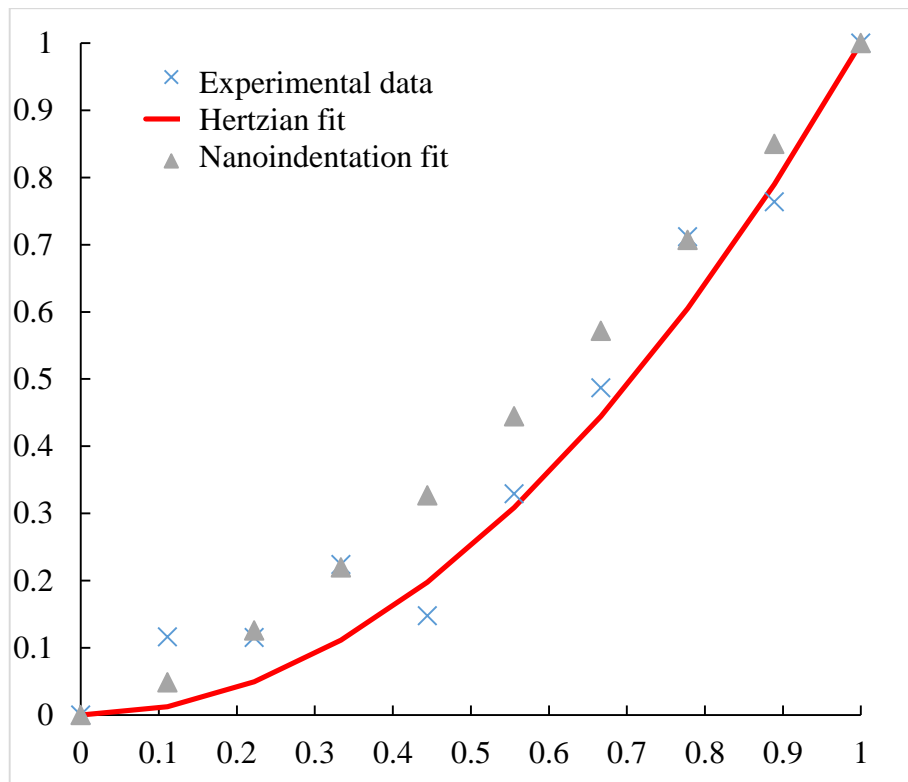
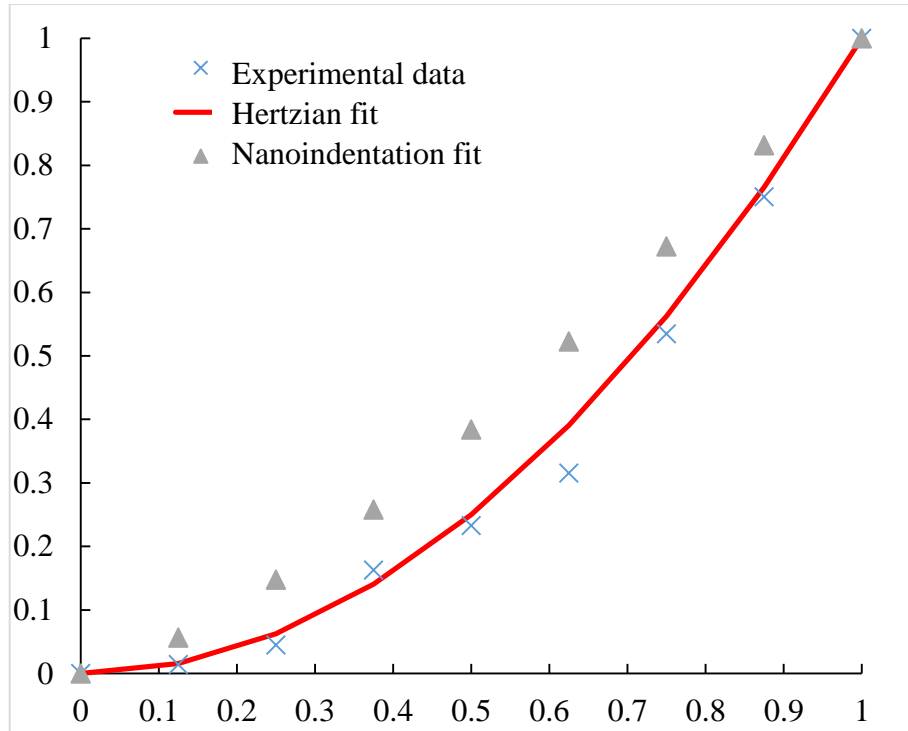


Figure A2.11: Qualitative comparison, for Tip 4 along the 45° - 225° profile cross section, of the experimental profile obtained with the reverse imaging method, the profile reconstructed with the spherical assumption (i.e. Hertzian fit) and that reconstructed by considering the d value of the power law function equal to that obtained from the nanoindentation tests.

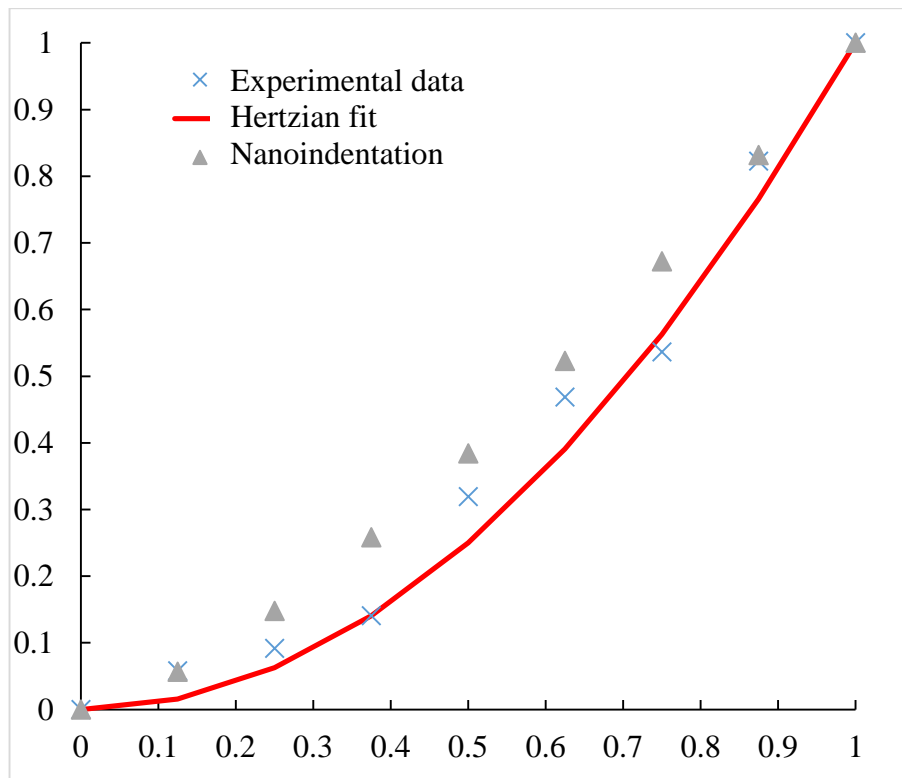
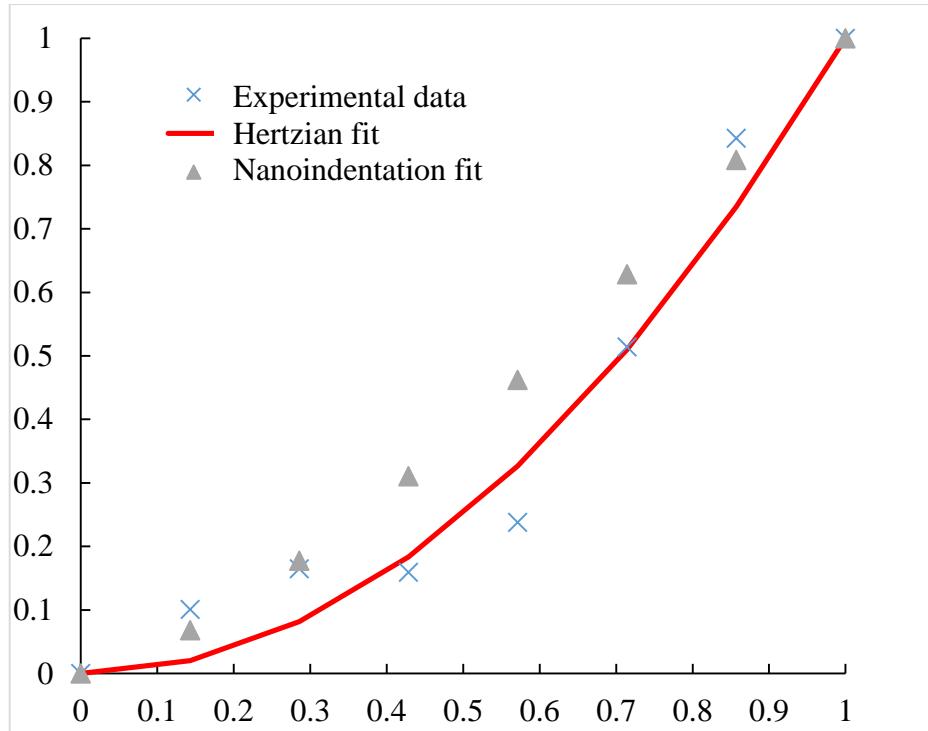


Figure A2.12: Qualitative comparison, for Tip 4 along the 135°-315° profile cross section, of the experimental profile obtained with the reverse imaging method, the profile reconstructed with the spherical assumption (i.e. Hertzian fit) and that reconstructed by considering the d value of the power law function equal to that obtained from the nanoindentation tests.

Description for the different region inside the tip apex geometry:

First, for simplicity, we consider the tip apex geometry as consisting of two parts: a spherical cup near the apex region connected to a cone (Figure A). For each part, the exact volume may be calculated. Hence, we have:

$$V_{ratio} = V_{tip} / V_{cylinder} = V_{(1+2+3)} / V_{cyl} \quad (A3-1)$$

where, the indexes (1, 2 and 3) are attributed to the spherical, inner cylinder and conical parts respectively.

The spherical part (the part 1) volume is:

$$V = \pi h / 6 (3r_1^2 + h_1^2) \quad (A3-2)$$

where r and h are the radius and height respectively. For the inner cylinder (part 2), we have:

$$V = \pi r^2 (h_2 - h_1) \quad (A3-3)$$

where H is the total height of the tip (depth of indentation), while h is the height of the spherical cup region.

The third part is the half shallow cylinder region considered by this equation:

$$V = \pi / 2 (h_2 - h_1) (r_2^2 - r_1^2) \quad (A3-4)$$

In this case, the total height must be considered as $(h_2 - h_1)$ to estimate the specific geometry magnitude above h_1 , the same condition must be done for radius measured value for the shallow cylinder above h_1 and beyond r_1 in which only $(r_2 - r_1)$ is the required radius measured for this region boundary.

Finally, the V_{ratio} for the entire region can be obtained by solving this equation:

$$V_{ratio} = [(\pi h / 6 (3r_1^2 + h_1^2)) + \pi r^2 (h_2 - h_1) + \pi / 2 (h_2 - h_1) (r_2^2 - r_1^2)] / (V_{outer cyl.}) \quad (A3-5)$$

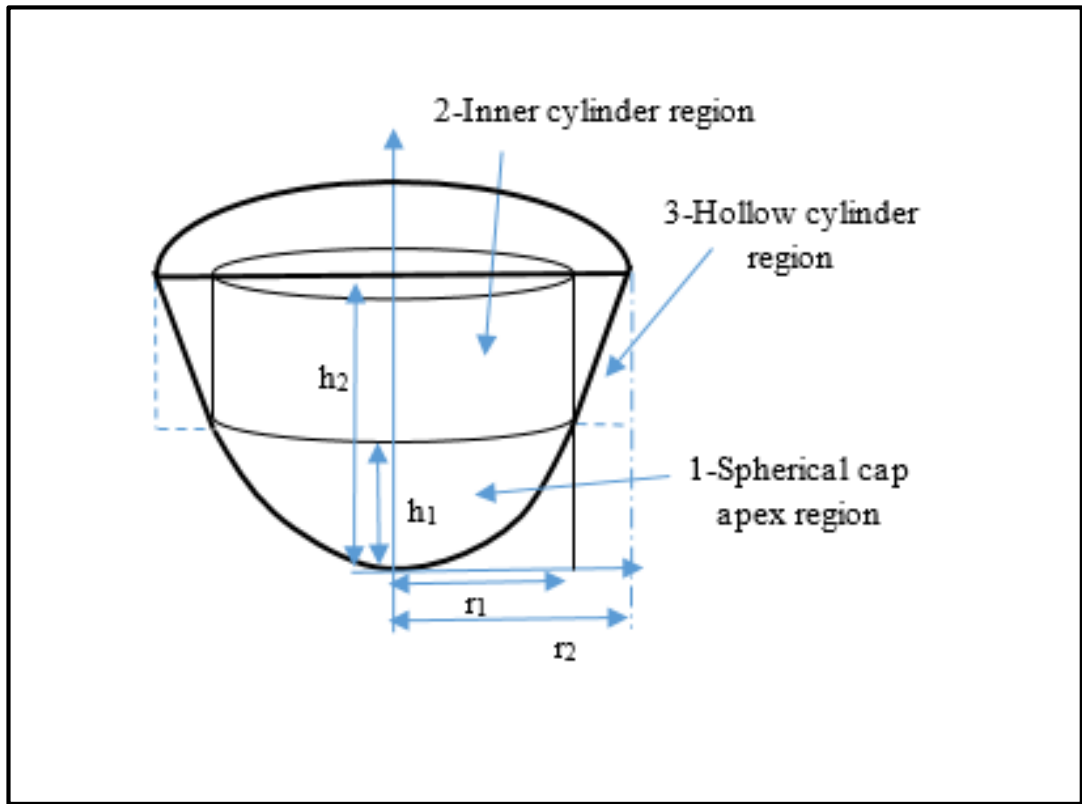


Figure A3.1, Schematic of the different geometrical region utilised to measure apex region volume theoretically.